A N N U A L R E P O R T

2021

and list of publications

Bayerisches Forschungsinstitut
für Experimentelle Geochemie und Geophysik
Universität Bayreuth

Bayerisches Geoinstitut
Universität Bayreuth
95440 Bayreuth
Germany

Telephone: +49-(0)921-55-3700
Telefax: +49-(0)921-55-3769
e-mail: bayerisches.geoinstitut@uni-bayreuth.de
www: https://www.bgi.uni-bayreuth.de

Editorial compilation by: Florian Heidelbach and Petra Buchert
Section editors: Andreas Audétat, Tiziana Boffa Ballaran, Audrey Bouvier,
Leonid Dubrovinsky, Dan Frost, Florian Heidelbach, Gregor Golabek,
Tomoo Katsura, Hans Keppler, Catherine McCammon,
Nobuyoshi Miyajima, Dave Rubie, Gerd Steinle-Neumann, Tony Withers

Staff and guests of the Bayerisches Geoinstitut in **July 2021**:

Die Mitarbeiter und Gäste des Bayerischen Geoinstituts im **Juli 2021:**

first row, from left (1. Reihe, v. links) Alexander Rother, Lisa Eberhard, Remco Hin, Catherine McCammon, Tiziana Boffa Ballaran, Dorothea Wiesner, Laura Czekay, Sergey Ovsyannikov, Marija Putak Juriček

second row, from left (2. Reihe, v. links) Florian Heidelbach, Dan Frost, Jonathan Dolinschi, Lucas Calvo, Rizaldi Putra, Petra Buchert, Caterina Melai, Serena Dominijanni, Daniela Bubmann, Ulrike Trenz

third row, from left (3. Reihe, v. links) Stefan Übelhack, Christopher Howard, Alexander Kurnosov, Sven Linhardt, Laura Cialdella, Elena-Marie Rogmann, Tony Withers, Heinz Fischer, Lianjie Man, Nicolas Walte

back rows, from left (hintere Reihen, v. links) Jingbo Zhang, Siqi Liu, Hongzhan Fei, Xiaoyu Wang, Ran Zhao, Anna Dinius, Melanie Pöppelbaum, Jie Yao, Kirsten Schulze, Timofey Fedotenko, Raphael Njul, Leonid Dubrovinsky, Nobuyoshi Miyajima, Gerd Steinle-Neumann, Adrien Néri, Hans Keppler, Lin Wang, Saiana Khandarkhaeva, Fei Wang, Jia Chang, Dominic Langhammer, Rebecka Matthäus, Andreas Audétat, Danilo Di Genova, Dan Liu, Detlef Krauße, Liang Yuan, Oliver Rausch, Dave Rubie, Dmitry Bondar, Audrey Bouvier

Absent (Es fehlten) Sumith Abeykoon, Alena Aslandukova, Gerald Bauer, Giacomo Criniti, Timofey Fedotenko, Michaela Flanigan, Gregor Golabek, Tomoo Katsura, Eun Jeong Kim, Edna Obengo, Esther Posner, Anke Potzel, Janina Potzel, Narangoo Purevjav, Greta Rustioni, Marcel Thielmann, Kirill Vlasov, Longjian Xie

The new laboratories for geochemistry and cosmochemistry on the second and third upper floor of the BGI building.

Contents

Foreword

The year 2021 at the Bayerisches Geoinstitut was again somewhat unusual due to the effects of the corona pandemic. However, we managed to keep our laboratories in normal operation without any interruption and the scientific productivity of the institute is unchanged. Scientific and technical staff members adapted quickly to the new circumstances and made enormous efforts to implement reasonable safety measures, while keeping daily operations as normal as possible. It was very pleasant to see that despite the additional complications, the construction of the new laboratories for isotope geochemistry and cosmochemistry (see the picture in front of the book) progressed rapidly. With the approval for funding of a newest generation mass spectrometer by the DFG, these laboratories are expected to be in full operation within this year.

The scientific contributions in this annual report cover a wide range of topics looking at processes in Earth's crust, mantle, and core, from the earliest days of planetary formation to ongoing processes. In addition to the experimental studies, which are the core expertise of the Bayerisches Geoinstitut, there is an increasing number of geodynamic modelling contributions and of analytical studies of extraterrestrial materials. Very often, some of our Ph. D. students are the leading authors of pioneering investigations. I am therefore very pleased that I can again highlight here two contributions from our young scientists.

Plate tectonics is a unique feature of Earth and does not occur on any other planet of our solar system. Geodynamic models suggest that for stabilizing plate tectonics on a planet, a channel of low viscosity below the plates may be required. This channel may be identical with the "LVZ", the seismic low velocity zone that is observed at depths of about 80 to 220 km below the surface. In this depth range, the velocities of seismic waves are reduced and a possible cause for this could be the presence of a small fraction of melt in the mantle peridotite. However, the temperatures at these depths are below the "dry" mantle melting temperatures and therefore, melting is only possible in the presence of traces of water or other volatiles, which may greatly reduce the solidus temperatures. How large this effect is, however, and whether it is sufficient to stabilize melts in the LVZ, has been the subject of major debates in recent years. One of the problems here is that it is very difficult to accurately control low water contents in experiments and the detection of small fractions of melt is also problematic. Accordingly, estimates of the melting point depression of water in mantle systems vary widely. In a contribution on page 104 of this annual report, Marija Putak Juricek has elegantly solved these problems. Rather than trying to load small fractions of water into sample capsules, she carried out melting experiments at low pressures where water fugacities can be precisely controlled by confining pressure. Moreover, she studied the diopside-anorthite system, where large melt fractions form immediately at the solidus and accordingly, melting temperatures can be determined with high precision. By comparing the melting point depression observed in these experiments with direct measurements of melt water contents, she derived a model for melting in the presence of traces of water in the mantle. The model shows that the effect of water in reducing melting

temperatures is at the upper limit of previous experimental data and much stronger than in currently used models. Accordingly, the presence of a small fraction of hydrous melt in the seismic low velocity zone is quite plausible.

In the uppermost mantle, the temperature profile is well constrained by mineral equilibria preserved in pieces of mantle rocks brought to the surface by active volcanoes. However, the deeper one looks into the mantle, the more uncertain temperatures become. This is because seismic data, the main information source about Earth's interior, do not directly constrain temperature. Current ideas about the temperatures in the deeper mantle are therefore all model-dependent. The contribution by Lianjie Man on page 80 could potentially change this situation. He experimentally investigated the solubility of aluminum in ferropericlase (Mg,Fe)O. This mineral is often found as inclusions in "ultradeep" diamonds originating from the lower mantle and sometimes it coexists with Al-rich phases. Lianjie Man observed experimentally that in this situation, the Al solubility in ferropericlase depends very strongly on temperature, but much less on pressure. This system could therefore be a very promising "geothermometer" to directly constrain temperatures in the deep mantle.

On the behalf of my colleagues, I would like to thank the *Free State of Bavaria* as represented by the *Bavarian State Ministry of Science, Research and Art*, as well as the *Commission for High-Pressure Research in Geoscience* for their continuing support and strong commitment to the Bayerisches Geoinstitut. I would further like to thank the *President and Leadership of the University of Bayreuth* for their high regard of our institute. We also gratefully acknowledge generous support from external funding agencies, in particular the *Alexander von Humboldt Foundation*, the *European Union*, the *German Science Foundation,* and the *Federal Ministry of Education and Research*, which continue to contribute greatly to the further development and success of the Geoinstitut.

Bayreuth, March 2022 Hans Keppler

Vorwort

Aufgrund der Corona-Pandemie war 2021 wieder ein etwas ungewöhnliches Jahr am Bayerischen Geoinstitut. Wir konnten jedoch unsere Labore ohne Unterbrechung im normalen Betrieb halten und die wissenschaftliche Produktivität des Instituts ist unverändert. Unsere Wissenschaftler und technischen Mitarbeiter haben sich sehr schnell an die neuen Bedingungen angepasst und mit großen Anstrengungen unter Berücksichtigung vernünftiger Schutzmaßnahmen den normalen Betrieb aufrechterhalten. Erfreulicherweise hat auch die Konstruktion der neuen Labore für Isotopen-Geochemie und Kosmochemie (siehe Bild am Anfang des Buches) trotz der schwierigen Umstände rasche Fortschritte gemacht. Mit der Genehmigung der Finanzierung eines Massenspektrometers neuester Generation durch die DFG sollten diese Labore noch in diesem Jahr im vollen Betrieb sein.

Die wissenschaftlichen Beiträge in diesem Jahresbericht beschäftigen sich mit Prozessen in der Kruste, dem Mantel und dem Kern der Erde, von den frühesten Zeiten der Planetenentstehung bis zur Gegenwart. Zusätzlich zu den experimentellen Arbeiten, die das Hauptarbeitsgebiet des Geoinstituts sind, gibt es eine zunehmende Anzahl von Arbeiten zur geodynamischen Modellierung sowie analytische Untersuchungen von extraterrestrischen Materialien. Sehr oft sind junge Doktoranden die Hauptträger des wissenschaftlichen Fortschritts. Ich freue mich daher sehr, dass ich hier wieder zwei Beiträge von jungen Wissenschaftlern besonders hervorheben kann.

Plattentektonik ist eine Besonderheit der Erde, die auf keinem anderen Planeten unseres Sonnensystems vorkommt. Wahrscheinlich kann Plattentektonik auf einem Planeten nur existieren, wenn es einen Kanal niedriger Viskosität unter den Platten gibt. Dieser Kanal ist möglicherweise identisch mit der "LVZ", der Zone niedriger seismischer Geschwindigkeiten in einer Tiefe von 80 bis 220 km unter der Oberfläche. In diesem Tiefenbereich sind die Geschwindigkeiten seismischer Wellen reduziert, was möglicherweise durch einen geringen Anteil von Schmelze im Mantel-Peridotit verursacht wird. Die Temperaturen in diesem Tiefenbereich sind jedoch unterhalb der "trockenen" Schmelztemperatur des Mantels. Schmelzbildung ist daher nur möglich in der Gegenwart von Wasser oder von anderen flüchtigen Bestandteilen, die die Schmelztemperatur stark herabsetzen. Wie groß dieser Effekt ist und ob er ausreicht, um Schmelze in der LVZ zu stabilisieren, ist jedoch nach wie vor umstritten. Eines der Probleme ist hier, dass es sehr schwer ist, geringe Wassergehalte in Experimenten genau einzustellen und der Nachweis geringer Schmelzmengen ist ebenfalls problematisch. Dementsprechend gibt es sehr unterschiedliche Vorstellungen über den Effekt kleiner Mengen an Wasser auf den Schmelzpunkt des Erdmantels. In einem Beitrag auf Seite 104 dieses Jahresberichts hat Marija Putak Juricek dieses Problem auf elegante Weise gelöst. Anstatt zu versuchen, geringe Mengen an Wasser in Probenkapseln zu laden, hat sie Schmelzexperimente bei niedrigem Druck ausgeführt, wo die Wasser-Fugazität durch den Umgebungsdruck genau eingestellt werden kann. Sie untersuchte das Diopsid-Anorthit-System, wo sich große Mengen an Schmelze unmittelbar am Solidus bilden, so dass die

Schmelztemperatur sehr genau bestimmt werden kann. Durch Vergleich der Schmelzpunkterniedrigung in diesen Experimenten mit direkten Messungen des Wassergehaltes in der Schmelze konnte sie ein Modell für das Schmelzen des Mantels in der Gegenwart von Spuren von Wasser entwickeln. Dieses Modell zeigt, dass Wasser die Solidustemperatur viel stärker herabsetzt, als in gängigen Modellen angenommen wird. Der beobachtete Effekt ist an der Obergrenze früherer Messungen. Es ist daher durchaus plausibel, dass geringe Anteile von Schmelze für die Zone niedriger seismischer Geschwindigkeiten im Mantel verantwortlich sind.

Im obersten Mantel ist das Temperaturprofil ziemlich gut bekannt. Die entsprechenden Daten stammen aus Gleichgewichten zwischen Mineralen in Bruchstücken des Erdmantels, die von Vulkanen an die Erdoberfläche transportiert wurden. Je tiefer man in den Mantel hineinschaut, umso unsicherer werden jedoch die Temperaturen. Dies liegt daran, dass seismische Daten, die Hauptinformationsquelle über das Erdinnere, nur indirekte Informationen über die Temperatur enthalten. Die gegenwärtigen Vorstellungen über die Temperaturen im tieferen Mantel sind daher alle Modell-abhängig. Der Beitrag von Lianjie Man auf Seite 80 könnte das möglicherweise ändern. Er hat experimentell die Löslichkeit von Aluminium in Ferroperiklas (Mg,Fe)O untersucht. Dieses Mineral wird oft als Einschluss in "ultratiefen" Diamanten gefunden, die aus dem unteren Mantel stammen. Ferroperiklas koexistiert hier oft mit Al-reichen Phasen. Lianjie Man beobachtete in seinen Experimenten, dass die Al-Löslichkeit in Ferroperiklas stark von der Temperatur abhängt, während sie vom Druck nur wenig beeinflusst wird. Dieses System könnte daher ein sehr gutes "Geothermometer" für die direkte Bestimmung von Temperaturen im tiefen Mantel sein.

Meine Kollegen und ich möchten dem *Freistaat Bayern*, vertreten durch das *Bayerische Staatsministerium für Wissenschaft, Forschung und Kunst*, und der *Kommission für Geowissenschaftliche Hochdruckforschung der Bayerischen Akademie der Wissenschaften* unseren Dank für ihre fortwährende Unterstützung des Bayerischen Geoinstituts aussprechen. Darüber hinaus möchten wir dem Präsidenten und der Hochschulleitung der Universität Bayreuth ausdrücklich für ihre zuverlässige und kontinuierliche Unterstützung unseres Instituts danken. Wir sind auch für die großzügige Förderung durch externe Geldgeber dankbar, insbesondere der *Alexander-von-Humboldt-Stiftung*, der *Europäischen Union* und der *Deutschen Forschungsgemeinschaft*, die ebenfalls wesentlich zur Entwicklung und zum Erfolg des Bayerischen Geoinstituts beigetragen haben.

Bayreuth, im März 2022 Hans Keppler

1. Advisory Board and Directorship

1.1 Advisory Board

The *Beirat für Geowissenschaftliche Hochdruckforschung der Bayerischen Akademie der Wissenschaften* advises on the organisation and scientific activities of the institute. Members of this board are:

Prof. Dr. Gerhard BREY *until September 2021*	Institut für Geowissenschaften der Johann Wolfgang Goethe-Universität, Frankfurt am Main
Prof. Dr. Ulrich CHRISTENSEN	Emeritus, Max-Planck-Institut für Sonnensystem-forschung, Göttingen
Prof. Dr. Rudolf GROSS (Vice Chairman)	Walther-Meißner-Institut für Tieftemperatur-forschung (WMI), Garching
Prof. Dr. Francois HOLTZ	Institut für Mineralogie der Leibnitz Universität Hannover
Prof. Dr. Klaus MEZGER	Institut für Geologie der Universität Bern
Prof. Dr. Herbert PALME	Emeritus, Institut für Mineralogie und Geochemie der Universität zu Köln – Senckenberg Forschungsinstitut und Naturmuseum Frankfurt/M.
Prof. Dr. Markus RIEDERER (Chairman)	Julius-von-Sachs-Institut für Biowissenschaften, Würzburg
Prof. Dr. Ekhard SALJE, FRS, FRSA	Department of Earth Sciences, University of Cambridge
Prof. Dr. Christine THOMAS	Institut für Geophysik der Westfälischen Wilhelms-Universität Münster

1.2 Leadership

Prof. Dr. Hans KEPPLER (Director)
Prof. Dr. Dan FROST (Deputy Director)
Prof. Dr. Tomoo KATSURA

2. Staff, Funding and Facilities

2.1 Staff

At the end of 2021 the following staff positions existed in the Institute:

- Scientific staff: **16**
- Technical staff: **14**
- Administrative staff: **2**
- Administrative officer: **1**

During 2021, 35 scientific positions (282.5 months) were funded by grants raised externally by staff members of the institute. In addition, 4 long-term scientific positions (26 months) were funded by the resources of the BGI Visiting Scientists' Programme (see Sect. 8), which also supported short-term visits for discussing future projects or presenting research results (see Sect. 5). 7 student assistants (72 months) were funded by externally raised grants. 10 scientists, 3 PhD students, and 1 master student (132.5 months) were supported by personal grants or stipends.

2.2 Funding

In 2021, the following financial resources were available from the Free State of Bavaria:

- Visiting Scientists' Programme: 164.000 €
- Consumables: 694.000 €
- Investment funding: 60.000 €

The total amount of national/international external funding *("Drittmittel"*) used for ongoing research projects in 2021 was 2.508.000 € (Positions: 1.855.000 €; equipment, consumables and travel grants: 653.000 €).

	positions	**equipment, consumables, travel grants**	**total**
• AvH	41.000 €	18.000 €	59.000 €
• BMBF	116.000 €	87.000 €	203.000 €
• DFG	1.336.000 €	428.000 €	1.764.000 €
• EU	255.000 €	111.000 €	366.000 €
• Others	107.000 €	9.000 €	116.000 €
	1.855.000 €	**653.000 €**	**2.508.000 €**

(AvH = Alexander von Humboldt Foundation; BMBF = Federal Ministry of Education and Research; DFG = German Science Foundation; EU = European Union; Others: DAAD, Chinese Science Council, Japanese Society for the Promotion of Science, Swiss National Science Foundation)

In the following list only the BGI components of the funding are listed in cases where joint projects involved other research institutions. Principal investigators and the duration of the grants are listed in brackets. Total project funding refers to the funding over the entire duration of this project.

Funding institution	Project, Funding	Total Project Funding
BMBF	05K19WCA (H. Keppler – 7/19-6/22) "Aufbau einer Hochdruckpresse vom Multi-Anvil-Typ an der Forschungs-Neutronenquelle FRM II in Garching" Total funding:	579.116 €
BMBF	05K16WC2 (T. Katsura – 7/16-6/21) "Erweiterung der Druckbereiche der In-Situ-Röntgen-beobachtung mit der Großvolumen-Hochdruckapparatur an der PETRA-III-Extension des Deutschen Elektronen-Synchrotrons DESY" Positions E 12-E 15: 349.727 € Consumables and travel funding: 421.540 € Equipment: 43.000 € Overhead: 162.857 €	977.124 €
Carnegie Institution	Carnegie Institution of Washington (H. Keppler, T. Katsura – 11/20-11/21) "Densities of hydrous silicate melts at high pressure"	83.850 €
DFG	AU 314/6-1 (A. Audétat – 1/21-12/22) "Bestimmung der Faktoren, die das Cu-Au Mineralisations-potenzial von Magmen in Kollisionszonen kontrollieren" Positions: E 13 (100 %), 24 months 151.000 € Consumables: 35.800 € Overhead: 41.100 €	227.900 €
DFG	BO 2550/10-1 (T. Boffa Ballaran, B. Mihailova – 7/21-6/24 "Mehrskaliges Hochdruckverhalten der bleifreien ferroelektrischen Perowskitmischkristalle $(1-x)Na_{0.5}BiTiO_{3-x}BaTiO_3$" Positions: student assistant 15.000 € Consumables: 6.900 € Overhead: 4.800 €	26.700 €
DFG	DI 2751/2-1 (D. Di Genova – 10/21-9/24) "Rheology of nanocrystal-bearing natural silicate melts" Positions: E 13 (75 %), 36 months 160.900 € student assistant 4.846 € Equipment: 18.000 € Overhead: 40.400 €	224.146 €

DFG	DU 393/13-2 (L.S. Dubrovinsky – 7/20-6/23) "Mantel-formende Materialien von Super-Erden bei statischen Drücken von über 500 GPa und hohen Temperaturen"			
	Positions:	E 13 (75 %), 36 months	158.600 €	
		student assistant	7.000 €	
	Equipment:		32.250 €	
	Overhead:		43.500 €	241.350 €
DFG	FR 1555/11-1 (D.J. Frost – 3/16-2/23) Gottfried Wilhelm Leibniz-Preis 2016			2.500.000 €
DFG	INST 91/455-1 (A. Bouvier) Major Research Instrumentation Individual Proposal for a Laser Ablation – Multi-collector Inductively Coupled Plasma Mass Spectrometer with collision reaction cell. 50 % from institution (UBT and BGI) – 50% from DFG. Total from DFG:			615.000 €
DFG	KA 3434/3-2 (T. Katsura – 7/18-6/21) "Dislocation recovery experiment of hydrous olivine as a function of water content and crystallographic orientation"			
	Positions:	E 13, 12 months	69.300 €	
		E 13 (75 %), 12 months	48.100 €	
		student assistant	5.000 €	
	Consumables:		20.000 €	
	Overhead:		31.300 €	173.700 €
DFG	KA 3434/11-1 (T. Katsura – 12/18-11/21) "Determining the water dissociation constant from the relationship between water solubility in ringwoodite and oxygen fugacity"			
	Positions:	E 13, 24 months	141.700 €	
	Consumables:		23.500 €	
	Overhead:		36.300 €	201.500 €
DFG	KA 3434/12-1 (T. Katsura – 10/18-12/21) "Determination of water partition coefficients between upper mantle minerals and melts as a function of pressure, temperature, and CO_2 content using a rapid quench cell in multi-anvil experiments"			
	Positions:	E 13, 24 months	142.700 €	
	Consumables:		40.000 €	
	Overhead:		40.200 €	
	Corona measures (incl. overhead):		22.290 €	245.190 €

DFG	KA3434/19-1 (T. Katsura – 02/21-08/23) "Evaluation of the aspect ratio of ferropericlase under lower-mantle conditions" Positions: E13, 24 months 152.200 € Consumables: 50.000 € Overhead: 44.400 €	246.600 €
DFG	KE 501/13-2 (H. Keppler – 2019-2021) "Nitrogen in the deep mantle" Total funding:	136.200 €
DFG	KE 501/16-1 (H. Keppler – 2020-2023) "Cassiterite solubility, tin partitioning, and the origin of porphyry tin deposits" Total funding:	242.288 €
DFG	KU 3447/1-1 (A. Kurnosov – 10/18-9/21) "Einkristall-Elastizität von Mars-Mineralen und ein flexibles CO_2 Laserheizsystem" Position: E 13, 36 months 217.700 € Consumables and travel funding: 15.250 € Overhead: 51.200 €	284.150 €
DFG	MC 3/20-2 (C.A. McCammon – 1/18-12/22) DFG FOR 2125 (CarboPaT) "Elastic properties of carbonates at high pressure and high temperature" Position: E 13 (67 %), 36 months: 132.800 € Equipment, consumables and travel funding: 27.750 € Overhead: 35.300 €	195.850 €
DFG	MC 3/21-1 (C.A. McCammon – 6/17-5/21) "Fe Spinübergang im Erdmantel: Einblicke durch Röntgen-Raman-Streuung und Röntgenabsorptionsspektroskopie" Position: student assistant (Bachelor) 9.482 € Equipment, consumables and travel funding: 6.000 € Overhead: 3.400 €	18.882 €
DFG	ME 5206/3-1 (L.S. Dubrovinsky, (T. Meier) – 6/19-5/22) "Wasserstoffbrückenbindungen unter extremen Bedingungen: Kernquanteneffekte und Symmetrisierung der Wasserstoff-brückenbindung untersucht mit ^{1}H-NMR in Diamantstempel-zellen" Position: E 13, 36 months: 221.500 € Consumables and travel funding: 29.250 € Overhead: 55.200 €	305.950 €

DFG	MI 1721/3-1 (N. Miyajima – 9/19-8/22) "Al, Si-Interdiffusion in Bridgmanit und die Viskosität des unteren Mantels" Position: E 13 (75 %), 36 months: 149.500 € student assistant 7.500 € Consumables and travel funding: 29.500 € Overhead: 41.000 €			227.500 €
DFG	OV 110/3-2 (S.V. Ovsyannikov – 12/20-11/22) "High-pressure synthesis and properties of novel simple oxides with unusual stoichiometries" Position: E 13, 24 months 151.600 € Consumables and travel funding: 39.550 € Overhead: 42.100 €			233.250 €
DFG	STE 1105/13-2 (G. Steinle-Neumann – 7/20-6/23) "Thermodynamic properties of silicate solids and liquids and iron to the TPa range from *ab initio* calculations" Positions: E 13 (75%), 36 months 158.600 € student assistant 7.000 € Consumables: 8.250 € Overhead: 38.200 €			212.050 €
DFG	TH 2076/7-1 (M. Thielmann – 6/21-5/24) "Quantifizierung des Oberflächensignals durch Lithosphärenablösung in den Alpen" Positions: personnel funds 244.700 € Consumables: 17.050 € Overhead: 57.600 €			319.350 €
DFG	TH 2076/8-1 (M. Thielmann – 11/21-10/24) "Identifizierung der Entstehungsprozesse tiefer Erdbeben" (Emmy-Noether-Programm) Positions: 670.913 € Consumables: 60.580 € Workshops: 5.000 € Overhead: 162.000 €			898.496 €
DFG	WI 5383/1-1 (A. Withers, A.B. Woodland – 04/20-03/23 "Gescherte Peridotite: Deformation, Metasomatose und beginnende Destabilisierung von Kratonen" Positions: student assistant 7.500 € Overhead: 1.700 €			9.200 €

EU	European Research Council (ERC) Advanced Grant No. 787 527 (T. Katsura – 10/18-9/23) "Chemistry and transport properties of bridgmanite controlling lower-mantle dynamics" ("UltraLVP") Positions (post docs): 860.144 € Travel funding: 187.380 € Equipment: 49.250 € Consumables: 997.722 € In-kind contributions: 24.000 € Overhead: 523.624 €	2.642.120 €
EU	European Research Council (ERC) Grant No. 949 417 (R. Hin – 1/21-12/25) "The chemical consequences of vapour loss during planetary accretion (VapLoss)" ("HORIZON 2020") Positions: 756.169 € Travel funding: 44.781 € Consumables: 129.403 € Equipment: 153.802 € Internally Goods and Services: 173.235 € Overhead: 314.348 €	1.571.738 €

2.3 Laboratory and office facilities

The institute occupies an area of

ca. 1470 m^2 laboratory space

ca. 480 m^2 infrastructural areas (machine shops, computer facilities, seminar room, library)

ca. 520 m^2 office space

in a building which was completed in 1994.

2.4 Experimental and analytical equipment

The following major equipment is available at the Bayerisches Geoinstitut:

I. High-pressure apparatus

15 MN/1500 tonne Kawai-type multianvil high-pressure apparatus (40 GPa, 2000 K)
6 x 8 MN/6x800 tonne independently acting-anvil press (25 GPa, 3000 K)
50 MN/5000 tonne multianvil press (25 GPa, 3000 K)
12 MN/1200 tonne multianvil press (25 GPa, 3000 K)
10 MN/1000 tonne multianvil press (25 GPa, 3000 K)

5 MN/500 tonne multianvil press (20 GPa, 3000 K)
5 MN/500 tonne press with a deformation DIA apparatus
5 piston-cylinder presses (4 GPa, 2100 K)
Cold-seal vessels (700 MPa, 1100 K, H_2O), TZM vessels (300 MPa, 1400 K, Ar), rapid-quench cold-seal vessels (400 MPa, 1200 K, H_2O)
Internally-heated autoclave (1 GPa, 1600 K)
High-pressure gas loading apparatus for DAC

II. Structural and chemical analysis
1 X-ray powder micro-diffractometer
1 X-ray powder diffractometer with furnace and cryostat
2 automated single-crystal X-ray diffractometers
High-brilliance X-ray system
Single crystal X-ray diffraction with super-bright source
1 Mössbauer spectrometer (1.5 - 1300 K)
3 Mössbauer microspectrometers
2 FTIR spectrometers with IR microscope
FEG transmission electron microscope (TEM), 200 kV analytical, with EDS
FEG scanning TEM, 80-200 kV analytical, with 4-SDDs EDS and post-column energy filter (EFTEM/EELS)
FEG scanning electron microscope (SEM) with BSE detector, EDS, EBSD and CL
Dual beam device, focused ion beam (FIB) and FEG SEM. In situ easy-lift manipulator, STEM, EDS and EBSD detectors, and beam deceleration option
3 Micro-Raman spectrometers with ultraviolet and visible lasers
Tandem-multipass Fabry-Perot interferometer for Brillouin scattering spectroscopy
Electron microprobe; fully-automated with 14 crystals, 5 spectrometer configuration, EDX, capability for light elements
193 nm Excimer Laser-Ablation ICP-MS
Water content determination by Karl-Fischer titration
GC/MS-MS for organic analyses
Confocal 3D surface measurement system
1.4 Tesla sweepable ESR magnet
Solid state 300 MHz NMR spectrometer

III. *In situ* determination of properties
Diamond anvil cells for powder and single crystal X-ray diffraction, Mössbauer, IR, Raman, optical spectroscopy, NMR specroscopy, electrical resistivity measurements over 200 GPa
Facility for in situ hydrothermal studies in DAC
Externally heated DACs for in situ studies at pressures to 100 GPa and 1200 K
1-atm furnaces to 1950 K, gas mixing to 1600 K, zirconia fO_2 probes
1-atm high-temperature creep apparatus

Megahertz ultrasonic interferometer
Freezing-heating stage for fluid inclusion studies
Impedance/gain-phase analyser for electrical conductivity studies
Apparatus for in situ measurements of thermal diffusivity at high P and T
Laser-heating facility for DAC
Portable pulsed laser heating system for DAC

The Geoinstitut maintains a well equipped machine shop, an electronic workshop and sample preparation laboratories. It has access to supercomputing resources at the University and Leibniz computer centres.

3. Forschungsprojekte

3.1 Struktur und Dynamik der Erde und Planeten

Die Bildung der Planeten begann schnell nach dem Abkühlen des Gasnebels, als sich die ersten Feststoffe bildeten. Die Mutterkörper von Eisenmeteoriten begannen sich ungefähr hunderttausend Jahre nach der Entstehung der Sonne zu bilden, während die Bildung der Planetesimale im äußeren Sonnensystem mehrere Millionen Jahre länger dauerte als in der inneren Scheibe. Chondritische Meteoriten, die der durchschnittlichen Zusammensetzung des Sonnensystems für nichtflüchtige Elemente am nächsten kommen, könnten die Relikte der Materialien sein, aus denen die Planeten gebildet wurden. Die chemische Zusammensetzung der terrestrischen Planeten ist jedoch für viele Elemente aufgrund von Differenzierungsprozessen wie der Entgasung von Magmaozeanen und der Bildung von Kern, Mantel und Kruste sowie von Impaktprozessen schwer abzuschätzen. Es wurden große Unterschiede zwischen Chondriten und terrestrischen Planeten beobachtet, sowohl für die Konzentration flüchtiger Elemente als auch für Hauptelementverhältnisse (z. B. Mg/Si, Al/Mg). Zusätzlich wurden deutliche Unterschiede in massenunabhängigen Anomalien stabiler Isotopen zwischen planetaren Materialien und Planeten identifiziert. Dies deutet darauf hin, dass die protoplanetare Scheibe eine heterogene Zusammensetzung aufwies. Diese Anomalien können nicht durch Differenzierungsprozesse modifiziert werden. Daher wurde vorgeschlagen, dass die Erde und andere terrestrische Planeten des inneren Sonnensystems wahrscheinlich aus zahlreichen kleineren primitiven und differenzierten Körpern gebildet wurden. Gegenstand der Untersuchungen in diesem Abschnitt sind die Bedingungen für die Bildung planetarer Materialien im Sonnensystem und die chemische und physikalische Entwicklung der Erde und der Planeten.

Heutige Kometen sind Relikte der Planetenentstehung im äußeren Sonnensystem. Sie enthalten große Mengen hochflüchtiger Verbindungen, obwohl sie schon früh in ihrer Entwicklung durch radioaktiven Zerfall und Kollisionen erhitzt wurden. Golabek und Jutzi untersuchen diese beiden Effekte mit kombinierten geodynamischen und SPH-Simulationen (Smoothed Particle Hydrodynamics). Sie stellen fest, dass die interne thermische Entwicklung die Menge des verbleibenden hochflüchtigen Materials ("Eis") in den großen Überresten nach einer Kollision steuert, während für die Objekte, die aus ungebundenem Material nach einer Kollision entstanden sind, die Erwärmung durch den Aufprall entscheidend ist.

Kollisionen zwischen Planetesimalen spielten auch eine wichtige Rolle bei der Entstehung der Pallasit-Meteoritengruppe. Walte und Golabek analysieren vier große Pallasitproben der Hauptgruppe und finden Hinweise darauf, dass bestimmte Regionen in diesen Meteoriten von der Kollision unberührt blieben und somit noch Mantelmaterial vor dem Aufprall darstellen, das noch einige Metalleinschlüsse enthielt. Darüber hinaus zeigen sie, dass Pallasit-Merkmale wie Brüche und mineralisierte Adern mit Verformungsexperimenten reproduziert werden können, also durch ein Aufprallereignis verursacht wurden.

Zwei Beiträge liefern weitere Hinweise auf die Zusammensetzung der Bausteine der Erde. Zuerst beschreiben Rubie et al. N-Körper-Simulationen und Verteilungsmodelle für das Verhalten von Kohlenstoff bei der Bildung der Erde. Sie stellen fest, dass der Kohlenstoffhaushalt der Erde mit ihrer Akkretions- und Differenzierungsgeschichte in Einklang gebracht werden kann, wenn kohlenstoffhaltiges chondritisches Material auch einen großen Anteil differenzierter Planetesimale enthielt. Die Erde würde dann aus einer Mischung von nicht-kohlenstoffhaltigen und geringen Mengen (≈ 0,5 %) kohlenstoffhaltigen Materialien einschließlich mindestens 40 % differenzierter Planetesimale bestehen.

Frossard et al. untersuchen ebenfalls die Bausteine der Erde. Kleine, aber auflösbare nukleosynthetische Isotopenanomalien in stabilen Neodym-Isotopen wie ^{145}Nd und ^{148}Nd (Mischungen aus s- und r-Prozessen) wurden in verschiedenen Chondriten und Achondriten aus den nicht kohlenstoffhaltigen (NC) und kohlenstoffhaltigen (CC) Gruppen gefunden. Die Überschüsse an ^{145}Nd und ^{148}Nd in NC-Achondriten im Vergleich zu NC-Chondriten (aber auch zu Erde, Mars und Mond) deuten auf eine Veränderung der Zusammensetzung des inneren Sonnensystems nach etwa 1,5 Millionen Jahren hin. Hierbei fand eine thermische Verarbeitung von präsolaren Körnern statt, den Trägern großer nukleosynthetischer Anomalien. Die Erde hat sich daher entweder aus Enstatit-Chondrit-ähnlichen Materialien oder aus einer Mischung unbekannter, durch den s-Prozess angereicherter Materialien gebildet, die anschließend mit Chondriten und Achondriten unterschiedlichen Ursprungs (nicht kohlenstoffhaltig oder kohlenstoffhaltig) vermischt wurden.

Mondproben liefern Informationen über die Entstehung des Mondes und die Geschichte der Impakt-Prozesse im frühen Sonnensystem. Apollo-Mondproben aus den Anorthositen und KREEP-Basalten liefern Hinweise auf die Kristallisation und Differenzierung des Magma-Ozeans auf dem Mond (LMO). Die magmatische "Mg-Serie" wurde durch teilweises Schmelzen von Mantelkumulaten aus dem tiefen Magmenozean gebildet. Die Mare-Basalte sind die letzten Teilschmelzen aus dem Inneren des Mondes bis vor ~ 2 Ga, wie kürzlich aus Proben von Chang'e 5 ermittelt wurde. Die Stadien und die Dauer der Kristallisation des Magmenozeans sind schwer zu rekonstruieren, da noch keine Mantelgesteine auf der Mondoberfläche oder als Mondmeteoriten beprobt wurden. Zusätzlich haben Einschlags-prozesse die magmatische Geschichte des Mondgesteins verändert.

Pöppelbaum et al. beschreiben chromreiche Komponenten in Schmelzeinschlüssen, die in Olivin-Klasten in einer Feldspat-Brekzie mit Apollo-17-Impaktschmelze gefunden wurden. Sie stammt aus der Entstehungszeit des Imbrium-Beckens. Ihre Zusammensetzung weist auf eine besondere Schmelzkomponente hin, die mit der Differenzierung des Magmenozeans und der Bildung der "Mg-Serie" zusammenhängen könnte.

Eine Studie von Zhang et al. über ein Bruchstück von Norit, das in einer Impaktschmelzbrekzie eingebettet ist, liefert den frühesten Beweis für die Kristallisation von Zirkon und damit für die Bildung einer mafischen unteren Kruste vor ~ 4,46 Ga, was ein neues Mindestalter für den

Mond liefert. Diese chronologischen Daten könnten jedoch durch eine mögliche nanoskalige Umverteilung von Pb-Isotopen während der Bildung der Impakt-Schmelzbrekzie in Frage gestellt werden. Die zweite Studie von Zhang et al. präsentiert U-Pb-Daten eines Baddeleyits in einem Norit aus der "Mg-Serie" des Mondes, die im Vergleich zu anderen Chronometern auf eine schnelle Abkühlung innerhalb der Mondkruste hinweisen. Die chronologischen Daten von Mondproben weisen auf Magmatismus vor ~ 4,3 Ga hin, der etwas jünger ist als die anorthositische Kruste (4,36 Ga). Diese Ergebnisse liefern neue Rahmenbedingungen für die magmatische Entwicklung des Mondes.

Auf der Erde kommen wasserhaltige Phasen wie Amphibole in Mantel-Xenolithen vor. Es wurde vermutet, dass das Dehydratations-Schmelzen von Amphibol die Verringerung der Scherwellengeschwindigkeit an der Grenze zwischen Lithosphäre und Asthenosphäre verursacht. Putak Juriček und Keppler untersuchen erneut experimentell die Stabilität von Amphibol im oberen Mantel und stellen fest, dass sie stark vom geothermischen Gradienten abhängt. Sie beobachteten, dass Amphibole entlang typischer geothermischer Gradienten im Mantel stabil sein könnten, aber bei den Abbaureaktionen meistens keine Schmelze entsteht. Daher ist es unwahrscheinlich, dass Schmelzbildung durch Dehydratation an der Amphibol-Stabilitätsgrenze die Verringerung der S-Wellen-Geschwindigkeit erklären kann.

Das Temperaturprofil der heutigen Erde bleibt umstritten. Katsura wertete daher experimentelle Daten für Olivin, Wadsleyit, Ringwoodit und Bridgmanit neu aus. Er zeigt, dass die thermische Ausdehnung in früheren Modellen überschätzt wurde und erhält ein aktualisiertes adiabatisches Temperaturprofil, das auf niedrigere Temperaturen im Inneren der Erde im Vergleich zu früheren Studien hindeutet.

3.2 Geochemie

Die in diesem Abschnitt beschriebenen Projekte liefern eine Reihe von Momentaufnahmen von Prozessen, die chemische Veränderungen auf verschiedenen Längenskalen, zu verschiedenen Zeiten und in verschiedenen Tiefen der Erde verursachen. Bei den meisten dieser Prozesse werden Elemente mobilisiert oder konzentriert, sodass sich neue Reservoire mit unterschiedlicher Zusammensetzung bilden. Bei einigen Projekten sind diese Reservoire kommerziell nutzbare Bodenschätze, während bei anderen Projekten die Bildung von Reservoiren größeren Ausmaßes, wie z. B. des Erdkerns, untersucht wird. In allen Fällen beschreiben die Projekte jedoch Ansätze, die uns helfen, Prozesse zu verstehen, von denen wir durch große Tiefen in der Erde und lange Zeiträume getrennt sind.

Die ersten beiden Beiträge in diesem Abschnitt befassen sich mit dem Verhalten flüchtiger Elemente bei der Entstehung der Erde und der Trennung des metallischen, eisenreichen Kerns vom äußeren Silikatmantel. Es gibt viele Theorien darüber, wie und wann flüchtige Elemente der Erde im Laufe ihres Wachstums zugeführt wurden. Durch die experimentelle

Untersuchung, wie sich eine Auswahl mäßig flüchtiger Elemente (Sn, Cd, Bi, Sb und Tl) zwischen dem Erdmantel und dem metallischen Kern verteilt haben könnte, gelingt es der ersten Studie in diesem Abschnitt, diesen Zeitpunkt ziemlich genau einzugrenzen. Es wird festgestellt, dass bei einem frühen Eintreffen der flüchtigen Elemente der Erdmantel zu arm an diesen Elementen gewesen wäre. Im einzigen Szenario, das mit geochemischen Daten übereinstimmt, wurden die flüchtigen Komponenten erst in einem späten Stadium zugeführt. Als sich der Erdkern abtrennte, wurden die flüchtigen Stoffe nur teilweise aus dem Mantel entfernt. Diese späte Ankunft und unvollständige Gleichgewichtseinstellung erklären daher, warum die äußeren Schichten der Erde höhere Konzentrationen zumindest einiger mäßig flüchtiger Elemente enthielten. Im zweiten Beitrag wird das Verhalten von Helium während der Kernbildung untersucht. Ozeanische Inselbasalte weisen ein höheres $^{3}He/^{4}He$-Verhältnis auf als die Basalte der mittelozeanischen Rücken, was auf eine relative Anreicherung von primordialem He im Erdkern schließen lässt. Um diese Hypothese zu überprüfen, wurde die Verteilung von He zwischen Silikat- und Metallschmelzen mit Hilfe von Computer-simulationen untersucht. Es wurde festgestellt, dass sich He im Allgemeinen in der silikatischen Schmelze anreichert, dass aber das Vorhandensein von Sauerstoff in der metallischen Schmelze die Menge an He, die in den Kern gelangt, stark erhöht. Dies zeigt die Fähigkeit der metallischen Schmelze, primordiales $^{3}He/^{4}He$ zurückzuhalten.

Die nächsten fünf Beiträge befassen sich mit Aspekten der Mineralogie des unteren Erdmantels und mit der Frage, wie sich die Zusammensetzung von Mineralen in Abhängigkeit von den extremen Bedingungen in dieser Region der Erde verändern kann. Im ersten Beitrag wird untersucht, wie Fe^{3+} in das Mineral Bridgmanit im unteren Erdmantel bei SiO_2-gesättigten Bedingungen eingebaut wird. Dies ist relevant für subduzierte ozeanische Kruste. Der Substitutionsmechanismus von dreiwertigen Kationen in Bridgmanit unter SiO_2-armen Bedingungen führt nachweislich zur Bildung von Leerstellen im Sauerstoffgitter, die die Transporteigenschaften wie die Festigkeit des Gesteins und seine Fließfähigkeit stark beeinflussen können. Diese Studie zeigt, dass unter SiO_2-reichen Bedingungen eher Leerstellen im Kationen- als im Sauerstoffgitter gebildet werden, was zu Unterschieden in den Transporteigenschaften von Mantelgestein führen kann. Die folgende Studie befasst sich ebenfalls mit dem Einbau von Eisen, diesmal in das Mineral Ferroperiklas. Dies ist eines der wenigen Minerale, das als Einschlüsse in Diamanten vorkommt, die offensichtlich aus dem tiefen Erdmantel stammen. In dieser Studie zeigen Hochdruckexperimente zur Bestimmung des Eisengehalts von Ferroperiklas während der Diamantenbildung Konzentrationen, die denen in natürlichen Proben entsprechen. Daraus wird gefolgert, dass sich Diamanten im unteren Erdmantel durch die Reduktion von Karbonatschmelzen bilden können, die aus subduzierten Platten in diesen Tiefen stammen. Die nächste Studie von Kim et al. zielte ebenfalls darauf ab zu verstehen, wie sich Eisen zwischen den Mineralphasen im unteren Erdmantel verteilt. Um die Konzentration von Eisen(III) in diesen Experimenten zu kontrollieren, wurde metallisches Eisen zugesetzt, was zu möglichst niedrigen Eisen(III)-Konzentrationen führen sollte. Ein faszinierendes und unerwartetes Ergebnis ist, dass die Minerale mit zunehmendem Druck extrem feinkörnig werden, sodass sie nur mit einem Transmissionselektronenmikroskop

untersucht werden können. Eine geringe Zunahme der Korngröße abseits des metallischen Eisens deutet darauf hin, dass unter hohem Druck und reduzierenden Bedingungen die Korngrenzdiffusion und damit das Kornwachstum erheblich verlangsamt sein könnten. Obwohl dies nur ein vorläufiges Ergebnis ist, könnte es sehr wichtige Auswirkungen auf die Rheologie des tiefen Erdmantels haben.

Die nächste Studie untersucht die Auswirkungen von Eisen auf das Schmelzen bzw. die Kristallisation von Gesteinen des unteren Mantels. Dies ist wichtig, um zu verstehen, ob die Basis des unteren Mantels geschmolzen sein könnte und wie der untere Mantel während der Kristallisation eines frühen Magmaozeans fraktioniert worden sein könnte. Wenn der Mantel in Oberflächennähe schmilzt, treten Komponenten wie Natrium und Wasser bei recht niedrigen Temperaturen in die Schmelze ein, was zu einem Temperaturintervall von mehreren hundert Grad führt zwischen dem Beginn der Schmelze und dem Zeitpunkt, an dem der Mantel vollständig geschmolzen ist. Im unteren Mantel scheint dies nicht mehr der Fall zu sein und die meisten Komponenten, einschließlich Na_2O, treten bei einer ähnlichen Temperatur in die Schmelze ein. Wie in dieser Studie festgestellt wurde, ist Eisen jedoch eine der wenigen Komponenten, die bei einer niedrigeren Temperatur in die Schmelze übergehen und seine Verteilung hat daher den größten Einfluss auf das Temperaturintervall, in dem der untere Mantel schmilzt. Die letzte Studie, die sich mit Prozessen im unteren Erdmantel befasst, untersucht die Rolle von Kalziumphosphaten im Kreislauf von Phosphor und inkompatiblen Spurenelementen in der tiefen Erde. Es wurden Multianvil-Experimente mit Phosphor-dotierten peridotitischen und basaltischen Ausgangsmaterialien unter Bedingungen durchgeführt, die denen des unteren Erdmantels entsprechen. Die wichtigste phosphorhaltige Phase ist Tuit, ein Hochdruck-Äquivalent von Apatit, das in stark geschockten Meteoriten gefunden wurde. Die Autoren kommen zu dem Schluss, dass Tuit ein wichtiger Träger von Phosphor, Halogenen und inkompatiblen Spurenelementen sowohl in Subduktionszonen als auch im konvektiven Mantel sein könnte.

Die folgenden beiden Beiträge stellen eine Verbindung zwischen tief liegenden geologischen Prozessen und der Entwicklung von Leben und lebensfreundlichen Bedingungen auf der Erdoberfläche her. Um das Schicksal von Eisenhydroxiden in subduzierten gebänderten Eisenerzformationen zu verstehen, untersuchten Dubrovinsky et al. die Stabilität von α-FeOOH (Goethit) mit *in situ*-Röntgenmethoden in einer laserbeheizten Diamantstempelzelle. Goethit zersetzt sich unter Bedingungen, die einer Tiefe von ca. 1000 km entsprechen, zu einer Reihe wasserfreier Eisenoxide, in denen das Eisen eine niedrigere Oxidationsstufe aufweist. Dies führt zur Freisetzung eines sauerstoffreichen wässrigen Fluids. Die Autoren argumentieren, dass solche Fluide, wenn sie zur Erdoberfläche aufstiegen, das große Oxidationsereignis vor 2,5 Milliarden Jahren ausgelöst oder zumindest dazu beigetragen haben könnten. In der folgenden Studie wird ein sogenannter magmaarmer Grabenrand untersucht, an dem die Kruste während der Öffnung des Atlantiks gedehnt wurde und die Ausdehnung zumindest teilweise dadurch kompensiert wurde, dass ein Teil des subkontinentalen Mantels an die Oberfläche gehoben wurde. Das Mantelgestein, in dem das Mineral Olivin vorherrscht, wurde rasch in das

wasserhaltige Mineral Serpentin umgewandelt, wobei auch Wasserstoff entsteht. Proben, die bei Bohrungen in diesem Randbereich vor der spanischen Küste entnommen wurden, werden in dieser Studie mit Hilfe der Mössbauer-Spektroskopie analysiert. Dadurch konnte das Ausmaß der Serpentinisierung in verschiedenen Tiefen und für verschiedene ursprüngliche Mantelgesteinstypen bestimmt werden. Die Ergebnisse zeigen, dass sich große Mengen an Wasserstoff in Tiefen gebildet haben, die knapp unter denen liegen, in denen Organismen überleben und den Wasserstoff als Energiequelle nutzen können. Solche Grabenränder könnten daher die Energiequelle darstellen, die es der Biosphäre ermöglichte, tief in das Gestein des neu entstandenen Ozeanbeckens vorzudringen.

Die nächsten beiden Beiträge befassen sich mit dem Verhalten von Spurenelementen in Subduktionszonen. Der erste Beitrag behandelt den Ursprung der Spurenelementsignatur von Magmen, die die Inselbögen über Subduktionszonen bilden. Fluid-Eklogit-Verteilungskoeffizienten wurden in Diamantfallen-Experimenten mit unterschiedlich salzhaltigen Fluiden unter Bedingungen der Subduktionszonen bestimmt. Ein quantitatives Modell wurde daraus entwickelt, das auch den Mengenanteil des Fluids in der Platte und im darüber liegenden Mantel, sowie den Aufschmelzgrad berücksichtigt. Die Ergebnisse zeigen, dass die Spurenelementsignatur von Inselbogen-Magmen nicht die Beteiligung von partiellen Schmelzen von Sedimenten erfordert. Die Zugabe von einigen Gewichtsprozenten mäßig salzhaltiger, aus der Subduktion stammender Fluide zum Ort der Schmelzbildung im darüber liegenden Mantelkeil kann die beobachteten Elementanreicherungen vollständig erklären. In einem weiteren Projekt untersuchten Liu et al. mit Hilfe von Diamantfallen-Experimenten speziell das Verhalten von Kupfer, Zink und Wolfram bei der Freisetzung von Fluiden aus subduzierenden Platten. Sie beobachteten, dass sich Cu und Zn stärker in salzhaltigeren Fluiden anreichern, während das Verhalten von W durch den Salzgehalt des Fluids nicht wesentlich beeinflusst wurde. Keines der drei untersuchten Elemente war jedoch in der fluiden Phase besonders stark angereichert, was darauf schließen lässt, dass die aus der Platte austretenden Fluide die Konzentrationen dieser Elemente in der Mantelquelle der Inselbogen-Magmen nicht wesentlich erhöhen würden und damit kaum einen Beitrag zur Entstehung wirtschaftlich wichtiger Erzlagerstätten liefern.

Die letzten vier Beiträge befassen sich mit dem Thema magmatisch-hydrothermaler Erzlagerstätten. Obwohl Gallium derzeit ausschließlich als Nebenprodukt von Bauxit- und Zinkerzen gewonnen wird, sind auch magmatisch-hydrothermale Anreicherungen von Gallium bekannt. In der ersten Studie dieses Unterabschnitts wird versucht, potenzielle Prozesse zur Anreicherung von Gallium in der magmatisch-hydrothermalen Umgebung zu ermitteln. In einem ersten Schritt wurde die Löslichkeit von Ga_2O_3 in Silikatschmelzen und unterschiedlich salzhaltigen wässrigen Fluiden bei 750-800 °C und 2 kbar experimentell untersucht. Die Löslichkeit von Ga_2O_3 in Fluiden wurde durch die Herstellung von synthetischen Flüssigkeitseinschlüssen bestimmt. Es wurde festgestellt, dass Gallium eine Affinität zu Alkalifeldspat hat und mit einem Fluid/Schmelze-Verteilungskoeffizienten von nur 1-2 in das Fluid fraktioniert. Diese vorläufigen Ergebnisse deuten darauf hin, dass es bei magmatischen

Temperaturen schwierig ist, Gallium in diesen Systemen auf ein wirtschaftliches Niveau anzureichern. Die folgende Studie von Fang und Audétat beschäftigt sich mit der Bildung von porphyrischen Molybdänerzlagerstätten. Die Verteilung von Molybdän zwischen Fluid und Magma ($D_{Mo}^{Fluid/Schmelze}$) wurde als Funktion von Druck, Temperatur, Schmelzzusammensetzung und der Fugazität von Schwefel und Sauerstoff experimentell untersucht. Es wurde festgestellt, dass $D_{Mo}^{Fluid/Schmelze}$ mit dem Druck und der Alkalinität der Schmelze stark ansteigt, mit zunehmender Sauerstoff- und Schwefel-Fugazität abnimmt und dass die Temperatur im untersuchten Bereich von 750-850 °C vergleichsweise wenig Einfluss hat. Die Ergebnisse deuten darauf hin, dass die Tiefe der Intrusion des Magmas bei der Bildung dieser wirtschaftlich wichtigen Art von Erzlagerstätten eine wichtige Rolle spielen könnte.

Ziel der folgenden Studie von Zhang et al. ist es, die weit verbreitete Hypothese zu prüfen, dass sich goldreiche Porphyr-Kupfer-Lagerstätten in Post-Kollisions-Umgebungen durch teilweises Aufschmelzen von sulfidreichen Kumulaten aus der unteren Kruste bilden. Um zu prüfen, ob tiefe Krustenkumulate sulfidreich sind, wurden natürliche Proben aus exhumierten Krustenabschnitten in Kohistan (Nordpakistan) und dem Gangdese-Gürtel (Südtibet) untersucht. Außerdem wurden an diesen Gesteinen Teilschmelzexperimente in Kolbenzylinderpressen durchgeführt. Die petrographischen Untersuchungen zeigen, dass die Kumulate ursprünglich tatsächlich sulfidreich waren und somit das Potenzial hatten, erhebliche Mengen an Schwefel und Metallen zu liefern. Die Teilschmelzexperimente deuten jedoch darauf hin, dass bei trockener Dekompression Schmelzen entstehen, die weitaus höhere Na/K-Verhältnisse aufweisen als die natürlichen, erzbildenden Magmen, was gegen diese gängige Hypothese spricht. Diese Schlussfolgerung wird in der letzten Studie dieses Abschnitts weiter untermauert. Mafische bis felsische kaliumreichen Magmen, die mit porphyrischen Kupfer-Gold-Lagerstätten in Westchina in Verbindung stehen und nach einer Kontinent-Kollision entstanden sind, wurden geochemisch untersucht. Diese Gesteine weisen Inselbogensignaturen und eine systematische Variation ihres Spurenelementgehalts in Abhängigkeit von der Entfernung zu einem ehemaligen Subduktionsgraben auf. Obwohl ihre Pb-, Nd- und Sr-Isotopenzusammensetzung einen großen Bereich abdeckt, ist die Isotopensignatur jeder kogenetischen Folge von mafischen bis felsischen Magmen sehr konstant. Diese Beobachtungen deuten darauf hin, dass sich die erzbildenden Magmen durch fraktionierte Kristallisation aus mafischen, aus dem Erdmantel stammenden Vorläufern entwickelt haben und dass keine nennenswerten Mengen an Krustengestein an ihrer Entstehung beteiligt waren.

3.3 Mineralogie, Kristallchemie und Phasenübergänge

Die Minerale im Inneren der Erde sind mit zunehmendem Druck und steigender Temperatur strukturellen und kristallchemischen Umwandlungen unterworfen. Die Forschung am Bayerischen Geoinstitut nutzt sowohl experimentelle als auch theoretische Ansätze, die auf Kenntnissen der Mineralogie und der Materialwissenschaften basieren, um die Veränderungen des Mineralbestands im Erdinneren besser zu verstehen. Dieser Abschnitt beschreibt neun

Forschungsprojekte an der Schnittstelle zwischen Mineralogie und Kristallchemie unter extremen Bedingungen.

Die ersten drei Beiträge befassen sich mit den Stabilitäten und Umwandlungen eisenhaltiger Phasen bei hohem Druck und hoher Temperatur unter Verwendung von Synchrotron-Röntgenbeugungstechniken. Die Phasenbeziehungen des Olivin-Ahrensit-Übergangs im System $(Mg,Fe)_2SiO_4$ wurden mit Multianvil-Techniken bestimmt, um eine genauere Abschätzung der Bedingungen der Schock-Metamorphose in eisenreichen Meteoriten zu ermöglichen. Die strukturelle Vielfalt von Magnetit und seinen Zersetzungsprodukten wurde an Einkristallen in Diamant-Stempelzellenexperimenten untersucht, die die Bildung von eisenreichen Fe-O-Verbindungen zeigten, was für eine wichtige Rolle von Magnetit im tiefen Sauerstoffkreislauf spricht. Die Phasenbeziehungen einer vereinfachten MORB-Zusammensetzung, die mit Hilfe von Multianvil-Experimenten untersucht wurden, zeigen die Auswirkung der Sauerstofffugazität auf die Stabilität der wasserhaltigen Phasen in den Mineralzusammensetzungen des unteren Erdmantels.

Die folgenden vier Beiträge befassen sich mit aluminiumhaltigen Phasen im Erdmantel. Berechnungen der Gitterposition des Wasserstoffs in δ-AlOOH in Kombination mit Hochdruck-NMR-Messungen ergaben keine Hinweise auf eine Tunnelungs-bedingte Protonenfehlordnung, was Auswirkungen auf den Wasserstofftransport im unteren Erdmantel hat. Die Synthese hochwertiger Einkristalle der aluminiumreichen Kalziumferrit-Phase mit einer Multianvil-Presse verbessert die Möglichkeiten zur Bestimmung der physikalischen und chemischen Eigenschaften subduzierter basaltischer und kontinentaler Kruste im unteren Erdmantel. Die Untersuchung von Bridgmanit im System $MgSiO_3$-$MgAl_2O_4$-Al_2O_3 mit Hilfe einer Multianvil-Presse zeigte das Vorhandensein signifikanter Sauerstoffleerstellen, die die Mantelviskosität beeinflussen und die Stagnation der Platten im unteren Mantel erklären können. Neue Ergebnisse zur Löslichkeit von Aluminiumoxid in MgO bei hohem Druck ergaben einen dramatischen Einfluss der Temperatur, der sowohl zur Temperaturkartierung von Multianvil-Proben verwendet werden kann als auch als Geothermometer für Ferroperiklas-Einschlüsse in Diamanten.

In den letzten beiden Beiträgen wird beschrieben, wie die Transmissionselektronenmikroskopie genutzt werden kann, um den Ursprung und die Entwicklung sowohl terrestrischer als auch extraterrestrischer Materialien zu ermitteln. Die pseudokinematischen Beugungsintensitäten von Omphazit, die mit Hilfe der Präzisions-Elektronenbeugung im TEM gemessen wurden, ermöglichten eine Bewertung der Kationenordnung in Omphazit im Submikrometerbereich und lieferten Anhaltspunkte für die thermische Geschichte metamorpher Gesteine. Spektrale und mineralogische Analysen, die an natürlich erhitzten kohlenstoffhaltigen Chondriten durchgeführt wurden, zeigen die Beziehung zwischen spektralen und mineralogischen Eigenschaften, die durch die Erhitzung beeinflusst werden. Diese können zur Interpretation der Zusammensetzung von Planetenoberflächen durch Fernerkundungsbeobachtungen mit Boden-, Luft- oder Weltraum-gestützten Teleskopen sowie durch Raumfahrtmissionen genutzt werden.

3.4 Physikalische Eigenschaften von Mineralen

Statische Kompressionsversuche gehören zu den häufigsten Methoden zur Messung der elastischen Verformung von Mineralien bei Druckänderungen. Es ist daher nicht überraschend, dass in vier Beiträgen dieses Kapitels über Kompressibilitätsmessungen berichtet wird, die in Diamantstempelzellen in Verbindung mit Röntgenbeugung durchgeführt wurden. Hierbei kamen sowohl hauseigene Diffraktometer als auch externe Synchrotronanlagen zum Einsatz. Alle diese Untersuchungen wurden an Einkristallen durchgeführt, um die Genauigkeit und Präzision der bei hohem Druck gemessenen Gitterparameter der Einheitszellen zu verbessern und einen Einblick in die strukturellen Veränderungen zu erhalten, die mit zunehmendem Druck auftreten.

Im ersten Beitrag wurde die Kompressibilität von Magnesioferrit bis zu 22 GPa bei Raumtemperatur bestimmt. Die Ergebnisse illustrieren das Hochdruckverhalten der Magnetit-Magnesioferrit-Mischkristalle und zeigen, dass Mischkristalle weniger kompressibel sind als die beiden Endglieder. Im zweiten Beitrag wurde das Hochdruckverhalten eines Fe^{2+}-reichen basaltischen Bridgmanits bis zu 60 GPa bei Raumtemperatur untersucht, um die Elastizität von subduzierenden Platten abzuschätzen. Der Raumdruck-Kompressionsmodul dieses Bridgmanits ist ähnlich wie der von zuvor analysierten basaltischen Bridgmanit-Proben, jedoch ist seine erste Druckableitung bemerkenswert niedrig. Wahrscheinlich haben Sauerstoff-leerstellen einen signifikanten Einfluss auf die Kompressibilität von basaltischem Bridgmanit bei den höchsten Drücken im unteren Erdmantel. Eine große Herausforderung bei Hochdruckstudien mit Einkristallen besteht darin, genaue Volumenmessungen bei gleichzeitig hohem Druck und hoher Temperatur zu erhalten. Im dritten Beitrag wird gezeigt, wie durch den Einsatz einer selbst entwickelten Widerstandsheizung die Volumenänderungen von Al-haltigem Bridgmanit bis zu 1000 K und 35 GPa gemessen werden konnten, um die Parameter der P-V-T-Zustandsgleichung für dieses Mineral zu bestimmen. Eine der meist diskutierten Fragen in den Geowissenschaften ist, ob Wasser in den unteren Erdmantel transportiert werden kann. Ein möglicher Wasserträger ist Al-haltiger Stishovit durch die gekoppelte Substitution eines Si-Atoms durch ein Al-Atom und ein H-Atom. Eine solche gekoppelte Substitution hat nicht nur erhebliche Auswirkungen auf das Kompressibilitätsverhalten von Stishovit, sondern auch auf seinen ferroelastischen Hochdruckphasenübergang, wie im vierten Beitrag gezeigt wird. Wasserhaltiger Al-haltiger Stishovit wird sich in geringerer Tiefe umwandeln und sein Vorhandensein könnte einige negative Schergeschwindigkeitsanomalien innerhalb seismischer Reflektionen erklären, die in der Nähe subduzierter Platten in 800-1200 km Tiefe beobachtet werden.

Messungen der Schallwellengeschwindigkeit sind für die Interpretation seismischer Beobachtungen von grundlegender Bedeutung. Oftmals sind solche Messungen jedoch auf einfache Zusammensetzungen beschränkt, die das Verhalten von Mineralen mit umfangreichen Kationensubstitutionen sowie von komplexen Aggregaten mit geringen Anteilen von Schmelzen nur unzureichend beschreiben. So dürfte sich beispielsweise die seismische

Signatur des Mars-Mantels aufgrund des höheren Fe-Gehalts im Marsgestein deutlich von derjenigen der Erde unterscheiden. Im fünften Beitrag wird über die Ergebnisse berichtet, die für einen Einkristall aus Fe-reichem Ringwoodit mittels Brillouin-Streuung und Röntgenbeugungsexperimenten bei hohem Druck erzielt wurden und die zeigen, dass die akustischen Gesamtgeschwindigkeiten dieses Minerals im Vergleich zum Ringwoodit-Endglied stark abnehmen. Die elastischen Eigenschaften von Fest-Flüssig-Gemischen hängen von den Fest-Fest- und Fest-Flüssig-Grenzflächenenergien ab, die die Ausdehnung des zusammenhängenden Flüssigkeitsnetzwerks bestimmen. Im sechsten Beitrag dieses Kapitels wurden Ultraschall-Interferometrie-Experimente durchgeführt, um die Schallwellen-geschwindigkeiten von Olivin-FeS-Aggregaten bei Drücken von 4 bis 6 GPa und bei Temperaturen bis 1800 K zu messen. Bei einem FeS-Volumenanteil von bis zu 9 % ist nur eine geringe Auswirkung auf die Scherwellengeschwindigkeit des Aggregats zu erkennen, selbst bei Temperaturen, bei denen flüssiges FeS erwartet wird.

Die physikalischen Eigenschaften von Gesteinen können auch durch ihre Mikrotextur stark beeinflusst werden. So sind beispielsweise mit Schmelze gefüllte Poren dafür bekannt, dass sie die Schallwellengeschwindigkeit polykristalliner Aggregate verringern, oder die Korngrößenverteilung kann sich erheblich auf die Fließfestigkeit des Materials auswirken. In den letzten beiden Beiträgen dieses Kapitels werden Rückstreuelektronenbilder verwendet, um die Fest-Flüssig-Grenzflächen und das Kornwachstum in Proben zu quantifizieren, die aus Hochdruck- und Hochtemperatursynthesen stammen. Diese Bildanalysen ermöglichten es im siebten Beitrag, die Variation der Kontiguität von Schmelztaschen in Olivin-Troilit-Gemischen zu bestimmen, wobei sich zeigte, dass mehr als 6 Vol.-% Troilit (d. h. viel mehr als in der Literatur angegeben) erforderlich sind, um die beobachtete Verringerung der Wellen-geschwindigkeit zu bewirken. Im letzten Beitrag wird die Kinetik des Kornwachstums von Bridgmanit, der mit Ferroperiklas koexistiert, als Funktion der Temperatur bei 27 GPa untersucht, um die Rheologie des unteren Erdmantels beim Diffusionskriechen abzuschätzen. Die geringere Korngröße von Bridgmanit in kälteren subduzierenden Platten könnte die Fließfestigkeit von Bridgmanit relativ zum normalen Mantel um eine Größenordnung verringern.

3.5 Fluide, Schmelzen und ihre Wechselwirkung mit Mineralen

Geringe Anteile von Silikatschmelze im Mantel können die Mantelkonvektion und die globale Tektonik auf der Erde erheblich beeinflussen. Viele geodynamische Modelle deuten darauf hin, dass Plattentektonik auf der Erde nur existieren kann mit einem Kanal niedriger Viskosität unter den Platten. Partielle Schmelzbildung könnte einen derartigen Kanal leicht erzeugen. Dies wäre auch konsistent mit dem abrupten Abfall der seismischen Geschwindigkeiten an der Grenze der Lithosphäre zur Asthenosphäre. Schmelzbildung ist jedoch nur möglich in Gegenwart flüchtiger Bestandteile wie Wasser, die die Solidustemperatur des Mantels herabsetzen. Leider ist jedoch der Effekt von Spuren von Wasser auf die Schmelztemperatur im Mantel wenig

verstanden, da sich die entsprechenden geringen Wasser-Fugazitäten in Experimenten schwer einstellen lassen und der Nachweis von kleinen Schmelzmengen in diesen Experimenten ebenfalls schwierig ist. Der erste Beitrag in diesem Abschnitt des Jahresberichts löst dieses Problem mit einem neuartigen Ansatz. Die Schmelzbildung im "Haplobasalt"-System Anorthit-Diopsid wurde unter genau kontrollierten Wasser-Fugazitäten in einer innenbeheizten Gasdruckapparatur untersucht. Dieses System ist eutektisch, sodass sich große Schmelzmengen unmittelbar am Solidus bilden und Schmelztemperaturen daher genau bestimmt werden können. Die Daten zeigen, dass der Einfluss von Wasser auf die Solidustemperaturen viel stärker ist, als bisher angenommen. Die Daten machen es sehr plausibel, dass in der Zone niedriger seismischer Geschwindigkeiten tatsächlich geringe Mengen von Teilschmelzen existieren, die das Gleiten tektonischer Platten erleichtern.

Partielle Schmelzen existieren möglicherweise im Mantel nicht nur an der Lithosphäre-Asthenosphäre-Grenze, d. h. in 80-120 km Tiefe, sondern auch unmittelbar oberhalb der 660 km-Diskontinuität, die die Grenze zum unteren Mantel darstellt. Eine wichtige Frage ist hier, ob Schmelzen in dieser Tiefe gravitativ stabil sind. Der nächste Beitrag in diesem Teil des Jahresberichts beschäftigt sich mit dieser Frage und untersucht dazu die genaue Zusammensetzung und den Wassergehalt dieser Schmelzen. Diese Daten werden dann benutzt, um die erwartete Dichte der Schmelzen zu berechnen. Die Dichte der Schmelzen liegt geringfügig unter der des umgebenden Mantels, sodass sie eigentlich aufsteigen sollten, anstatt sich an der 660 km-Diskontinuität anzusammeln. Der Dichteunterschied ist jedoch so klein, dass unter bestimmten dynamischen Bedingungen die Bildung einer Schmelzlage immer noch möglich ist.

Wasserhaltige Fluide infiltrieren den Mantel in Subduktionszonen und die Bewegung solcher Fluide ist auch in der Kruste an vielen Prozessen beteiligt, wie etwa der Bildung hydrothermaler Erzlagerstätten. Die Art und Weise, wie sich Fluide in einem Gestein bewegen, hängt von den Benetzungseigenschaften der Oberflächen, der Rekristallisation der Matrix und der Bildung eines kontinuierlichen Fluid-Netzwerkes ab. Drei Beiträge beschäftigen sich mit diesen Prozessen. In einem Projekt wurden die Grenzwinkel in einem Olivin-Fluid-System unter den Bedingungen des oberen Mantels gemessen. Die Experimente zeigen, dass unter bestimmten Bedingungen die Grenzwinkel zwischen Fluid und Olivin-Kristallen für facettierte Flächen größer sind als für nicht-facettierte Flächen. Aufgrund der Daten erscheint es auch denkbar, dass die Vorzugsorientierung von Kristallen, wie sie durch Mantelkonvektion erzeugt wird, möglicherweis zu einer Anisotropie der Permeabilität führt. In einem weiteren Beitrag wurde die Bewegung von Wasser durch eine Olivin-Matrix direkt in Multianvil-Experimenten gemessen. Wie man erwarten würde, hängt die Mobilität des Wassers von der Korngröße der Probe ab. Die Abhängigkeit von der Korngröße kehrt sich jedoch mit zunehmender Versuchszeit um, was wahrscheinlich durch die Bildung eines dreidimensional verknüpften Netzwerks von wassergesättigten Korngrenzen verursacht wird. Solche Netzwerkstrukturen wurden in einem anderen Projekt in einem fluidgesättigten Quarzit direkt durch Röntgen-Tomographie abgebildet.

Die Löslichkeit von Wasser in den Mineralen des Mantles bestimmt die Verteilung von Wasser über die einzelnen Mantelreservoire und beeinflusst die Stabilität von wasserhaltigen Silikatschmelzen. Dieses Thema wird daher am BGI seit Jahrzehnten untersucht. Trotzdem sind immer noch viele wichtige Details, wie etwa die Abhängigkeit der Wasserlöslichkeit von Temperatur und Mineralzusammensetzung nicht hinreichend bekannt. Vier Beiträge beschäftigen sich mit diesen Problemen. Die Wasserlöslichkeit sowohl in Fe-haltigem Wadsleyit als auch in Majorit, jeweils im Gleichgewicht mit einer wasserhaltigen Silikatschmelze, sinkt mit steigender Temperatur. Die Löslichkeit von Wasser in Al-freiem Stishovit ist wohl viel geringer als in neueren Untersuchungen angenommen wurde. Neutronen-Beugungsdaten an Einkristallen von wasserhaltigem Olivin deuten auf Leerstellen auf dem Silizium-Gitterplatz hin, was möglicherweise mit dem Einbau von Protonen zusammenhängt. Wassergehalte in Mineralen und auch in Silikat-Gläsern werden oft durch Infrarot-Spektroskopie bestimmt. Die Neuentwicklung einer Apparatur zum extrem schnellen Abschrecken von Multianvil-Experimenten am BGI hat es hier ermöglicht, erstmals wasserhaltige Peridotit-Gläser herzustellen und den Infrarot-Extinktionskoeffizienten von H_2O und OH in diesen Proben zu bestimmen. Die Daten folgen dem Trend, der von anderen Zusammensetzungen bekannt ist. Dies zeigt auch, dass die entsprechenden Infrarot-Banden nicht nur einen Teil der OH-Spezies in der Probe repräsentieren, wie gelegentlich angenommen wurde.

Die Viskosität eines Magmas bestimmt weitgehend den Stil vulkanischer Aktivität, aber für manche Magmen-Zusammensetzungen lassen sich die Viskositäten nur schwer messen. Zwei Beiträge zeigen unkonventionelle Methoden auf, mit denen Viskositäten aus spektroskopischen oder kalorimetrischen Daten bestimmt werden können. Der letzte Beitrag in diesem Abschnitt des Jahresberichts untersucht die Struktur und Eigenschaften von Metallschmelzen im Fe-Ni-C-System, die relevant sind für den äußeren Kern der Erde. Die *ab initio*-Molekular-Dynamik-Simulationen zeigen, dass sich Ni ziemlich anders verhält als Fe und dass daher realistische Vorhersagen der Eigenschaften des äußeren Kerns nur möglich sind, wenn der Beitrag von Ni explizit berücksichtigt wird.

3.6 Rheologie und Metamorphose

Rheologie beschreibt, wie sich Materialien als Reaktion auf eine äußere Belastung verformen. Für die Erde und andere terrestrische Planeten ist die Rheologie von grundlegender Bedeutung für eine Reihe von dynamischen Prozessen wie die Bildung von Verwerfungen, Erdbeben und das plastische Fließen von Gesteinen im festen Zustand. Die Rheologie des Erdmantels bestimmt die Geschwindigkeit der großräumigen Festkörperkonvektion, die für die thermische Entwicklung der Erde, die Plattentektonik, die Vermischung chemischer Heterogenitäten und das Schicksal subduzierter Platten entscheidend ist. Um solche Prozesse zu verstehen, werden seit vielen Jahren experimentelle und theoretische Studien zur Rheologie von Gesteinen durchgeführt.

Bei experimentellen Studien wird die Dehnungsrate einer Probe gemessen, die einer Spannung ausgesetzt ist. Eine Schwierigkeit besteht darin, dass die Zeitskalen von Laborexperimenten notwendigerweise um viele Größenordnungen kürzer sind als die Zeitskalen der Verformung in der Erde. Dies bedeutet, dass sowohl die experimentellen Spannungen als auch die Verformungsraten viel höher sein müssen als in der Natur. Um experimentelle Ergebnisse auf das Erdinnere zu übertragen, sind große Extrapolationen erforderlich, die möglicherweise nicht immer gültig sind, da sich die Verformungsmechanismen auf atomarer Ebene in Experimenten und in der Erde aufgrund der sehr unterschiedlichen Spannungsniveaus unterscheiden können. Weitere Probleme ergeben sich daraus, dass die Rheologie von einer Vielzahl von Faktoren abhängt, darunter Spannung und Dehnungsrate, Temperatur, Druck, Korngröße, Dichte und Art der Kristalldefekte, Mineralogie und das Vorhandensein oder Fehlen von Fluiden.

Das Verständnis der Rheologie von Bridgmanit (Silikat-Perowskit), dem am häufigsten vorkommenden Mineral im unteren Erdmantel, ist für die Modellierung des großräumigen Prozesses der Mantelkonvektion unerlässlich. Die Untersuchung der Rheologie von Bridgmanit mit herkömmlichen Verformungsexperimenten ist äußerst schwierig, da die Proben extrem klein sind, der Druck über 25 GPa liegen muss und so die Messung der angelegten Spannung problematisch ist. Ein alternativer Ansatz besteht darin, die Diffusionsraten von Atomen zu untersuchen, von denen man annimmt, dass sie das duktile Fließen kontrollieren. Dieser Ansatz wird im folgenden ersten Beitrag verfolgt, der eine Untersuchung der Si-Al-Interdiffusion in Bridgmanit bei 24 GPa und 2023-2300 K beschreibt. Vorläufige Ergebnisse deuten darauf hin, dass die Geschwindigkeit der Si-Al-Interdiffusion um 2 bis 3 Größenordnungen langsamer ist als die bisher gemessenen Geschwindigkeiten der Silizium-Selbstdiffusion.

Die Geschwindigkeit plastischer Verformung wird im Allgemeinen sowohl durch einen Temperaturanstieg als auch durch eine Verringerung der Korngröße erhöht, da ersterer die Diffusionsrate erhöht und letztere die Abstände, über die die Diffusion stattfinden muss, verkürzt. Die Auswirkungen dieser beiden Parameter auf subduzierende Platten sind Gegenstand des zweiten Beitrags. Dabei handelt es sich um eine numerische Studie darüber, wie die Verringerung der Korngröße in Verbindung mit einer Schererwärmung dazu führen kann, dass der tiefe Teil einer subduzierenden Platte aufgrund seines negativen Auftriebs vom oberen Teil abbricht. Die Ergebnisse zeigen, dass die Abbruchtiefe stark von der Subduktionsgeschwindigkeit abhängt. Die Vorhersagen des Modells stimmen mit den beobachteten Tiefen von Erdbeben mittlerer Tiefe überein.

Tiefe Erdbeben treten im Bereich von 440-660 km unterhalb der Erdoberfläche auf. Ihre Ursache ist rätselhaft und seit vielen Jahren Gegenstand von Debatten. Aufgrund der sehr hohen Drücke in diesem Tiefenbereich kann Sprödbruch als Erdbebenmechanismus ausgeschlossen werden. Eine Möglichkeit besteht darin, dass eine sich selbst verstärkende Kombination aus Korngrößenverringerung und Schererwärmung zu einer lokalisierten Störung führt. Alternativ kann die Umwandlung von metastabilem Olivin in seine Hochdruckpolymorphe, Wadsleyit

und Ringwoodit, zu "Transformationsverwerfungen" führen. Dies ist möglich, wenn die Produkte der Umwandlung eine sehr kleine Korngröße haben, was hohe Verformungsraten in lokalisierten Verwerfungszonen aufgrund einer starken rheologischen Schwächung ermöglichen würde. Im dritten Beitrag werden vorläufige Ergebnisse von Verformungsexperimenten an Mg_2GeO_4-Olivin vorgestellt, der sich bei viel niedrigeren Drücken als Silikat-Olivin in die Spinell-Struktur umwandelt. Ziel dieser Studie ist es, den Effekt der Korngröße von Olivin auf die Bildung von Transformationsverwerfungen zu bewerten.

Die Hochdruckmetamorphose von basaltischer ozeanischer Kruste zu Eklogit, der hauptsächlich aus omphazitischem Pyroxen und Granat besteht, ist das Thema des letzten Beitrags in diesem Abschnitt. In einer Eklogitprobe wurde eine sehr feine oszillierende Zonierung an den Rändern eines Omphazitkorns in der Nähe seines Kontakts mit Granat beobachtet. Die fehlende Homogenisierung dieser Zonierung bedeutet aufgrund von Diffusionsmodellierungen, dass Fluide im Gestein nur für extrem kurze Zeiträume vorhanden waren, in der Größenordnung von 50-5000 Jahren.

3.7 Materialwissenschaften

Die am Bayerischen Geoinstitut zur Verfügung stehende Kombination an Hochdruck-ausrüstung, analytischen Geräten und der dazugehörigen Expertise erlaubt die Durchführung anspruchsvoller Experimente und Synthesen neuer Materialien. In diesem Jahr steht im Kapitel zu Materialwissenschaften die Beschreibung unerwarteter chemischer Eigenschaften von Materialien im Mittelpunkt, die unter hohem Druck und unter hohen Temperaturen synthetisiert wurden, im Gegensatz zu den vergangenen zwei Jahren, in denen das Kapitel weitgehend durch methodische Fortschritte in der Einkristall-Röntgenbeugung bestimmt wurde.

Die ersten zwei Beiträge zeigen solche chemischen Veränderungen exemplarisch auf, für sehr unterschiedliche Materialtypen. Während N_2-Stickstoffdimere als Anionen in Festkörpern typischerweise nur ganzzahlige Ladungen aufweisen, treten N_2-Anionen in festen Verbindungen mit Alkali- und Erdalkalimetallen unter hohem Druck mit gebrochenen Ladungswerten auf. Dieses unerwartete chemische Verhalten kann durch den Übertrag von Ladung von den metallischen Kationen auf die N_2-Dimere verstanden werden. NaCl (Kochsalz) gilt normalerweise als äußerst stabiler und reaktionsarmer ionischer Festkörper. Hochdruckexperimente, in denen es mit Yttrium in die Diamantstempelzelle geladen wird, zeigen jedoch, dass sich nach Erhitzung ein faszinierender Festkörper bildet, Y_2ClC. Die Struktur von Y_2ClC ist eine kubisch dichteste Packung der C- und Cl-Atome, mit den Yttrium-Atomen in den oktaedrischen Leerstellen. NaCl wird oft als inaktiver Isolator in die Diamantstempelzelle geladen. Die hier beschriebene Reaktion zeigt, dass Proben aus solchen Experimenten auf chemische Verunreinigungen untersucht hin werden sollten.

Als äußerst refraktäre Materialien gehören Karbide zu den ersten Mineralien, die sich im Sonnennebel gebildet haben. Karbide werden technologisch als Schleifmittel genutzt, als Alternative zu Diamanten, da sie eine größere Temperaturstabilität aufweisen. In einem Beitrag dieses Kapitels wird die Stabilität und Zustandsgleichung eines Polymorphs von SiC (6H α-SiC) untersucht, mit dem Ergebnis, dass diese Form von SiC relativ zu Diamant und Silizium stabil sein sollte. Einige Karbide von Dysprosium mit Zusammensetzungen Dy_4C_3 und Dy_2C_3, wurden bei hohem Druck synthetisiert und untersucht, wobei Dy_2C_3 zuvor noch nie beschrieben wurde. Dieser Block der Beiträge schließt mit der Vorstellung der refraktären Rheniumboride ReB_3 und ReB_4 ab, die sich bei hohem Druck bilden.

Zwei Hochdruckuntersuchungen zu Manganoxiden setzen ein langes Forschungsprogramm zu Übergangsmetalloxiden am Bayerischen Geoinstitut fort. Ähnlich wie bei Eisen führt der variable Oxidationszustand des Mn zu zahlreichen Oxidphasen. Hier werden zwei Syntheseprodukte aus Vielstempelpressen-Experimenten vorgestellt und untersucht, mit Zusammensetzungen Mn_2O_3 (Ilmenit-Typ) und Mn_3O_4 (Marokit-Typ).

Durch die Beschreibung von Hochtemperatur-Supraleitung in Metallhydriden unter Druck ist diese Materialklasse in den Fokus der Hochdruckphysik geraten. Yttriumhydride mit ungewöhnlichen Zusammensetzungen spielen dabei eine wichtige Rolle, und hier werden experimentelle Ergebnisse zur Synthese eines neuen Yttriumhydrids vorgestellt. Dieses Syntheseprodukt zeichnet sich durch zwei interessante Eigenschaften aus: (i) Im Gegensatz zu bisher bekannten Phasen ist das zugrundeliegende Yttrium-Kristallgitter nicht durch dichtest gepackte Yttrium-Schichten charakterisiert, (ii) der Wasserstoffgehalt des Hydrids ändert sich unter Druck. Die Phase enthält bei Normalbedingungen keinen Wasserstoff. Die hexagonale Struktur für das zugrundeliegende Yttriumgitter wurde durch weitere Experimente am reinen Metall als neue Yttrium-Hochdruckphase bestätigt.

Der letzte Beitrag dieses Kapitels geht der Frage nach, was einen einfachen molekularen Festkörper definiert und wie er sich unter Kompression verhält. Die Systeme, die üblicherweise dafür betrachtet werden (H_2, N_2 oder O_2) zeigen aufgrund von Vielkörper-Wechselwirkungen ein komplexes Verhalten. Im Gegensatz dazu haben Kohlenstoff-Tetrahalide (CX_4) einfache Bindungen, und das hier untersuchte CF_4 kann als Prototyp betrachtet werden. Unter Kompression zeigt CF_4 einen Übergang von Strukturen, die von Molekülen bestimmt werden, zu solchen, die von einer dichtesten Packung der Halogenatome bestimmt werden.

3.8 Methodische Entwicklungen

Das Bayerische Geoinstitut steht seit seiner Gründung an der Spitze der methodischen Entwicklungen in der Hochdruckforschung. Die kontinuierliche Entwicklung neuer und verbesserter experimenteller, analytischer und modellierender Methoden ist erforderlich, um bei der Erforschung der Struktur, Dynamik und Entwicklung der Erde und der Planeten auf dem neuesten Stand zu bleiben.

In diesem Kapitel werden sechs Beispiele für die Entwicklung von Hochdruckexperimenten und zwei Beispiele für die Softwareentwicklung im Jahr 2021 vorgestellt. Im ersten Beispiel wird eine Methode zum Einfangen von Fluiden bei hohem Druck und hoher Temperatur mit Hilfe eines Diamant-Einkristalls entwickelt. Bestehende Techniken zum Einschluss von Fluiden in Hochdruckexperimenten mit Hilfe von Poren in Diamantpulvern liefern manchmal nur schlecht reproduzierbare Resultate. Im Gegensatz dazu liefert die neu entwickelte Methode in sich konsistente Ergebnisse. Der zweite Beitrag berichtet über die Entwicklung eines BDD-Ofens (Bor-dotierter Diamant) zur Erzeugung ultrahoher Temperaturen in Multanvil-Experimenten. Durch Sintern von BDD-Pulver mit einem Pech-Bindemittel wurde ein neues, maschinell bearbeitbares BDD-Material geschaffen, um die Probleme der übermäßigen Härte und Sprödigkeit früherer BDD-Ofenkonstruktionen zu lösen. Mit diesem neuen Material konnten Temperaturen von bis zu 3300 K stabil erzeugt werden. In der dritten Studie werden piezoelektrische Kristalle in Verformungsexperimenten verwendet, um mechanische Spannungen in Proben bei hohen Drücken und Temperaturen zu messen. Da hohe Temperaturen zu Signalverlusten aus dem piezoelektrischen Kristall führen, wurde ein besser isolierter Ofenaufbau entwickelt, um Signalverluste zu minimieren. Die piezoelektrische Dehnungsmessung wird die Möglichkeit zur *in situ*-Spannungsmessung eröffnen, so dass wir am BGI quantitative Deformationsstudien durchführen können, die bisher nur an Synchrotron-Anlagen möglich waren. Der vierte Beitrag stellt Messungen von Temperaturverteilungen in Proben aus der Kolben-Zylinder-Presse vor, die mit gestuften Öfen beheizt werden. Die Entwicklung dieser neuen Öfen mit geringen Temperaturgradienten für die Kolben-Zylinder-Presse wird das Spektrum der am Bayerischen Geoinstitut durchführbaren Experimente erweitern. Die fünfte Studie berichtet über die Entwicklung von Multanvil-Techniken, die für Tieftemperatur-Experimente bei hohem Druck an der Neutronenanlage FRM-II optimiert sind. Diese Entwicklung ebnet den Weg für die Untersuchung der inneren Struktur der äußeren Planeten des Sonnensystems.

Im Gegensatz zu diesen fünf Berichten über Entwicklungen in der Hochdrucktechnik berichten die beiden letzten Studien über die Entwicklung von Softwarepaketen. Die sechste berichtet über die Entwicklung einer neuen Software für die Analyse von Röntgenbeugungsdaten von polykristallinen Proben in der Diamantstempel-Presse. Die Software bietet eine Lösung für das Problem der Verarbeitung großer Datenmengen, die in Beugungsexperimenten mit Röntgenstrahlen hoher Energie erzeugt werden. Der siebte Beitrag stellt ein neues Softwarepaket für die Visualisierung von geowissenschaftlichen Daten in 3D vor. Die Software dient der Erstellung von Datensätzen, die als Ausgangspunkt für numerische Modelle verwendet werden können.

3. Research Projects

3.1 Earth and Planetary Structure and Dynamics

Planetary formation started rapidly after condensation, upon cooling of the nebular gas, forming the first solids. Iron meteorite parent bodies proposedly started to form only a hundred thousand years after the formation of the Sun, while planetesimal formation in the outer solar system lasted for several million years longer than in the inner disk. Chondrite meteorites which are the closest to the average composition of the solar system for non-volatile elements may be the relicts of materials that formed the planets. The bulk chemical composition of the terrestrial planets is nevertheless difficult to constrain for many elements because of differentiation processes such as magma ocean degassing and core-mantle-crust formation, and impact processes. Large differences have been found between chondrites and terrestrial planets for volatile element budgets and also major elemental ratios (*e.g.*, Mg/Si, Al/Mg). Additionally, distinct mass-independent stable isotopic anomalies for many elements were identified between planetary materials and planets indicating that the protoplanetary disk was heterogeneous in composition. These anomalies cannot be modified by differentiation processes. Therefore, it has been proposed that Earth and other terrestrial planets of the inner solar system are likely the results of the accumulation of numerous smaller primitive as well as differentiated bodies. Constraining the formation conditions of planetary materials in the Solar System and how they contributed to the chemical and physical evolution of Earth and planetary interiors are the subjects of investigation in this section.

Present-day comets, relicts of planet formation in the outer solar system, contain large amounts of highly volatile compounds despite experiencing heating due to radioactive decay and collisions early on in their evolution. Golabek and Jutzi study these two effects using combined geodynamical and SPH (smoothed particle hydrodynamics) simulations and determined that internal thermal evolution controls the amount of remaining highly volatile ices in the large post-collision remnants, while for the objects formed from unbound post-collision material the impact heating is dominant.

A collision among planetesimals also played a major role in the formation of the pallasite meteorite group. Walte and Golabek analyze four large main group pallasite slabs and find evidence that certain pallasite regions in these meteorites remained unaffected by the collision and thus represent the pre-impact mantle that still contained some metal pockets. Additionally, they demonstrate that pallasite features like fractures and veinlets can be reproduced with deformation experiments, and were thus caused by an impact event.

Two contributions bring further constraints on the nature of the building blocks of the Earth. First, Rubie *et al.* describe N-body simulations and partitioning models for carbon using chondrites and achondrites from the non-carbonaceous and carbonaceous regions. They find that the Earth's carbon budget can be reconciled with its accretion and differentiation history if carbonaceous chondrite materials include also a large portion of differentiated planetesimals. Earth would be then formed by a mixture of non-carbonaceous and limited amounts (≈ 0.5 %) of carbonaceous materials including at least 40 % of differentiated planetesimals.

Frossard *et al.* provide further constraints on the Earth's building blocks. Small but resolved nucleosynthetic isotopic anomalies in stable neodymium isotopes such as ^{145}Nd and ^{148}Nd (mixtures of *s*- and *r*-processes) are found in various chondrites and achondrites from the non-carbonaceous and carbonaceous groups. The excesses in ^{145}Nd and ^{148}Nd in NC achondrites compared to NC chondrites (but also Earth, Mars, and the Moon) suggest a change at about 1.5 million years for the inner solar system composition associated with the thermal processing of pre-solar grains, the carriers of large nucleosynthetic anomalies. Consequently, either Earth may have formed from enstatite chondrite-like materials or from a mixture of unknown *s*-process enriched materials subsequently mixed with chondrites and achondrites from various origin (non-carbonaceous or carbonaceous).

Lunar samples provide records of Moon's formation and impact bombardment history in the early solar system. Lunar Apollo samples from the anorthosite and KREEP-rich suites provide constraints on the crystallization and differentiation of the lunar magma ocean (LMO). The Mg-magmatic suite formed by partial melting of deep LMO cumulates as a consequence of mantle overturn. The mare basalts are the latest products of partial melting of the lunar interior until ~ 2 Ga, as recently measured in Chang'e 5's return samples. The stages and duration of LMO crystallization are difficult to track as no mantle rocks have been sampled yet on the Moon's surface or as lunar meteorites. Impact processes have also altered the igneous records of the lunar rocks.

Pöppelbaum *et al.* report evidence of preserved chromium-rich components in melt inclusions found in olivine clasts in an Apollo 17 impact melt feldspathic breccia, originating from the Imbrium basin formation. Their composition points toward a distinct melt component which may be related to the LMO differentiation and Mg-suite formation.

A study by Zhang *et al.* of a norite clast embedded within an impact melt breccia provides the earliest evidence of zircon crystallization and therefore mafic lower crust formation by ~ 4.46 Ga, providing a new minimum age for the Moon. These chronological records may be, however, questioned due to the possible nano-scale re-distribution of Pb isotopes during the formation of the impact melt breccia. The second study by Zhang *et al.* presents lunar baddeleyite U-Pb records of a Mg-suite norite which, when compared with other chronometers, indicates their rapid cooling within the lunar crust. The chronological records of lunar samples point towards a major episode of magmatism at ~ 4.3 Ga that is slightly younger than the anorthositic crust (4.36 Ga). These results provide new constraints on the magmatic evolution of the Moon.

On Earth, hydrous phases like amphibole have been found in mantle xenoliths, and dehydration melting of amphibole has been suggested to cause the shear-wave velocity reduction at the lithosphere-asthenosphere boundary. Putak Juriček and Keppler reinvestigate the amphibole stability in the upper mantle experimentally and find it highly dependent on the geothermal gradient. They find that along typical mantle geotherms amphibole might be stable, but it does not cause melting at the amphibole-out boundary. Thus, it is unlikely that dehydration melting at the amphibole stability limit can explain the S-wave velocity reduction.

The temperature profile of present-day Earth remains debated. For this purpose, Katsura reevaluated experimental data for olivine, wadsleyite, ringwoodite and bridgmanite. Showing that the thermal expansivity in previous models was overestimated, Katsura obtains an updated adiabatic temperature profile suggesting lower temperatures inside Earth compared to previous studies.

a. *Modification of cometesimal interiors by early thermal evolution and collisions (G.J. Golabek and M. Jutzi/Bern)*

Comets and small Kuiper belt objects are considered to be among the most primitive objects in the solar system as comets like C/1995 O1 Hale-Bopp are rich in highly volatile ices like CO. It has been suggested that early in the solar system evolution the precursors of both groups, the so-called icy planetesimals, were modified by both short-lived radiogenic heating and collisional heating. We employ 2D finite-difference numerical models to study the internal thermal evolution of these objects, where we vary formation time, radius and rock-to-ice mass fraction. Additionally, we perform 3D Smoothed Particle Hydrodynamics (SPH) collision models with different impact parameters, thus considering both cratering and catastrophic disruption events. Combining the results of both numerical models, we estimate under which conditions highly volatile ices like CO, CO_2 and NH_3 can be retained inside present-day comets and Kuiper belt objects. Results indicate that for present-day objects derived from the largest post-collision remnant the internal thermal evolution controls the amount of remaining highly volatile ices, while for the objects formed from unbound post-collision material the impact heating is dominant.

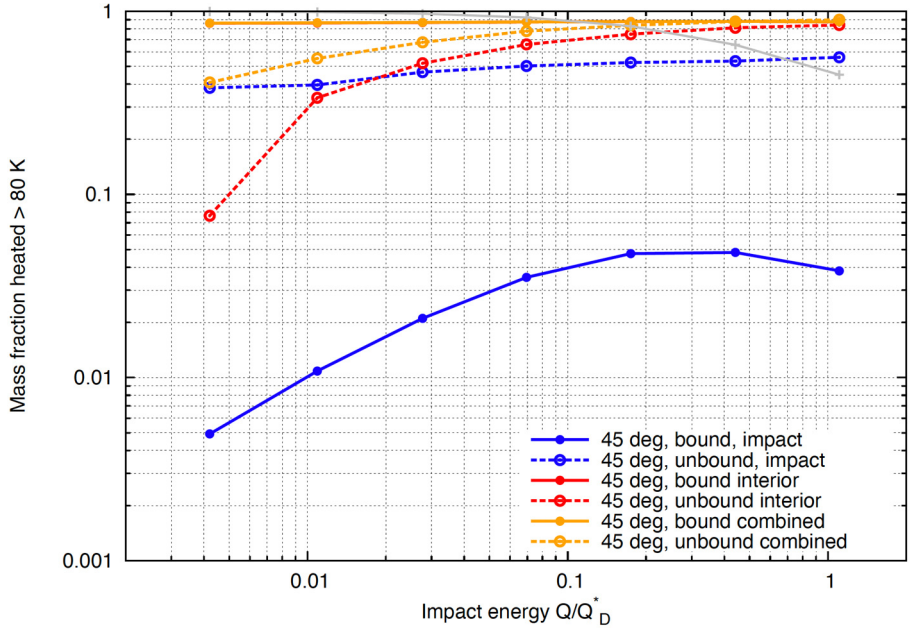

Fig. 3.1-1: Mass fraction of material that experienced T_{max} > 80 K (CO_2 sublimation temperature) by either impact or interior heating, as a function of normalized specific impact energy Q_D*. Shown is the case with radius R = 50 km, impact velocity v_{imp} = 3 km/s, impact angle θ = 45 ° and a formation time of t_{form} = 3 Myr. The gray line shows the relative size of the largest post-collision remnant.

b. *Understanding the early evolution of Pallasite Parent Bodies by investigating olivine aggregates of Main Group Pallasites (N. Walte/Garching and G.J. Golabek)*

Olivine aggregates are coherent bodies of polycrystalline olivine with minor inclusions of troilite and Fe-Ni metal that are found inside angular pallasites (Fig. 3.1-2a) that represent little-altered samples from the mantle of their parent bodies. We investigated olivine aggregates from the main group pallasites Seymchan, Imilac, Esquel, and Fukang and compared their textures to the results of deformation experiments. The experiments were performed with the SAPHiR multianvil press that is situated at the FRM II neutron source in Garching. Main group pallasites are suggested to be derived from a single pallasite parent body (PPB). Hence, the differences between the four samples reflect differences in a common mantle.

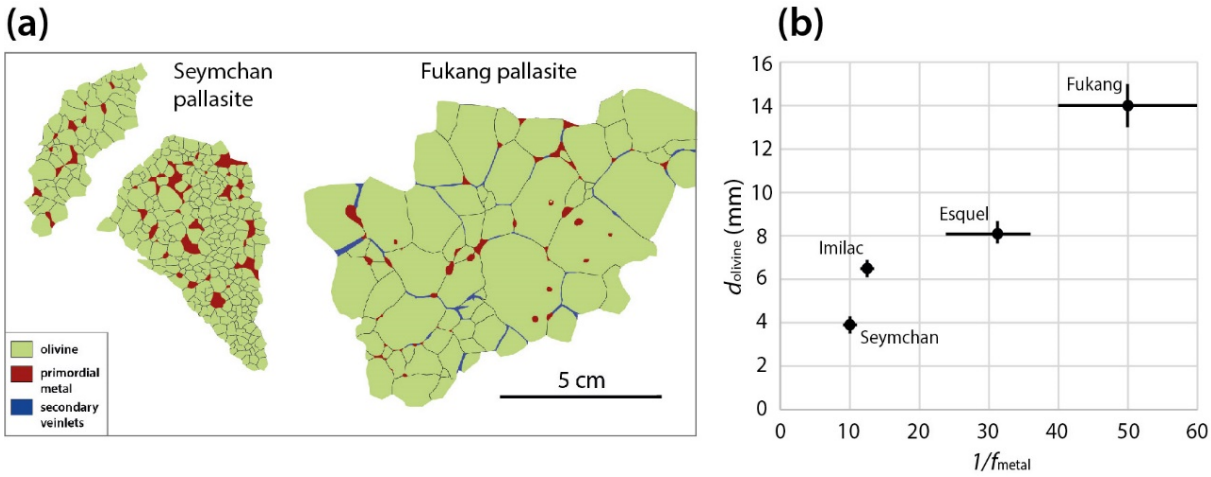

Fig. 3.1-2: (a) Redrawn olivine aggregates of Seymchan and Fukang pallasite. Note the differences in olivine grain size (green) and primordial metal fraction (red). (b) Average grain size and inverse fraction of primordial metal pockets of four main group pallasites. The relationship can be explained by Zener Pinning inhibited static grain growth in the PPB mantle.

One characteristic feature of pallasites is the generally large size of the olivine grains that has previously been explained by static grain growth in a warm PPB (see previous annual reports). However, our investigations show that the average grain size varies between different pallasites by a factor of more than three from Seymchan (3.9 mm) to Fukang (≈ 14 mm) (Fig. 3.1-2a). Our analyses show that the grain size of our samples is approximately inversely proportional to the volume fraction of roundish metal pockets inside olivine aggregates (Fig. 3.1-2b). These 'primordial' metal pockets were already present in the mantle before the pallasite formation event that led to deformation and break-up of most aggregates (likely during an impact). We interpret the relation between grain size and the metal fraction by Zener pinning inhibited grain growth in the mantle prior to the impact, which means that different mantle regions must have contained various amounts of primordial metal.

Most olivine aggregates also contain secondary fractures and veinlets formed during the pallasite formation. We found that the secondary features have been altered by various degrees among the investigated samples (Fig. 3.1-3). This alteration could be experimentally reproduced with deformation–annealing experiments. The samples contained a mixture of olivine plus FeS and Au that was heated to 1300 °C so that FeS and Au formed two immiscible melt phases and deformed at a strain rate of 5×10^{-3} s^{-1}. The first experiment was quenched immediately, and the second was allowed to anneal for two hours prior to quenching. The resulting microstructures reproduced the differences between the different pallasites (Fig. 3.1-3, right side), which indicates that the textural differences between the pallasites are caused by different times of static annealing at high temperature after the pallasite formation. We interpret this difference by different burial depths of the pallasites after the impact in the order Seymchan (rapid cooling below the Fe-Ni-S solidus within months to years according to previous results), Imilac, Esquel, and Fukang. Since this represents, at the same time, the order of decreasing primordial metal content, the PPB may have been characterized by a decreasing metal content in the dunitic parts of the mantle from ≈ 10 vol. % close to the surface to ≈ 2 vol. % at greater depths. Such an inverse gradation of dense phases is not compatible with gravitational differentiation mechanisms, which may imply a complex multi-impact history of the PPB.

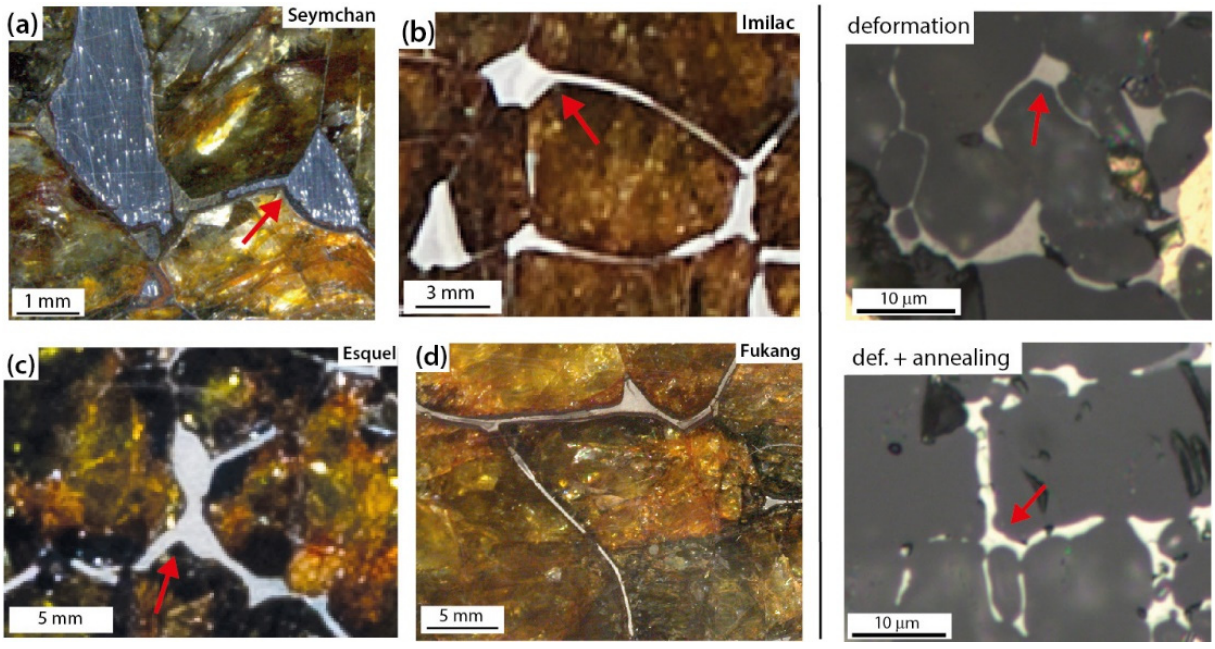

Fig. 3.1-3: Olivine metal textures inside olivine aggregates (left and middle) and olivine – FeS textures of experiments (right) that were immediately quenched after deformation and that were annealed for two hours after deformation. Note a progressively increasing rounding of nooks and merging of primordial metal pockets from (a) to (d) with the veinlets that is reproduced in the experiments (red arrows) that indicates post-deformation annealing at high temperature. Credit: (b) © The Trustees of the National History Museum, London, UK (c) Denis Finnin, American Museum of Natural History, NY City, USA (d) Dolores Hill, Univ. Arizona, Lunar & Planetary Laboratory; Arizona, USA.

c. *Determination of the fraction of planetesimals in the outer solar system that underwent core-mantle differentiation. (D.C. Rubie, I. Blanchard/Potsdam and A. Morbidelli/Nice)*

Carbonaceous chondrite meteorites are derived from small parent planetary bodies that formed early in the outer solar system and are considered to be representative of planetesimals from this region that were accreted to the Earth and other terrestrial planets. Some carbonaceous chondrite meteorites (*e.g.*, C1 chondrites) are fully oxidized, have high water contents, and contain no metal. However, certain iron meteorites also originated in this region and demonstrate that some fraction of parent bodies were metal-bearing and underwent early differentiation that resulted in the formation of iron-rich metallic cores. Here we present results of a model of the evolution of carbon in Earth's mantle and core during accretion that provide an estimate of the fraction of planetesimals in the outer solar system that underwent early core-mantle differentiation.

We have recently determined the metal-silicate partitioning of carbon through laser-heated diamond anvil cell experiments at 41-79 GPa and 3600-4000 K (see previous BGI Annual Reports). At relatively low pressures and temperatures, carbon is strongly siderophile, but our results show that it becomes progressively less siderophile as pressures and temperatures increase. We have used the partitioning results in a combined accretion/multistage core formation model that successfully reproduces Earth's mantle composition for a large number of elements. The model is based on N-body accretion simulations that start with up to 200 Mars-size embryos embedded in a protoplanetary disk consisting of a few thousand much smaller planetesimals that are initially dispersed over heliocentric distances out to 9 au. Embryos grow through accretional collisions with other embryos and planetesimals, and a small number of these survive to form the terrestrial planets. Most accretional collisions involve a core formation event in which accreted metal equilibrates with silicate liquid in an impact-induced magma ocean before segregating to the core. Using a combination of mass balance and element partitioning, the evolving compositions of Earth's mantle and core are tracked throughout accretion. The bulk chemical compositions of all starting embryos and planetesimals are required and, in the present context, estimates of their bulk carbon concentrations are necessary. Carbonaceous chondrite (CC) meteorites from undifferentiated parent bodies contain ~ 2.2-3.35 wt. % C. whereas non-carbonaceous (NC) meteorites from undifferentiated parent bodies in the inner solar system contain on average ~ 0.16 wt. % C (Table 3.1-1). It has been shown recently, based on very low carbon concentrations in iron meteorites, that all differentiated parent bodies were highly depleted in carbon due to sublimation at high temperatures during core-mantle differentiation (Table 3.1-1). These estimates show that almost all of the Earth's carbon budget was delivered by the accretion of undifferentiated carbonaceous chondrite planetesimals.

According to the accretion simulation, the total mass of material accreted from the CC region is 0.56 % of Earth's final mass. Assuming that undifferentiated carbonaceous chondrite bodies contain on average 3.35 wt. % C and that 40 % of these planetesimals were differentiated, the

evolution of Earth's mantle carbon concentration when the multistage core-mantle differentiation model is combined with a Grand Tack N-body accretion simulation is shown in Figure 3.1-4: The final mantle C concentration is 155 ppm, which lies within a recent bulk-silicate earth (BSE) estimate of 140±40 ppm. The effect of varying the percentage of differentiated planetesimals from 10 % to 90 % is shown in Figure 3.1-5. Again, if undifferentiated CC bodies contain on average 3.35 wt. % C, a BSE C concentration of 140±40 ppm is achieved when the percentage of differentiated planetesimals is 45±15 %; the corresponding bulk Earth concentration is 500±100 ppm and the concentration in the core is 1270±300 ppm. If undifferentiated CC bodies contain on average 2.2 wt. % C, the same BSE concentration is achieved when the percentage of differentiated planetesimals is 25±15 %; the corresponding bulk Earth concentration is then 600±150 ppm.

Table 3.1-1: Estimates of average bulk carbon concentrations of planetesimals and embryos in the early solar system.

	Undifferentiated	Differentiated
Carbonaceous chondrite (CC) bodies (> 4.5 AU)	2.2-3.35 wt. %	0.002 wt. %
Noncarbonaceous chondrite bodies (NC) (< 3 AU)	0.16 wt. %	0.004 wt. %

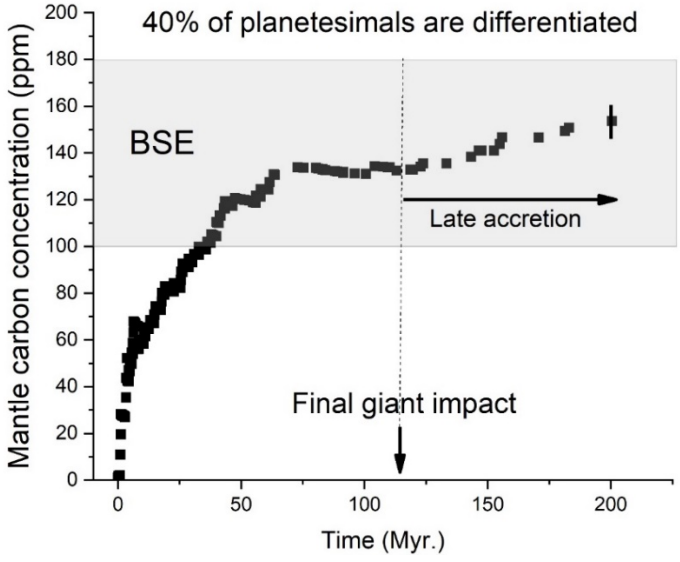

Fig. 3.1-4: Evolution of the modelled carbon concentration in Earth's mantle as a function of time during accretion using a Grand Tack N-body accretion model. Each symbol represents an accretion event. The time of the final (Moon-forming) giant impact is 113 Myr. Accretion that follows this event is termed "late accretion" and is considered to postdate core formation. The carbon concentrations in starting bodies are shown in Table 3.1-1. The shaded grey region shows a recent estimate of the BSE carbon concentration of 140±40 ppm.

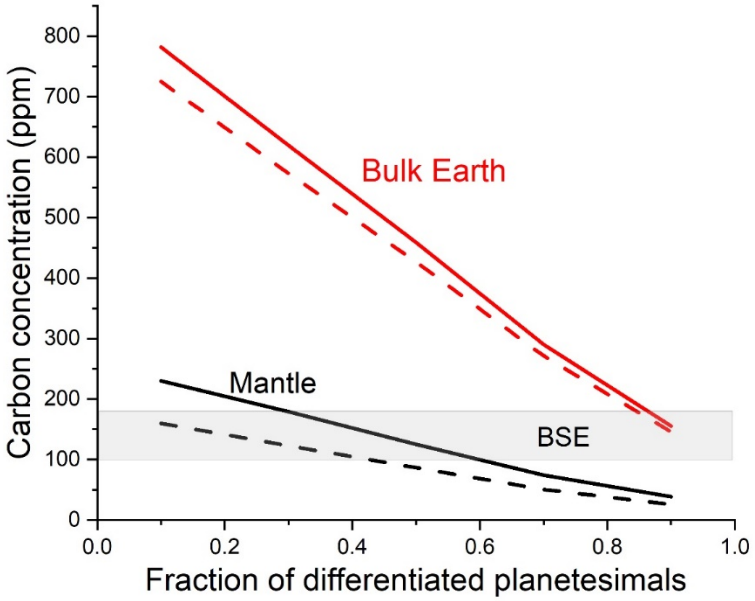

Fig. 3.1-5: Final carbon concentrations in Earth's mantle (black lines) and in the bulk Earth (red lines) as a function of the fraction of differentiated planetesimals in the CC region of the protoplanetary disk (outer solar system). The solid lines show results obtained when undifferentiated CC bodies contain 3.35 wt. % C (CI value) and the dash lines show results when this value is 2.2 wt. % (CM value) (Table 3.1-1). The concentration of C in Earth's core is 1270±300 ppm when the calculated BSE concentration is 140±40 ppm.

d. *Evidence from achondrites for a temporal change in Nd nucleosynthetic anomalies within the first 1.5 million years of the inner solar system formation (P. Frossard/Clermont-Ferrand, Z. Guo and M. Spencer/London, Ontario, M. Boyet/Aubière and A. Bouvier)*

Heterogeneity in isotopic compositions within the protoplanetary disc has been demonstrated for a number of elements measured in extra-terrestrial materials, mostly based on chondrite meteorite analyses. However, precise ^{182}Hf-^{182}W and ^{26}Al-^{26}Mg ages of iron meteorites, achondrites, and chondrules show that chondrites accreted later than achondrites and therefore do not strictly represent the early (< 2 Ma) solar system composition. Here we present the Nd mass-independent stable isotopic compositions of a suite of diverse achondrites to better constrain the Nd isotope evolution of the early solar system. Carbonaceous (C) achondrites are indistinguishable from their chondritic counterpart. However, early formed planetesimals as sampled by silicate-rich non-carbonaceous (NC) achondrite meteorites have higher ^{145}Nd/^{144}Nd and ^{148}Nd/^{144}Nd ratios ($3.9 < \mu^{145}Nd < 11.0$ and $9.1 < \mu^{148}Nd < 17.9$ in part per million deviation, or μiNd) compared to NC chondrites ($2.7 < \mu^{145}Nd < 3.3$ and $2.2 < \mu^{148}Nd < 8.1$). Moreover, the three terrestrial planets for which we have samples available (Earth, Mars, and the Moon) as well as the silicate inclusions from the non-magmatic IIE iron meteorite Miles present a systematic deficit in μ^{145}Nd and μ^{148}Nd compared to early-formed NC achondrites. Unlike chondrites, the Nd anomalies in achondrites are not correlated to the heliocentric distance of

accretion of their respective parent bodies as inferred from redox conditions. Chronological constraints on planetesimal accretion suggest that Nd (and other elements such as Mo and Zr) nucleosynthetic compositions of the inner part of the protoplanetary disc significantly changed around 1.5 Ma after Solar System formation due to thermal processing of dust in the protoplanetary disc. Our mass balance calculations show that up to 2 % of the Nd mass needs to be destroyed between the accretion of the early achondrite parent bodies and terrestrial planets.

This relatively late event coincides with the beginning of chondrule formation or at least their preservation. Terrestrial planets formed subsequently by a complex accretion regime during several million years. Therefore, two scenarios are envisioned considering the reported Nd isotope composition of early planetesimals: 1) Terrestrial planets accreted mostly chondritic material similar in composition to enstatite chondrites, or 2) early planetesimals constitute substantial parts of terrestrial planets building blocks mixed with highly thermally processed material enriched in s-process, still unsampled by meteorites.

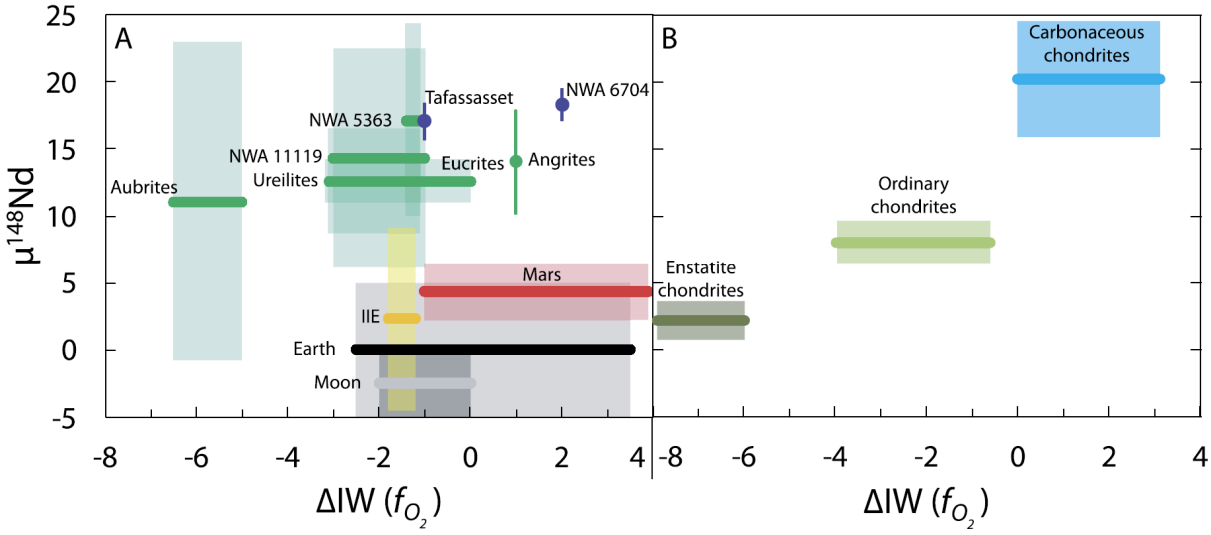

Fig. 3.1-6: μ^{148}Nd (in parts per million) shown against a proxy of the heliocentric distance using the redox conditions expressed relative to the IW (Fe-FeO) equilibrium, in (A) achondrites and (B) chondrites. Unlike chondrites, the Nd anomalies in achondrites are not correlated to the heliocentric distance of accretion of their respective parent bodies as inferred from redox conditions.

e. *Petrological study of olivine inclusions in Apollo 17 lunar impact melt breccia 73155 (M. Pöppelbaum, A. Néri, N. Miyajima, A.C. Withers and A. Bouvier)*

The Apollo, Luna and more recently the Chang'e 5 space missions have returned samples collected on the Moon, providing constraints on its formation, differentiation, and impact history. In this study, we investigated melt inclusions found in the Apollo 17 impact-melt breccia (IMB) thin-section 73155,69. The IMB consists of a crystallised melt matrix with

poikilitic texture containing plutonic rock and mineral clasts as plagioclase, orthopyroxene, clinopyroxene, and olivine phenocrysts.

Crystallised melt inclusions were investigated in two olivine phenocrysts and differ both texturally and compositionally in the two Cr-poor olivine hosts but also within each olivine. In olivine #1 (Fig. 3.1-7), there are (1) pyroxene-rich inclusions with ~ 2 µm chromian spinel rim, (2) poikilitic inclusions similar to the impact melt, and (3) symplectic inclusions consisting of a pyroxene-plagioclase intergrowth, spinel rim, and Fe-Ni metal in and around the inclusions (Fig. 3.1-7). In olivine #2, on the other hand, there are crystallized melt inclusions consisting mainly of either pyroxene or plagioclase, together with minor amounts of scattered spinel grains. Closure temperatures were determined to be 1357 K (± 39 K) using the Ca-Mg exchange reaction between high-Ca and low-Ca pyroxene, and 1259 K (± 44 K) using the Fe-Mg exchange reaction between spinel and olivine. At these temperatures, the oxygen fugacities calculated from the compositions of the phases in the quartz-iron-ferrosilite (QIFs) and the quartz-iron-fayalite (QIFa) assemblages vary between ~ IW-1.2-1.6 (QIFs) and ~ IW-1.1-1.3 (QIFa).

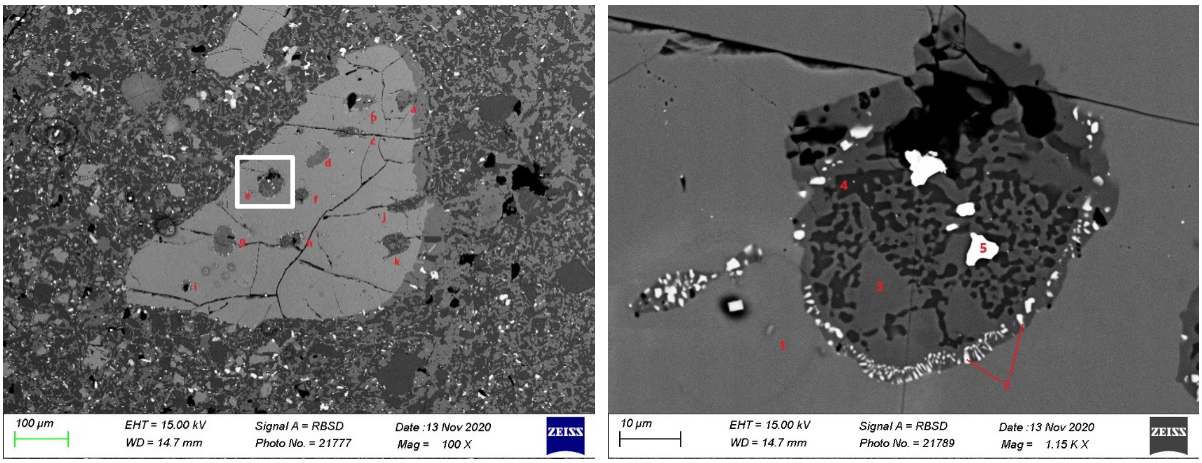

Fig. 3.1-7: Left: BSE image of olivine #1 and poikilitic impact melt host in 73155,69. Letters correspond to individual inclusions with 1e location indicated by the frame. Right: BSE image of symplectic inclusion 1e. Numbers mark different phases: 1 – olivine, 2 – spinel, 3 – clinopyroxene, 4 – plagioclase, 5 – Fe-Ni metal.

Meteoritic contamination is observed from the Ni and Co content in the FeNi-metal within the inclusions, supporting prior reports based on highly-siderophile trace-element abundances in the IMB. From the Cr-content of the spinel and the Mg-content of the olivines, the olivines can probably be linked to a norite to gabbronorite from the Mg-suite. The melt inclusions in olivine #1 probably represent mixtures of two different melts which produced the symplectites. The composition of these inclusions resembles mixtures of the impact melt matrix related to the low-K Fra Mauro formation (and Imbrium ejecta) with a Fe- and Cr-rich, pyroxene-normative, exogenous melt. A similar formation mechanism was previously proposed for lunar chromite

symplectites found in Apollo troctolite 76535 from the highlands Mg-suite. The formation process of olivine #2 seems different as there is barely any spinel and the phase proportions and textures are quite different. The mechanical processes leading to compositionally and texturally different inclusions in such homogenous olivines is, however, unknown.

f. *Timing of lunar Mg-suite magmatism constrained by SIMS U-Pb dating of Apollo norite 78238 (B. Zhang/London, Ontario/Los Angeles, Y. Lin and J. Hao/Beijing, P.H. Warren/Los Angeles, D.E. Moser, I.R. Barker and S.R. Shieh/London, Ontario and A. Bouvier)*

The lunar Mg-suite magmatic rocks are commonly thought to represent mafic intrusions into the anorthositic flotation crust of the lunar magma ocean (LMO). Their geochronology is, therefore, important for constraining evolution models of the LMO. Petrogenetic models of the Mg-suite hold that their parent magmas were derived from primary LMO sources (Mg-cumulates, An-rich plagioclase, and melts enriched in KREEP (potassium, rare earth elements, and phosphorus).

Previous radiogenic isotopic age interpretations of Mg-suite and putatively older, related ferroan anorthosites (FANs) overlap over a 200-million-year interval. The Apollo 78238 norite is an exemplary Mg-suite rock with a relict coarse igneous texture modified by shock metamorphism. *In situ* nano secondary ion mass spectrometry U-Pb analyses of zircon and baddeleyite in 78238 yield discordant arrays, attributed to recent impact metamorphism, with upper intercepts that constrain its crystallization age. The four oldest baddeleyite analyses give a weighted mean $^{207}Pb/^{206}Pb$ age of 4332 ±18 Ma (2σ, MSWD =0.06, P =0.98), which is interpreted as the crystallization age of the norite. The overlap of the baddeleyite age with previously reported Sm-Nd and Pb-Pb mineral isochron ages for 78238 (Edmunson *et al.*, 2009) supports a moderately fast cooling of the norite. Moreover, it is distinguishably younger than the most precisely dated sample of FAN (Apollo 60025), measured at 4360 ±3 Ma by Sm-Nd and Pb-Pb mineral isochrons (Borg *et al.*, 2011). Together with the baddeleyite $^{207}Pb/^{206}Pb$ age of Apollo Mg-suite troctolite 76535 at 4328 ±8 Ma (White *et al.*, 2020), the chronological record of the 78238 norite indicates a significant Mg-suite magmatic event at 4.33 Ga and a lower age limit on LMO differentiation.

When associated with the microstructural analysis of U-rich accessory minerals, the *in situ* U-Pb dating of U-rich micro-accessory minerals in lunar highland rocks provides a powerful tool to constrain the origin and timescale of the Mg-suite magmatism. So far, 76535 and 78238 are the only two Mg-suite rocks that have been dated using the SIMS U-Pb method in U-rich minerals. If such high-resolution SIMS dating of U-rich minerals is performed on numerous Apollo Mg-suite rocks, we might be able to better understand the timescale of Mg-suite magmatism and the temporal relationship within the troctolite-norite-gabbro sequence, and furthermore, how endogenic thermal processes worked together with exogenic heating

(impacts) to form the lunar lithological units. Thus, this study offers insights into a path forward for obtaining a precise timeline for the Mg-suite that has been limited by mineral isochron age determinations with relatively lower precision.

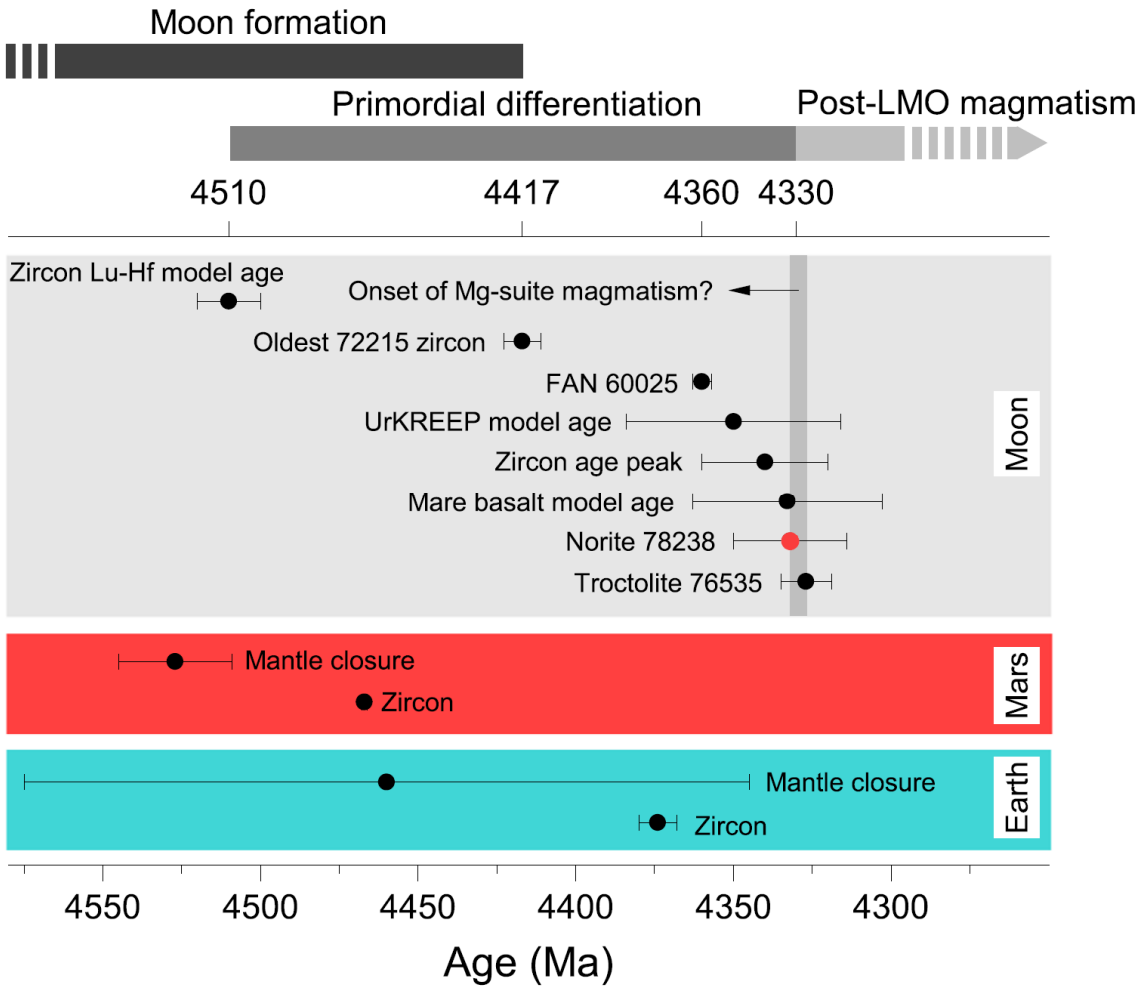

Fig. 3.1-8: Geochronological summary of the early Moon, Mars, and Earth differentiation including our new constraint on the lunar magma ocean crystallisation from Mg-suite norite baddeleyite U-Pb dating by NanoSIMS.

g. *Radiogenic Pb mobilization induced by shock metamorphism of zircons in the Apollo 72255 Civet Cat norite clast (B. Zhang/London, Ontario/Los Angeles, Y. Lin, J. Hao, Y. Liu, J. Zhang and Q. Li/Beijing, D.E. Moser, S.R. Shieh and I.R. Barker/London, Ontario and A. Bouvier)*

In situ U-Pb radiometric dating of zircons is regarded as one of the most widely used and reliable methods to acquire geochronologic ages. However, it has been recently reported that radiogenic Pb (Pb*) mobilization within zircon may, in some cases, cause inaccurate age determinations with no geological significance. Such Pb* mobilization can be caused by deformation, a-coil damage, fluid-assisted annealing, and recrystallization.

In this study, we report an investigation of Pb* mobilization in shock metamorphosed lunar zircons. NanoSIMS (nano-scale secondary ion mass spectrometry) and IMS 1280HR ion microprobe dating, EBSD (electron backscatter diffraction) and CL (cathodoluminescence) mapping, and scanning ion imaging (SII) were applied to micro-zircon grains from the Apollo 72255 Civet Cat norite clast. Based on a large number of grains with similarities in internal zoning, habit and trace element geochemistry, and host mineral context, the Civet Cat norite zircons are interpreted to be primary, igneous grains. The chronology obtained for three consecutive surfaces (at different depths) by NanoSIMS, SII, and IMS 1280HR, respectively, indicates that the radiogenic Pb distribution of the Civet Cat norite zircons is heterogeneous among different polished or sputtering surfaces.

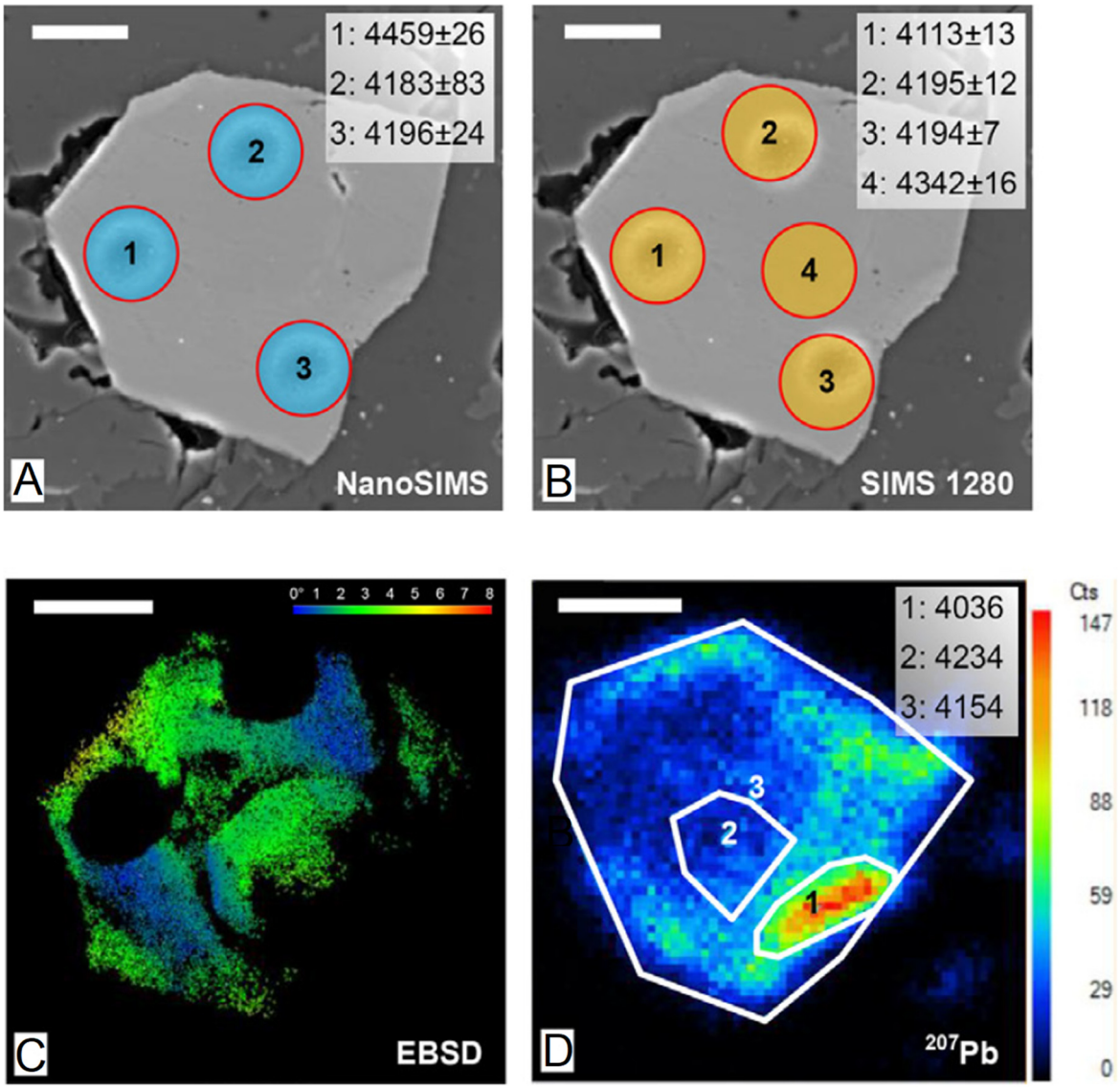

Fig. 3.1-9: Zircon Z5 NanoSIMS dating (in BSE; A), IMS 1280HR dating (in BSE; B), EBSD crystallographic orientation mapping (C), and SII ^{207}Pb data (D) in thin section 72255,126. The opaque pits result from the primary-beam bombardment of NanoSIMS. All the listed ages are in a million years (Ma).

Forty-two NanoSIMS U-Pb ages (beam size of 5 μm) are concordant on a Wetherill Concordia diagram, and their corresponding $^{207}Pb/^{206}Pb$ ages spread from 4015 Ma to 4459 Ma. More notably, the six oldest spots of the 42 define a concordant U-Pb age of 4460 ± 31 Ma (2σ, MSWD = 0.47, P = 0.92) and a weighted mean $^{207}Pb/^{206}Pb$ age of 4453 ± 34 Ma (MSWD = 0.056, P = 0.998). These dates are among the oldest in the lunar highland rocks. However, the $^{207}Pb/^{206}Pb$ ages of repolished surfaces of these zircons by IMS 1280HR (beam size of 5 μm) do not reproduce the NanoSIMS results (up to 300 Ma younger). The SII (spatial resolution of 2 μm) confirms a heterogeneous distribution of radiogenic Pb within single grains. The EBSD mapping of these zircon grains shows that they have 3-20° of cumulative lattice misorientation. It is proposed that shock-related deformation has facilitated Pb* migration after primordial crystallization.

With currently available data, we cannot preclude the possibility that the large errors of the U-Pb ages obscure reverse discordance that would bias our oldest $^{207}Pb/^{206}Pb$ ages to older values. Conversely, our data could be explained by mixing of Pb-retention and Pb-loss nanodomains as seen in shocked terrestrial zircon such that the U-Pb date of 4460 ± 31 Ma approximates the norite formation.

h. *Amphibole stability in the upper mantle (M. Putak Juriček and H. Keppler)*

The stability of hydrous phases in the upper mantle has received considerable interest ever since the first reports of accessory amphibole and mica occurring in mantle xenoliths. A key question is whether the hydrous phases are thermodynamically stable at the reduced water activity typical for the upper mantle, or whether they are products of secondary metasomatic events. Early experimental studies suggested that the origin of seismic shear-wave velocity reductions at the lithosphere-asthenosphere boundary may be related to dehydration melting of a hydrous phase. The interest in this idea was recently renewed by experimental studies of amphibole stability in the peridotite-H_2O system at very low nominal water concentrations.

Low bulk water contents are experimentally difficult to control due to surface adsorption effects on powdered starting materials. Rather than attempting to maintain the starting materials dry and then directly introducing ppm level water concentrations to the sample, a more reliable approach is to use a high bulk water content and to dilute the aqueous fluid phase with an additional (inert) component in order to precisely control water activity. We reinvestigated amphibole stability in the upper mantle using this method. The samples were prepared by enclosing appropriate amounts of N_2 and H_2O into PtRh capsules, along with a synthetic peridotite oxide mixture. We used AgN_3 as the source of N_2, and liquid H_2O or $Mg(OH)_2$ as sources of water. Experiments were performed in the piston-cylinder apparatus using ½" talc/pyrex assemblies. We experimentally determined amphibole stability in equilibrium with N_2-H_2O fluids that had a molar fraction of water (X_{H2O}) equal to 1, 0.5, 0.25 and 0.1 at pressures

of 2 to 5 GPa and temperatures between 900 and 1350 °C. The bulk water content was kept constant at 1 wt. % in all experiments. The samples were analyzed by EPMA and powder XRD. Run product phase assemblages are summarized in Figure 3.1-10.

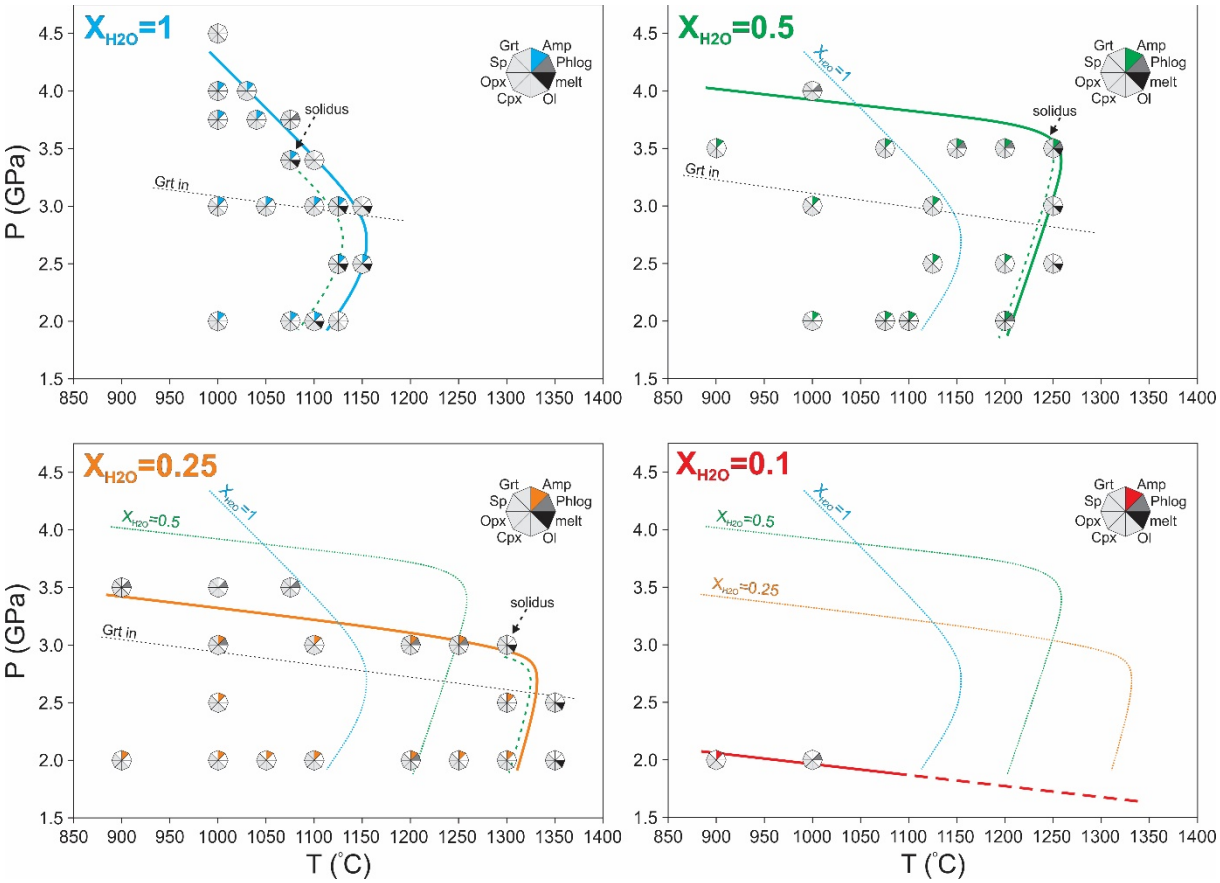

Fig. 3.1-10: An overview of run conditions and the observed phase assemblages. Amphibole stability limits were experimentally determined in equilibrium with nominal fluid compositions of X_{H2O}=1 (blue line), X_{H2O}=0.5 (yellow), X_{H2O}=0.25 (orange) and X_{H2O}=0.1 (red). The solidus is indicated by the dashed green line.

We observed that with decreasing water activity in the fluid phase, the amphibole stability field simultaneously shifted to lower pressures and expanded toward higher temperatures (Fig. 3.1-11). This dual effect of water activity on amphibole stability is a result of two different chemical reactions occurring at the amphibole-out boundary. At high pressures, but low temperatures, amphibole stability is governed by a subsolidus dehydration reaction. As the water activity in the fluid phase is lowered, amphibole is destabilized. Toward high temperatures, a melting reaction occurs at the amphibole stability limit. In our experiments, large melt fractions were stabilized immediately at the solidus, and the onset of melting was easy to recognize. The solidus – which also defines the amphibole stability limit – was clearly displaced to higher temperatures with decreasing water activity.

Nominally anhydrous minerals may dissolve several hundred ppm of water at realistic upper mantle conditions, and excess water may not be available to stabilize an additional hydrous phase. To properly model amphibole stability in the upper mantle, water solubilities in nominally anhydrous phases need to be taken into account. We used the published calibrations of water solubility in major nominally anhydrous peridotite minerals to estimate the water activity along several typical geotherms. The water activity–depth profiles were correlated with the experimentally determined amphibole stability fields. Therefore, we constrained the depth intervals and minimum bulk water contents required to stabilize amphibole along particular geotherms.

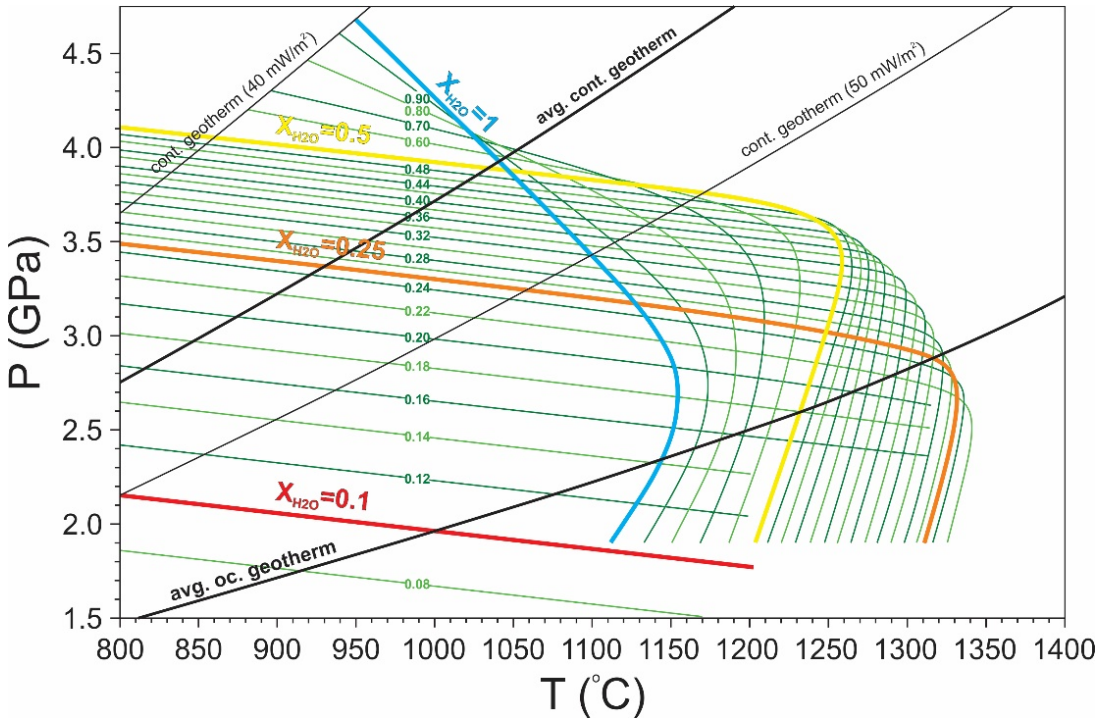

Fig. 3.1-11: Summary of amphibole stability in the mantle. Experimentally determined stability fields at reduced water activity are indicated by the blue (X_{H2O} = 1), yellow (X_{H2O} = 0.5), orange (X_{H2O} = 0.25) and red (X_{H2O} = 0.1) bold lines. Thin green lines are the interpolated amphibole stability limits at intermediate fluid compositions. Typical continental and oceanic geotherms are also shown (bold black lines).

Amphibole stability in the upper mantle is highly dependent on the geothermal gradient. Along with steeper geothermal gradients, the amphibole may be stabilized in equilibrium with lower bulk water contents. The stability limit is reached at lower pressures, and the amphibole-out reaction is more likely to produce a hydrous melt. We estimated that along an average oceanic geotherm, accessory amphibole may indeed be stable in equilibrium with 150 ppm of water, but higher water contents (> 250 ppm) are required to produce melt at the amphibole-out boundary. The amphibole stability limit in the oceanic lithosphere is expected at depths between 75 and 85 km for a wide range of bulk water contents. Along an average continental geotherm, water solubility in pyroxene is considerably higher, and approximately 400 ppm of water is

required to stabilize amphibole. In the continental lithosphere, the amphibole-out reaction occurs at depths between 100 and 120 km, and melt is not stabilized by amphibole decomposition.

Most estimates suggest that the ambient upper mantle contains less than 200 ppm of water. Thus, dehydration melting at the amphibole stability limit is unlikely to be a general explanation for the shear-wave velocity reduction at the lithosphere-asthenosphere boundary.

i. *Adiabatic temperature profile in the mantle, revised (T. Katsura)*

Temperature is one of the essential parameters for modeling the dynamics of the Earth's interior. Therefore, estimating the temperature distribution in the mantle is a vital task in solid Earth geophysics. For this reason, a previous study estimated the adiabatic temperature distribution in the mantle. In the previous study, the temperature at the 410-km seismic discontinuity (D410) was estimated by comparing the global average depth of the D410 with the olivine-wadsleyite transition pressure as a function of temperature. The temperatures above and below the D410 were estimated using the adiabatic temperature gradient, $\left(\frac{dT}{dz}\right)_S = \frac{\alpha g T}{C_p}$, where T is the temperature, z is the depth, α is the thermal expansivity of the constituent, g is the gravitational acceleration, and C_P is the isobaric heat capacity per weight of the constituent, based on the *P-V-T* relations and heat capacities of major mantle minerals. However, the previous adiabatic profile should be revised for two reasons. First, the pressure correction of the temperature-emf relations of W-Re thermocouple was recently proposed, using which the *P-V-T* relations of mantle minerals should be corrected. Second, the calculation program in the previous study contained errors, leading to incorrect thermal expansivity evaluation. For these reasons, the current study re-evaluates the adiabatic temperature profile using the pressure correction of thermocouple emf and a newly built calculation program.

By following the previous study, the temperature at D410 is first evaluated. The phase relations of the olivine-wadsleyite transition in the $(Mg,Fe)_2SiO_4$ were determined nominally at 1600 and 1900 K. The pressure correction of emf suggests that the actual temperatures should be 1644 and 1962 K. The transition pressures of the Mg_2SiO_4 and hypothetical Fe_2SiO_4 end-members, respectively are found to be 14.12 ± 0.13 and 3.6 ± 1.0 GPa at 1644 K and 15.42 ± 0.17 and 4.7 ± 1.0 GPa at 1962 K. The transition pressures with Mg/(Mg + Fe) = 0.9 corresponding to the D410 are found to be 13.09 ± 0.07 and 14.34 ± 0.08 GPa at 1644 and 1962 K, respectively. The comparison of the average depth of D410 with these phase relations leads to the average temperature at D410 of 1805 ± 18 K. This estimation is slightly lower than the previous one (1830±48 K) but identical within the errors.

The *P-V-T* data of olivine, wadsleyite, ringwoodite, and bridgmanite after the pressure correction for the emf, are fitted to the Mie-Grüneisen-Debye thermal equations of state with

the 3rd-order Birch-Murnaghan isothermal equations of state, with fixed values of the isothermal bulk moduli at ambient conditions and Debye temperatures. In this way the pressure derivative of the isothermal bulk modulus, K_0', the Grüneisen parameter without compression, γ_0, and the volume exponent of the Grüneisen parameter, q are obtained. The (K_0', γ_0, q) of the four minerals are found to be (4.2 ± 0.4, 1.00 ± 0.02, 2.4 ± 0.5), (4.2 ± 0.2, 1.23 ± 0.06, 1.5 ± 1.1), (4.8 ± 0.4, 1.34 ± 0.06, 2.9 ± 0.7), and (4.09 ± 0.04, 1.53 ± 0.03, 1.6 ± 0.4), respectively.

Based on these re-evaluations of the experimental data, a revised adiabatic temperature profile is obtained. Figures 3.1-12, 3.1-13, and 3.1-14 show the thermal expansivity, the adiabatic temperature gradient, and the temperature profile obtained in the current and previous studies. Because the adiabatic temperature gradient is primarily proportional to the thermal expansivity, these two parameters show similar behaviours. For example, both parameters increase in association with the phase transitions but gradually decrease with depth. As is seen, the thermal expansivity was overestimated in the previous study. As a result, the adiabatic temperature gradient and the temperatures in the deeper regions were also overestimated. The present estimation suggests that the temperatures on the adiabatic geotherm are 1617 ± 16, 1959 ± 19, 1925 ± 19, and 2530 ± 30 K, respectively, at a 50-km depth, just above and below the 660-km discontinuity, and at 2800-km depth.

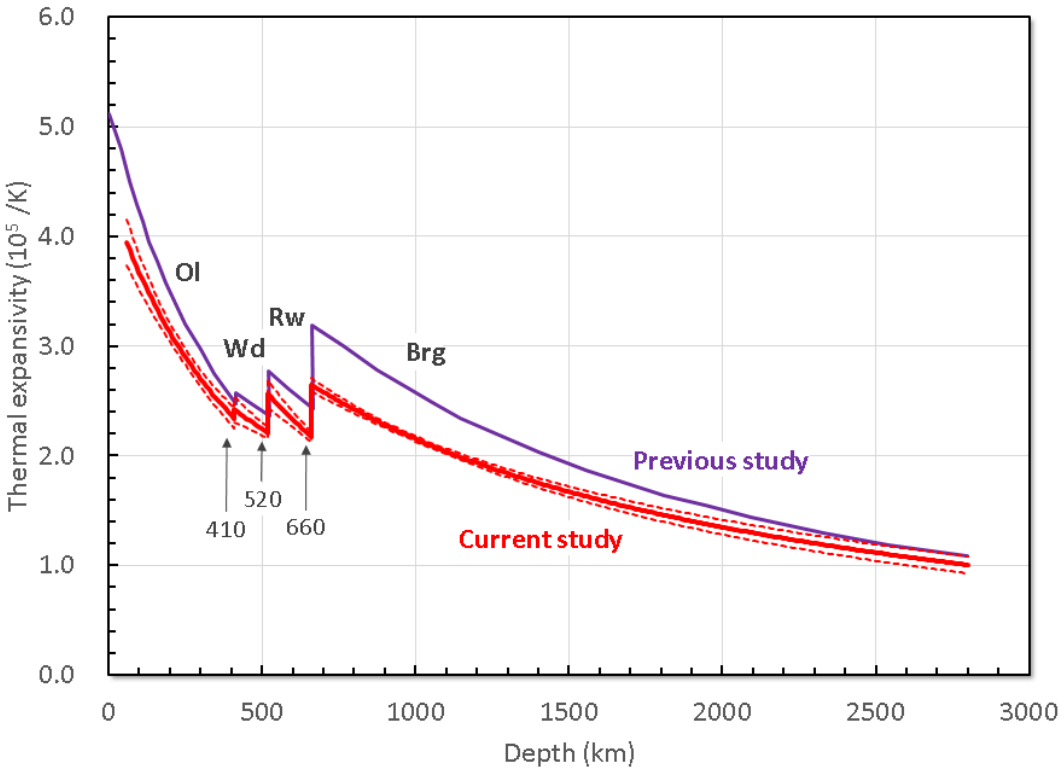

Fig. 3.1-12: Thermal expansivity in the mantle. Red: the current study; violet: the previous study. The solid and dashed curves show the most probable values and 68 % confidence intervals, respectively.

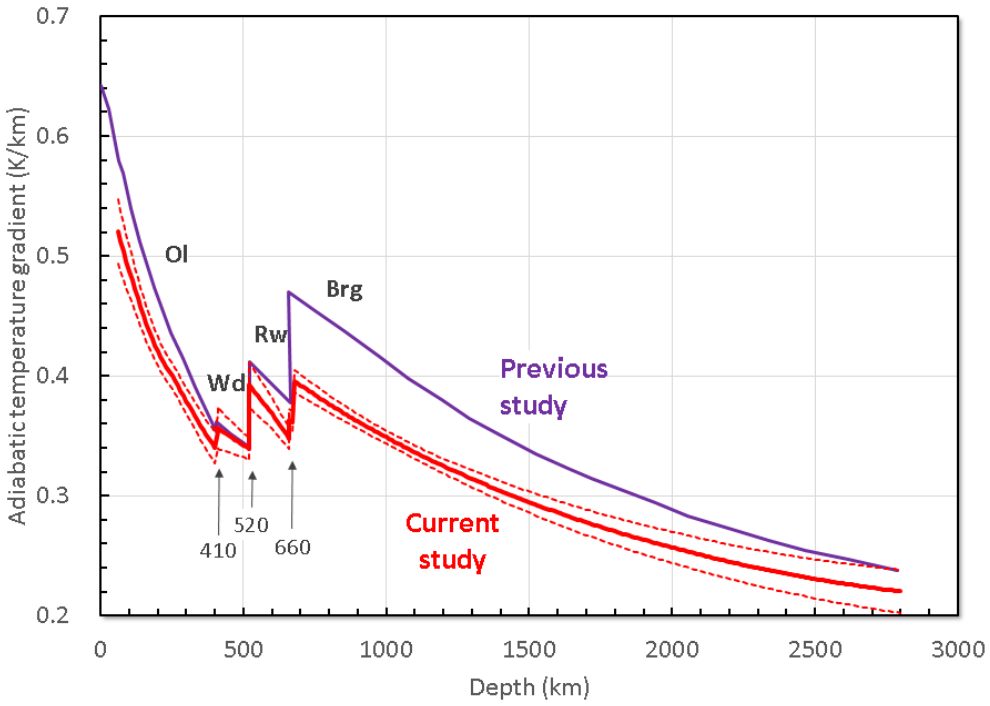

Fig. 3.1-13: Adiabatic temperature gradients in the mantle. Red: the current study; violet: the previous study. The solid and dashed curves show the most probable values and 68 % confidence intervals, respectively.

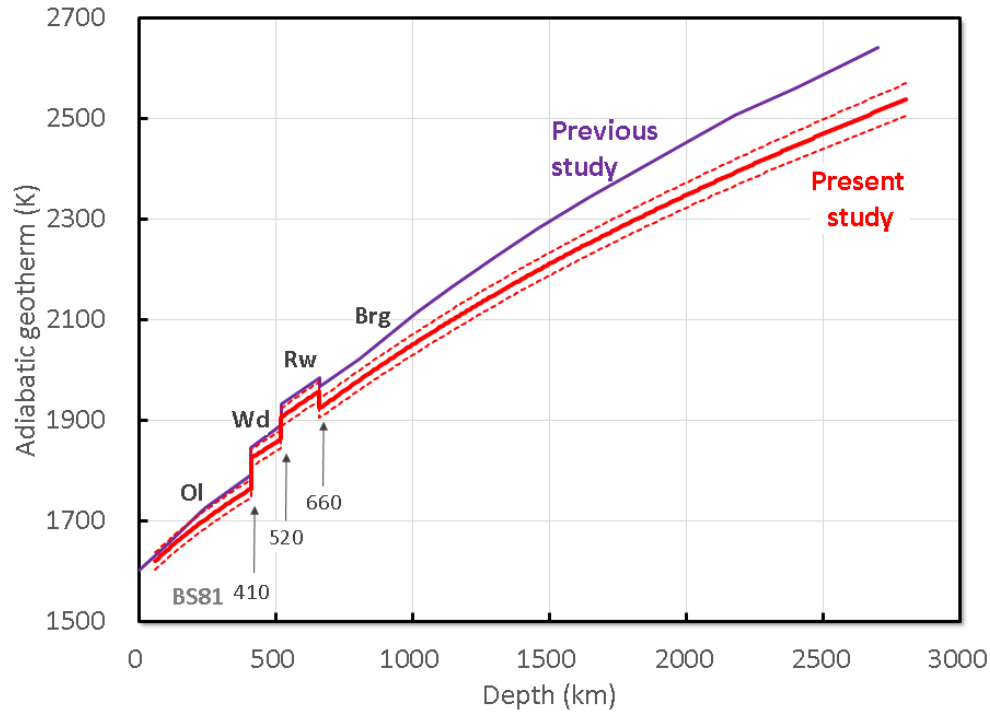

Fig. 3.1-14: Adiabatic temperature profiles in the mantle. Red: the current study; violet: the previous study. The solid and dashed curves show the most probable values and 68 % confidence intervals, respectively.

3.2 Geochemistry

The projects described in this section provide a series of snap-shots that capture processes in the act of causing chemical changes at different length scales, times and depths in the Earth. In most of these processes, elements are mobilized or concentrated so that new reservoirs are formed with different compositions. In some of the projects, these reservoirs might be commercially viable ore deposits, whereas in others the formation of larger-scale reservoirs such as the Earth's core are being investigated. In all cases, however, the projects describe approaches that help us to understand processes from which we are separated by great depths in the Earth and long periods of time.

The first two contributions in this section focus on the behaviour of volatile elements as the Earth formed and the metallic iron-rich core separated from the outer silicate mantle. There are many theories as to how volatile elements were added to the Earth as it grew, which mainly vary in the proposed timing of when volatile materials arrived. By experimentally examining how a selection of moderately volatile elements, (Sn, Cd, Bi, Sb and Tl), would have partitioned between the Earth's mantle and metallic core, the first study in this section manages to put quite tight constraints on this timing. It is found that scenarios of early volatile arrival would have left the mantle too depleted in these elements. The only scenario that fits, is one where the volatiles were only accreted in a late stage but that as core material separated it only partially stripped volatiles from the mantle. This late arrival and incomplete equilibration, therefore, explains why the outer layers of the Earth retained higher concentrations of at least some moderately volatile elements. The second contribution examines the behaviour of helium during core formation. Ocean island basalts show higher $^{3}He/^{4}He$ ratios than mid-ocean ridge basalts, which has been suggested to signify retention of primordial He in the Earth's core. To test this hypothesis, the partitioning of He between silicate and metallic melts was investigated using computer simulations. It was found that He generally partitions in the silicate melt, but that the presence of oxygen in the metallic melt greatly enhances the amount of He entering the core, confirming the ability of the latter to retain primordial $^{3}He/^{4}He$.

The next five contributions deal with aspects of lower mantle mineralogy and how the compositions of minerals may change as a function of the extreme conditions that characterise this region of the Earth. The first examines how Fe^{3+}, *i.e.*, ferric iron, would be incorporated in the lower mantle mineral bridgmanite within silica-saturated assemblages, potentially associated with subducting oceanic crust. The substitution mechanism of trivalent (3+) cations into bridgmanite under silica-poor conditions has been shown to lead to the formation of oxygen vacancies, which may strongly affect transport properties such as rock strength and their propensity to flow. This study shows that under silica rich-conditions cation, rather than oxygen, vacancies are formed, which may result in differences in transport properties between silica saturated and undersaturated mantle rocks. The following study also examines ferric iron incorporation, this time in the lower mantle mineral ferropericlase, which is one of the few minerals with an obviously deep mantle origin that is found as an inclusion in diamonds. In this study high-pressure experiments to determine the ferric iron content of ferropericlase during diamond formation reveal concentrations that actually match those found for such inclusions in

diamonds. It is concluded that diamonds may form in the lower mantle as a result of the reduction of carbonate melts emanating from subducting slabs at these depths. The next study, by Kim *et al.*, was also aimed at understanding how iron partitions between mineral phases in the lower mantle. In order to control the concentration of ferric iron in these experiments, metallic iron was added, which should result in the lowest possible ferric iron concentrations. A fascinating and unexpected result occurs, in that as experiments are performed with increasing pressure, the recovered mineral assemblage becomes extremely fine-grained, such that its submicron length scale can only be visualised using a transmission electron microscope. A small increase in the grain size away from the metallic iron implies that under high pressure and reducing conditions grain-boundary diffusion, and therefore grain growth, may be slowed down significantly. Although this is only a preliminary result, it may have very important implications for how the rheology of the deep mantle may change with depth.

The next study is aimed at understanding the effect of iron on the melting or crystallisation of lower mantle rocks, which is important for understanding whether the base of the lower mantle may be molten and how the lower mantle may have fractionated during crystallisation of an early magma ocean. When the mantle melts near the surface, components such as sodium and water enter the melt at quite low temperatures, which results in a temperature interval between when the mantle starts to melt and when it is fully molten, of many hundreds of degrees. In the lower mantle, this appears to be no longer the case and most components, including Na_2O, enter the melt at a similar temperature. As constrained in this study, however, iron is one of the few components to enter the melt at a lower temperature and its partitioning, therefore, exerts the main influence on the temperature interval over which the lower mantle melts. The final study to address lower mantle processes aims to assess the role of calcium phosphates in the cycling of phosphorous and incompatible trace elements in the deep Earth. Multianvil experiments were performed on phosphorous doped peridotitic and basaltic starting materials at conditions up to those found in the lower mantle. The main phosphorous bearing phase is found to be tuite, a high-pressure equivalent of apatite that has been found in strongly shocked meteorites. The authors conclude that tuite could be an important carrier of phosphorous, halogens and incompatible trace elements both in subduction zones as well as in the convecting mantle.

The following two contributions forge a link between deep-seated geological processes and the development of life and habitable conditions. To understand the fate of iron hydroxides in subducted banded iron formations, Dubrovinsky *et al.*, studied the stability of α-FeOOH (goethite) using *in situ* X-ray methods in a laser-heated diamond anvil cell. They found that at conditions corresponding to a depth of *ca.* 1000 km, goethite decomposes to a suite of anhydrous iron oxides in which the iron has a lower oxidation state, leading to the release of an oxygen-rich aqueous fluid. The authors argue that if such fluids rose to the Earth's surface they could have triggered, or at least contributed to, the great oxidation event 2.5 billion years ago. The following study examines a so-called magma-poor rift margin, where the crust was stretched during the opening of the Atlantic, and the extension was at least partly accommodated by dragging a section of the sub-continental mantle towards the surface. The mantle rocks, dominated by the mineral olivine, were rapidly altered to produce the hydrous

mineral serpentine, a process which also generates hydrogen. Samples recovered by drilling into this margin, off the coast of Spain, are analysed in this study using Mössbauer spectroscopy, which allows the extent of serpentinization to be determined at different depths and for different initial mantle rock types. The results show that large amounts of hydrogen would have formed at depths just below those where organisms could survive and use the hydrogen as an energy source. Such rift margins may, therefore, provide the energy source to allow the biosphere to extend deeply into the rocks of the newly formed ocean basin.

The next two contributions focus on the behaviour of trace elements within subduction zones. The first of these deals with the origin of the trace element signature of arc magmas. Fluid–eclogite partition coefficients were determined in diamond trap experiments conducted with variably saline fluids at subduction zone conditions and were used to set up a quantitative model that considers also the amount of fluid expelled from the slab, the amount of fluid arriving at the source of mantle partial melting, and the degree of partial melting. The results demonstrate that the trace element signature of arc magmas does not require the involvement of partial melts of sedimentary rocks, but can be simply obtained by adding a few weight percent of moderately saline, subduction-derived fluids to the site of partial melting within the mantle wedge. In the second of these projects, Liu *et al.*, also used diamond trap experiments to look specifically at the behaviour of copper, zinc and tungsten during fluid release from subducting slabs. They found that Cu and Zn partition more strongly into saline fluids, whereas the behaviour of W was not significantly affected by the fluid salinity. However, none of the three investigated elements were sufficiently enriched in the fluid phase, implying that fluids emanating from the slab would not significantly raise the concentrations of these elements in the mantle source of arc magmas.

The last four contributions deal with the subject of magmatic-hydrothermal ore deposits. Although gallium is currently exclusively recovered as a by-product from bauxite and zinc ores, magmatic-hydrothermal enrichments of gallium have also been recognised. The first study in this subsection, seeks to identify potential Ga-enriching processes in the magmatic-hydrothermal environment. As a first step, the solubility of Ga_2O_3 in silicate melts and variously saline aqueous fluids was experimentally investigated at 750-800 °C and 2 kbar. The solubility of Ga_2O_3 in fluids was determined through the creation of synthetic fluid inclusions. It was found that Ga has an affinity for alkali feldspar and fractionates into the fluid with a calculated fluid/melt partition coefficient of about 1-2. These preliminary results suggest that at magmatic temperatures it is difficult to enrich Ga to economic levels in this environment. The following study, by Fang and Audétat, was performed to identify factors that lead to the formation of porphyry molybdenum ore deposits, by experimentally examining the partitioning of Mo between fluid and magma ($D_{Mo}^{fluid/melt}$) as a function of pressure, temperature, silicate melt composition and the availability of sulphur and oxygen. It was found that $D_{Mo}^{fluid/melt}$ increases strongly with pressure and melt alkalinity, that it decreases with increasing oxygen and sulphur availability, and that temperature has comparatively little influence in the investigated range of 750-850 °C. The results suggest a potential key role of magma emplacement depth in the formation of this economically important type of ore deposit.

The aim of the following study, by Zhang *et al.*, is to test the popular hypothesis that gold-rich porphyry copper deposits in post-collisional settings, formed by partial melting of sulphide-rich lower crustal cumulates. To check whether deep crustal cumulates are sulphide-rich, natural samples from exhumed crustal sections in the Kohistan (Northern Pakistan) and the Gangdese belt (Southern Tibet) were examined. In addition, partial melting experiments on these rocks were conducted in piston-cylinder presses. The petrographic studies reveal that the cumulates were indeed originally sulphide-rich and thus had the potential to provide substantial amounts of sulphur and metals. However, the partial melting experiments suggest that dry decompression melting produces melts that have far higher Na/K ratios than the natural, ore-forming magmas, speaking against the popular hypothesis. This conclusion is further supported in the following, final study in this section, which is a geochemical investigation of mafic to felsic potassium-rich magmas, associated with post-collisional porphyry copper-gold deposits in Western China. These rocks display arc signatures and a systematic variation in their trace element content as a function of the distance to a former subduction trench. Although their Pb, Nd and Sr isotopic compositions cover a large range, the isotopic signature of each cogenetic suite of mafic-to-felsic magmas is very constant. These observations suggest that the ore-forming magmas evolved through fractional crystallization from mafic, mantle-derived precursors, and that no significant amount of crustal rocks were involved in their genesis.

a. *Investigating Earth's volatile delivery with moderately volatile and siderophile elements (E. Kubik, in collaboration with J. Siebert, B. Mahan and J. Creech/Paris, I. Blanchard/Potsdam, S. Shcheka/Sydney, A. Agranier/Brest and F. Moynier/Paris)*

The accretion of volatile elements to Earth continues to be debated despite intense research focusing on the topic. Geochemical and cosmochemical observables have been explained by a wide variety of scenarios ranging from an accretion of the volatile elements during the main phases of Earth's formation to an accretion of volatile-poor material followed by a late accretion of volatile-rich material after core formation ceased, called the late veneer (Fig. 3.2-1). The mantle signature of elements that are both volatile and siderophile constitutes a record of volatile-related processes as well as differentiation-related processes. Studying the distribution of such elements between metal and silicate at high pressure and high temperature allows us to decorrelate the effect of differentiation from volatile-related processes on their abundances, and hence to discriminate scenarios capable of explaining the abundances observed in the present-day mantle.

This study aims to determine one or a variety of accretion scenarios explaining the moderately volatile and siderophile element (MVSE) abundances in the Earth's mantle. High-pressure metal-silicate experiments (Fig. 3.2-2) were performed using a piston-cylinder at the Institut de Physique du Globe de Paris and using multianvil presses at the BGI. Forty-four experiments ranging from 2 to 20 GPa and 1700 to 2600 K were completed in order to resolve the elemental and isotopic behaviour of a selection of MVSE.

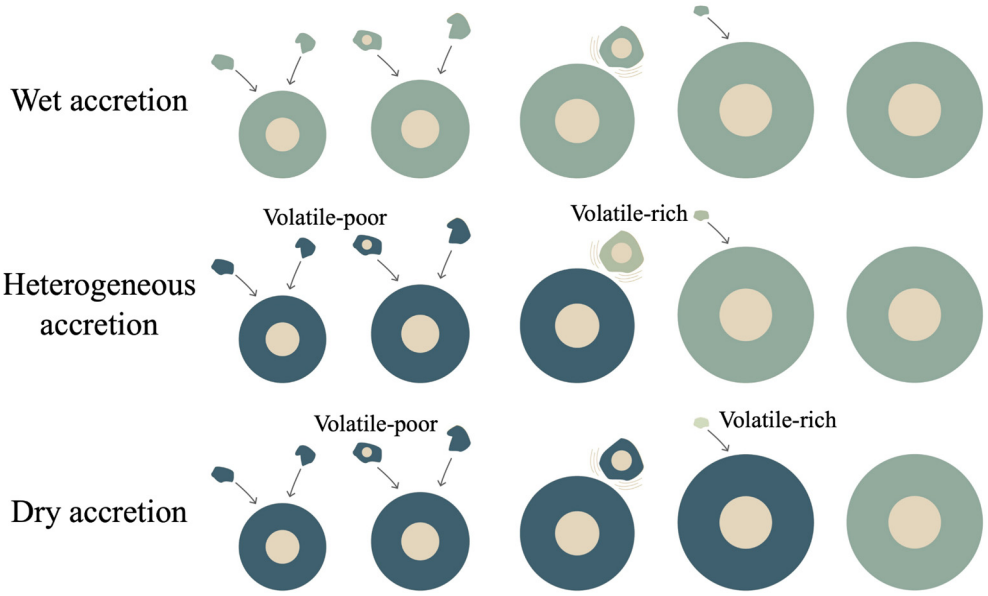

Fig. 3.2-1: The three main accretion scenarios proposed to explain the delivery of volatile elements to Earth.

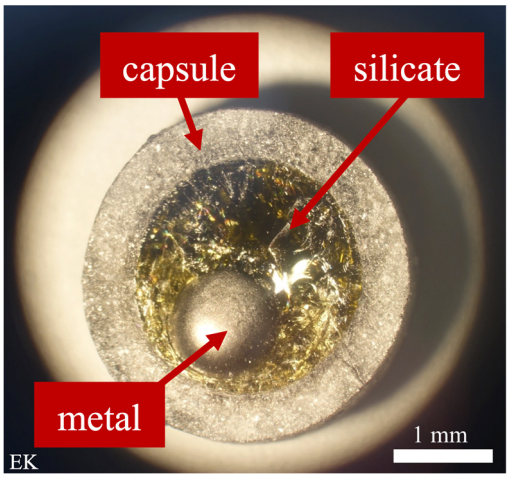

Fig. 3.2-2: An optical photograph of a recovered experiment showing a rounded ball of metal sitting inside a quenched silicate glass, after an experiment in which the two liquids were equilibrated at 2 GPa and 1700 °C. The liquids were contained in a crushable MgO capsule.

From the partitioning experiments it is possible to determine the effects of temperature, pressure, fO_2, and metal S content on the affinity of Sn, Cd, Bi, Sb and Tl for the metallic liquid relative to the silicate melt. By reporting the resulting partitioning data as an exchange coefficient K_d, the effects of fO_2 can be removed. The K_d for Sn, for example, is defined as;

$$K_{\mathrm{d}} = \frac{X_{\mathrm{Sn}}^{\mathrm{met}}(X_{\mathrm{FeO}}^{\mathrm{sil}})}{X_{\mathrm{SnO}}^{\mathrm{sil}}\ (X_{\mathrm{Fe}}^{\mathrm{met}})} \qquad (1)$$

where $X_{\mathrm{Sn}}^{\mathrm{met}}$ and $X_{\mathrm{FeO}}^{\mathrm{sil}}$ are, for example, the mole fractions of Sn and FeO in the metal (met) and silicate (sil) respectively. Except for Cd, all elements investigated show a significant pressure and temperature dependence in K_D, as shown in Figure 3.2-3 for Sn, and become more siderophile with increasing pressure.

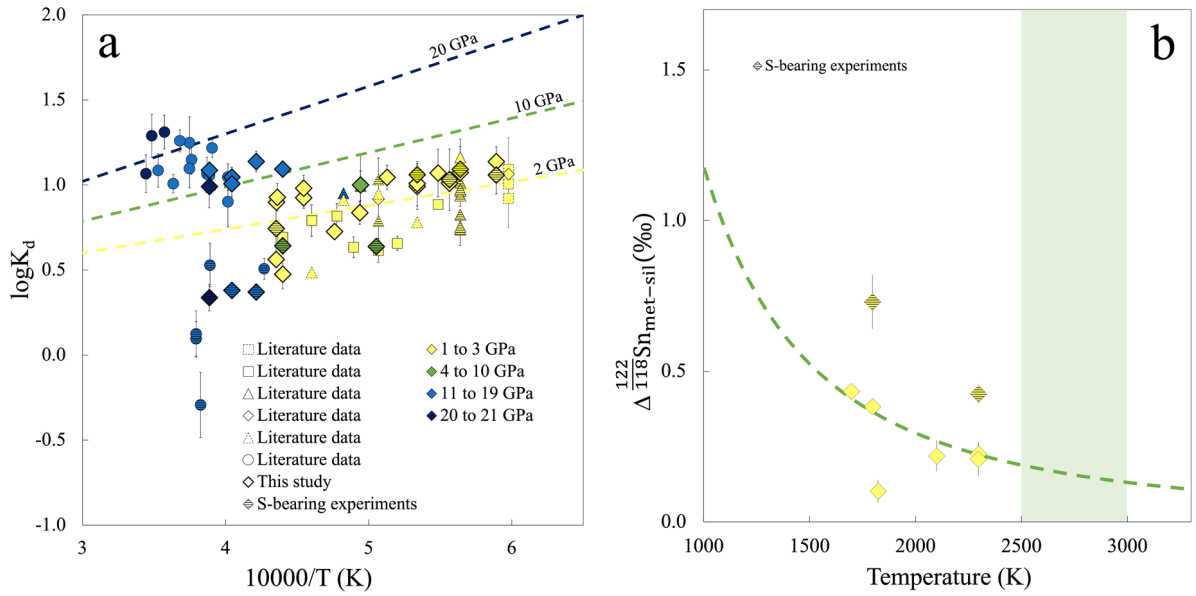

Fig. 3.2-3: (a) Partitioning behaviour of Sn between metal and silicate expressed as the exchange coefficient log K_d as a function of reciprocal temperature. Errors correspond to 1 standard deviation propagated from the uncertainties on the analyses made in this study and in the associated literature data. (b) Experimental results of Sn isotopic fractionation between metal and silicate. The shaded zone indicates temperature conditions relevant to Earth's core formation, suggesting that core formation could result in the Sn isotopic composition of the mantle being lighter than the core.

The partitioning of Sn, Cd, Bi, Sb and Tl between the Earth's core and mantle were modelled at appropriate pressure and temperature conditions assuming different accretion scenarios, as in Figure 3.2-1. The affinity of these elements for core-forming metal implied by the experimental results, is difficult to reconcile with their relatively high mantle abundances, which is an indication that these particular elements provide important constraints. However, a scenario involving partial equilibration of the mantle with the core, as well as a late delivery of volatile elements in the last 10 to 20 % of Earth's accretion, by a large impactor, is able to explain the abundances of all the studied elements (Fig. 3.2-4). Around 3 wt. % of S in the core is needed to explain the mantle Sn abundance and a late veneer consisting of 0.5 % of Earth's mass is required to explain the Bi abundance in the mantle.

The study of Sn isotopic fractionation between metal and silicate yields a significant factor of ~0.3 ‰ at 2 GPa and 2000 K ($\Delta^{122/118}Sn_{metal-silicate}$), suggesting that Sn isotopes could be fractionated at core formation conditions, enriching the mantle in light isotopes (Fig. 3.2-3b). Contrary to enstatite and ordinary chondrites which have light Sn isotope signatures, carbonaceous chondrites have an identical Sn isotopic composition to the silicate Earth, making them the most likely contributors to the source of Earth's volatile elements according to this study. Furthermore, the isotopic fractionation results are consistent with the favoured accretion scenario derived from the elemental partitioning section of this study. A unifying model for the delivery of volatile elements to the Earth is presented in Figure 3.2-5.

	Sn	Cd	Bi	Sb	Tl
Volatile delivery in the **last 10 to 20 %** of accretion					
Partial equilibration					
As a **giant impactor**					
Late veneer					
~3 wt.% S in core					
Homogeneous delivery and **full equilibration**					

Fig. 3.2-4: (a) Summary of the core formation modelling results. For each MVSE, the parameters required in the models in order to reconcile the experimental data with the observed abundances in the mantle appear in green.

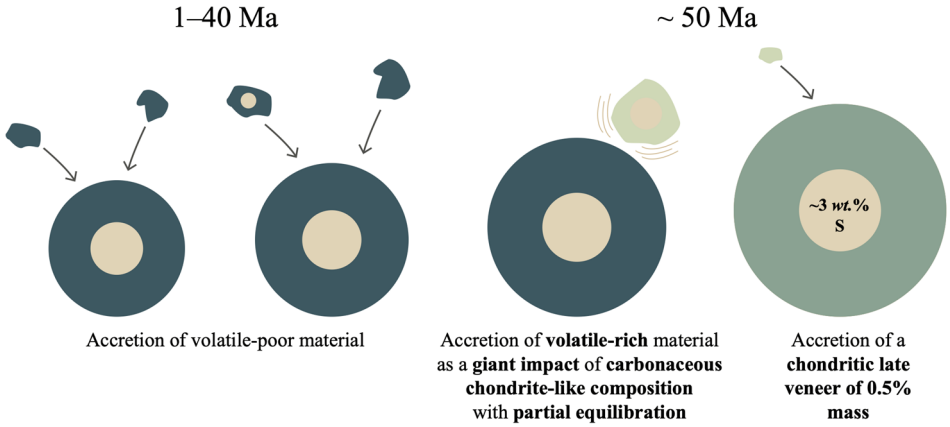

Fig. 3.2-5: A model for the delivery of volatile elements to Earth based on the findings of this study (in bold). In this scenario, the volatile elements are accreted in the last 10 to 20 % of Earth's main accretion stages, through a giant impact of carbonaceous chondrite-like composition, followed by only partial equilibration between the core and mantle materials. A late veneer of chondritic composition was subsequently accreted after core formation ceased. The S budget of the core is estimated to be ~ 3 wt. %.

b. *The helium elemental and isotopic compositions of the Earth's core based on* ab initio *simulations (L. Yuan and G. Steinle-Neumann)*

The Earth's core has been suggested to be a long-term host for the isotope ^{3}He that must be preserved from the formation of the Earth more than four billion years ago. ^{3}He has been shown to be present in higher amounts in ocean island basalts (OIB, for example, Hawaii or Iceland) than in mid-ocean ridge basalts (MORB). Any core influence on the OIB ^{3}He/^{4}He budget would require a significant amount of He to be incorporated into the core during core–mantle segregation, which hinges on the partitioning of He between metallic and silicate melt at high

pressure (P) and temperature (T). In this study, we use density functional theory-based molecular dynamics simulations to predict the metal–silicate partitioning behaviour of He over a wide range of P, T, and three core compositions: Fe, Fe-S, and Fe-O alloys.

We find that He always favours silicate phases over metallic melts, which we illustrate in a straightforward way using a two-phase approach, and we quantify the metal–silicate partition coefficient ($D^{m/s}$, which is defined by the ratio of mass fractions of He in metal and silicate) of He by thermodynamic integration. We find that He generally becomes more compatible in the metallic melt with increasing P and T (Fig. 3.2-6): $\log_{10}D^{m/s}$ for Fe–$MgSiO_3$, Fe-S alloy–$MgSiO_3$, and Fe-O alloy–$MgSiO_3$ are -4.73 (±0.40), -4.39 (±0.33), and -2.79 (±0.32), respectively, at low P–T (10 GPa and 3000 K), but increase to -1.24 (±0.20), -1.55 (±0.23), and -0.22 (±0.17) at high P–T (130 GPa and 5000 K). These results indicate that He is always lithophile at the P–T conditions relevant for the deep mantle, but it is approximately two orders of magnitude less lithophile at deep magma ocean conditions (40-50 GPa and 3800-4000 K) compared to the results at 10 GPa and 3000 K. We find that light element species, particularly oxygen, promote He incorporation into the core by one to two orders of magnitude. By

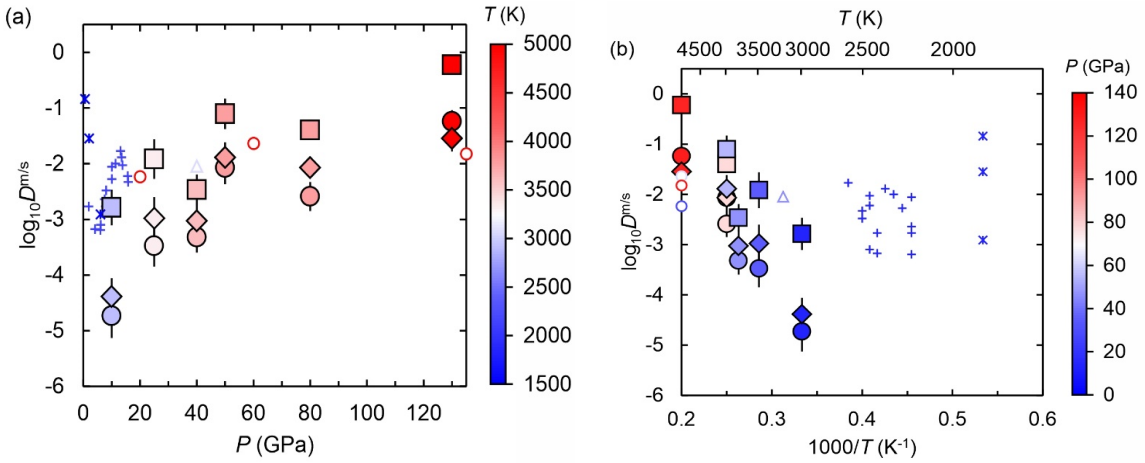

Fig. 3.2-6: Calculated partition coefficients between metallic and silicate melts, $D^{m/s}$, as a function of (a) pressure (P) and (b) temperature (T). Results of this study are shown as large symbols with filled colours representing P/T: Fe–$MgSiO_3$ (circles); Fe-O alloy–$MgSiO_3$ (squares); Fe-S alloy–$MgSiO_3$ (diamonds). Previous results are shown as small symbols with colours reflecting the P-T conditions.

including a parameterization to experimental partitioning data on uranium and thorium in core formation models to estimate the core ^{4}He budget, we find the He content of the core to be 1.0×10^{-6} mol/kg (corresponding to ~ 4.2 ng/g), and determine its isotopic composition as ^{3}He/^{4}He ratio < 3 R_a (where R_a is the atmospheric ratio) using $D^{m/s}$ values determined for pure Fe, but a higher ^{3}He/^{4}He ratio of ~ 140 R_a using larger $D^{m/s}$ values determined for a core composition that contains some amount of oxygen. To explain the Earth's core density deficit, oxygen is required as a major light element in the core. Thus, our results suggest that the core possibly retains a high primordial ^{3}He/^{4}He, potentially accounting for the high ^{3}He/^{4}He ratios identified in OIB.

c. *High-pressure chemistry of Fe_2O_3-bearing bridgmanite in the SiO_2-saturated system (A. Chanyshev, H. Fei, D. Bondar, B. Wang, Z. Liu, T. Ishii, R. Farla, C.A. McCammon and T. Katsura)*

Earth's most common mineral is bridgmanite with the formula ABO_3, where the A site can be occupied by Mg^{2+}, Fe^{2+}, Fe^{3+} and/or Al^{3+} and the B site by Si^{4+}, Fe^{3+} and/or Al^{3+}. Our understanding of deep geodynamics is largely based on an understanding of the rheological properties of bridgmanite. It was proposed in the literature that rheological properties of minerals are controlled by diffusivity of rate-limiting species under high-temperature and low-strain-rate conditions and that the diffusivity of chemical species should be proportional to vacancy concentration because diffusion is driven by exchange of a vacancy and the relevant chemical species. Although the average lower mantle is considered to be reduced, a significant amount of Fe^{3+} could be released when slabs subduct because of the disproportionation reaction of Fe^{2+} into Fe^{3+} and metallic Fe. Fe^{3+} is thought to be partitioned strongly into bridgmanite rather than ferropericlase. Fe^{3+} can be accommodated in both A and B sites by a charge-coupled substitution mechanism as well as an A-site-vacancy substitution mechanism; however, it is not well understood how the substitution mechanisms work to accommodate Fe^{3+} in $MgSiO_3$ bridgmanite.

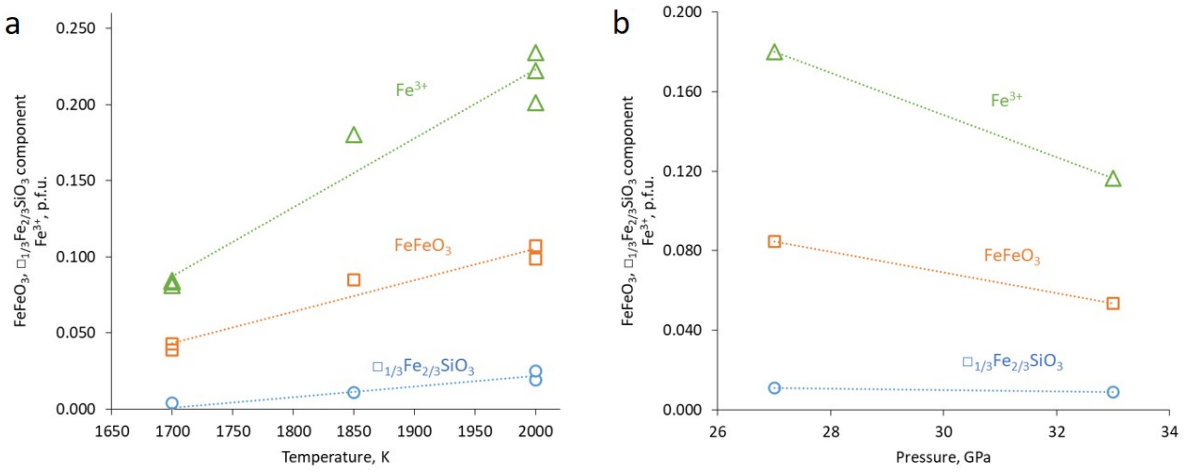

Fig. 3.2-7: Atomic concentrations of $FeFeO_3$ and $□_{1/3}Fe^{3+}{}_{2/3}SiO_3$ components and total Fe^{3+} per formula unit (oxygen = 3) in bridgmanite, assuming $□_{1/3}Fe^{3+}{}_{2/3}SiO_3$ + $FeFeO_3$ + $MgSiO_3$ = 100 % at (a) 27 GPa and 1700-2000 K and (b) 27-33 GPa and 1850 K.

To investigate this question, we performed several experiments in the system SiO_2-Fe_2O_3-MgO at 27-35 GPa and 1700-2000 K using 1500-ton multianvil press (IRIS-1500) at BGI and the 3×5-MN six-axis multianvil press (Aster-15) at DESY. To create oxidized conditions, IrO_2 powder was placed at the bottom of each capsule. Recovered samples were analysed using microfocus X-ray diffraction, scanning electron microscopy, electron microprobe analysis and Mössbauer spectroscopy. Our results showed that all run products consisted of three phases:

bridgmanite, iron oxide and stishovite. With increasing temperature from 1700 to 2000 K at 27 GPa the Fe^{3+} content and abundance of $\square_{1/3}Fe^{3+}_{2/3}SiO_3$ and $Fe^{3+}Fe^{3+}O_3$ components in bridgmanite increase from 0.081(7), 0.004 and 0.039 p.f.u. to 0.232(7) p.f.u., 0.019 and 0.107 p.f.u., respectively (Fig. 3.2-7a). The corresponding change with increasing pressure (27 to 35 GPa at 1850 K) is a decrease from 0.180(8) 0.011 and 0.085 p.f.u. to 0.116(24) p.f.u., 0.009 and 0.054 p.f.u., respectively (Fig. 3.2-7b). At 27 GPa Fe^{3+} is mainly substituted in bridgmanite through a charge-coupled substitution mechanism.

d. *Ferric iron content of synthetic and natural ferropericlase inclusions in sublithosperic diamond from Rio Soriso (Juina, Brazil): Implications for redox mechanisms of diamond formation (S. Dominijanni, V. Stagno/Rome, C.A. McCammon, G. Marras/Rome, F. Kaminsky/Moscow, N. Miyajima, D.J. Frost, A. Rosenthal/Grenoble, in collaboration with T. Arimoto and T. Irifune/Matsuyama)*

Ferropericlase ($(Fe_xMg_{1-x})O$, $x \leq 0.5$) is one of the main mineral phases forming Earth's lower mantle according to the pyrolite compositional model. Although it constitutes only ~ 20 vol. % of the lower mantle assemblage, it is one of the most commonly found inclusions (> 50 % occurrence) in sub lithospheric diamonds. Over the past decades, mineral inclusions have been extensively studied, giving new insights into diamond-forming processes simulated by laboratory and theoretical works. In this context, the determination of the ferric iron content of natural ferropericlase inclusions in diamonds provides important constraints in modelling the lower mantle redox state, being sensitive to the oxygen fugacity at high pressure. Although numerous advancements have been made combining both natural and experimental evidence, we still have an incomplete picture of the complex redox processes occurring at extreme conditions due to local variation of oxygen fugacities induced, for example, by the influx of carbonated subducting slabs.

In this study, we examine the ferric iron content using Mössbauer spectroscopy of both natural diamond inclusions from the Rio Soriso (Juina area, Mato Grosso State, Brazil, Fig. 3.2-8) and synthetic ferropericlase equilibrated with magnesite and diamond at lower mantle P-T conditions using the multi anvil press. We analysed natural samples using the Synchrotron Mössbauer Source (SMS) at the ID18 beamline at the European Synchrotron Radiation Facility. We collected 10 spectra with an average acquisition time of ~ 3 hours for each spectrum. Synthetic samples were measured using a ^{57}Fe Mössbauer point source at the BGI. We acquired 5 spectra, one for each sample, with a collection time ranging between 1 to 7 days each. Data processing was performed using MossA software package to extract the $Fe^{3+}/\Sigma Fe$ based on the Mössbauer relative areas. Experiments were performed at pressures of 25 and 45 GPa and temperatures between 1500 and 1700 °C using the multi anvil apparatus both at BGI and GRC of Ehime University (Japan). A starting composition made of a mixture of natural magnesite, graphite, synthetic ferropericlase, iridium powder (to act as a redox sensor), and Ni metal was chosen as representative of a simplified carbonated lower mantle mineral assemblage. Sample characterization was performed firstly using the scanning electron microscope and the electron

microprobe for chemical analyses and textural observations, and additionally using Focused Ion Beam (FIB) milling and Transmission Electron Microscope (TEM) at BGI to explore possible evidence of redox reactions at the nanoscale. The experimental fO_2 of the synthetic carbonated lower mantle rocks was calculated using a newly established oxybarometer employing Ir as a redox sensor.

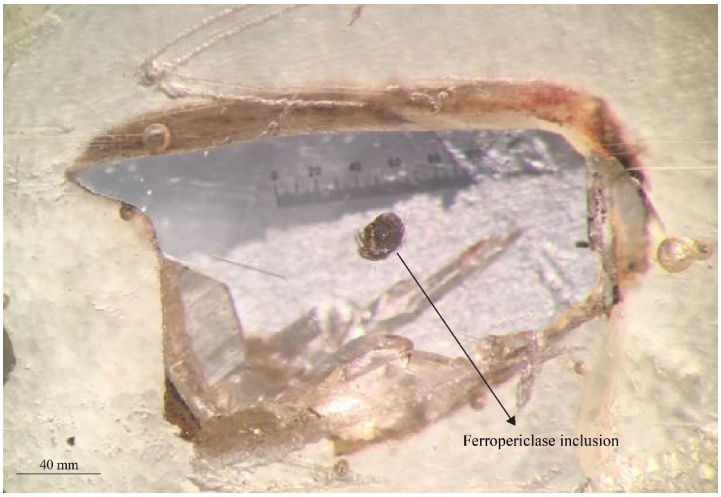

Fig. 3.2-8: A ferropericlase inclusion in sub-lithospheric diamond from Rio Soriso (Juina, Brazil).

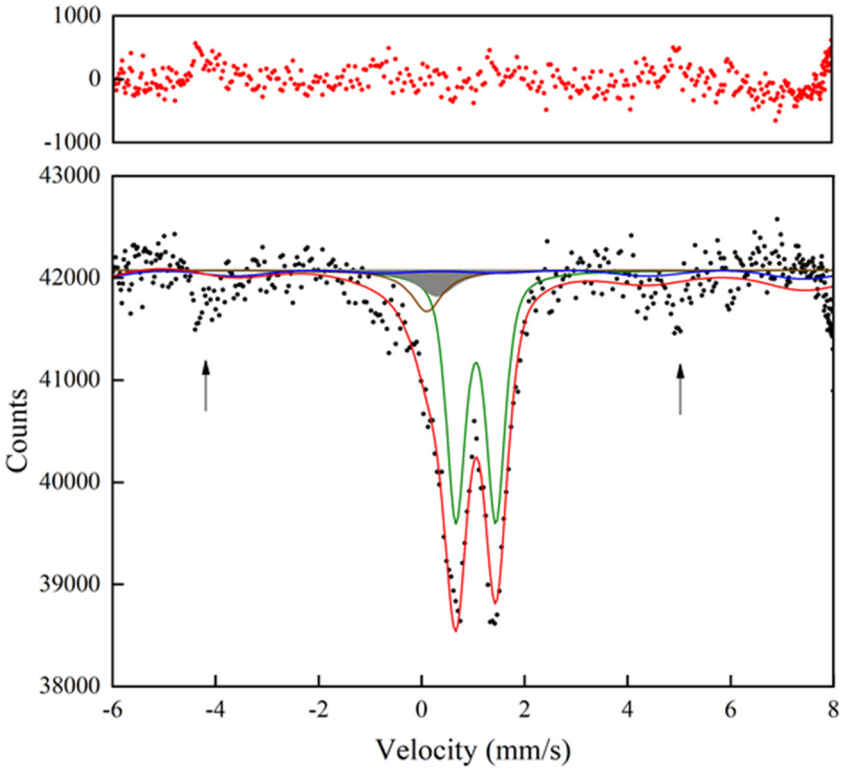

Fig. 3.2-9: A SMS spectrum of ferropericlase inclusion in a sub-lithospheric diamond. The red line shows the full transmission integral fit of the data. The quadruple doublet (green) and the singlet (brown) are the Fe^{2+} and Fe^{3+} in ferropericlase, respectively. Arrows indicate the position of magnetic peaks due to absorption of magnesioferrite hyperfine splitting.

Results of this study provide unique information on the maximum ferric iron content that ferropericlase can incorporate during redox-driven diamond formation. The $Fe^{3+}/\Sigma Fe$ ratio in experimental ferropericlase ranges between 4(2) and 9(2) % and it is consistent with that estimated for natural inclusions in this study (0-14 ± 2 %) and previous works. Noteworthy is the occurrence of magnesioferrite exsolutions in some natural inclusions (Fig. 3.2-9) likely as a result of ferric iron saturation within ferropericlase during decompression. No magnesioferrite was observed in the synthetic ferropericlase (as shown by TEM XRD selected area electron diffraction (SAED) results, Fig. 3.2-10). We suggest a possible mechanism of diamond formation at lower mantle conditions related to the influx of carbonates into the lower mantle via subducting slabs which promoted diamond formation through redox freezing. At these conditions calculated oxygen fugacity is ~ 1 log unit above the iron-wustite buffer.

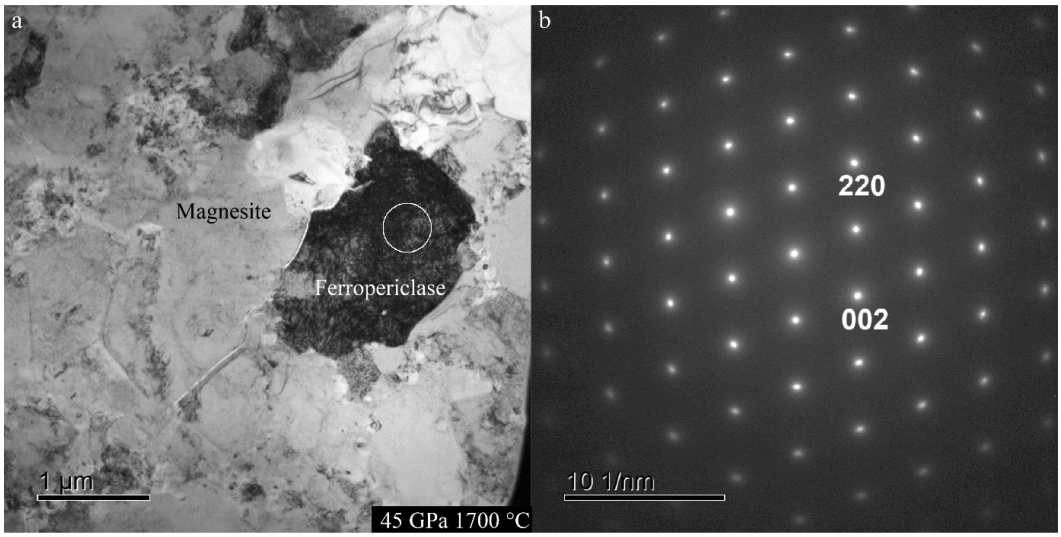

Fig. 3.2-10: a) A bright field TEM image of ferropericlase coexisting with magnesite obtained from a multianvil experiment performed at 45 GPa and 1700 °C; b) A SAED pattern of the indicated region (circle in the ferropericlase grain) showing the absence of magnesioferrite exsolutions.

e. *The chemistry of bridgmanite coexisting with ferropericlase and the Al-rich CF phase under reducing conditions up to 40 GPa (E.J. Kim, H. Fei, K. Nishida, N. Miyajima and T. Katsura)*

While the physical and chemical properties of bridgmanite have long been studied due to its importance in the transport properties of the lower mantle, it is still unclear what is the proportion of Fe^{3+} in bridgmanite and how this relates to the Al content and the presence of other Al-bearing minerals. Previous studies using a multianvil apparatus up to 26 GPa have shown that the fraction of $Fe^{3+}/\Sigma Fe$ in bridgmanite is ~ 60-70 %, even under the reduced condition expected for the disproportionation of Fe^{2+} (periclase) into Fe^{3+} (bridgmanite) and Fe metal. A recent diamond anvil cell study indicated that the fraction of Fe^{3+} may reduce from ~ 60 % at 26 GPa to ~ 10 % at 50 GPa and then increase to ~ 60 % upon further compression. In

the presence of Al, the partitioning of Fe has not been well understood. In this study, we aim to identify the chemical composition of bridgmanite with ferropericlase and/or the $MgAl_2O_4$ composition CF-phase under reduced conditions from 27 to 40 GPa by using a multianvil apparatus.

Starting materials were prepared in two ways. Firstly, ball-milled nano-powders were used for sample synthesis at 27 and 33 GPa. MgO, Fe_2O_3, Al_2O_3 and SiO_2 oxide were ground using a ball-milling machine at the Earthquake Research Institute, University of Tokyo, and then dried in a gas-mixing furnace at 680 °C for 3 h. Secondly, a glass made using the levitation method in an Ar atmosphere was used for sample synthesis at 40 GPa. The ball-milled nano powders were used as the starting materials for the glass. Iron metal was added and ground together with the starting materials to produce reducing conditions during the experiments. Starting materials were dried in a vacuum furnace at ~ 400 K before loaded in a 7/3 or 5.7/1.5 multianvil assembly. High-pressure samples were synthesized in the IRIS-15 at the BGI in the pressure range 27 to 40 GPa.

An Al-rich composition synthesised at 27 GPa was found to contain bridgmanite, ferropericlase, and the CF-phase, while an Al-poor composition at the same conditions contained just bridgmanite and ferropericlase. The compositions of bridgmanite, ferropericlase, and CF-phase are $Mg_{0.92}Fe_{0.11}Al_{0.28}Si_{0.80}O_3$, $Mg_{2.41}Fe_{0.31}Al_{0.10}Si_{0.18}O_3$, and $Mg_{0.81}Fe_{0.08}Al_{0.92}Si_{0.19}O_3$, respectively. The sample obtained at 33 GPa showed the presence of bridgmanite and CF-phase with the compositions $Mg_{0.87}Fe_{0.21}Al_{0.43}Si_{0.83}O_3$ and $Mg_{0.89}Fe_{0.15}Al_{1.13}Si_{0.27}O_3$, respectively. Ferropericlase is not observed in the sample at 33 GPa. It is possible that ferropericlase fell out during polishing or it may simply become unstable within the Al-rich bulk composition at higher pressures. The fraction of both Fe and Al in the bridgmanite increases with increasing pressure. A sample synthesised at 40 GPa and 2000 K for 20 hrs from the levitation glass sample does not appear to contain a multiphase assemblage in back-scattered electron images made using a scanning electron microscope. When viewed using a transmission electron microscope (TEM), however, it turns out that the grain size of the sample at 40 GPa is extremely small (50-150 nm). From the TEM images, the grain size appears to depend on the proximity to the iron metal buffer, being smaller closer to the buffer (~ 50 nm) and larger (~ 150 nm) further away. This may indicate that the low oxygen fugacity causes a drastic change in the rate of cation diffusion along grain boundaries at high pressure. Further study will be performed using the Al-rich ball-milled nano-powder sample at 40 GPa in order to compare with the current result and understand the Fe behaviour in bridgmanite in the Fe^{2+}- and Al-rich environment.

f. *Iron partitioning and melting phase relations of $MgSiO_3$-$FeSiO_3$ at uppermost lower mantle conditions (J. Yao, D.J. Frost and G. Steinle-Neumann)*

The FeO component in the silicate portion of the Earth exerts an important influence on its structure and evolution as it strongly affects physical properties of minerals and melting relations. At 24 GPa, significant variations occur in experimentally determined partitioning of

FeO between bridgmanite and the coexisting liquid, with values for the equilibrium constant K_D=(Fe^{solid}/Mg^{solid})/(Fe^{liquid}/Mg^{liquid}) varying in the range 0.2-0.5 for natural and model compositions. However, competing influences of chemistry and temperature (T) on K_D have not been explored systematically. Here, we perform multianvil experiments to investigate melting relations in the model system $(Mg_{1-x}Fe_x)SiO_3$ at 24 GPa, with x = 0.1, 0.2, 0.3 and 0.5, and in a T range of 2510-2650 K (Fig. 3.2-11). We extract thermodynamic information from the data to model melt relations in the $MgSiO_3$-$FeSiO_3$ system and compare the results to other experiments where available. To achieve a similar degree of partial melting in the four experiments, the T was decreased linearly as the $FeSiO_3$ content was increased bridgmanite. We find K_D to increase from 0.22±0.02 to 0.31±0.07 with decreasing iron content in the coexisting solid bridgmanite (Fig. 3.2-12), the latter similar to K_D=0.32 for a composition of peridotite plus 30 wt. % metallic iron at 24 GPa (Fig. 3.2-11).

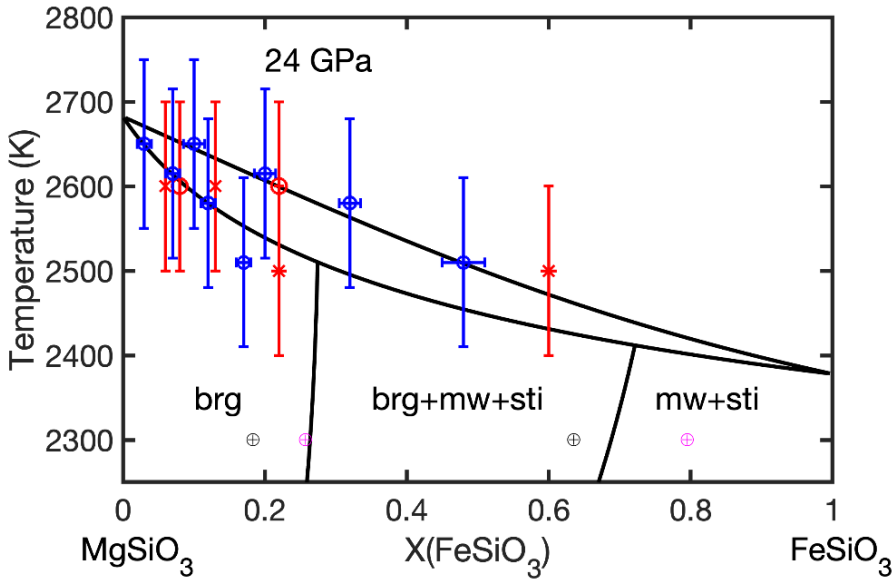

Fig. 3.2-11: Melting phase relations at 24 GPa. The thermodynamic model (solid lines) reproduces the solid and liquid compositions from our experiments (blue symbols). Red symbols show previous studies on peridotite plus Fe metal (circles), CI chondritic analogue (asterisks), and Al-rich peridotite (crosses). Experimental data on the solid phase boundaries at 22 GPa (black) and 27 GPa (magenta circles) are shown.

Along the $MgSiO_3$-$FeSiO_3$ join, the solidus and liquidus curves are well constrained by the measured bridgmanite and liquid compositions (Fig. 3.2-11) and are reproduced by the thermodynamic model. The solidus curve between $MgSiO_3$ and $FeSiO_3$ is convex, while the liquidus T decreases quasi-linearly with $FeSiO_3$ content at a rate of ≲4 K per mol. % of $FeSiO_3$ up to X_{FeSiO_3} ~ 0.5, before this curve also becomes slightly convex. The $FeSiO_3$ content of bridgmanite and the liquid from the model is in very good agreement with prior experiments on melting of peridotite plus 30 wt. % Fe metal and in reasonable agreement with data from a chondrite starting composition, indicating that small CaO and Al_2O_3 contents (≲ 4 wt. %) do not influence iron partitioning strongly. By contrast, a prior experiment on an Al_2O_3-rich (~ 7

wt. %) peridotite results in a liquid composition that is depleted in $FeSiO_3$ compared to our model, probably caused by the charge-coupled substitution $Mg^{2+} + Si^{4+} = Al^{3+} + Fe^{3+}$ shifting the iron equilibrium towards bridgmanite. For $X_{FeSiO_3} < 0.27$ the only phase predicted on the solidus is bridgmanite. Bridgmanite exceeds its $FeSiO_3$ solubility limit in the model at a value somewhat larger, $X_{FeSiO_3} = 0.16 \pm 0.02$, than directly measured in the experiments for the $(Mg_{0.5}Fe_{0.5})SiO_3$ composition. At this point the phase assemblage at the solidus becomes bridgmanite, magnesiowustite and stishovite. In our model, bridgmanite disappears from the solidus phase assemblage for $X_{FeSiO_3} = 0.72$. These boundaries of the solidus assemblages bracket prior measurements at 2270 K for 22 and 27 GPa reasonably well. The higher bridgmanite X_{FeSiO_3} for saturation predicted in the model compared to the experimental data may be due to the assumption of ideal mixing between $MgSiO_3$ and $FeSiO_3$ bridgmanite.

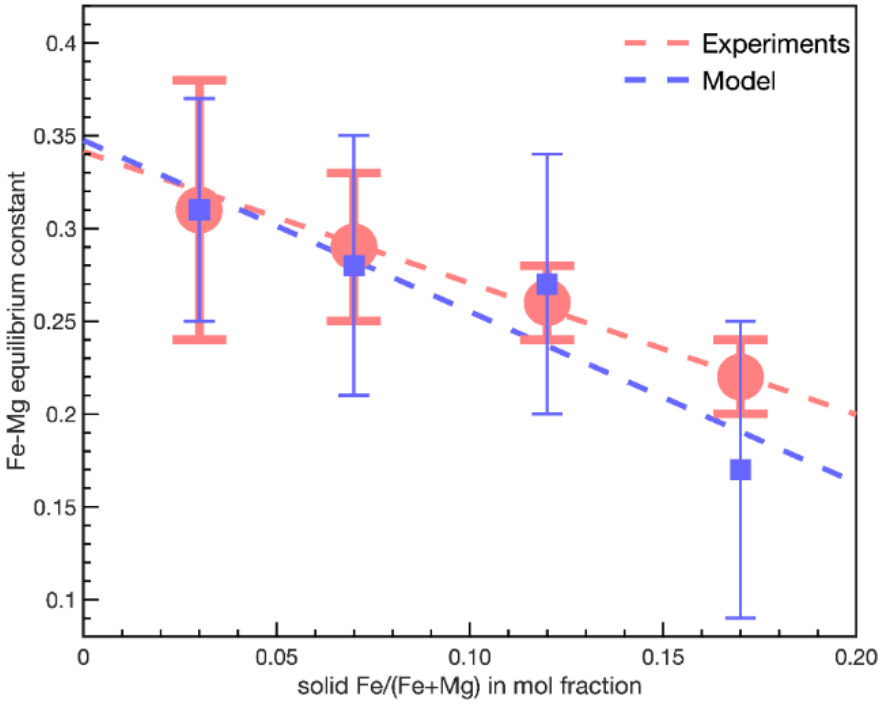

Fig. 3.2-12: Fe-Mg equilibrium constants K_D between bridgmanite and melt as a function of the iron content of bridgmanite at 24 GPa. The starting compositions are $(Mg_{1-x}Fe_x)SiO_3$, x = 0.1, 0.2, 0.3 and 0.5 from left to right. Experimental data are shown by red circles, and results from the thermodynamic model by blue squares.

g. *The role of Ca-phosphates in the deep Earth's phosphorus, volatile and incompatible trace element cycles (T. Pausch, J. Vazhakuttiyakam, B. Joachim-Mrosko and J. Konzett/Innsbruck; A.C. Withers)*

Ca-phosphates play a unique role in the mineral inventory of the silicate Earth because they are major carriers of phosphorus, hydrogen, and halogens, all of which are essential for the origin and evolution of life. They are also important hosts for incompatible trace elements, which are

indispensable for modelling the origin and evolution of magmatic rocks. However, virtually nothing is known about the role of Ca-phosphates for lower mantle segments of the global phosphorus, volatile and incompatible trace element cycles.

In our ongoing experimental study, we seek to investigate (1) the stability, phase relations and composition of Ca-phosphates in peridotitic and basaltic bulk compositions at *P-T* conditions of the upper-to-lower mantle transition, (2) the (trace-) element partitioning between Ca-phosphates and coexisting lower mantle solids and partial melts, and (3) the crystal chemistry of high-pressure phosphates. Eight multianvil experiments have been conducted so far in the *P-T* range 15 to 25 GPa and 1600 to 2000 °C. The starting material for the experiments was a representative peridotite bulk composition that was doped with a range of incompatible trace elements, including rare-earth, high-field-strength, and large-ion lithophile elements, together with Cl and Br.

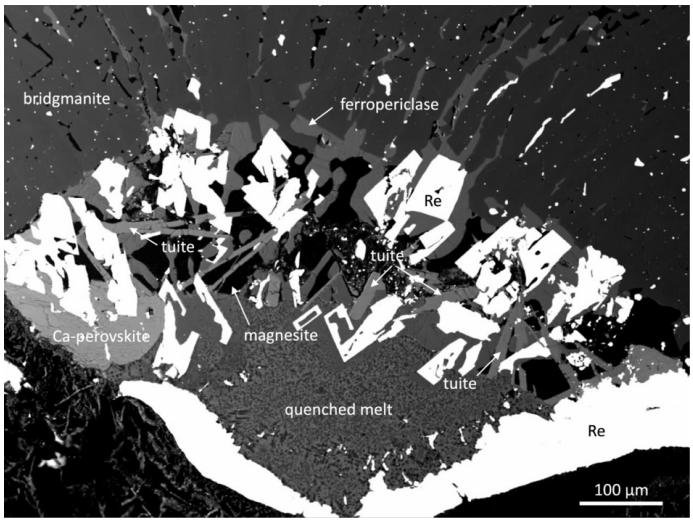

Fig. 3.2-13: A backscattered electron photomicrograph of the phase assemblage tuite + bridgmanite + Ca-perovskite + ferropericlase + quenched melt + magnesite stabilized in a representative peridotite bulk composition at 25 GPa and 1600 °C; magnesite formed from traces of CO_2 inherited from the starting material.

The phases that were found to be stable within this *P-T* range include tuite, majoritic garnet, ringwoodite, bridgmanite, Ca-perovskite, ferropericlase, and melt. Small amounts of additional magnesite are thought to have formed from traces of CO_2 inherited from the starting material. Tuite, a high-pressure form of $Ca_3(PO_4)_2$, was found so far to be stable in runs at 20 and 25 GPa at 1600 °C, in which it takes the form of lath-shaped to needle-like crystals up to approximately 100 × 20 µm in size (Fig. 3.2-13). At 1800 °C tuite is not stable anymore in the investigated pressure range, which indicates that the upper temperature stability of tuite is close to the average current mantle adiabat (ACMA). Therefore, tuite is eminently suitable as a halogen and incompatible trace-element carrier in both, subduction zones and convecting mantle P-T regimes.

h. *Iron oxides and oxyhydroxides as agents of oxygen recycling in the early Earth's history (L.S. Dubrovinsky, E. Koemets, T. Fedotenko, S. Khandarkhaeva, E. Bykova, M. Thielmann, C.A. McCammon, S. Chariton/Chicago, G. Aprilis and M. Hanfland/Grenoble, K. Glazyrin and H.-P. Liermann/Hamburg)*

Water and water-bearing species have a strong impact on life at the Earth's surface as well as on numerous processes in Earth's interior. The presence of water affects properties of mantle minerals and causes large-scale global phenomena such as arc volcanism and plate tectonics. Water circulation mechanisms between geospheres, which are crucial for geodynamic and geochemical cycles, are still actively debated and discussed. Recent studies suggest that iron-bearing minerals present in Banded Iron Formations (BIFs), such as goethite, could transport water to Earth's deep interior through subducting slabs. There are reports that FeOOH remains stable in the sinking slab until it reaches the bottom of the lower mantle. These studies revealed by means of *in situ* powder X-ray diffraction that at pressures corresponding to depths of ~ 1800-2000 km and at moderately high temperatures, FeOOH undergoes a phase transition to form the stable pyrite-type phase FeO_2H_x with $0 \leq x \leq 1$ (Py-phase). Goethite and its high-pressure polymorphs have therefore been considered to be candidates for water and/or hydrogen transfer to the lower mantle and the core-mantle boundary. While FeOOH was intensively studied at the conditions of the upper mantle and core-mantle boundary, there is a lack of data on its behaviour in the P-T range corresponding to the lower mantle conditions. Here we present a detailed study of the behaviour of FeOOH at conditions of the subducting slab using advanced *in situ* single-crystal X-ray diffraction techniques in laser-heated diamond anvil cells.

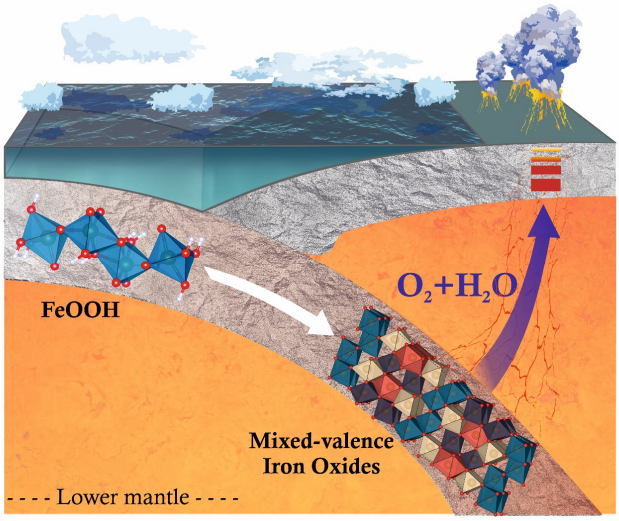

Fig. 3.2-14: A schematic view of a possible deep oxygen cycle in the early Earth. FeOOH ("rust"), which was produced by anoxygenic photosynthesis and accumulated on the ocean floor, was transferred to the lower mantle by subducting slabs. At high pressures and temperatures, FeOOH decomposes into a mixture of complex iron oxides, water, and oxygen. Oxidizing fluids, possibly rising to the Earth's surface, could then contribute to (or even be one of the main causes of) the Great Oxidation Event about 2.5 billion years ago.

Goethite, α-FeOOH, is a major phase among oxidized iron species, commonly called rust, which can be formed in many ways including as a by-product of anoxygenic prokaryote metabolism that took place from about 3.8 billion years (Ga) ago until the Great Oxidation

Event roughly 2.2 Ga ago. Rust was buried on the ocean floor and was transported into the mantle as a consequence of plate tectonics that started at least 2.8 Ga ago. The fate and the geological role of rust at pressure and temperature conditions of the lower mantle have been unknown up to now. We studied the behaviour of FeOOH up to 81(±2) GPa and 2100(±100) K using *in situ* synchrotron single-crystal X-ray diffraction. At these conditions, which correspond to the coldest slabs at depths of about 1000 km, α-FeOOH decomposes to iron oxides (Fe_2O_3, Fe_5O_7, Fe_7O_{10}, $Fe_{6.32}O_9$) and an oxygen-rich fluid. Our results suggest that recycling of rust in Earth's mantle could contribute to redox conditions of the early Earth (Fig. 3.2-14).

i. *Mössbauer investigation of serpentinites to estimate hydrogen production at slow-spreading mid-ocean ridges (C.A. McCammon, in collaboration with E. Albers, W. Bach, M. Pérez-Gussinyé and T. Frederichs/Bremen)*

Mantle peridotite reacts with seawater at low temperatures to form serpentinite, releasing hydrogen that provides energy to the deep biosphere. Hydrogen production at mid-ocean ridges has been extensively studied in the past, but reactions at magma-poor margins have received less attention. The latter is particularly relevant to understanding the evolution from continental rifting to mid-ocean ridge spreading in the North Atlantic. The most prominent example of a magma-poor margin is the one at West Iberia (west of Spain), which formed during the break-up of Pangea.

Fifteen drill core samples were collected from the West Iberia margin during ODP Leg 103, Hole 637A, which is within the transition from subcontinental to the oceanic mantle. The samples originate from ~230 to 267 m below the seafloor and consist of strongly serpentinized harzburgites and lherzolites. In addition to chemical and magnetic analysis, each sample was measured at room temperature using Mössbauer spectroscopy. Mössbauer spectra are well resolved, and it is straightforward to deconvolute them into contributions from serpentine, spinel, and iron oxides (magnetite, goethite, hematite) (Fig. 3.2-15a). The relative areas of subspectra provide a unique and direct measure of distribution of iron between phases (Fig. 3.2-15b) as well as $Fe^{3+}/\Sigma Fe$ in serpentine. Combined with chemical data, the volume abundance of phases can be estimated from relative areas. Analytical data are complemented by thermodynamic calculations to model the inflow of seawater into peridotite, changes in fluid chemistry during the reaction with rock, and the serpentinization of peridotite by the seawater-derived fluid.

Our results reveal that hydrogen yields during seawater-peridotite interactions strongly depend on rock type and alteration temperature. Hydrogen yields were likely higher by a factor of two or more from seawater–lherzolite reactions during continental rifting and break-up, compared to those resulting from the hydration of harzburgites/dunites at the early, ultraslow-spreading mid-Atlantic Ridge. We speculate that sufficient energy (in the form of H_2) is available at magma-poor rifted margins and ultraslow-spreading ridges to support life. Indeed, particularly

large volumes of serpentinite should form at temperatures close to those at/below the limit of life, which likely favours geological-biological interactions and a biosphere containing organisms that are able to metabolise molecular hydrogen.

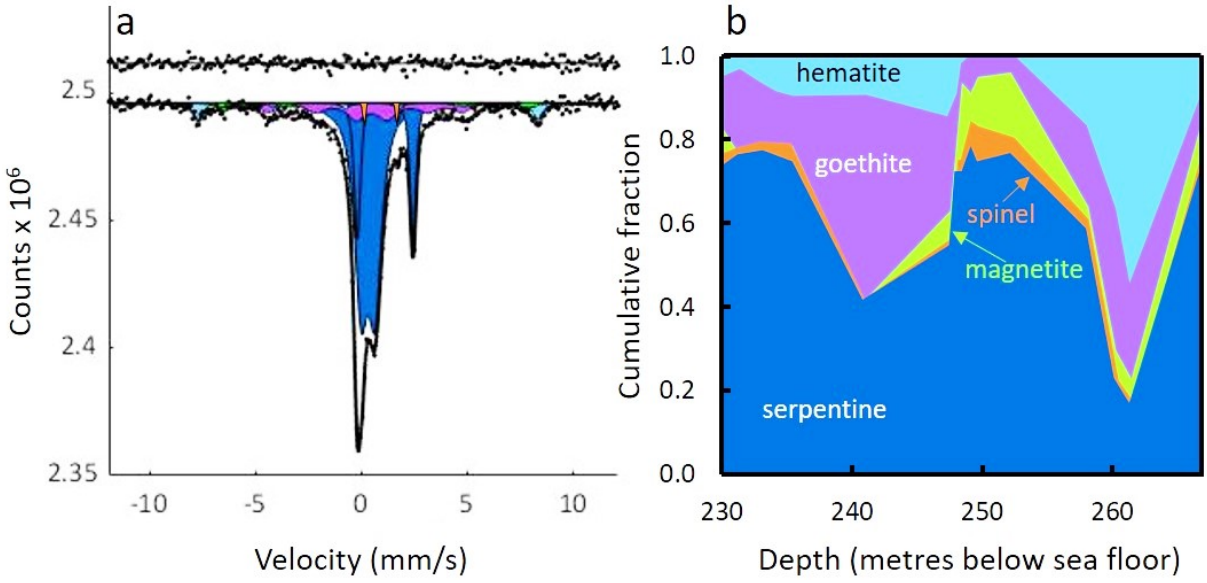

Fig. 3.2-15: (a) A Mössbauer spectrum of serpentinized peridotite recovered from 230 m below the sea floor. Data were fit to two doublets assigned to Fe^{2+} and Fe^{3+} in serpentine (dark blue), one doublet assigned to spinel (orange), two sextets assigned to magnetite (green), one sextet assigned to hematite (light blue) and one sextet assigned to goethite (purple). (b) The distribution of iron between phases in serpentinized peridotite as a function of depth.

j. *A quantitative model for the trace element signature of primitive arc magmas from partitioning experiments (G. Rustioni and H. Keppler)*

Although arc magmatism is considered to be the main mechanism for continental crust growth, the causes of magma generation in subduction zones are still not fully understood. While it is generally accepted that partial melting is likely triggered by addition of a fluid to the mantle wedge, the exact nature of this slab-derived mobile phase is still debated. Many models assume that it is an aqueous fluid released by the breakdown of hydrous minerals contained in the subducting slab that metasomatizes the mantle. However, one of the main arguments against this idea used to be that such fluid would not be very efficient in transporting trace elements and they may therefore hardly explain the typically enriched trace element signature of arc magmas. On the other hand, it was experimentally demonstrated by previous work at BGI that addition of Cl to aqueous fluids is very effective in enhancing the fluid/rock partition coefficients of many trace elements.

In order to better constrain the process that leads to arc magma generation, we therefore used our recent experimental data to model the fluid-mediated transport of trace elements from the

subducting slab up to the mantle wedge and thus to obtain the composition of primitive arc magmas produced by partial melting of the metasomatized mantle. For this model, we use fluid/eclogite partition coefficients determined at 4 GPa and 800 °C for an eclogite composed of 59 wt. % omphacite, 39 wt. % garnet and 2 wt. % rutile and a fluid salinity range of 0 to 15 wt. % NaCl. We therefore calculate the trace element concentration in the fluid released by the basaltic portion of the slab as a function of fluid salinity and fluid fraction in the slab, assuming batch equilibrium. The composition of the mantle wedge metasomatized by such fluid is then modeled as a function of fluid added to the melting source. We can thus calculate the trace element signature of primitive arc magmas assuming batch partial-melting of the metasomatized peridotite composed of 60 wt. % olivine, 30 wt. % orthopyroxene, 5 wt. % garnet and 5 wt. % clinopyroxene.

The results of such a model ultimately depend on four independent parameters: (i) the fluid salinity, (ii) the amount of fluid contained in the basaltic portion of the slab, (iii) the fluid fraction added to the source of melting, and (iv) the degree of melting in the mantle wedge. Among these, the by far most important variable is the fluid salinity, as the addition of a few wt. % of Cl can enhance the fluid/eclogite partition coefficients of some elements such as large ion lithophile elements and light rare earth elements by orders of magnitude. Moreover, as the salinity has a very minor effect on the solubility of other trace elements, like for example high field strength elements, it also effectively fractionates trace elements relatively to each other. In contrast to this, the other parameters mentioned do influence the absolute trace element concentrations, but not so much the fractionation pattern.

Figure 3.2-16 shows a comparison between the trace element signatures predicted by our model and a worldwide compilation of natural primitive arc basalts. For these calculations, we assumed 2 wt. % of fluid in the eclogite and a degree of melting of 20 % in the mantle wedge. We then explored a Cl content in the fluid ranging from 0 to 10 wt. % and an addition of 2.5, 5 and 10 wt. % of fluid to the source of melting. Our results show that a pure aqueous fluid is always too diluted to produce the natural trace element enrichment. However, if we consider in the calculations Cl contents that are in the range of typical subduction zone fluid salinities, our model is able to reproduce most features present in natural primitive arc magmas signatures already with a fluid addition of only 2.5 wt. % to the mantle source. Overall, our results suggest that saline aqueous fluids released from the basaltic layer of the subducting slab are most likely the main agent of trace element enrichment in the mantle wedge and the trigger of melting in subduction zones.

We also tested whether partial melts from sediments could generate the typical arc magma trace-element signature, using the compositions of partial melts from sediments reported in previous studies. While sediment melts are indeed very efficient in enriching certain trace elements, the predicted enrichment pattern very strongly depends on the type of sediment subducted. Therefore, one would expect major differences in the trace element enrichment pattern of magmas generated in arcs associated with pelite-rich subduction versus those with carbonate-rich subduction or with little sediment contribution. This is, however, not observed.

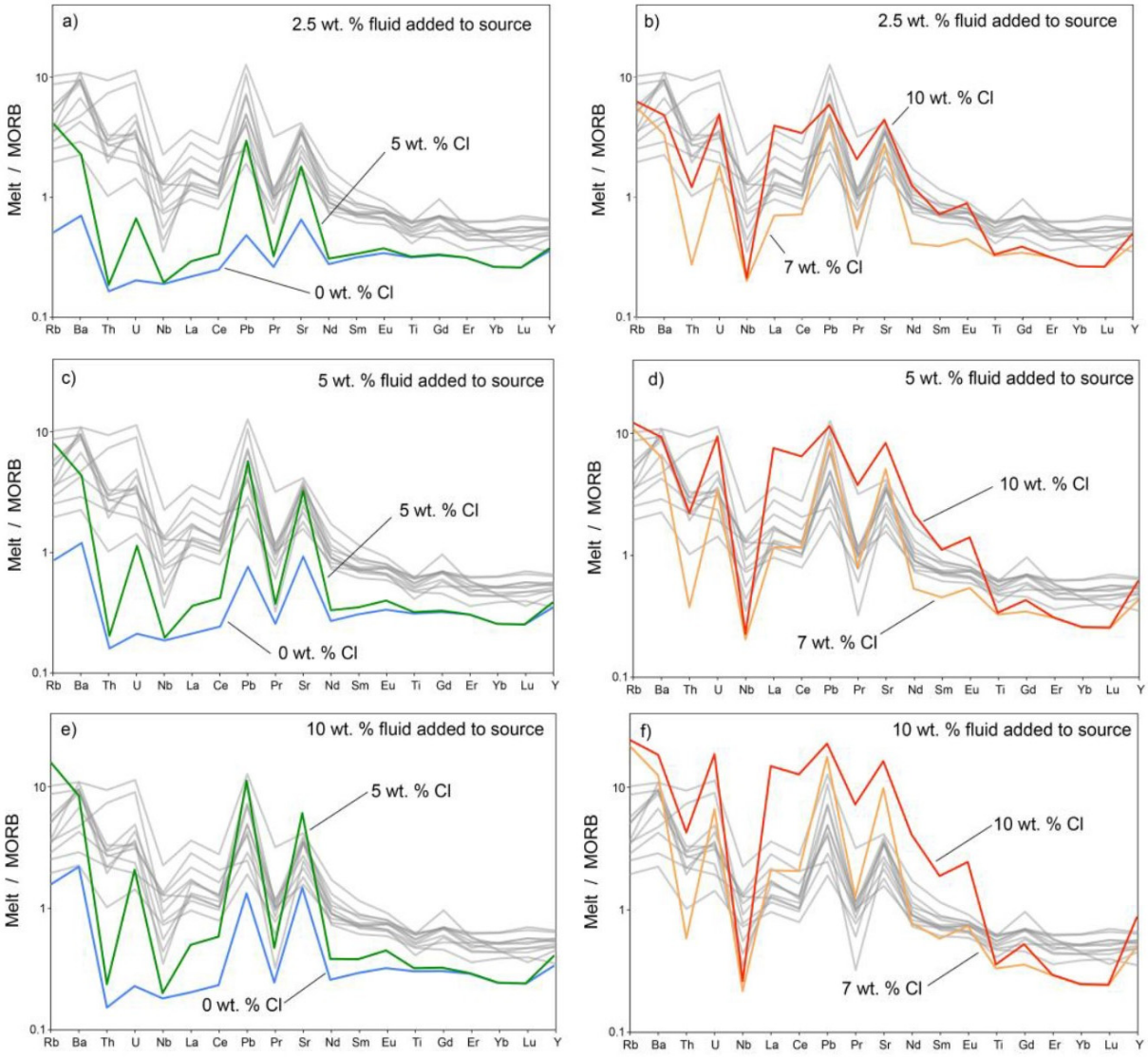

Fig. 3.2-16: Trace element patterns predicted from modeling the partial melting of the mantle wedge metasomatized by an aqueous fluid released from the subducting slab. The results of calculations for 2.5 to 10 wt. % fluid addition to the source of melting and fluid salinities ranging from 0 to 10 wt. % of Cl are shown. Gray lines represent trace element signatures of natural primitive arc basalts from various subduction zones worldwide.

k. *Mobility of Cu, Zn, and W in subduction zone fluids (S. Liu, A. Audétat and H. Keppler)*

Subduction zones are the site of long-term chemical cycling between Earth's surface and its interior. During subduction, aqueous fluids and melts liberated from the downgoing oceanic slab metasomatize the overlying mantle wedge, leading to partial melting in the mantle wedge and causing arc magmatism. In this process, mobile elements are recycled into the mantle wedge and arc system. Recent work has demonstrated that saline aqueous fluids released from the basaltic layer of the subducted slab can effectively transport LILE and LREE and may

generate the typical trace element signature observed in arc magmas. Accordingly, slab-derived saline fluids are likely the main metasomatic agent. However, it remains largely unknown if such fluids can effectively transport Cu, Zn, and W into the mantle wedge and therefore contribute to the metal enrichment processes leading to ore deposits hosted by arcs.

The partitioning behaviour of Cu, Zn, and W between saline aqueous fluids and eclogitic minerals at subduction zone conditions was investigated by piston-cylinder experiments at 4 GPa and 800 °C. A MORB glass doped with trace amounts of Cu, Zn and W was used as starting material. The initial composition of the fluids ranged from pure water to brines containing up to 10 wt. % NaCl, covering the most common salinities observed in subduction zone fluids. The diamond trap technique was employed to separate fluids from the solid residue and capture them. A diamond powder layer was placed in the central part of the capsule, sandwiched between two MORB layers. After the experiments, the fluids trapped in pore space between diamonds were analysed in the frozen state by LA-ICP-MS. The capsules were then embedded in epoxy resin and polished to expose minerals for EPMA and LA-ICP-MS measurements.

All fluids were found to be in chemical equilibrium with a metamorphic assemblage consisting of garnet, clinopyroxene, coesite, and accessory rutile. Mass fractions and $D_{fluid/mineral}$ for all major solid phases were determined from fluid and mineral compositions. Bulk fluid/eclogite partition coefficients $D_{fluid/eclogite}$ were then calculated from the individual fluid/mineral partition coefficients (Fig. 3.2-17).

Our preliminary results show that the addition of chlorine moderately enhances the partitioning of Cu and Zn into aqueous fluids, while the effect on W is very minor. The fluid/eclogite partition coefficients of Cu and W are slightly greater than 1 with $D_{fluid/eclogite}$ of Zn < 1, indicating that even chlorine-bearing fluids may not make a significant contribution of these elements to the mantle wedge and arc system. This is supported by studies and global compilations of natural samples, which indicate that Cu concentrations in primitive arc basalts are similar to those of MORBs.

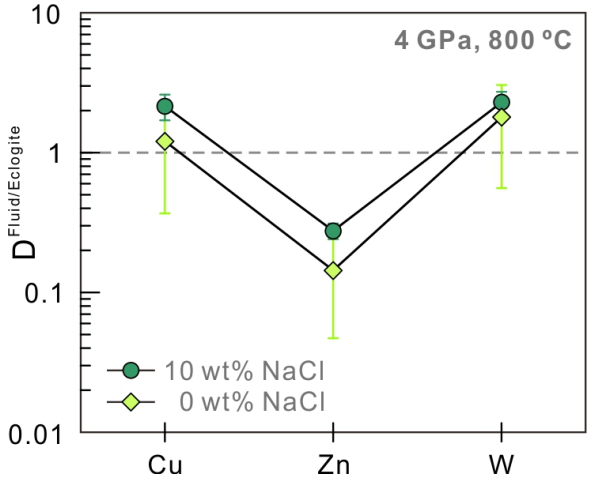

Fig. 3.2-17: Fluid/rock partition coefficients of Cu, Zn, W for eclogites in equilibrium with Cl-free and Cl-bearing aqueous fluids.

I. *The magmatic-hydrothermal geochemistry of gallium (R. Zhao and H. Keppler)*

Gallium is a rare element that is currently in high demand for semiconductor applications, including light-emitting diodes and photodetectors. It is usually recovered as a by-product during the processing of bauxite and sphalerite ores. Because of its rarity and numerous industrial uses, it is considered a "critical metal" for high-tech applications. Since it may be difficult to cover the future demand of gallium from conventional resources, a better understanding of gallium geochemistry in magmatic-hydrothermal systems would be desirable in order to identify conditions under which gallium could be enriched to economically viable ore deposits. We have therefore carried out some exploratory experiments in order to determine the solubility of Ga_2O_3 in silicic melts and saline aqueous fluids, as well as the partitioning of gallium between granitic melts and alkali feldspar.

The experiments were carried out at 2 kbar and 750 to 800 °C in cold-seal pressure vessels at an oxygen fugacity near the Ni-NiO buffer. In one type of experiment, excess Ga_2O_3 was equilibrated with a haplogranitic melt. During the run duration of 14 days, alkali feldspar also crystallized from the melt (Fig. 3.2-18). The experiments showed that Ga_2O_3 solubility in the melt strongly increases with temperature, from 0.8 wt. % Ga_2O_3 at 750 °C to 2.6 wt. % at 800 °C. Gallium was found to be compatible in alkali feldspar, with $D_{Ga}^{feldspar/melt}$ of 3.91 ± 1.03 at 750 °C and 1.59 ± 0.16 at 800 °C. In the second type of experiment, we equilibrated saline aqueous fluids with Ga_2O_3 and trapped the fluid as synthetic fluid inclusions in quartz. Laser-ablation ICP-MS analyses allowed to constrain the gallium concentration in the fluid. Preliminary data suggest that gallium becomes quite soluble in aqueous fluids containing 10 wt. % NaCl, and the fluid/melt partition coefficient estimated from the data on Ga_2O_3 solubility in the melt and in the saline fluid is about 1-2.

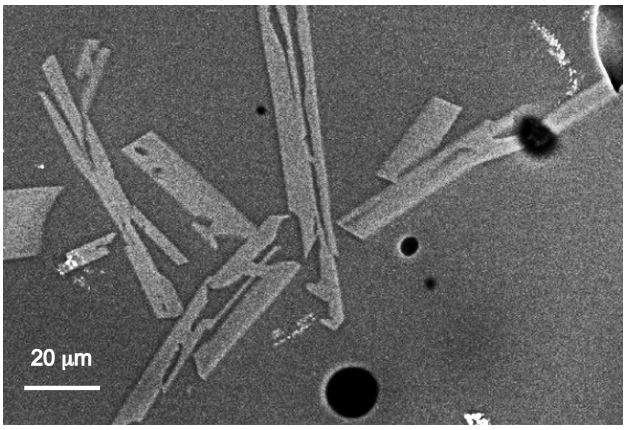

Fig. 3.2-18: A backscattered electron image of a sample containing gallium-bearing alkali feldspar crystallized from a haplogranitic melt at 800 °C and 2 kbar.

Overall, our preliminary experimental data show that it is very difficult to enrich gallium to high concentrations in natural magmatic-hydrothermal fractionation processes. In particular, the compatibility of gallium in alkali feldspar pretty much rules out any gallium enrichment during fractional crystallization of a felsic magma. A possible enrichment mechanism could be the early exsolution of a very Cl-rich fluid phase from a magma, but even this mechanism is

not very efficient. Moreover, such a process will only rarely occur in nature, as it would require unusually high initial water and Cl contents.

m. *The effects of pressure, fO_2-fS_2 and melt composition on the fluid–melt partitioning of Mo (J. Fang and A. Audétat)*

Porphyry Mo deposits, which represent one of our two main sources of Mo, are genetically associated with rift-, subduction- and collision-related granitic magmas emplaced in the upper crust. The Mo mineralization potential of upper crustal granitic magmas may be partly determined by the depth at which magmas emplace, since emplacement depth determines the solubility of volatiles and metals in the magmas, the mode of fluid release, and the evolution path of the exsolved fluids.

In order to assess the Mo mineralization potential of upper crustal granitic magmas emplaced at different depth levels, the partitioning behaviour of Mo between aqueous fluids and granitic melts was experimentally investigated at temperatures of 750-850 °C, and pressures ranging from 0.8 to 3 kbar, which encompasses the common depth range (~ 5-10 km) of magma chambers associated with porphyry Mo deposits. Fluids in equilibrium with silicate melt, MoS_2, magnetite and pyrrhotite (±pyrite) and fO_2+fS_2 controlled by either an external NiNiO buffer or internally by the magnetite-pyrrhotite-pyrite assemblage were trapped after three days of equilibration by *in situ* cracking in quartz and then held for four more days at high pressure and temperature to produce synthetic fluid inclusions. Through analyzing the recovered fluid inclusions and the run product glass by LA-ICP-MS and electron microprobe, the compositions of coexisting fluid and silicate melt, and, hence, Mo fluid/melt partition coefficients (D_{Mo}(fluid/melt)) were determined.

Experimental results obtained at a constant temperature of 750 °C are summarized in Figure 3.2-19. The D_{Mo}(fluid/melt) values increase substantially with pressure but depend also strongly on melt composition and fO_2+fS_2. Over the range of 750 °C to 850 °C no significant temperature effect was observed. Most of our experimentally determined D_{Mo}(fluid/melt) values fit within the range of partitioning values derived from coexisting fluid and melt inclusions in miarolitic cavities of granitic intrusions that crystallized at ≤ 1.8 kbar. Rayleigh fractionation modeling (Fig. 3.2-20) shows that in metaluminous magmas crystallizing at relatively low pressures (*e.g.*, 1.6 kbar) the Mo concentration in the residual melt increases during both fluid-undersaturated (from point A to B) and fluid-saturated (after point B) crystallization, whereas at higher pressures (*e.g.*, 2.0, 2.5, 3.0 kbar) the Mo concentration in the residual melt decreases, indicating a higher Mo extraction efficiency. In addition, magmas that evolve at deeper levels can dissolve more H_2O and thus attain lower viscosities than magmas that evolve at shallow levels, which may promote more efficient segregation of crystal-poor melts into the upper parts of magma chambers, a process that has been highlighted to play a critical role in the formation of Climax-type Mo deposits. Taken together, it is suggested that the Mo-mineralization potential of granitic magmas may critically depend on magma emplacement depth.

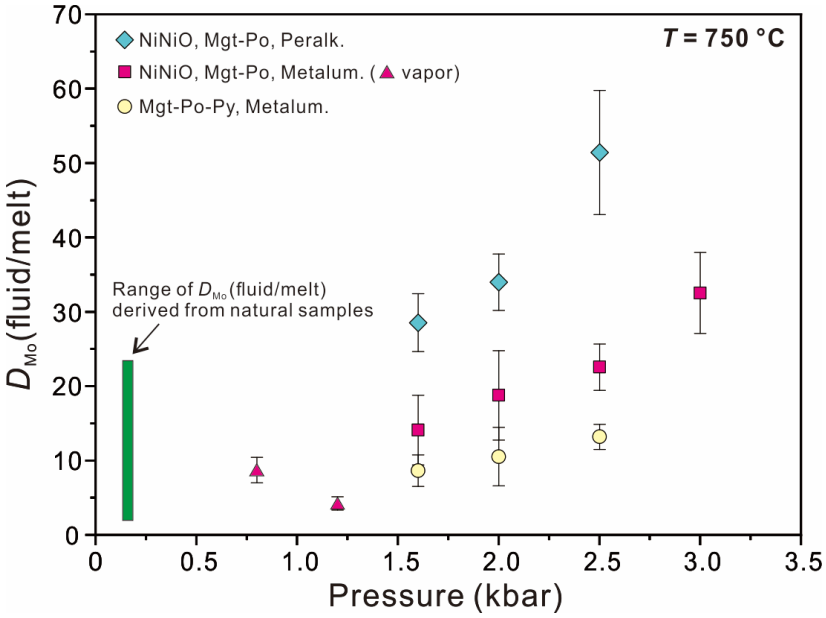

Fig. 3.2-19: D_{Mo}(fluid/melt) as function of experimental pressure. The vertical green bar marks the range of D_{Mo}(fluid/melt) derived from coexisting fluid and melt inclusions in granite intrusions that crystallized at relatively shallow depth (≤1.8 kbar).

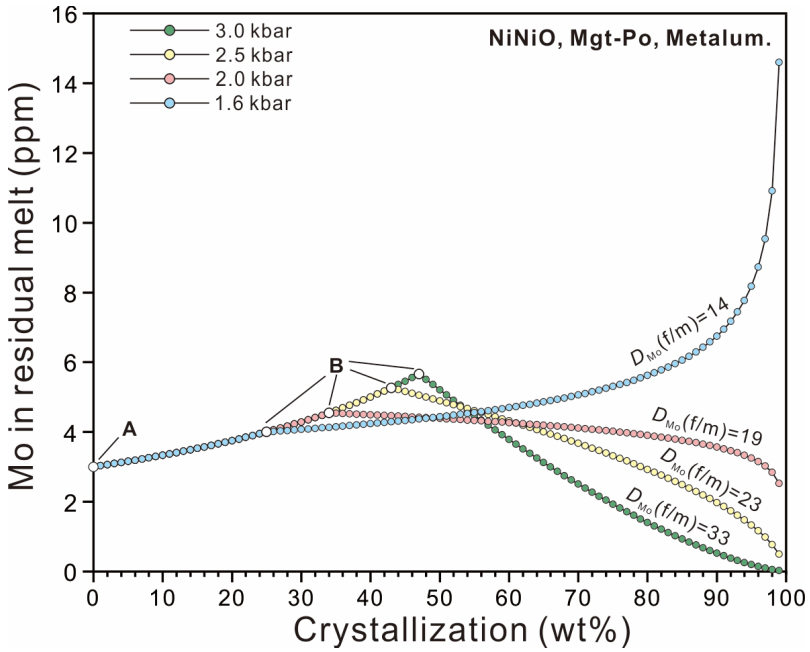

Fig. 3.2-20: A Rayleigh fractionation model of magnetite+pyrrhotite-saturated, metaluminous magmas crystallizing at an fO_2 that is equal to the NiNiO buffer, illustrating the evolution of Mo concentration in the residual melt as a function of the degree of magma crystallization at 1.6, 2.0, 2.5 and 3.0 kbar confining pressure. The modeling assumes that the starting melt contains 4 wt. % H_2O and 3 ppm Mo (point A), and that Mo is 100 % incompatible in the crystallizing minerals. Fluid saturation is reached at point B, which occurs at different degrees of crystallization due to the increasing H_2O solubility in the silicate melt with increasing pressure.

n. *Can post-collisional porphyry magmas form by partial melting of typical lower-crustal hydrous cumulates? Constraints from the Kohistan and Gangdese arc roots and partial melting experiments (J. Zhang, J. Chang and A. Audétat)*

There is growing evidence that mafic arc magmas tend to fractionate sulphides in the lower crust despite their relatively high oxidation state, thus leading to the formation of sulphide-rich cumulates. Such observations seemingly support the model that post-collisional porphyry-copper magmas are derived from partial melting of lower-crustal, hydrous cumulates produced by previous arc magmatism. The Kohistan and Tibetan Gangdese arcs, which are part of the Tethyan tectonic domain that hosts numerous post-collisional porphyry copper deposits, record significant crustal thickening and modification during the transition from subduction- over collisional- to post-collisional setting. In this study we performed detailed petrography, thermobarometry, LA-ICP-MS analysis of sulphide inclusions, and piston-cylinder partial melting experiments on hornblende-rich lithologies from the exposed Kohistan and Gangdese arc roots. The aims are to reveal the petrogenesis and metal content of the hornblende-rich lithologies, and to gain insights into the genesis of post-collisional porphyry copper magmas.

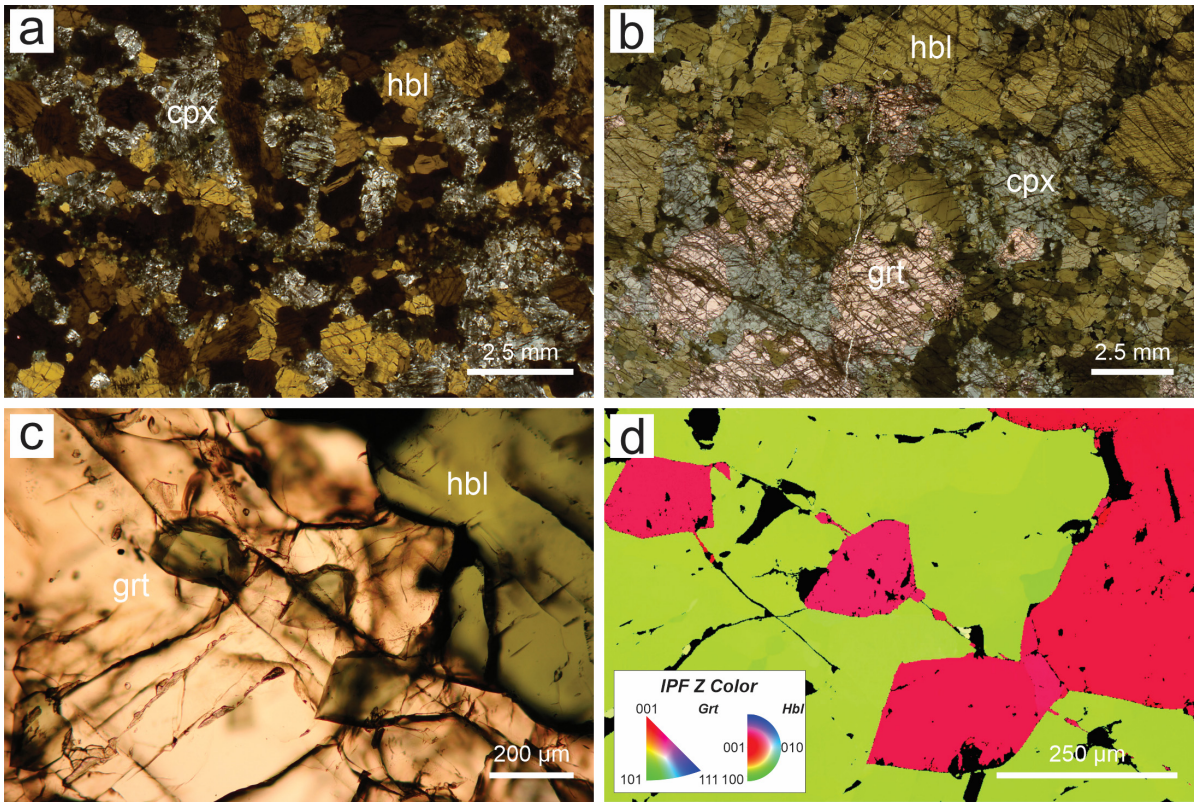

Fig. 3.2-21: (a-b) Scans of polished thick sections of a clinopyroxene hornblendite from the Gangdese arc and of a garnet hornblendite from Kohistan. (c-d) A photomicrograph and EBSD map showing spatially separated hornblende grains within a garnet crystal from a Kohistan hornblendite. The identical optical orientation of the hornblende grains suggests that an originally larger hornblende crystal was partly replaced by garnet. Images a-c were taken in transmitted light. Abbreviations: cpx – clinopyroxene; grt – garnet; hbl – hornblende.

The Gangdese hornblende-rich lithologies, consisting of hornblendites and hornblende gabbros, show relatively well-preserved primary magmatic mineral assemblages and cumulate texture (Fig. 3.2-21a). Thermobarometric results suggest that these cumulates formed at 0.28-0.52 GPa and 830-1050 °C. By contrast, the Kohistan arc root is dominated by garnet hornblendites and garnet granulites (Fig. 3.2-21b). Notably, garnets in the garnet hornblendites crystallized at the expense of hornblende ± clinopyroxene (Figs. 3.2-21c, d), and they occasionally contain fully enclosed quartz inclusions. These observations support previous interpretations that the Kohistan arc garnet-bearing lithologies formed as garnet-free cumulates and then experienced metamorphic dehydration melting during crustal thickening. The peak P-T conditions during crustal thickening were likely 1.0-1.8 GPa and 800-1000 °C.

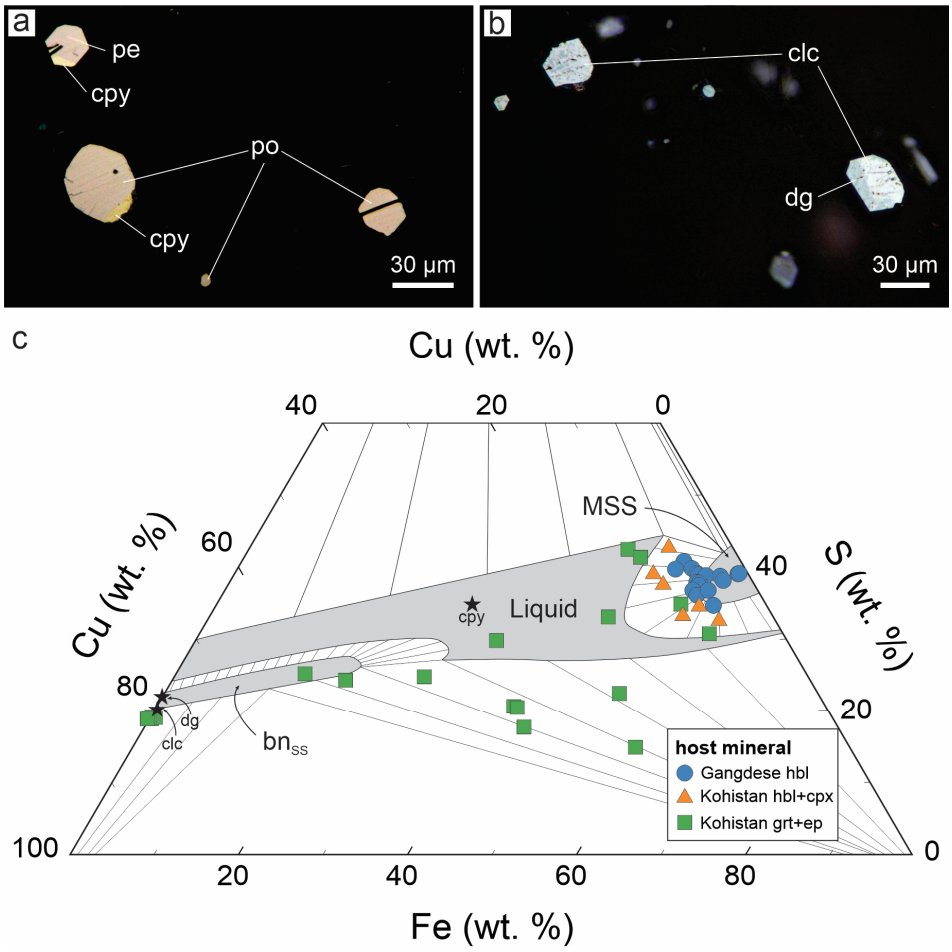

Fig. 3.2-22: (a) Reflected-light photomicrograph of Cu-poor sulphide inclusions in hornblende of a Gangdese hornblendite. The sulphide inclusions are dominated by pyrrhotite and contain minor chalcopyrite and pentlandite. (b) Reflected-light photomicrograph of Cu-rich sulphide inclusions in garnet of a Kohistan garnet hornblendite. The sulphide inclusions show reproducible volume proportions of chalcocite and digenite. (c) A Fe-Cu-S diagram at 1 bar and 1000 °C showing the bulk compositions of mostly unexposed sulphide inclusions analyzed by LA-ICP-MS. The star symbols show the compositions of chalcopyrite, digenite and chalcocite. Abbreviations: clc – chalcocite; cpy – chalcopyrite; dg – digenite; pe – pentlandite; po – pyrrhotite; MSS – monosulphide solid solution; bn_{ss} – bornite solid solution.

The Gangdese hornblendites and hornblende gabbros commonly contain abundant magmatic sulphides (up to ~ 0.4 vol. %). Well-preserved sulphide inclusions, consisting of pyrrhotite plus minor amounts of chalcopyrite and pentlandite (Fig. 3.2-22a), are rather common in hornblende. In contrast, the Kohistan garnet hornblendites and garnet granulites are generally very poor in magmatic sulphides (< 0.1 vol. %), but one garnet hornblendite sample contains ~ 0.5 vol. % magmatic sulphides. Primary hornblende and clinopyroxene in garnet hornblendites occasionally contain a few fresh sulphide inclusions whose composition is dominated by pyrrhotite. Garnet in garnet hornblendites contains rare sulphide inclusions whose dominant phase ranges from pyrrhotite over chalcopyrite to chalcocite (Figs. 3.2-22b, c). These observations suggest that primary sulphides present in the Kohistan cumulates were mostly destroyed during metamorphic dehydration melting.

Partial melting experiments of hornblendite and hornblende gabbro from the Gangdese arc conducted at a pressure of 1.5 GPa reproduce well the major mineral phases in the Kohistan garnet hornblendites and garnet granulites. However, partial melts of these experiments are characterized by extremely high Na/K ratios and are unable to dissolve considerable amounts of sulphides. Taken together, we conclude that post-collisional porphyry copper-forming magmas cannot have formed through partial melting of typical, lower-crustal hornblende-rich arc cumulates.

o. *Post-collisional porphyry magmas formed by fractionation of lithospheric mantle-derived potassic mafic magmas (J. Chang and A. Audétat)*

Porphyry copper deposits are mostly related to calc-alkaline, andesitic to dacitic porphyry intrusions in magmatic arcs above subduction zones. However, some economically important porphyry copper deposits are also found in continental collision zones, where the ore-forming magmas are higher in potassium than their equivalents in subduction settings. Popular models suggest that post-collisional, ore-forming magmas were derived from partial melting of lower-crustal, sulphide-rich hydrous cumulates related to previous subduction-related magmatism, with or without minor contributions of mantle-derived potassic magmas. In this study we compiled 439 whole-rock major- and trace-element data and 265 whole-rock Sr-Nd-Pb isotopic data of potassic porphyry intrusions and volcanic rocks from the Sanjiang metallogenic belt (27–37 Ma) that formed during the Indian-Asian continent collision (Fig. 3.2-23a). Combined with detailed petrographic studies on these rocks and Laser-Ablation Inductively-Coupled-Plasma Mass-Spectrometry trace-element analysis of melt inclusions and coexisting magmatic minerals, we demonstrate that the post-collisional porphyry magmas formed solely by fractionation of lithospheric mantle-derived potassic mafic magmas.

Potassic mafic rocks (≤55 wt. % SiO_2) in the Sanjiang region show high abundances of large ion lithophile elements and a negative Nb-Ta anomaly, which suggest that these magmas were

derived from a lithospheric mantle source modified by slab fluids ± melts of previous subduction events. From southwest to northeast, the mafic rocks display conspicuous trends in Sr-Nd-Pb isotopes and fluid-immobile, incompatible trace elements (Figs. 3.2-23, 3.2-24a-c). The variable radiogenic isotopes likely reflect mantle heterogeneity, whereas the increasing La/Yb ratios and increasing La and Th concentrations can be explained by decreasing maximal degrees of mantle partial melting. Importantly, the isotopic and trace-element compositions of the evolved rocks (> 55 wt. % SiO_2), including the ore-forming porphyry intrusions (65–72 wt. % SiO_2), show a strong inheritance from the potassic mafic rocks (Figs. 3.2-23b-d, 3.2-24d-i). With increasing magma SiO_2 content in individual magma systems the La/Yb ratios remain almost constant, La concentrations start to decrease from ~ 60 wt. % SiO_2, and Th concentrations increase until ~ 70 wt. % SiO_2 and then strongly decrease. These trends are consistent with the typical mineral crystallization sequence of the potassic magmatic systems, *i.e.*, early crystallization of clinopyroxene and phlogopite/biotite, joined by apatite at ~ 60 wt. % SiO_2, and by titanite at ~ 70 wt. % SiO_2. The combined evidence suggests that the post-collisional, ore-forming magmas in the Sanjiang region formed through fractionation of mafic potassium-rich magmas without significant involvement of crustal rocks.

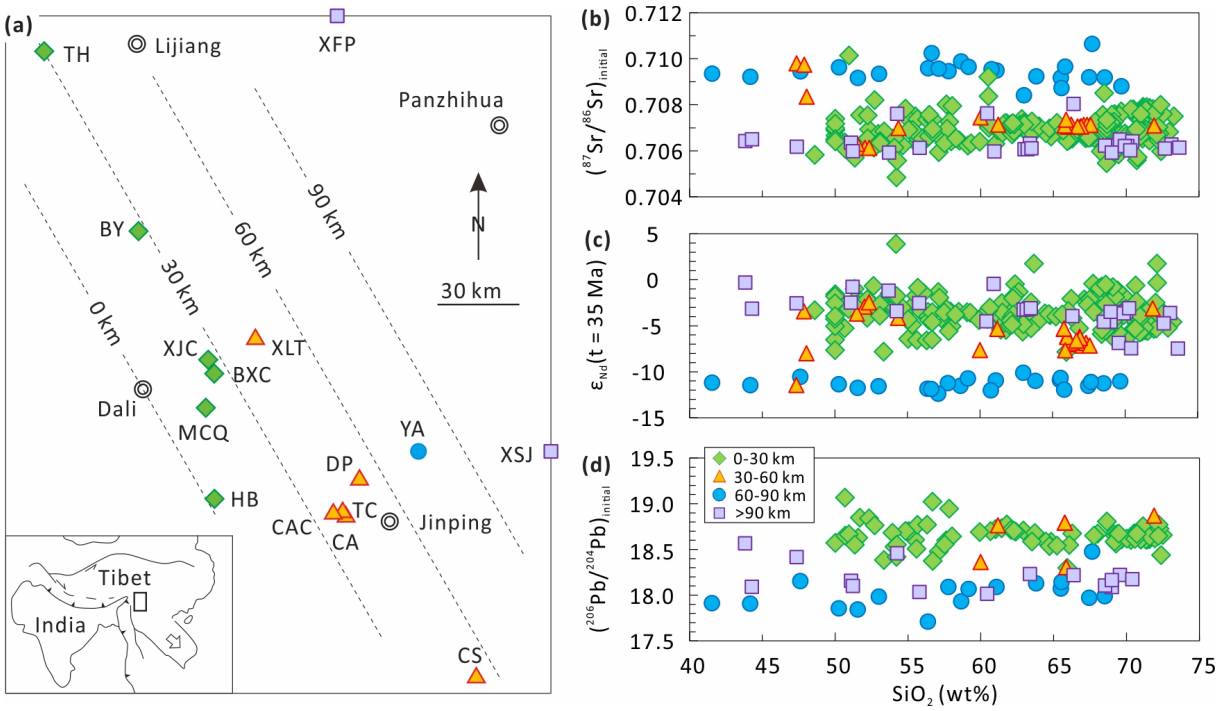

Fig. 3.2-23: (a) A reconstructed distribution of ore-forming magmatic systems in the Sanjiang region in the Yunnan and Sichuan provinces before late-kinematic faulting. The km values refer to the distance from the Indian–Asian continental collision front, and the zonal distribution is consistent with the movement direction of the Indian continent, the orientation of the lithosphere domain that was thinned to a thickness of ≤80–100 km, and the gradual decreasing emplacement age of the magmatic rocks. (b)-(d) Sr-Nd-Pb isotopic compositions of variously evolved magmatic rocks in the individual zones. Notice that the isotopic signatures remain constant over the entire magma evolution.

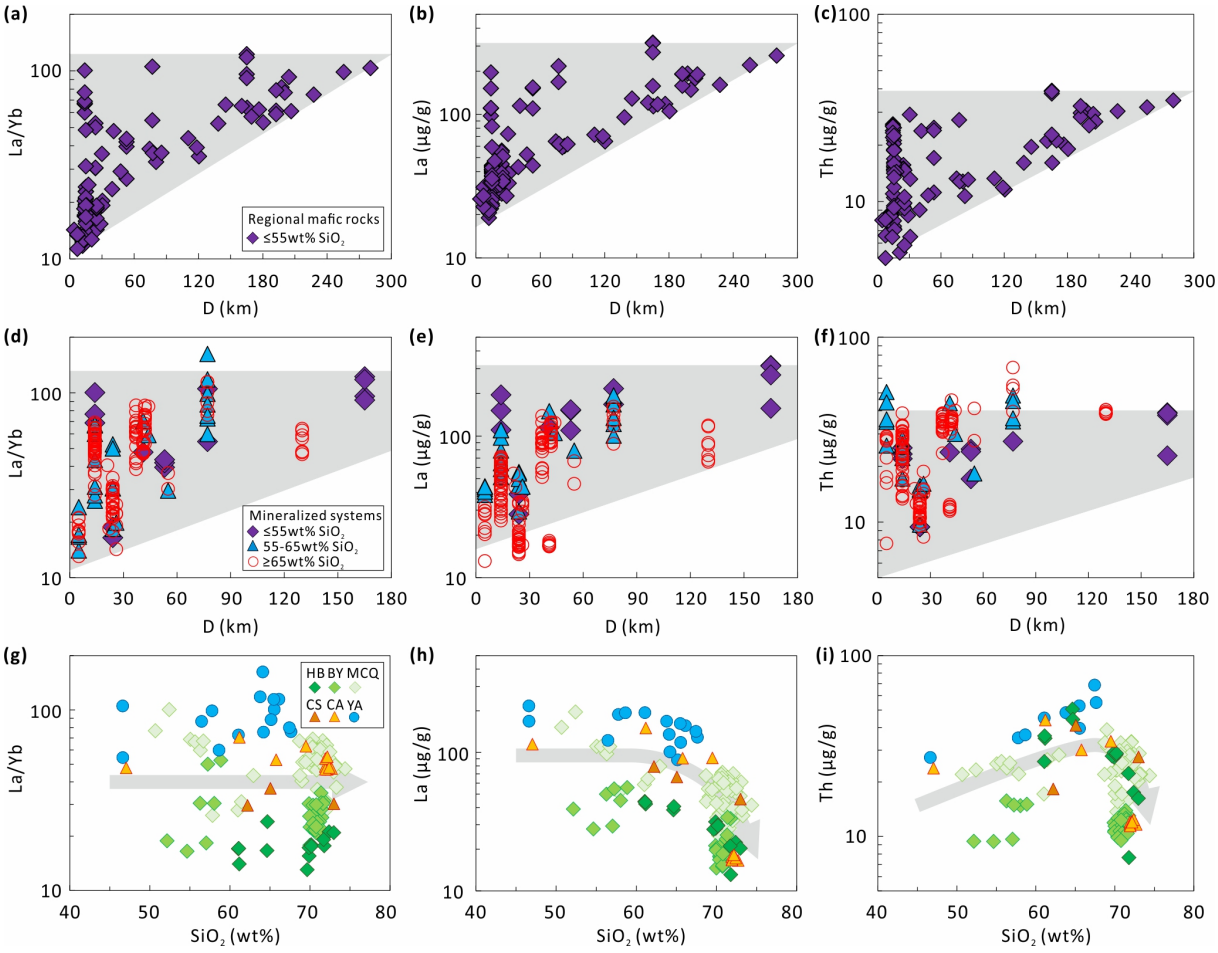

Fig. 3.2-24: La/Yb ratio, La and Th concentrations as a function of the distance to the Indian–Asian continental collision front or the SiO_2 content. The grey-shaded areas in (a)-(f) highlight that at each distance the degree of partial melting can vary, but the maximal degree of partial melting decreases consistently with increasing distance from the collision front. The trends with increasing SiO_2 content can be explained by variable starting values in the mafic precursor magmas and by the crystallizing mineral sequence during magma evolution.

3.3 Mineralogy, Crystal Chemistry and Phase Transformations

Earth's constituents change as they transform with increasing pressure and temperature throughout Earth's cross section. Research at the Bayerisches Geoinstitut employs both experimental and theoretical approaches based on knowledge of mineralogy and materials science to better understand Earth's interior. This section describes nine research projects at the intersection of mineralogy and changes to structure and crystal chemistry at extreme conditions.

The first three contributions address stabilities and transformations of iron-bearing phases at high pressure and high temperature using synchrotron X-ray diffraction techniques. Phase relations of the olivine-ahrensite (iron-rich ringwoodite) transition in the system $(Mg,Fe)_2SiO_4$ were determined using multianvil techniques to allow more precise estimation of shock metamorphic conditions in iron-rich meteorites. The structural diversity of magnetite and its decomposition products were investigated in single-crystal diamond anvil cell experiments that revealed formation of ferric-rich Fe-O compounds, arguing for an important role of magnetite in the deep oxygen cycle. Phase relations of a simplified MORB composition investigated by multianvil experiments demonstrate the effect of oxygen fugacity on the stability of hydrous phases in lower mantle assemblages.

The next four contributions focus on phases containing aluminium in Earth's mantle. Calculations of hydrogen in δ-AlOOH combined with high-pressure NMR measurements found no evidence of tunnelling-induced proton disorder, which has implications for hydrogen transport to the lower mantle. Synthesis of high-quality single crystals of the aluminium-rich calcium ferrite phase using a multianvil press improves possibilities to determine physical and chemical properties of subducted basaltic and continental crust at lower mantle conditions. Investigation of bridgmanite in the system $MgSiO_3$-$MgAl_2O_4$-Al_2O_3 using a multianvil press showed the presence of significant oxygen vacancies that can affect mantle viscosity and explain slab stagnation in the lower mantle. New results on the solubility of alumina in MgO at high pressure show the dramatic effect of temperature with application to temperature mapping of multianvil assemblages and a geothermometer for ferropericlase inclusions in diamonds.

The final two contributions describe how transmission electron microscopy can be used to ascertain the origin and evolution of both terrestrial and extraterrestrial materials. The pseudo-kinematical diffraction intensities of omphacite, measured using precession electron diffraction in the TEM, enabled an evaluation of cation ordering in omphacite at the sub-micrometre scale, providing constraints on the thermal history of metamorphic rocks. Spectral and mineralogical analysis performed on naturally-heated carbonaceous chondrites clarified the relationship between spectral and mineralogical properties affected by heating. These can be used to interpret planetary surface composition by remote-sensing observations using ground-based or airborne/space telescopes or spacecraft missions.

a. *Determination of the phase relations of the olivine-ahrensite transition in the system $(Mg,Fe)_2SiO_4$ at 1700 K using modern multianvil techniques (A. Chanyshev, D. Bondar, H. Fei, N. Purevjav, T. Ishii and K. Nishida; S. Bhat and R. Farla/Hamburg; T. Katsura)*

High-pressure studies of iron-rich olivine polymorphs are important for planetary sciences and meteoritics, since these minerals are the main constituents of terrestrial planetary interiors and shocked meteorites. Iron-rich olivine transforms to a high-pressure polymorph with spinel structure, named ahrensite, at 7-13 GPa. As previously determined, the olivine-ahrensite transition forms a binary loop. Determination of olivine-ahrensite phase relations is valuable also for high-pressure technology. When olivine solid solutions are loaded into a sample chamber to produce coexisting olivine and ahrensite, the sample pressure can be estimated by measuring the Mg# of coexisting phases in the run product based on the phase diagram. Previously the olivine-ahrensite binary loop was observed at 7-13 GPa and 1473-1837 K, but determination of the precise pressure in the experimental studies was difficult.

We determined the binary loop of the olivine-ahrensite transition in the system $(Mg,Fe)_2SiO_4$ at 1740 K in the range 7.5(1) to 11.2(1) GPa using multianvil apparatus and *in situ* X-ray diffraction, compositional analysis of quenched run products using an electron microprobe, and thermochemical calculation (Fig. 3.3-1). High-pressure experiments were conducted using the 3×5-MN six-axis multianvil press (Aster-15) on beamline P61B at DESY in Hamburg.

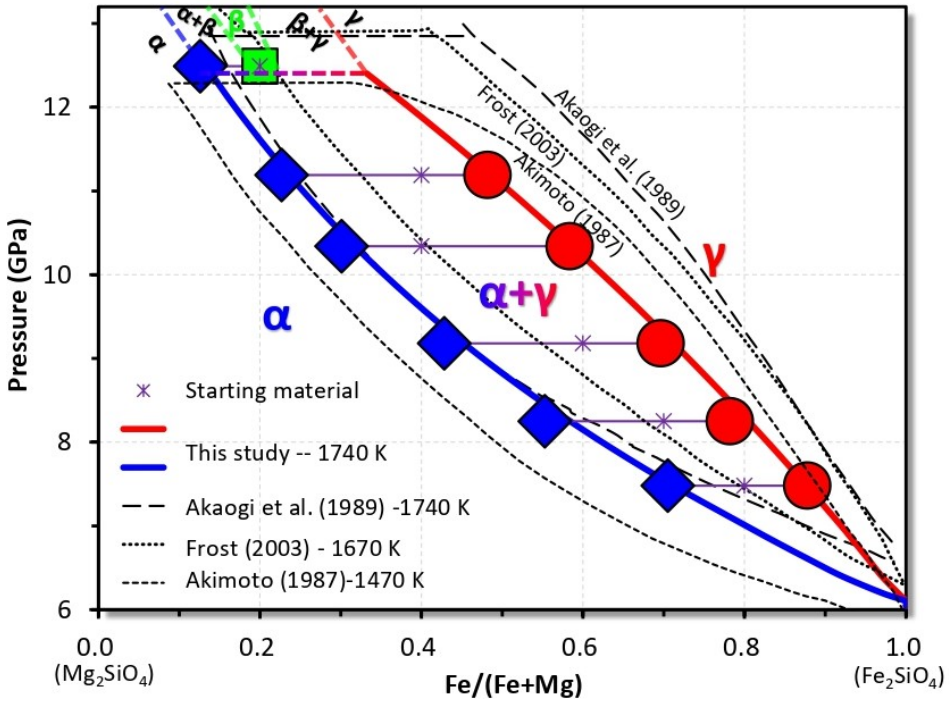

Fig. 3.3-1: Comparison of olivine-ahrensite loops determined in our study with previous data [Akaogi *et al.*, JGR 94,15671-15685, 1989; Frost, EPSL 216, 313-328, 2003; Akimoto, *High-Pressure Research in Geophysics*, 1-13, 1987]. The blue, red and green symbols are the compositions from electron microprobe analysis of olivine, ahrensite and wadsleyite, respectively. α: olivine, γ: ahrensite, β: wadsleyite.

Since olivine and ahrensite (ringwoodite) are common minerals in shocked meteorites, it is expected that shock pressures and temperatures can be estimated using the compositions of coexisting minerals based on the phase diagram of olivine-ahrensite. We estimated shock conditions of L6-type chondrites Asuka-09584 and Château-Renard based on our experimental results to be 1550 K / 11.9 GPa and 1650 K / 11.6 GPa, respectively. These values do not indicate peak shock conditions, because both meteorites contain higher pressure phases, such as bridgmanite and maskelynite. These meteorites would have experienced complex pressure-temperature (P-T) paths after passing the peak pressure, and more detailed estimates are necessary to reconstruct their P-T paths.

b. *Structural diversity of magnetite and products of its decomposition at extreme conditions (S. Khandarkhaeva, T. Fedotenko, E. Bykova, S.V. Ovsyannikov, N.A. Dubrovinskaia/ Bayreuth and L.S. Dubrovinsky; K. Glazyrin and H.-P. Liermann/Hamburg; S. Chariton and V.B. Prakapenka/Chicago)*

Magnetite, Fe_3O_4, is the oldest known magnetic mineral and archetypal mixed-valence oxide. At ambient conditions, magnetite adopts an inverse spinel structure (Fig. 3.3-2a) with Fe^{3+} ions in tetrahedral sites and a mixture of Fe^{3+} and Fe^{2+} ions in equal proportion in sites with octahedral oxygen coordination (Fig. 3.3-2a). Due to its importance in geoscience, Fe_3O_4 has been extensively investigated at high pressure. On compression to ~ 25 GPa at room temperature, magnetite (designated here as α-Fe_3O_4) undergoes a structural phase transition to a "post-spinel phase" (sometimes called "HP-Fe_3O_4", which we designate as β-Fe_3O_4) (Fig. 3.3-2b). This transition is associated with significant changes in magnetic and electrical properties. Kinetics of the phase transition strongly depend on temperature. The history over decades of structural studies of β-Fe_3O_4 has been highly controversial, with the current general consensus being that this phase adopts a $CaTi_2O_4$-type structure. However another phase transformation of β-Fe_3O_4 upon laser heating (between approximately 1500 to 2000 K) at 64 to 73 GPa was reported. Powder diffraction data were interpreted as formation of an orthorhombic phase with a $CaFe_2O_4$-type structure. However, assignment of the space group and interpretation of diffraction data remain ambiguous.

Here we report single-crystal synchrotron X-ray diffraction experiments up to ~ 80 GPa and 5000 K in diamond anvil cells. Results reveal two previously unknown Fe_3O_4 polymorphs: γ-Fe_3O_4 (Fig. 3.3-2c) with an orthorhombic Yb_3S_4-type structure (space group *Pnma*, a = 8.574(10) Å, b = 2.6356(13) Å, c =8.761(3) Å at 78(1) GPa,) and δ-Fe_3O_4 (Fig. 3.3-2d) with a modified Th_3P_4-type structure (space group $I\bar{4}2d$ a = 5.8648(1) Å, c = 5.948(2) at 78(1) GPa). The latter has never been predicted for iron compounds. We also found that Fe_3O_4, pressurised above ~ 75 GPa and heated above ~ 2000 K becomes chemically unstable and undergoes a series of self-redox or decomposition reactions. Among the chemical products of these processes are pure *hcp* Fe and two exotic iron oxides with unusual crystal structures: Fe_5O_7

(Fig. 3.3-2e) and $Fe_{25}O_{32}$ (Fig. 3.3-2f). Available single-crystal X-ray diffraction data allowed us to perform a complex analysis of the compressional curves of different iron oxide phases and determine volume variations for many Fe-O polyhedra. We conclude that ferrous iron in prismatic oxygen environments in iron oxides does not undergo spin crossover up to at least 80 GPa, and ferric iron in oxygen coordinated octahedra transforms from the high to the low spin state above ~ 45 GPa when $Fe^{3+}/\Sigma Fe \geq 2/3$. Interestingly, octahedral volumes in Fe_5O_7 are larger than predicted for pure Fe^{3+}, indicating partial charge transfer between iron atoms in prismatic and octahedral sites. Our experiments demonstrate that high-pressure/high-temperature conditions promote the formation of ferric-rich Fe-O compounds, thus arguing for the possible involvement of magnetite in the deep oxygen cycle.

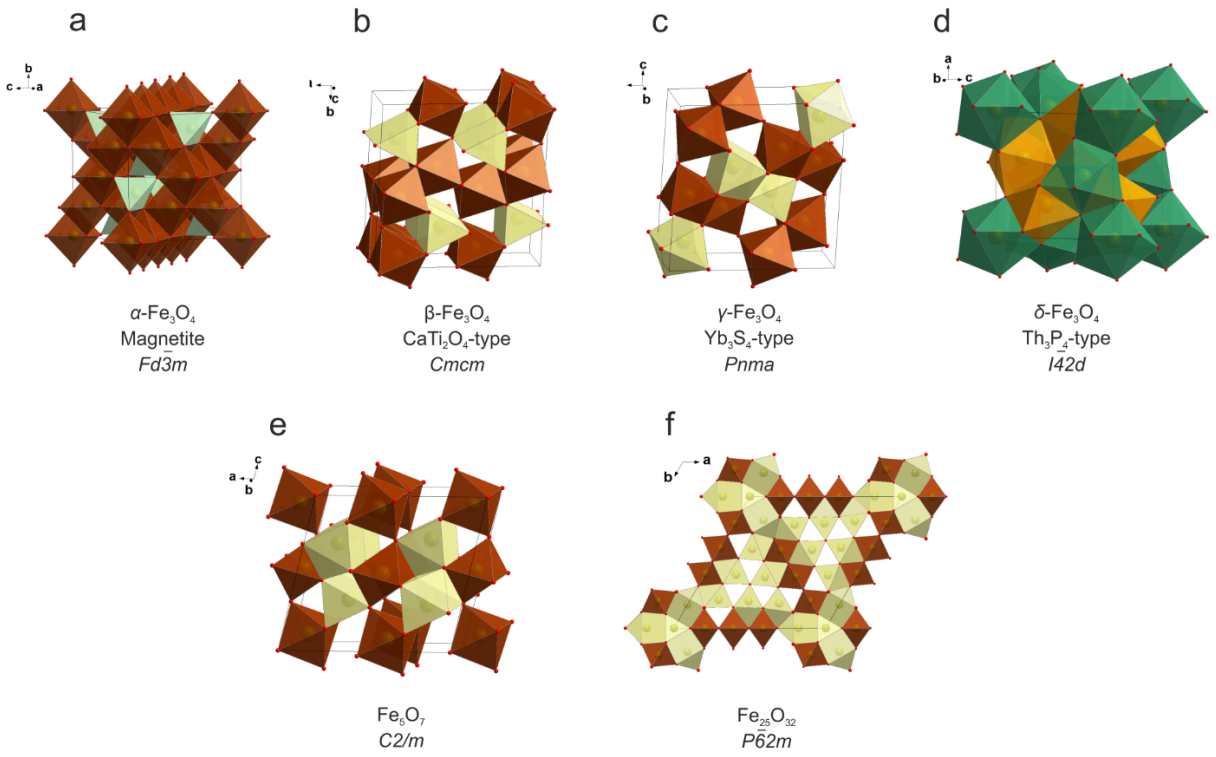

Fig. 3.3-2: Crystal structures of iron oxides observed in the present study. (a) α-Fe_3O_4, magnetite (inverse spinel structure, space group $Fd\bar{3}m$); (b) β-Fe_3O_4 ($CaTi_2O_4$-type, space group *Cmcm*); (c) γ-Fe_3O_4 (Yb_3S_4-type, space group *Pnma*); (d) δ-Fe_3O_4 (Th_3P_4-type, space group $I\bar{4}2d$) (e) Fe_5O_7; and (f) $Fe_{25}O_{32}$.

c. *Effect of oxygen fugacity on hydrous phase stability in a basaltic composition at 24-27 GPa (E.-M. Rogmann, G. Criniti, T. Boffa Ballaran and D.J. Frost)*

Even small amounts of water can significantly affect the physical properties of mantle rocks, such as their elasticity, rheology and melting temperature. The main mechanism by which water is delivered to the mantle is subduction of cold hydrated oceanic lithosphere, composed of a

thin basaltic layer at the top and a thicker harzburgitic layer underneath. The stability of hydrous phases in these two systems at high pressure and high temperature has therefore been studied extensively over the last decades. A recent study suggested that a continuous chain of stable hydrous phases in mid-ocean ridge basalt (MORB) along a subduction geotherm could enable the transport of water down to Earth's lower mantle. However, the specific hydrous phases that are stable at lower mantle pressures is still the subject of debate, as well as the effect of oxygen fugacity (f_{O_2}) on phase relations of hydrous MORB.

Here we report phase relations of a simplified MORB composition investigated by multianvil experiments at 24-27 GPa and 1200-1400 °C. The powdered starting material was packed either in a Pt tube or in double Fe foil and Pt-tube capsules to attain different f_{O_2} conditions. Ir metal was added in order to use the Fe activity in (Ir,Fe) alloy to measure oxygen fugacity within sample capsules at the synthesis conditions. The recovered phase assemblages were characterised using scanning electron microscopy, electron probe microanalysis and X-ray powder diffraction.

Bridgmanite, stishovite and a (Ir,Fe) alloy were present in all experimental run products. In experiments conducted at more oxidising conditions, water-bearing phases, observed as quenched melt and/or hydrous phases, were also present (Fig. 3.3-3). At more reducing conditions, ferropericlase and a Na-bearing phase were observed, but no water-bearing phases were identified. The formation of a Na-rich anhydrous phase in these runs is likely the result of H-loss through the capsule walls. Regarding hydrous phase stability, phase Egg was found to be stable to at least 27 GPa and 1300 °C, exceeding the pressure range where it was reported in previous experimental studies and coexisting with δ-AlOOH containing a significant amount of phase H ($MgSiO_2(OH)_2$) and ε-FeOOH. The presence of melt together with hydrous phases in some experimental runs suggests that our experiments were performed at water-saturated conditions.

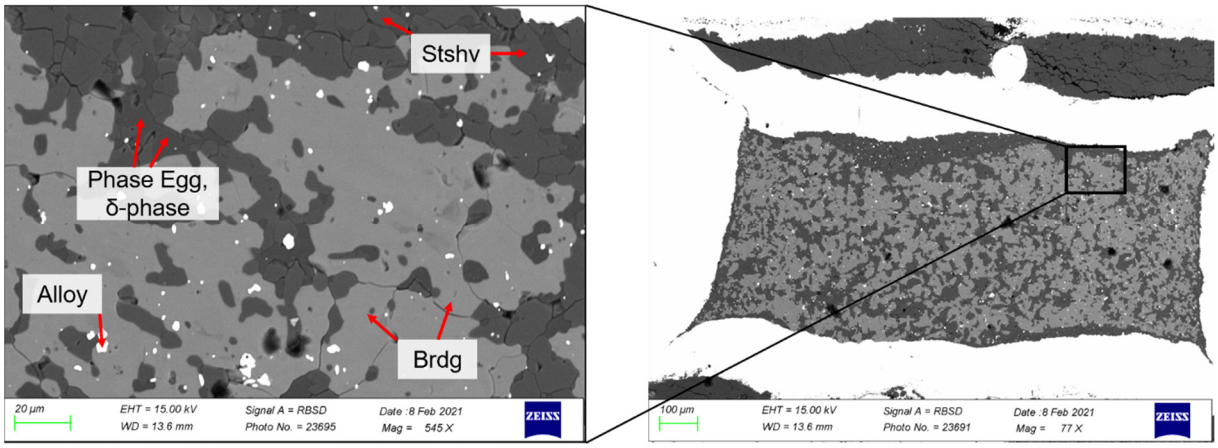

Fig. 3.3-3: Backscattered electron images of the run products of experiment I1156 conducted at 27 GPa and 1300 °C with a Pt capsule. The recovered phases are phase Egg, δ-phase, bridgmanite (Brdg), stishovite (Stshv) and a (Fe,Ir) alloy.

Among nominally anhydrous phases, stishovite was found to incorporate significant amounts of Al, whose concentration increased with increasing pressure as well as temperature. For bridgmanite, an increase in both Al and Fe content with temperature was observed, while no pressure dependence was identified over the experimental pressure range. For the Na-bearing phase, variations in composition were observed, although no distinct trend could be identified. Based on the (Ir,Fe) alloy composition, experiments conducted using an inner Fe foil within an outer Pt capsule capsule exhibited f_{O_2} values approximately one log unit more reducing than those conducted at the same conditions using only a Pt capsule. For the run products, oxygen fugacities ranging from IW+2.9 to IW+1.0 were calculated, which are slightly more oxidised than what is expected for Earth's lower mantle.

d. *Absence of proton tunnelling in δ-AlOOH (F. Trybel, T. Meier, B. Wang and G. Steinle-Neumann)*

Hydrogen is an important chemical component in Earth's mantle, as even a small amount can strongly affect key properties of minerals such as melting temperature, rheology, electrical conductivity and atomic diffusion. Over the past 20 years, many hydrous minerals such as dense hydrous magnesium silicates have therefore been synthesised at high pressure (P) and high temperature (T) and investigated as potential candidates for hydrogen transport to the lower mantle. One candidate is δ-AlOOH which crystallises in a primitive orthorhombic lattice with space group $P2_1nm$ at ambient conditions with two distinct oxygen positions (O1 and O2). With increasing compression, hydrogen-bond symmetrisation as well as a phase transition to the *Pnnm* space group take place, where O1 and O2 positions become equivalent.

We investigated the phase transition, hydrogen bond symmetrisation (central uni-modal proton distribution between two respective oxygen atoms) and the possibility of proton tunnelling in δ-AlOOH by combining density functional theory-based calculations (Fig. 3.3-4a) and high- (Fig. 3.3-4b) and low-field (Fig. 3.3-4c) high-P nuclear magnetic resonance (NMR) spectroscopy.

We performed a stepwise computational optimisation of the host lattice and hydrogen positions over a wide volume range and analysed the potential seen by hydrogen atoms as well as the geometry of AlO_6 octahedra. We displaced hydrogen atoms along the diagonal oxygen-oxygen direction and constructed a proton potential by spline interpolating the energy difference as a function of the displacement of hydrogen atoms at each sampled volume. We found an asymmetric potential showing decreasing asymmetry with increasing compression (Fig. 3.3-4a). A fully symmetric state was found for $P > 14.7 \pm 0.4$ GPa. In contrast to prior suggestions, we did not find any evidence of double-well character (Fig. 3.3-4a), even though calculating the potential from Kohn-Sham density functional theory should strongly overestimate barriers without further consideration of the quantum nature of hydrogen atoms.

We searched for characteristic features of a phase transition by analysing the signal shift of Lee-Goldburg (LG) NMR spectra. LG-decoupling reduced the line width to ~ 1.5 ppm (Fig. 3.3-4b) and therefore enabled analysis of chemical shifts on the order of ~ 10 ppm (Fig. 3.3-4c), and the full width at half maximum (FWHM) of ^{1}H solid echoed at 1045 mT and up to 40 GPa. We found an abrupt jump in the chemical shift at 9.9 ± 0.6 GPa, indicating a structural change in the chemical environment of hydrogen atoms as expected for a phase transition. Over the full pressure range, we found a single proton signal indicating a unique, geometrically well-defined proton position. The ^{1}H-NMR solid echoes showed a minimum in line width at 12.7 ± 0.4 GPa (Fig. 3.3-4e), indicating a change in proton mobility.

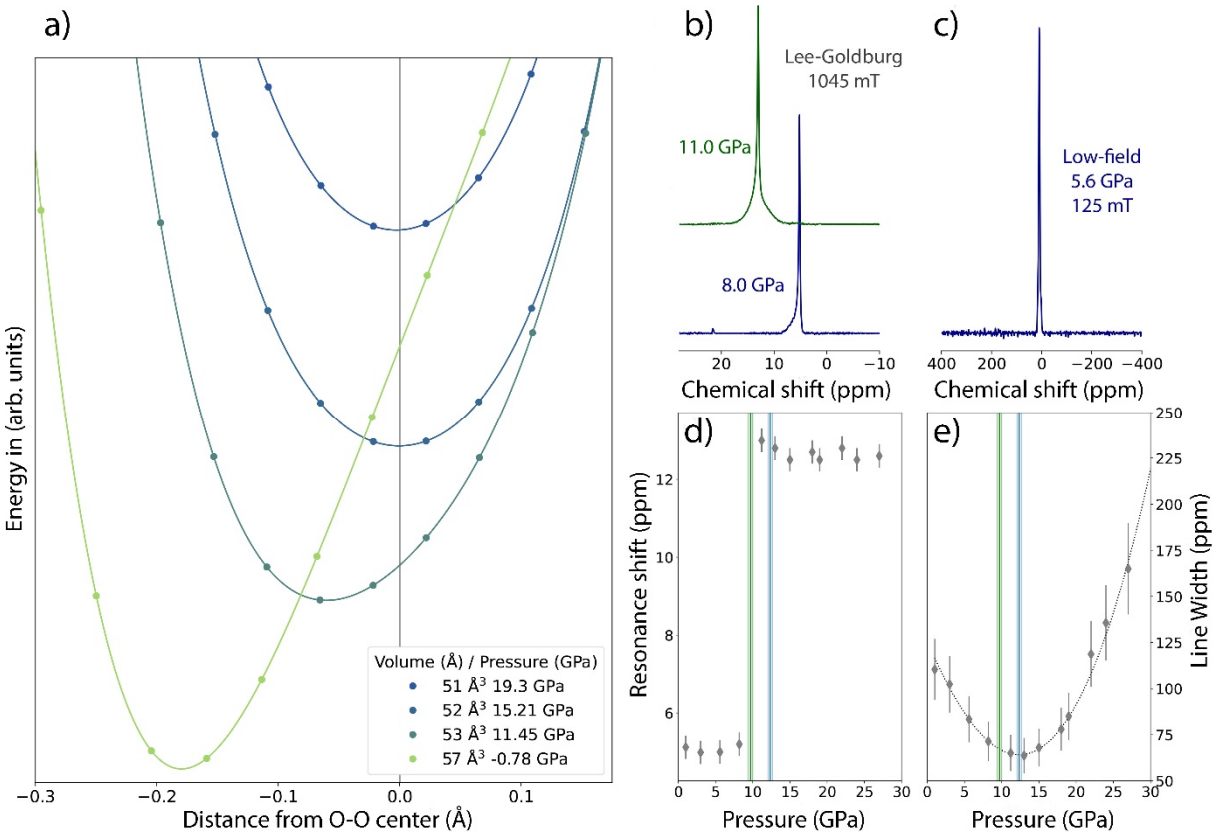

Fig. 3.3-4: (a) Calculated proton potentials as a function of the distance from the O-O centre (indicated by the grey vertical line) for different unit cell volumes/pressures. (b) Exemplary high-field NMR spectra using Lee-Goldburg decoupling at 8 and 11 GPa at a field of 1045 mT. (c) Low-field measurement at 5.6 GPa at a field of 125 mT. (d) Chemical shift and (e) FWHM values as a function of pressure. In panels (d) and (e) the jump in the shift and the minimum in FWHM are indicated by the green and blue lines, respectively.

Proton tunnelling should lead to zero-field splitting accompanied by detectable tunnelling side bands. In earlier work on the ice-VII to ice-X transition in high-pressure H_2O, we showed that such tunnelling side bands can be resolved using low-field NMR. We therefore employed the same low-field setup at 5.6 GPa (Fig. 3.3-4c) and found no indication for tunnelling sidebands

in δ-AlOOH, in agreement with the pressure evolution of calculated potentials, showing no double-well character over the respective compression range.

Comparing our results to recently published experiments and computations, we matched the phase transition at ~ 10 GPa measured via neutron and X-ray diffraction to results from NMR experiments and the calculations. We reproduced hydrogen bond symmetrisation estimates from earlier calculations based on an analysis of elastic constants at ~ 15 GPa in our potential analysis. The absence of a double well in our mapping of the hydrogen potential at any volume, accompanied by the absence of tunnelling side bands in low-field NMR measurements, suggests that, in contrast to the ice-VII to ice-X transition, there is no tunnelling-induced proton disorder in δ-AlOOH.

e. *Synthesis and characterisation of basaltic calcium ferrite single crystals (T. Ishii/Beijing, G. Criniti and T. Boffa Ballaran)*

The aluminium-rich calcium ferrite (CF) phase is abundant in stable assemblages formed from subducted basaltic and continental crust and sedimentary rock at lower mantle conditions. Its chemical composition is typically expressed as $NaAlSiO_4$-$(Mg,Fe^{2+})(Al,Fe^{3+})_2O_4$-$(Mg,Fe^{2+})_2SiO_4$ solid solution. Physical and chemical properties of the CF phase are essential for understanding lower mantle structure and dynamics; however, studies are limited. We have therefore synthesised single crystals of CF phase using a multianvil press and characterised their crystal chemistry by single crystal X-ray diffraction, electron microprobe, and Mössbauer spectroscopy.

High-pressure experiments were conducted at 23 GPa and 2000-2200 °C with a 1200-ton Kawi-type multianvil press installed at Bayerisches Geoinstitut. Starting materials were synthetic oxide powders with three different compositions: $NaAlSiO_4$, 80 $NaAlSiO_4$-20 $MgAl_2O_4$, and 70 $NaAlSiO_4$-20 $MgAl_2O_4$-10 Fe_3O_4. We obtained single crystals of calcium ferrite phases with 100-200 micron grain size (Fig. 3.3-5). Mossbauer spectroscopy of recovered Fe-bearing crystals from two batches showed $Fe^{3+}/\Sigma Fe$ ratios ranging from 0.34(1) to 0.47(1). By combining Mössbauer data and chemical compositions determined by electron microprobe analysis, CF phases can be described in terms of their end-members. Mg,Fe-free CF shows 98 % $NaAlSiO_4$ and 2 % $Al_{8/3}O_4$ component, which has been previously reported in other CF phases at very high temperature. Mg-bearing Fe-free CF phase has an average composition of 79 % $NaAlSiO_4$ and 21 % $MgAl_2O_4$. Mg,Fe-bearing CF phase can be expressed as 62-67 % $NaAlSiO_4$, 25-34 % $(Mg,Fe^{2+})(Al,Fe^{3+})_2O_4$, 0-6 % $Al_{8/3}O_4$ and traces of $(Mg,Fe^{2+})_2SiO_4$. The compositions of recovered Mg,Fe-bearing CF crystals are similar to those of basaltic calcium ferrite phase previously reported in phase relation studies with regard to both composition and oxidation state of Fe. Physical property measurements such as sound velocity and thermal conductivity of CF single crystals synthesised in this study can thus provide new insights into the nature of chemical heterogeneities in the lower mantle, as well as their effect on lower mantle structure and dynamics.

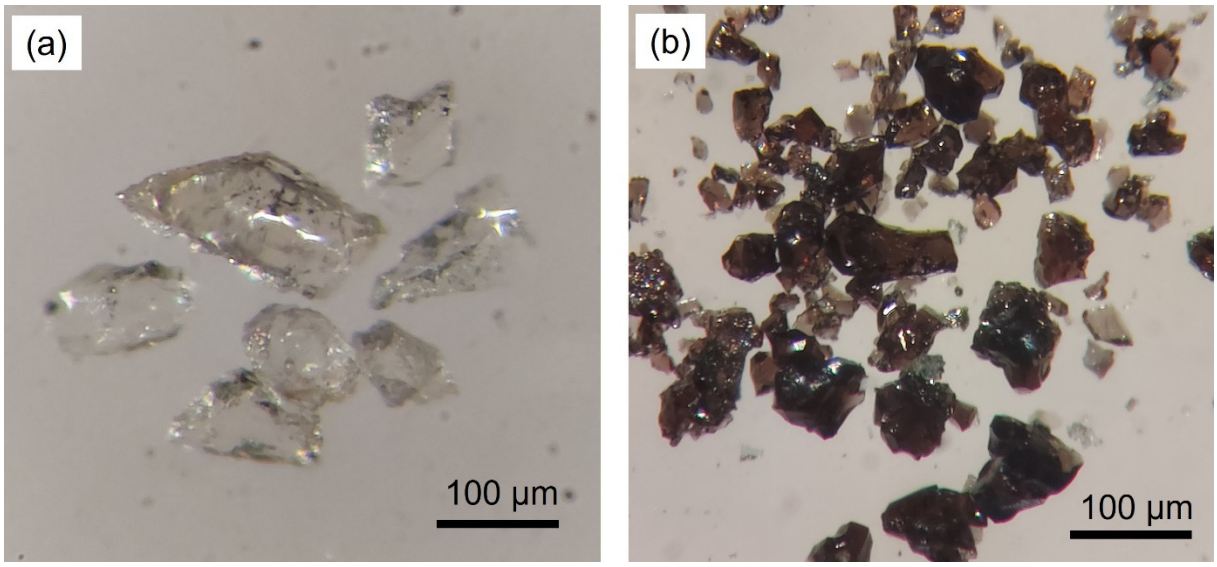

Fig. 3.3-5: Optical photomicrographs of single crystals of calcium ferrite phase with compositions of (a) $NaAlSiO_4$, and (b) $NaAlSiO_4$-$(Mg,Fe^{2+})(Al,Fe^{3+})_2O_4$.

f. *Effect of temperature on aluminium components in bridgmanite coexisting with corundum and CF phase (L. Wang, Z. Liu/Changchun, S. Koizumi/Tokyo, T. Boffa Ballaran and T. Katsura)*

Bridgmanite, the most abundant mineral in Earth's mantle, can accommodate aluminium (Al) into its structure via formation of charge-coupled (CC) and oxygen-vacancy (OV) components as $AlAlO_3$ and $MgAlO_{2.5}$, respectively. The OV and CC contents in bridgmanite are controlled by the MgO and Al_2O_3 activities of the system. Coexistence of bridgmanite with periclase and corundum maximizes the OV and CC components, respectively. In an intermediate composition where bridgmanite coexists with periclase and CF phase, the OV and CC components in bridgmanite change only slightly with temperature. Between phase regions with corundum only and with periclase and CF phase, there is a region where bridgmanite coexists with CF phase and corundum. Knowledge of the compositional variation of bridgmanite in this region as a function of pressure and temperature is important for a comprehensive understanding of bridgmanite chemistry. Also, this assemblage could be present when crustal rocks with high Al_2O_3 content are subducted into the lower mantle. Therefore, we investigated phase relations in the system $MgSiO_3$-$MgAl_2O_4$-Al_2O_3 at 27 GPa and 2000-2600 K using a multianvil apparatus.

Our results show that the CC component concentration in bridgmanite increases from 8.6 to 20.0 mol. % with increasing temperature from 2000 to 2600 K, while the OV component concentration remains nearly constant, *i.e.*, 3-4 mol. %, at these temperatures (Fig. 3.3-6, upper). The presence of an additional Al-bearing phase therefore suppresses oxygen vacancy substitution for Al^{3+} in bridgmanite. In contrast, significant amounts of the $Al_{8/3}O_4$ component can be dissolved into calcium-ferrite type $MgAl_2O_4$-Mg_2SiO_4-$Al_{8/3}O_4$ phase (CF phase), implying that the CF phase likely contains some amount of vacancies (Fig. 3.3-6, lower).

Combined with previous studies, we conclude that when Al per formula unit (pfu) exceeds 0.12 in bridgmanite, the abundance of $MgAlO_{2.5}$ component remains nearly constant, and the $AlAlO_3$ component becomes dominant (Fig. 3.3-7).

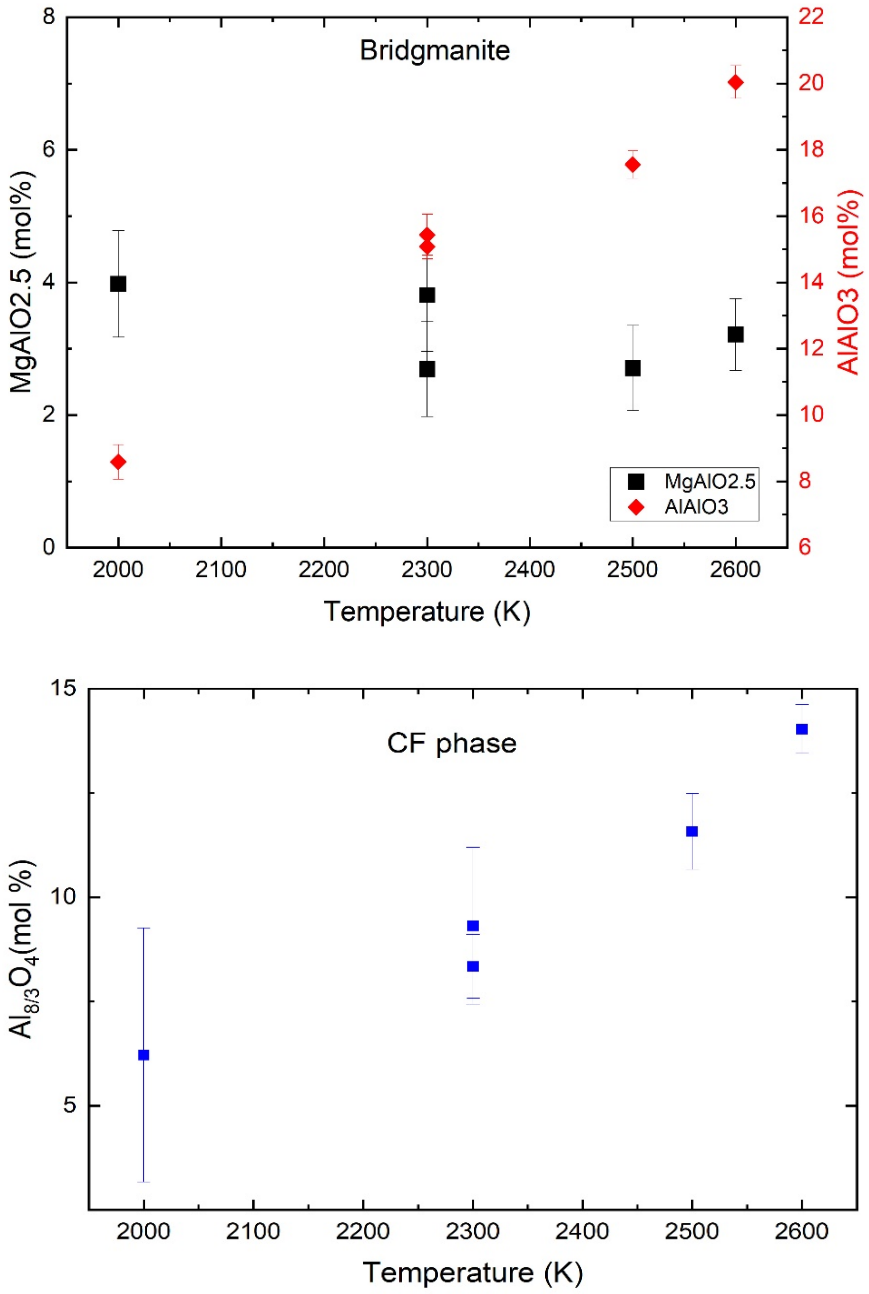

Fig. 3.3-6: Upper: oxygen vacancy ($MgAlO_{2.5}$) and charge coupled ($AlAlO_3$) component concentrations in bridgmanite at 27 GPa and different temperatures. Lower: $Al_{8/3}O_4$ concentration in CF phases at 27 GPa and different temperatures.

Bridgmanite coexists with the CF phase in subducting slabs. Since bridgmanite could contain up to 4 mol. % OV component, our results suggest that bridgmanite could transport a certain amount of volatiles such as water and noble gases into the lower mantle. In addition, because

the OV content in bridgmanite coexisting with the CF phase is lower than that in bridgmanite coexisting with periclase, the viscosity of bridgmanite in slabs could be higher than that of the surrounding mantle under the assumption that the viscosity of bridgmanite decreases with OV content. This behaviour can therefore explain slab stagnation in the lower mantle.

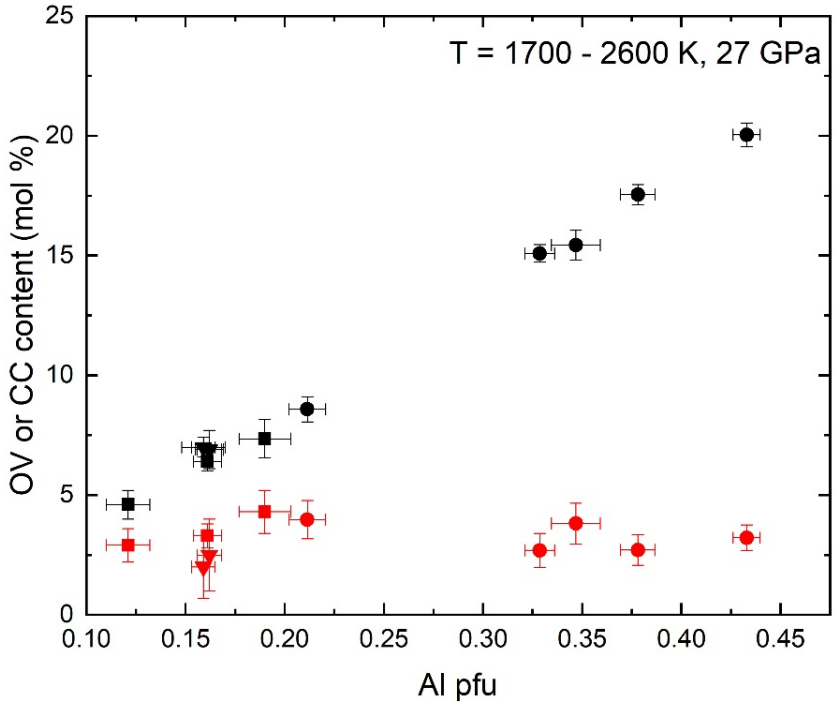

Fig. 3.3-7: Effect of Al content (pfu) of bridgmanite on oxygen vacancy (OV, red circles) and charge coupled (CC, black circles) component contents in bridgmanite coexisting with an additional Al-bearing phase. Squares [Liu *et al.*, EPSL 505, 141, 2019] and triangles [Liu *et al.*, EPSL 523, 11567, 2019] indicate bridgmanite coexisting with CF phase and periclase.

g. *Solubility of alumina in periclase at high pressure and high temperature (L. Man, E.J. Kim, A. Néri, H. Fei and D.J. Frost)*

MgO and Al_2O_3 are major components in the silicate Earth as well as important refractory ceramic materials. At ambient pressure Al_2O_3 and MgO form $MgAl_2O_4$ spinel, but coexisting halide-structured periclase also forms a solid solution with Al_2O_3, the extent of which depends on temperature. The solid solution can be represented by the formula $(Mg^{2+}, Al^{3+}, Va^0)O$, where Va^0 is a vacancy. In the Al_2O_3 endmember of this halide-structured solid solution, Al^{3+} fills two-thirds of cation sites and the remaining one-third are vacant, which can be described as $(Al_{2/3}, Va_{1/3})O$. The MgO-$(Al_{2/3}, Va_{1/3})O$ solid solution in equilibrium with spinel has been investigated by several previous studies at ambient pressure, with results showing that the solubility of alumina in periclase is highly sensitive to temperature. Up to 18 wt. % Al_2O_3 can be dissolved into periclase at around 2000 °C, whereas the value is negligible below 1400 °C.

This behaviour can be potentially used as a thermometer for both high-pressure experiments and for inclusions of ferropericlase found in diamonds. However, there are no systematic studies on the pressure effects of alumina solubility in periclase, which prohibits practical applications.

In this study, we performed a series of experiments from 12 to 33 GPa and 1500 °C to 2350 °C using multianvil presses to investigate the solubility of alumina in periclase at high pressure. A mixture of MgO and Al_2O_3 powder with ~ 1 µm grain size was used as the starting material. A thin layer of the starting material (typically ~ 50 µm) was placed close to the hot junction of the thermocouple (TC) in every experiment to make sure the TC reading was as close as possible to the sample temperature. Another capsule was usually placed under the MgO-Al_2O_3 mixture for a separate purpose. The chemical compositions of the run products were quantified by electron microprobe analysis.

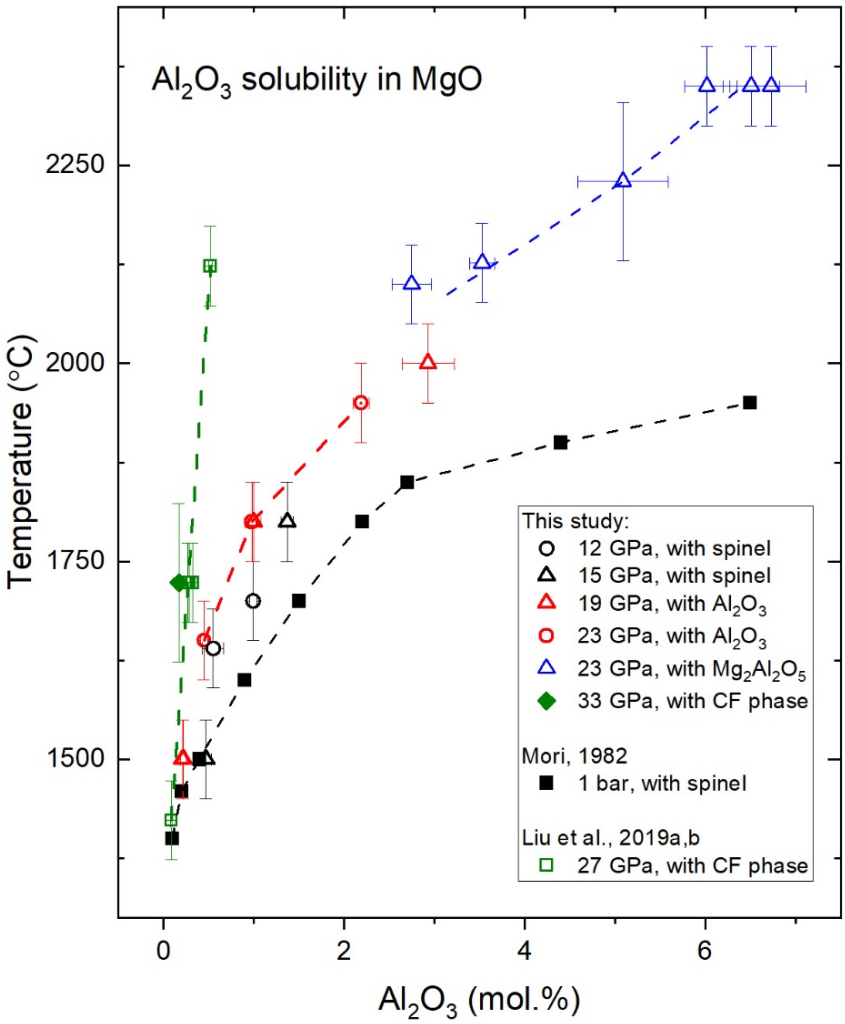

Fig. 3.3-8: Solubility of Al_2O_3 in periclase at high pressure. Periclase coexists with either $MgAl_2O_4$ spinel, $Mg_2Al_2O_5$ ludwigite, $MgAl_2O_4$ calcium ferrite phase, or corundum, depending on the pressure and temperature. Previous data from Mori [Yogyo-Kyokai-Shi, 90, 75-76, 1982]; Liu *et al.* [EPSL 505, 141-151, 2019a; EPSL 523, 115697, 2019b].

Relations between Al_2O_3 solubility, pressure and temperature, as well as coexisting phases are shown in Figure 3.3-8. The solubility of alumina in periclase is strongly controlled by coexisting phases, as the activity of Al_2O_3 differs among the MgO-Al_2O_3 phases stable at various P-T conditions ($Mg_2Al_2O_5$ ludwigite, $MgAl_2O_4$ calcium ferrite phase, Al_2O_3 corundum, and $MgAl_2O_4$ spinel). However, within the same phase stability region, the pressure effect is not pronounced. The P-T-solubility relation we calibrated here can be used to monitor the temperature in multianvil experiments. We filled the central part of a 10/4 assembly with MgO-Al_2O_3 mixture and heated it at 23 GPa (Fig. 3.3-9). We measured the spatial distribution of Al_2O_3 concentration in periclase in the recovered sample and then mapped the temperature field based on the P-T-solubility relation in Figure 3.3-8. The axial temperature gradient is around 120 °C/mm in the central region of the assembly in this experiment. Based on this method, one can determine the actual sample temperature from the thermocouple reading and estimated temperature distribution within the sample. In addition to applications in high-pressure experiments, our results could be used to constrain the thermal state of Earth's mantle by analysing the alumina concentration in ferropericlase inclusions found in diamonds from the deep mantle.

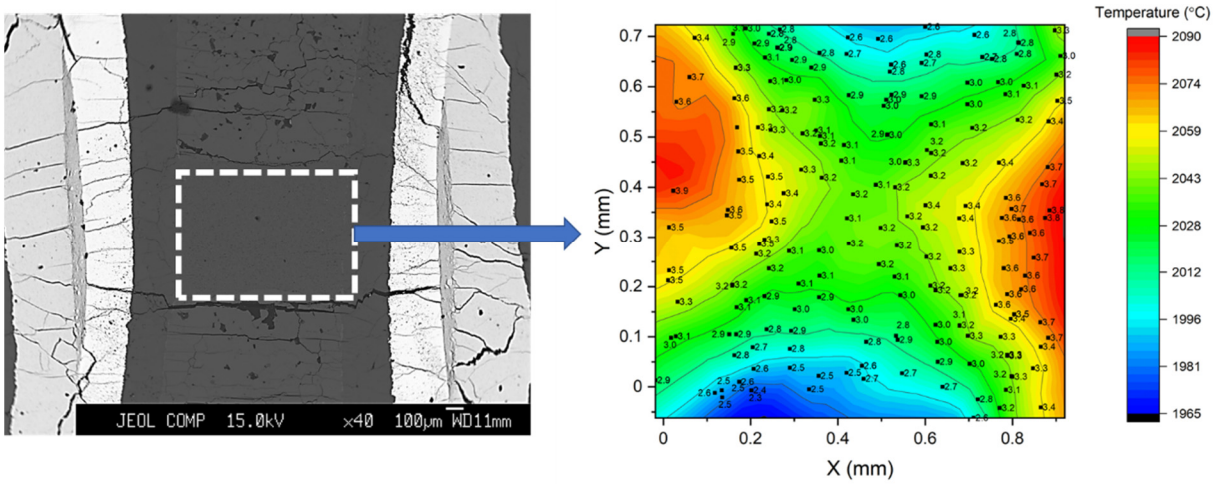

Fig. 3.3-9: Two-dimensional temperature map for 10/4 multianvil assembly at 23 GPa. The coexisting phases are Al_2O_3-bearing periclase and corundum. Values beside the black dots show the molar concentration of Al_2O_3 in periclase. Temperatures are determined from the concentration of Al_2O_3 in periclase based on its temperature dependence (Fig. 3.3-8).

h. *Diffraction intensities of ordered omphacite, measured from precession electron diffraction (N. Miyajima, L.M. Calvo and T. Boffa Ballaran)*

Cation ordering in minerals at high temperatures is important for understanding metamorphic processes in Earth's interior. Because ordering is controlled by cation diffusion exchange at high temperature, diffraction intensities of reflections related to cation ordering, which are often determined by single crystal X-ray diffraction, are indispensable parameters for evaluating the

degree of ordering. Symmetry decrease and intensities of new reflections that appear in the diffraction pattern are usually taken to be proportional to cation ordering. Omphacite, Na and Ca-rich clinopyroxene, is one of the major minerals in blueschist- and eclogite-facies metamorphic rocks, and also in metasomatic sodic pyroxene-rich rocks such as jadeitite and omphacitite. Omphacite at compositions around $(Na_{0.5},Ca_{0.5})(Al_{0.5},Mg_{0.5})Si_2O_6$ undergoes an ordering transition from *C2/c* to *P2/n* at about 865 °C, in which the degree of Mg, Al order on two alternate M1 sites is coupled to Ca, Na ordering on two alternate M2 sites to maintain local charge balance. The ordering temperature is higher than the crystallisation temperature of most metamorphic omphacites. However, almost all omphacites have antiphase domain microstructures, because crystals grow with metastable short-range order, and long-range order occurs after crystallisation with the development of antiphase domain microstructures. The size of regular equidimensional antiphase domains in omphacites shows a distinct trend such that their size increases with peak metamorphic temperature, due to the sluggishness of cation ordering of Na and Ca. The determination of diffraction intensities related to cation ordering in omphacite is, therefore, important for understanding kinetics of cation ordering in omphacite and its thermal history in metamorphic rocks.

Here we report the determination of diffraction intensities of an ordered omphacite using precession electron diffraction in a transmission electron microscope (TEM). An ordered omphacite (space group *P2/n*), which coexists with almandine, zoisite, rutile and phengite, was collected from a kyanite-free eclogite in the Münchberg Massif, North East Bavaria, Germany. The selected area electron diffraction (SAED) pattern of the omphacite was recorded on a CCD camera using precession mode of the TEM. The TEM thin foils were prepared with a conventional Ar-milling machine. Single crystal X-ray diffraction data of an omphacite on the same rock were also collected to characterise kinematical diffraction intensities. The chemical composition of single crystal omphacite was analysed using an electron microprobe.

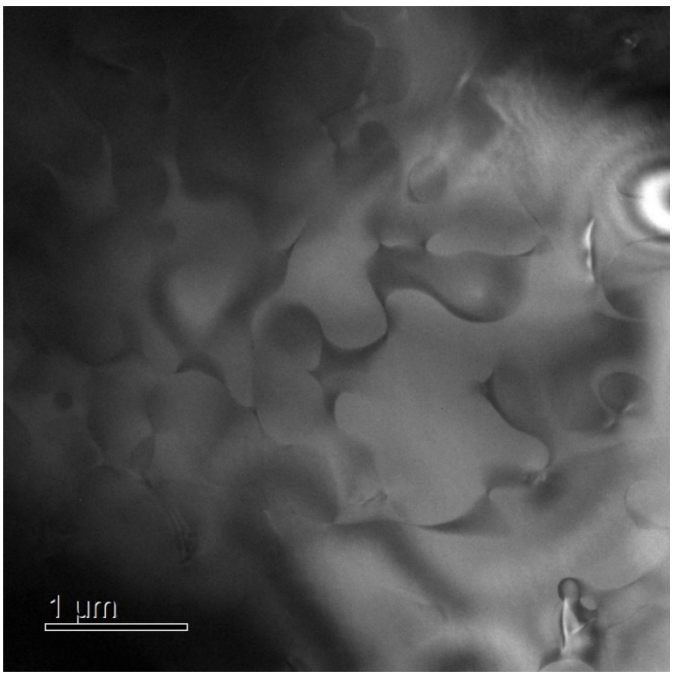

Fig. 3.3-10: Antiphase domains in omphacite ($Jd_{39}Hd_4Acm_1Di_{52}$) from a kyanite-free eclogite collected from the Münchberg Massif, Bavaria, Germany.

The dark-field TEM image with reflection g = [005] (Fig. 3.3-10) shows antiphase domains in the omphacite $Jd_{39-41}Hd_{4-5}Acm_{1-2}Di_{50-52}$ (Jd: jadeite, Hd: hedenbergite, Acm: acmite, Di: diopside). The SAED pattern in precession mode displays a larger reciprocal space and more kinematical intensity distributions of reflections than the conventional SAED pattern (Fig. 3.3-11ab). To evaluate the degree of cation ordering in omphacite, the intensities of reflections with $h + k$ = odd, *e.g.*, (050), and $h + k$ = even, *e.g.*, (060), were integrated with a Gaussian function (Fig. 3.3-11c). The obtained intensity ratio of 0.06(1) in (050)/(060) reflections from precession SAED measurements was comparable with the value 0.067(5) obtained from single crystal X-ray diffraction data of omphacite from the same rock. Using precession electron diffraction in the TEM, we measured pseudo-kinematical diffraction intensities of omphacite, enabling cation ordering in omphacite to be evaluated at the sub-micrometre scale.

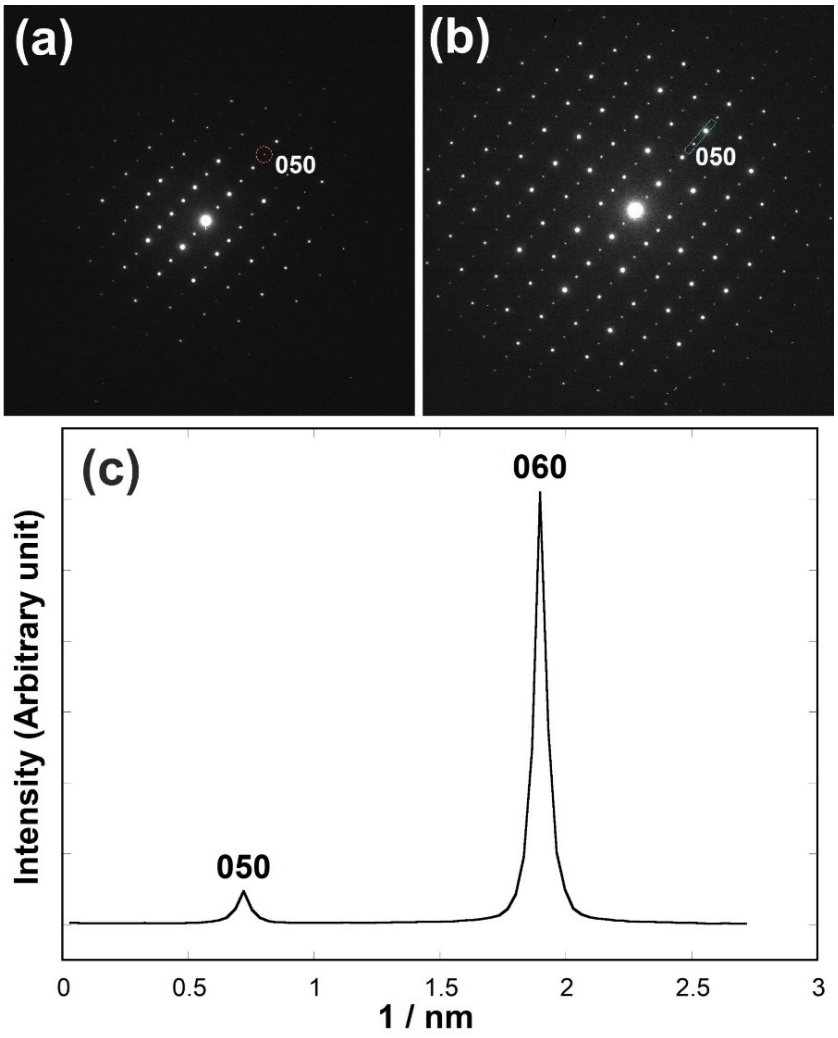

Fig. 3.3-11: (a) Conventional selected area electron diffraction (SAED) pattern and (b) precession (Ps) SAED pattern of the [101] zone axis of omphacite. The (050) reflection is indicated by a dotted circle in pattern (a) and a rectangular integration window in pattern (b). (c) Integration of peak intensities of the (050) and (060) reflections along the *b*-axis in the Ps-SAED pattern (b), fitted with a Gaussian function.

i. *Spectral and mineralogical alteration processes of naturally-heated CM and CY chondrites (M. Matsuoka and T. Nakamura/Sendai, N. Miyajima, T. Hiroi/Providence, N. Imae and A. Yamaguchi/Tokyo)*

C-type asteroids are thought to be parent bodies of carbonaceous chondrites based on results of spectroscopic studies. It is known that many carbonaceous chondrites and C-type asteroids experienced low-temperature hydration which results in hydrated phase formation. However, some carbonaceous chondrites dehydrated within their parent bodies, it has been found. Details of spectral and mineralogical properties of those naturally-heated carbonaceous chondrites are still unclear.

In this study, spectral analysis in the visible (Vis)-infrared (IR) range and mineralogical analysis at the microscopic scale were performed on nine naturally-heated carbonaceous chondrites classified into various heating stages (HS) to clarify the relationship between spectral and mineralogical properties affected by heating. Reflectance spectra of unheated (HS-I) samples show a positive Vis-IR slope and obvious evidence for the 0.7- and 3-μm absorption bands. The 0.7-μm band appears only in HS-I spectra. With increasing temperature of heating, (1) the Vis-IR slope decreases, (2) the 3-μm band becomes shallower, and (3) the Christiansen feature (CF) and Reststrahlen bands (RBs) shift towards longer wavelength. Microscopic analysis using a transmission electron microscope (TEM) equipped with an energy dispersive X-ray (EDX) spectrometer revealed that the matrix of strongly-heated chondrites consists of tiny olivine, low-Ca pyroxene, and (Fe,Ni) metallic particles mostly smaller than 100 nm in diameter, instead of the Fe-rich serpentines and tochilinite observed in the HS-I chondrite (Fig. 3.3-12).

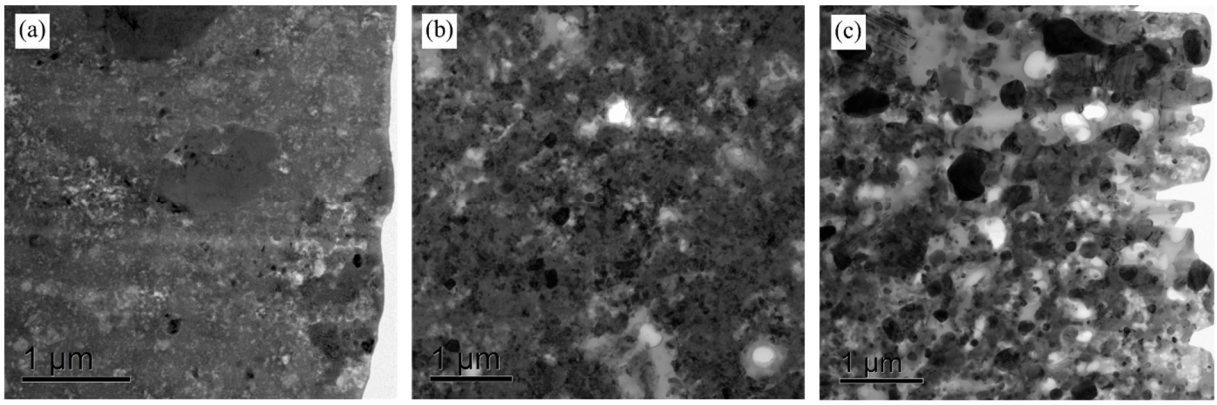

Fig. 3.3-12: Bright field TEM images of chondrites: (a) matrix TCI in LEW87022, (b) matrices in Dhofar 735, and (c) Murchison heated at 900 °C.

In proportion to heating degree, amorphisation and dehydration of serpentines and tochilinite from HS-I to moderately heated HS-II may cause 0.7- and 3-μm band weakening, spectral bluing and darkening of chondrite spectra. In addition, formation of secondary anhydrous

silicates and (Fe,Ni)-rich metal grains in strongly heated HS-IV would be responsible for the 3-μm band depth decrease, spectral reddening and brightening, CF peak shift, and RBs change. These spectral changes in response to mineralogical alteration processes will be useful for interpreting planetary surface composition by remote-sensing observations using ground-based or airborne/space telescopes or spacecraft missions.

3.4 Physical Properties of Minerals

Static compression experiments are among the most widespread methods for measuring the elastic response of minerals to changes in pressure. It is, therefore, not surprising that four contributions of this chapter report on compressibility measurements performed in diamond anvil cells coupled with X-ray diffraction using both *in-house* diffractometers as well as external synchrotron facilities. All these studies have been performed on single crystals in order to improve the accuracy and precision of the unit-cell lattice parameters measured at high-pressure, as well as to obtain insight into the structural changes which occur with increasing pressure. In the first contribution, the compressibility of magnesioferrite has been determined up to 22 GPa at room temperature. The results are used to constrain the high-pressure behaviour of the magnetite–magnesioferrite solid solution and indicate that mixed compositions are less compressible than the two end-members. In the second contribution, the high-pressure behaviour of an Fe^{2+}-rich basaltic bridgmanite has been studied up to 60 GPa at room temperature in order to constrain the elasticity of subducting slabs. The room pressure bulk modulus of this bridgmanite is similar to those of previously analysed basaltic bridgmanite samples, however, its first pressure derivative is remarkably low, suggesting that oxygen vacancies have a significant effect on the compressibility of basaltic bridgmanite at topmost lower mantle pressures. A major challenge in high-pressure studies using single crystals is to obtain accurate volume measurements at simultaneously high pressure and high temperature. In the third contribution, it is shown how the use of an *in-house* designed resistive heater has allowed to measure the volume changes of Al-bearing bridgmanite up to 1000 K and 35 GPa in order to constrain the *P-V-T* equation of state parameters for this mineral. One of the highly debated questions in Earth Sciences is whether water can be transported into the Earth's lower mantle. A possible carrier of water may be Al-bearing stishovite through the coupled substitution of an Si atom by one Al atom and one H atom. Such coupled substitution has major effects not only on the compressibility behaviour of stishovite but also on its high-pressure ferroelastic phase transition, as shown in the fourth contribution. Hydrous Al-bearing stishovite will transform at shallower depths, and its presence may explain some negative shear velocity anomalies within seismic scatterers observed in the proximity of subducted slabs at 800-1200 km depth.

Acoustic wave velocity measurements are fundamental for interpreting seismic observations, however, often such measurements are limited to simple compositions, which poorly constrain the behaviour of minerals having extensive cation substitutions as well as complex aggregates containing small fractions of melts. For example, the seismic signature of the Martian mantle is expected to be significantly different from the one of Earth due to the larger amount of Fe present in Martian rocks. The results obtained for a single-crystal of Fe-rich ringwoodite by means of Brillouin scattering and X-ray diffraction experiments at high pressure are reported in the fifth contribution showing a major decrease of the aggregate acoustic velocities of this mineral with respect to the ringwoodite end-member. The elastic properties of solid-liquid mixtures depend on the solid-solid and solid-liquid interfacial energies, which will determine the extension of the interconnected liquid network. In the sixth contribution of this chapter

ultrasonic interferometry experiments have been performed to measure the acoustic wave velocities of olivine-FeS aggregates at pressures of 4 to 6 GPa and at temperatures up to 1800 K. For a volume fraction of FeS up to 9 % only a slight effect on the shear wave velocity of the aggregate is visible even at temperatures where liquid FeS is expected.

The physical properties of rocks can also be strongly affected by their microtextures, for example, melt pockets are known to reduce the acoustic wave velocities of polycrystalline aggregates or the grain size distribution may have a significant impact on their flow strength. The last two contributions of this chapter make use of backscattered electron images to quantify solid-liquid interfaces and grain growth in samples recovered from high-pressure and high-temperature syntheses. These image analyses allowed to determine in the seventh contribution the variation of contiguity of melt pockets in olivine-troilite mixtures showing that more than 6 vol. % of troilite (*i.e.*, much more than reported in the literature) is needed to produce observed wave velocity reductions. In the last contribution, the grain growth kinetics of bridgmanite coexisting with ferropericlase is investigated as a function of temperature at 27 GPa in order to constrain the rheology of the lower mantle in diffusional creep. The results suggest that the grain size of bridgmanite in colder subducting slabs will be up to 10 times smaller than that of bridgmanite in the surrounding mantle, potentially decreasing their flow strength.

a. *Study of the compressibility behaviour of the magnetite-magnesioferrite solid solution by means of single crystal X-ray diffraction (C. Melai, T. Boffa Ballaran and D.J. Frost)*

Spinel structured minerals are the second most common mineral found as inclusions in diamonds. These minerals have been observed both as single inclusions (*e.g.*, Cr-bearing spinels) and as exsolutions mainly in ferropericlase inclusions hosted in diamond (in this case, they are Fe^{3+}-rich spinels). Cr-bearing spinels represent about 14 % of the reported inclusions in lithospheric diamonds that come from the first 200 km below the cratonic crust. On the other hand, ferropericlase often containing (Mg,Fe)-bearing spinel exsolution, is the most abundant inclusion in the so-called sublithospheric diamonds, which may come from the Earth's lower mantle and therefore may give important constraints on the composition of at least local parts of the deep Earth. The Fe^{3+}-rich spinel exsolutions that have been identified so far in ferropericlase inclusions occurring in diamonds show compositions very close to the magnetite (Fe_3O_4)-magnesioferrite ($MgFe_2O_4$) solid-solution. Very little is known about the compressibility of this system, though, in spite of the fact that knowledge of the thermodynamic properties of these minerals are essential for constraining their phase relations and high-pressure stability and thus for constraining the conditions at which exsolution occurs.

In the present study, the compressibility of pure magnesioferrite has been investigated up to ~ 22 GPa by means of single-crystal X-ray diffraction. Until now, only powder X-ray diffraction data have been published, yielding contradictory results that do not allow straightforward modelling of the magnetite-magnesioferrite solid solution.

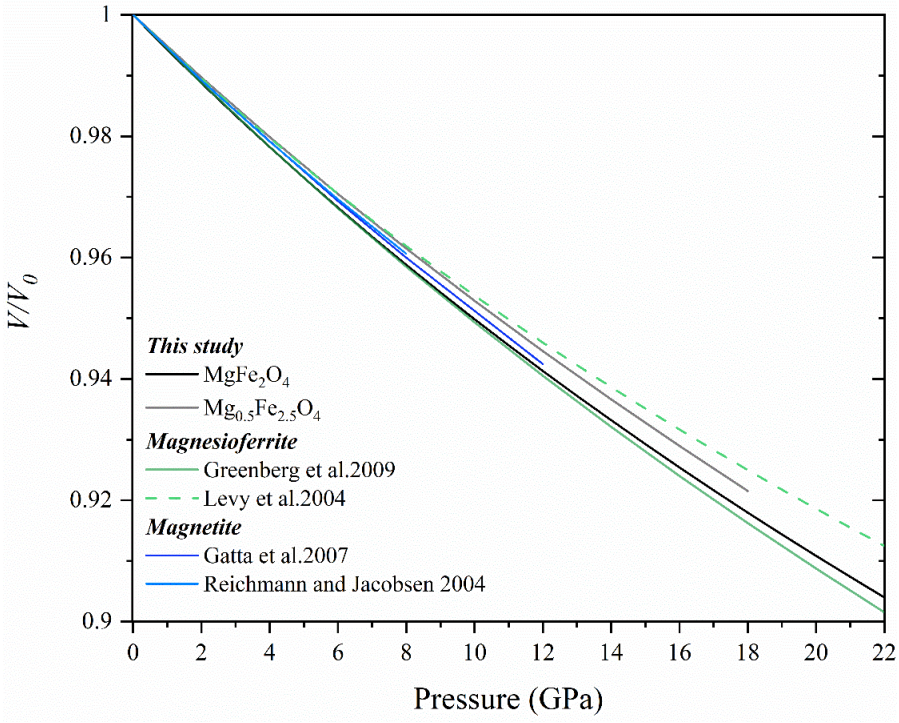

Fig. 3.4-1: Evolution of the compressibility (V/V_0) as a function of pressure for the magnetite-magnesioferrite solid solution. The black and grey curves represent fits of the third-order Birch-Murnaghan EoS to the *P-V* data measured in the present study. Literature data for magnesiferrite: Greenberg *et al.*, High Pressure Res., 29, 764-779, 2009 (green solid line) and Levy *et al.*, Phys. Chem. Miner., 31, 122-129, 2004 (green dotted line) and for magnetite: Gatta *et al.*, Phys. Chem. Miner., 34, 627-635, 2007 (dark blue line) and Reichmann and Jacobsen, Am. Min., 89, 1061-1066, 2004 (light blue line) are plotted for comparison.

Magnesioferrite was synthesized in the multianvil press at 5 GPa and 1300 °C under oxidizing conditions to ensure that only Fe^{3+} was present in the synthesized samples. Structural refinements of $MgFe_2O_4$ have been performed by means of single-crystal X-ray diffraction at ambient conditions in order to constrain the degree of ordering of this sample. Compressibility data of $MgFe_2O_4$ were then obtained *in situ* up to 21.5 GPa at room temperature. The volume variation with pressure can be described using a third-order Birch-Murnaghan equation of state. Figure 3.4-1 shows a comparison with the high-pressure data of $Mg_{0.6}Fe_{2.4}O_4$ (from Melai *et al.*, annual report 2017) and with the powder data present in the literature having a similar degree of order. The two end-members magnesioferrite and magnetite have very similar compressibility, $MgFe_2O_4$ being just slightly more compressible than Fe_3O_4. However, the sample with mixed composition is stiffer than both end-members, suggesting that a simple linear relationship of the bulk moduli along the magnesioferrite-magnetite solid solution cannot properly describe the high-pressure behaviour of minerals with mixed compositions along this join. The accurate determination of the equation of state for $MgFe_2O_4$ and $Mg_{0.6}Fe_{2.4}O_4$ by means of single crystal X-ray diffraction provides valuable information for estimating the depth of formation of diamond-inclusion pairs.

b. *Crystal chemistry and compressibility of Fe^{2+}-rich basaltic bridgmanite (G. Criniti, T. Ishii/Beijing, N. Miyajima, A. Kurnosov and T. Boffa Ballaran, in collaboration with N. Siersch/Paris and K. Glazyrin/Hamburg)*

Bridgmanite is widely accepted to be the most abundant mineral in Earth's lower mantle, where it constitutes at least 80 vol. % of pyrolite and about 30 vol. % of basalt. Due to its structural flexibility, the crystal chemistry of bridgmanite is rather complex and can change significantly as a function of pressure (*P*), temperature (*T*) and bulk composition of the system. Basaltic bridgmanite is usually rich in Al and Fe, and its composition is expressed as a combination of the end-members $MgSiO_3$, $Fe^{3+}AlO_3$, $Fe^{2+}SiO_3$, $AlAlO_3$ and $Fe^{3+}Fe^{3+}O_3$. Recently, it was shown that under low oxygen fugacity and uppermost lower mantle *P-T* conditions basaltic bridgmanite has a significantly low $Fe^{3+}/\Sigma Fe$ ratio and at the same time incorporates up to 10 mol. % of an $(Mg,Fe^{2+})AlO_{2.5}$ oxygen vacancy (OV) component. The concentration of the OV component generally decreases with pressure and in fact Fe^{2+}-rich basaltic bridgmanite has no OVs above 35 GPa. Therefore, around this pressure, the structural and physical properties of basaltic bridgmanite are expected to change in response to the variation of its crystal chemistry. To date, however, no experimental studies on the physical properties of Fe^{2+}- and OV-rich bridgmanite exist, hampering the resolution of current thermodynamic and mineral physical models of basalt at lower mantle conditions. For this reason, we investigated the structure and compressibility of an Fe^{2+}- and OV-rich bridgmanite sample in a diamond anvil cell (DAC) using single-crystal X-ray diffraction (SCXRD).

The sample investigated in this study was synthesized at 27 GPa and 1700 K in a multianvil apparatus from the reaction of two layers composed of corundum + phase egg and $(Mg_{0.6}Fe^{2+}_{0.4})(Al_{0.4}Si_{0.6})O_{2.8}$, respectively. The sample was then characterised using electron probe microanalyses (EPMA) and electron energy loss spectroscopy (EELS). While EELS analyses showed an almost constant $Fe^{3+}/\Sigma Fe$ value of ~ 0.25, the chemical composition was found to change as a function of the distance from the reaction boundary. The most Fe and Al enriched grains displayed $LiNbO_3$-type structure with an average composition of $Mg_{0.386(14)}Si_{0.548(8)}Fe^{2+}_{0.460(17)}Fe^{3+}_{0.170(5)}Al_{0.437(10)}O_{2.851(3)}$. A single crystal measuring 8 x 4 x 4 μm^3 was hand-picked from the reaction boundary and analysed at high pressure by SCXRD at the Extreme Conditions Beamline P02.2 of PETRA-III (Hamburg, Germany). The sample was loaded in a BX90-type DAC equipped with diamonds anvils having culets of 150 μm in diameter. A piece of Au and a ruby sphere were placed in the sample chamber together with the sample before the DAC was loaded with pre-compressed He gas at 1.3 kbar. Pressure was then increased online using a gas-driven membrane from 11 GPa up 60 GPa at steps of 2-3 GPa. We found that the sample, although being recovered as $LiNbO_3$-type phase, had completely transformed to bridgmanite upon gas loading to 11 GPa. No further transitions, either structural or electronic, were observed up the maximum investigated pressure.

A 3rd-order Birch-Murnaghan equation of state was fit to the experimental data points (Fig. 3.4-2) and yielded the following values for the isothermal bulk modulus and its pressure derivative:

K_{T0} = 242(4) GPa, K'_{T0} = 3.15(12). While K_{T0} has a similar value to previously analysed basaltic bridgmanite samples, K'_{T0} is remarkably low, suggesting that OV-bearing basaltic bridgmanite is softer than OV-free bridgmanite at topmost lower mantle pressures. Once integrated in already existing thermodynamic and mineral physical models, our findings will enable to better characterise the evolution of density and bulk sound velocities of basalt in the top- and mid-lower mantle.

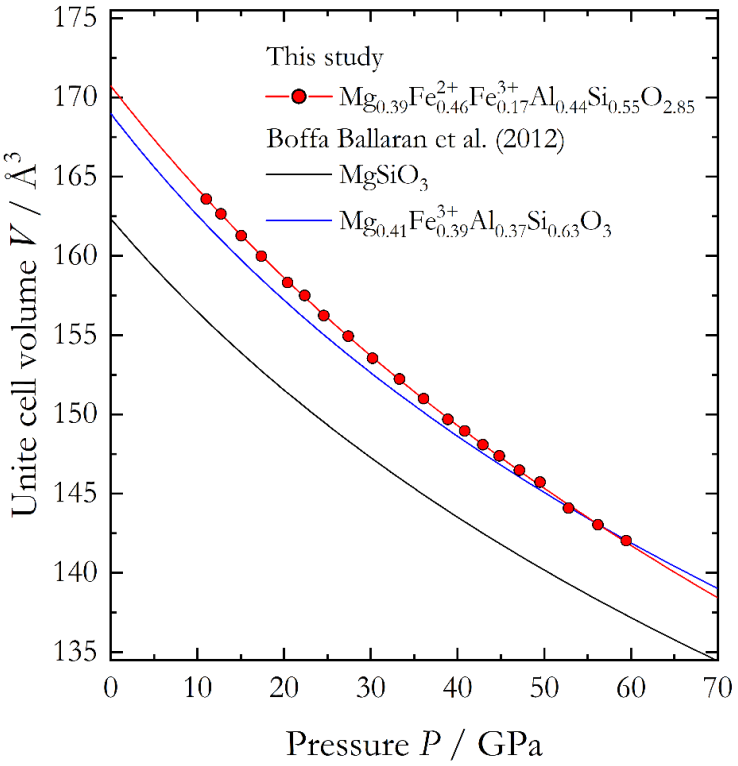

Fig. 3.4-2: Unit cell volume of $Mg_{0.386(14)}Si_{0.548(8)}Fe^{2+}_{0.460(17)}Fe^{3+}_{0.170(5)}Al_{0.437(10)}O_{2.851(3)}$ bridgmanite as a function of pressure (red circles and line). It can be seen that, due to its low K'_{T0}, the unit cell volume of OV-rich bridgmanite decreases more steeply than that of $MgSiO_3$ (black line) and $Fe^{3+}AlO_3$-rich (blue line) bridgmanite (Boffa Ballaran *et al.*, Earth Planet. Sci. Lett., 333-334, 2012). This indicates that OVs enhance the compressibility of bridgmanite at high pressure.

c. *Single-crystal thermal equation of state of Al-bearing bridgmanite (G. Criniti, A. Kurnosov, T. Boffa Ballaran and D.J. Frost, in collaboration with Z. Liu/Jilin, K. Glazyrin and R. Husband/Hamburg)*

Bridgmanite, (Mg,Fe,Al)(Al,Si)O_3 with perovskite-type structure, is believed to constitute at least 80 vol. % of the lower mantle, thus defining, for the most part, the physical properties of this region of Earth's interior. The crystal chemistry of bridgmanite is known to change as a function of pressure (P) and temperature (T), even when the chemical bulk composition of the lower mantle is assumed to be constant. As a consequence, it is convenient to describe the

physical and chemical properties of bridgmanite solid solutions in terms of their end-member components. In a pyrolite system, the incorporation of Al in the uppermost lower mantle occurs through the charge coupled (CC) substitution by $AlAlO_3$ and $Fe^{3+}AlO_3$ components and through the oxygen vacancy (OV) substitution by the $MgAlO_{2.5}$ component, while in the mid-to-bottom lower mantle CC components become dominant and the OV component disappears. The presence of OVs is of particular interest, as it is expected not only to affect the thermodynamic properties but also the rheology of bridgmanite. However, determining the $MgAlO_{2.5}$ and $AlAlO_3$ concentration in bridgmanite is not always straightforward, especially if samples are synthesized directly in a diamond anvil cell (DAC) in order to study their compressibility by powder X-ray diffraction. Additionally, Al-bearing and Fe-free bridgmanite samples often exhibit, to some extent, both CC and OV substitutions, whose abundance is difficult to control in synthesis experiments. As a result, the relatively poor chemical characterisation of Al-bearing bridgmanite samples employed in high-pressure powder diffraction experiments prevented previous studies from accurately constrain the thermoelastic properties of the $MgAlO_{2.5}$ and $AlAlO_3$ bridgmanite components.

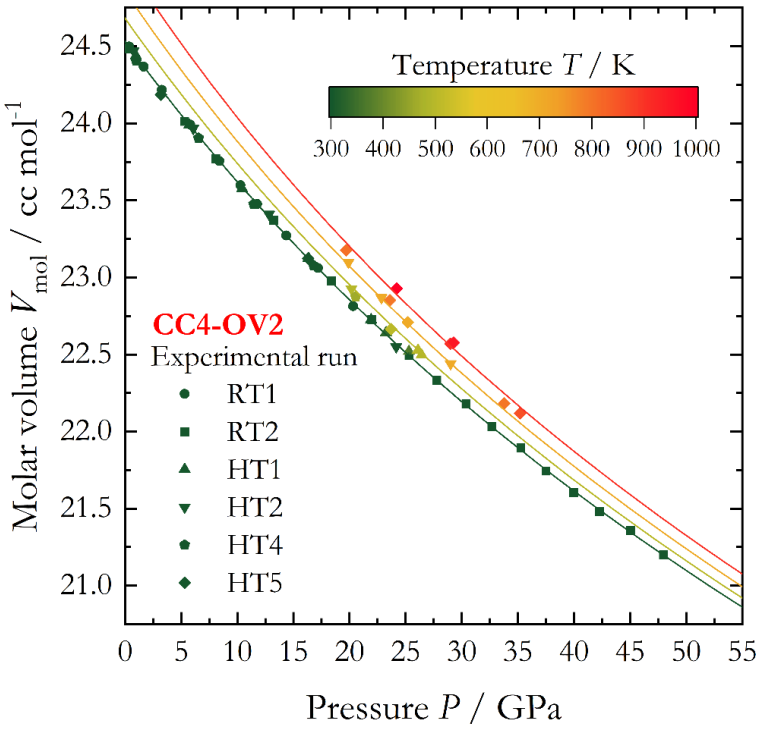

Fig. 3.4-3: Experimentally measured molar volumes of single crystals of $(Mg_{0.96}Al_{0.04})(Al_{0.06}Si_{0.94})O_{2.99}$ bridgmanite (CC4-OV2) as a function of pressure and temperature. Measurements were carried out over six different runs at room T (RT1, RT2) or high T (HT1, HT2, HT4, HT5). Temperature is expressed by the color scale at the top right of the graph.

To solve this issue, we performed high-pressure and high-temperature single-crystal X-ray diffraction (SCXRD) measurements on two well-characterised Al-bearing Fe-free bridgmanite

samples in order to define the *P*- and *T*-dependence of their molar volume (*V*). SCXRD measurements were performed at the Extreme Conditions Beamline P02.2 of PETRA-III (Hamburg, Germany). We employed resistively-heated DACs equipped with diamond anvils having culets of 350-400 μm in diameter. Temperature was generated using a 1 mm-thick Pt wire wrapped around a ceramic ring, and was monitored using a Pt-Pt/Rh (type S) thermocouple. Pressure was measured using the ruby fluorescence scale ($T < 700$ K) and the equations of state (EOS) of Au and W metals, which were loaded together with the two bridgmanite samples in each DAC. Ne gas was loaded in the sample chamber, ensuring a quasi-hydrostatic stress environment around our samples. In the *T*-range where the three pressure sensors could be used simultaneously, we noticed that *P* determined using ruby fluorescence was up to 1.5 GPa lower than determined by Au and W, which were typically in good agreement ($\Delta P < 0.5$ GPa) with one another at both low and high *T*. The simultaneous refinement of *P* and *T* using the three pressure sensors yielded differences of about 0.2 GPa and 40 K from the values obtained using the thermocouple reading and the EOS of Au or W. Third-order Birch-Murnaghan and Mie-Grüneisen-Debye EOS were combined to fit our experimental data points at room and high temperature, respectively (Fig. 3.4-3). In the fitting procedure, the logarithmic derivative of the Grüneisen parameters with respect to volume (q) was fixed to the value of 1 due the limited number of data points and the resulting high correlation between q and the Grüneisen parameter itself (γ). Further high-*T* measurements at $P > 35$ GPa will help to better constrain these two parameters and discriminate between the contributions of OV and CC components to the thermal EOS of Al-bearing bridgmanite.

d. *Phase transition and equation of state of hydrous Al-bearing silica (G. Criniti, A. Kurnosov and T. Boffa Ballaran, in collaboration with T. Ishii/Beijing and K. Glazyrin/Hamburg)*

Stishovite, a high-pressure polymorph of SiO_2, has rutile-type structure (space group $P4_2/mnm$) and constitutes up to 25 % of basaltic phase assemblages at lower mantle depths. At about 50 GPa and room temperature, SiO_2-stishovite undergoes a second-order ferroelastic phase transition to a post-stishovite phase having a $CaCl_2$-type structure (space group *Pnnm*), with a decrease from tetragonal to orthorhombic symmetry. This phase transformation is driven by tilting of the SiO_6 octahedra, which couples with the B_{1g} optic mode of stishovite. As a result of this coupling, stishovite experiences extensive elastic shear softening at the transition pressure, which causes both compressional and shear wave velocities to drop considerably. In the lower mantle, however, stishovite is not pure SiO_2, but can accommodate up to several wt. % of Al_2O_3 in its crystal structure, which in turn is expected to affect the post-stishovite transition. Recently, it was also reported that stishovite and its high-pressure polymorph can host significant amounts of water, which substitutes for SiO_2 either as H_2O or in combination with Al as AlOOH. Both Al and H are believed to reduce the stability field of tetragonal stishovite and to cause the post-stishovite transformation to occur at lower pressure. To date, however, only few results are available on the combined effect of Al and H on the post-stishovite transformation and no experimental study has ever investigated stishovite samples displaying stoichiometric $Si^{4+} = Al^{3+} + H^{+}$ substitution.

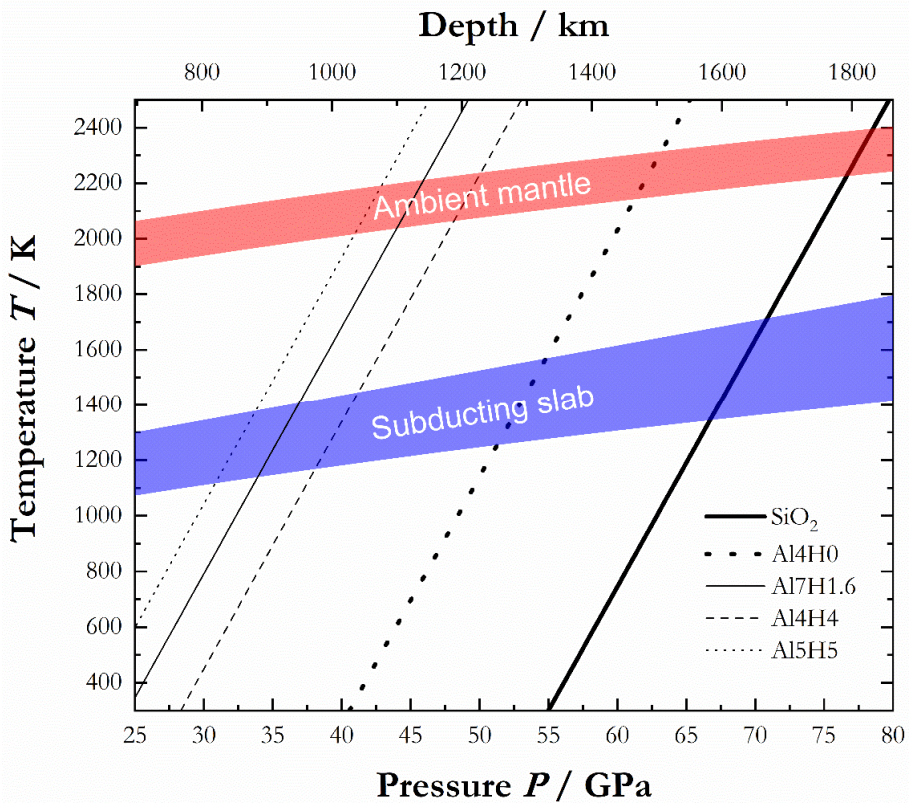

Fig. 3.4-4: Modelled *P-T* conditions for elastic softening of stishovite solid solutions (black lines) are compared with subducting slab (blue area: Eberle *et al.*, Phys. Earth Planet. Inter., 134, 191-202, 2002; Kirby *et al.*, Rev.Geophys., 34, 261-306, 1996) and ambient mantle (red area: Katsura *et al.*, Phys. Earth Planet. Inter., 183, 212-218, 2010) geotherms. It can be seen that 4-5 mol. % AlOOH-bearing SiO_2 (dotted and dashed thin lines) intersects both coloured regions at top-to-mid lower mantle conditions, matching the depth interval observed for seismic scatterers in the proximity of subducted oceanic plates.

In this study, we investigated the high-pressure behaviour of AlOOH-enriched tetragonal $Si_{0.951}Al_{0.049}O_{1.996}H_{0.04}$ (Al5) and orthorhombic $Si_{0.880}Al_{0.110}O_2H_{0.13}$ (Al11) by means of synchrotron single-crystal X-ray diffraction (SSC-XRD) and Raman spectroscopy in a diamond anvil cell. We found that the combined effect of Al and H on the post-stishovite transition is much larger than that of Al or H alone, causing the Al5 sample to transform to post-stishovite already at 15 GPa. Furthermore, we observed that the B_{1g} mode of stishovite is at least partially decoupled from the evolution of the unit cell lattice parameters, which means that the frequency of the optic mode continued to decrease even after the Al5 sample became orthorhombic and started to increase only above 30 GPa. The reason for this decoupling may lie in the large concentration of H atoms in our samples. In fact, O-H···O bonds in isostructural AlOOH are known to become symmetric at high pressure in response to the shrinkage of O···O distances without much affecting the tilting of AlO_6 octahedra. Our hypothesis is confirmed by single-crystal structural refinement obtained from our SSC-XRD data that clearly show that octahedral tilting is frozen up to about 20 GPa, suggesting that elastic softening is to be expected around

this pressure. Using our results together with those reported in previous studies, we determined the individual effect of Al and H substitution on the pressure at which elastic softening is expected. We have been able to show in this way that silica having 4-5 mol. % AlOOH would exhibit such softening at depths of the uppermost lower mantle along slab (800-1000 km) or ambient mantle (1000-1200 km) geotherms (Fig. 3.4-4). Because elastic softening in stishovite would significantly affect the sound wave velocity of a basaltic phase assemblage, the presence of hydrous Al-bearing post-stishovite could explain some negative shear velocity anomalies within seismic scatterers observed in the proximity of subducted slabs at 800-1200 km depth. Our results suggest that the water cycle in the lower mantle may occur not only through hydrous phases, but also through nominally anhydrous silica.

e. *The elastic behaviour of Fe-rich ringwoodite (A. Kurnosov, T. Boffa Ballaran, G. Criniti and D.J. Frost)*

Observations of the seismic wave velocity structure of the Martian interior are becoming increasingly available from the SEIS seismometer on the NASA InSight lander. The interpretation of such data relies crucially on the ability to model the mineralogy and seismic velocities of the Martian interior in order to test plausible compositions and temperature gradients. The usual procedure followed for constructing such models is to extrapolate the thermoelastic properties of Fe-poor or Fe-free minerals obtained in experimental studies to higher Fe concentrations by assuming a linear dependence of density and elastic moduli on the Fe content when possible, or neglecting such effect altogether. When actually measured, however, the effect of Fe substitution on the thermoelastic parameters of minerals appears to be quite large. Iron, therefore, can significantly influence the seismic signature of the Martian mantle in comparison to Earth. Ringwoodite, $(Mg,Fe)_2SiO_4$ (Rw) is a high-pressure polymorph of olivine and is likely the main mineral at the base of the Martian mantle, where it is expected to contain a much larger amount of Fe than its terrestrial counterpart. There are conflicting experimental results reported in the literature on the effect of iron on the room-temperature elastic properties of Rw, with Brillouin scattering and ultrasonic interferometry studies pointing to different gradients of the elastic moduli with Fe content, making any estimate based on velocity modelling subject to significant uncertainties. For this reason, we have decided to determine the variation of the full elastic tensor of an Fe-rich Rw with pressure in order to better constrain the role of Fe on its elastic properties.

High-quality single-crystals of $(Mg_{0.7}Fe_{0.3})_2SiO_4$, Rw70, have been synthesised in a multianvil apparatus and characterised using single-crystal X-ray diffraction, electron microprobe analysis and Mössbauer spectroscopy. $MgCl_2$ was used as a flux to aid the growth of large high-quality single crystals, having the additional effect of lowering the H_2O activity to levels where the H_2O content in ringwoodite will be negligible. A crystal oriented along the [100] direction was double-side polished down to a thickness of 15 μm and cut into circular disks of 40 to 60 μm in diameter using a Focused Ion Beam (FIB) instrument. An FIB-cut sample was then loaded together with a ruby chip in a DAC with He as a pressure-transmitting medium to ensure quasi-hydrostatic conditions at all pressures.

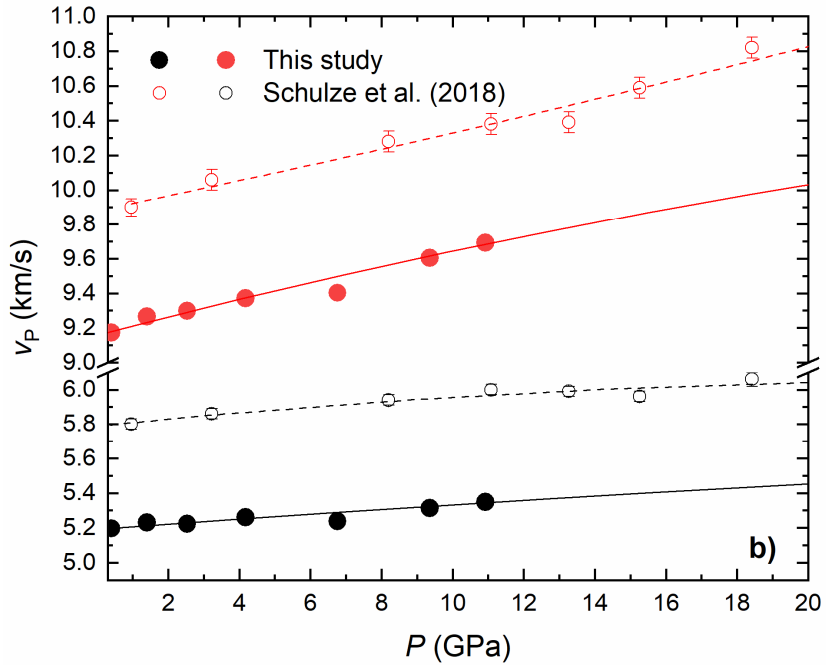

Fig. 3.4-5: Variations of the aggregate wave velocities of Rw70 obtained with pressure up to 11 GPa (v_P: red, v_S: black). Data for the Mg_2SiO_4 ringwoodite end-member from Schulze *et al.* (EPSL, 498, 9-16, 2018) (empty symbols) are reported for comparison.

Simultaneous Brillouin scattering measurements and single-crystal X-ray diffraction have been performed at the same conditions in order to determine the elastic tensor of Rw70 in a self-consistent manner, without having to rely on the use of a secondary pressure standards or previously determined pressure-volume equations of state. Data have been collected so far up to 11 GPa at room temperature. Rw70 appears elastically anisotropic at room pressure with a variation of v_S and v_P of ~ 400 m/s between minima and maxima. Such variation, however, decreases rapidly with increasing pressure and the anisotropy of Rw70 is below 100 m/s already at 11 GPa. Moreover, whereas v_P increases rapidly with pressure, the maxima of the shear acoustic-velocity remain practically constant, suggesting a very shallow slope of the shear modulus of this material with pressure. Although the faster shear wave velocity, v_{S2}, is never visible in the Brillouin spectra, the observed v_P and v_{S1} signals together with the measured densities are sufficient for constraining the three stiffness coefficients (c_{11}, c_{12} and c_{44}) of a cubic sample such as Rw70 at each pressure point. The variation of the aggregate velocities of Rw70 with pressure is reported up to 11 GPa in Figure 3.4-5 and compared with that obtained in a Brillouin scattering experiments on Mg_2SiO_4 ringwoodite end-member reported in the literature. Substitution of Fe into the ringwoodite structure gives rise to a major decrease in both aggregate v_S and v_P.

f. *Acoustic wave velocities of olivine sulphide-melt mixtures by* in situ *ultrasonic interferometry (A. Néri, L. Man, T. Boffa Ballaran and D.J. Frost, in collaboration with J. Chantel/Lille)*

The elastic behaviour of mixtures is generally assumed to follow a mixing law based on volume fractions, considering that either the stress or the strain is constant. However, such mixing laws cannot be simply applied to solid-liquid mixtures as the small-scale geometry has an important

impact. Indeed, depending on the solid-solid and solid-liquid interfacial energies, expressed in a sample as dihedral angles, the contact length between solid and liquid may strongly differ. If the solid-liquid interfacial energy is much smaller than that of the solid-solid, the liquid tends to increase its total contact area with the solid and is likely to form an interconnected network. In that case, it is likely that the elastic properties of the aggregate are affected, and the P- and S-wave velocities will be reduced. In the opposite case, if the solid-solid interfacial energy is the smallest, then liquid pockets will be distributed at triple junctions between solid grains to minimize the solid-liquid contact length and maximize that of the solid-solid interface. Most likely, the effect on wave velocity reduction will be smaller. However, little to no experimental studies report direct measurements of the elastic properties of such composite aggregates.

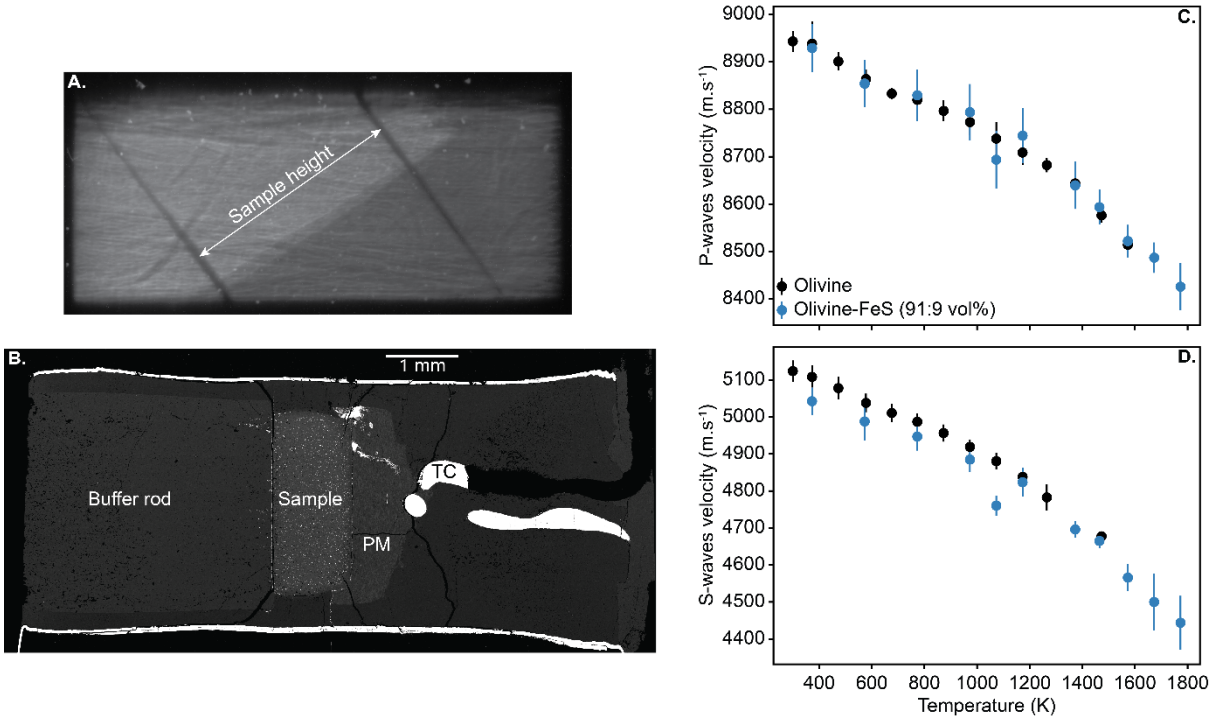

Fig. 3.4-6: A. An X-ray radiography image of a sample comprised of 91 vol. % of olivine and 9 vol. % FeS. Thin platinum foils were placed on top and bottom of the sample to facilitate its length measurement. B. A SEM map of the recovered assembly. The top and bottom interfaces of the sample remained flat during the time of the experiment. C. P-wave velocity and D. S-wave velocity for samples composed of pure olivine (black dots) and olivine + 9 vol. % of FeS (blue dots). For the experiment with pure olivine, no data were collected above 1473 K for the S-waves and 1573 K for the P-waves because our piezoelectric crystal overheated, and the signal was lost. Whether the iron-sulphide is solid or molten, the P-waves velocities are perfectly superimposed to that of the pure-olivine sample. However, a slight deviation is observed above 1500 K for the FeS-bearing sample, marking the onset of iron-sulphide melting.

As a first attempt to tackle the behaviour of solid-liquid mixtures, we conducted *in situ* ultrasonic interferometry experiments to measure the P- and S-wave velocities of olivine-FeS

aggregates (see also Néri *et al.*, next contribution). To do so, mixtures with different FeS contents were pre-sintered in a piston-cylinder and subsequently machined into disks of the desired dimensions. These samples were loaded into a 14/8 multianvil assembly, compressed and heated up to 15 GPa and 1873 K using the Aster-15 press at the P61B beamline at the DESY synchrotron in Hamburg. For each experiment, the two-way travel times within the sample were collected at different frequencies, the sample height was measured using X-ray radiography (Fig. 3.4-6A) and XRD patterns were collected to estimate pressure and determine the state of the iron-sulphide – solid or molten. Recovered samples do not show any signs of extensive deformation and/or stress (Fig. 3.4-6B).

Our preliminary data in the range 4-6 GPa (Fig. 3.4-6C,D) on samples composed of pure olivine and olivine plus 9 vol. % of FeS indicate a slight sensitivity of the S-waves to the presence of such non-wetting iron-sulphide melt, while P-waves do not seem to be affected. Uncertainties on the S-wave velocities seem to be increasing with temperature, especially once the iron-sulphide phase is molten. This feature is most likely explained by a stronger scattering of the waves once the liquid is present. Different iron-sulphide melt contents are being investigated to better constrain the wave speed reduction due to the presence of the liquid.

g. *Predicting the wave speed reduction caused by isolated troilite melt pockets: microtextural investigation of olivine-troilite aggregates (A. Néri and D.J. Frost)*

Small melt fractions in polycrystalline aggregates are known to decrease P- and S- wave velocities. Liquids of different nature have been invoked to explain some seismic anomalies in the Earth's upper mantle. Some low-seismic velocity regions are located in old tectonic settings, that have not experienced activity for more than ≈ 50 Myr. Such timescales provide strong constraints on the melt's nature. Indeed, due to their low dihedral angles and interconnection thresholds (volume fraction at which a phase forms a percolative network), silicate and carbonate melts can be ruled out as likely candidates, as they would have been able to migrate. However, iron-sulphide melts have much larger interconnection thresholds and can remain isolated for long timescales as long as they are not interconnected. Furthermore, their low melting temperatures ensure their long-term persistence. Altogether, these arguments make iron-sulphur melts plausible candidates for producing long-lasting seismic velocity perturbations.

Geometrical models allow to predict the elastic properties of a solid-liquid aggregate based on the individual properties of each phase. These models assume that the small-scale geometry, more precisely described by a parameter named "contiguity", controls the mixing law that predicts the wave velocities of the mixture. Contiguity is determined from the crystal-crystal boundary length compared to the total boundary length within the sample and is a function of the dihedral angle, grain size and melt volume fraction. Based on some dihedral angle – contiguity relation, some studies have proposed that up to 1-2 vol. % of iron-sulphide melt

would be enough to explain the observed velocity reductions. However, the dihedral angle – contiguity relations seem to be mostly valid for melts with dihedral angles lower than 80°, a criterion that is not respected for iron-sulphide melts (≈ 135°). An important observation here is that contiguity can be directly measured on recovered samples.

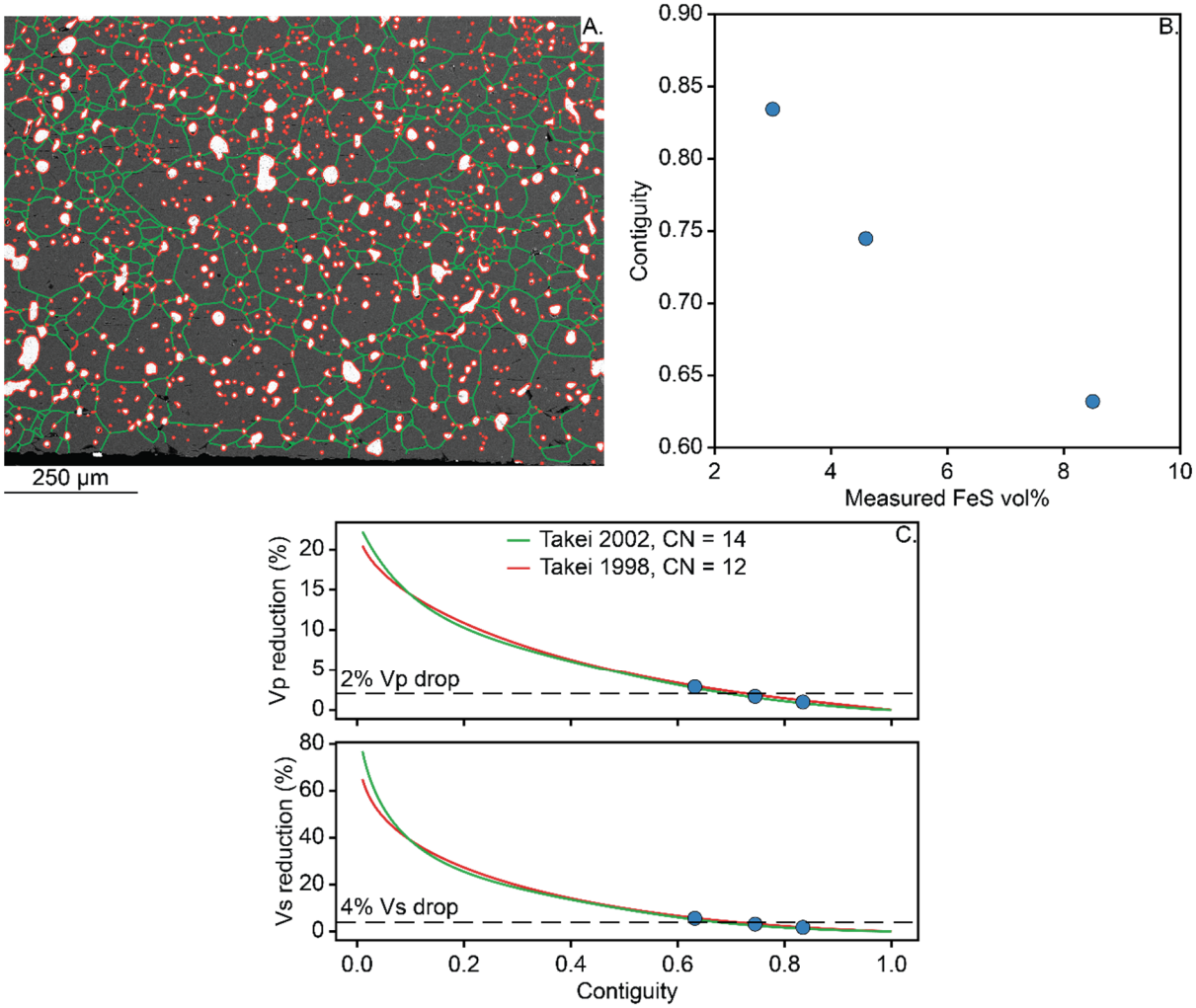

Fig. 3.4-7: A. SEM image of a sample bearing 90 vol. % of olivine and 10 vol. % of troilite. Green boundaries delimit the olivine-olivine interfaces while the red ones highlight the olivine-troilite interfaces. B. Contiguity measured for different troilite melt contents. C. Wave speed reduction as a function of contiguity. The blue dots correspond to the measured contiguity values.

In order to better estimate the iron-sulphide melt fractions that would cause the observed wave speed reductions, we conducted a series of experiments on mixtures of olivine and troilite, with varying troilite contents. Samples were equilibrated at 1400 °C and 6 GPa for 4 hours and Scanning Electron Microscope (SEM) images were subsequently collected. From these images, we measured the olivine-olivine and the olivine-troilite contact lengths (Fig. 3.4-7A) and the troilite fraction on the surface using the FiJi distribution of the ImageJ software. As expected,

we observe that contiguity decreases with increasing fractions of troilite (Fig. 3.4-7B), *i.e.*, the olivine-olivine contact length is reduced. Using established geometrical models and from our determined contiguities, we can estimate that ≈ 6 vol. % of troilite would actually be needed to produce the observed wave speed reduction (Fig. 3.4-7C). Such a volume fraction is well below the interconnection threshold of iron-sulphide melts. To further investigate the accuracy of such geometrical models, we are currently conducting ultrasonic interferometry measurements to measure the wave speeds in such olivine-troilite aggregates at high pressures and temperatures.

h. *The grain growth kinetics of bridgmanite at the topmost lower mantle (H. Fei and T. Katsura, in collaboration with U. Faul/Cambridge)*

The grain size of minerals is a fundamental parameter that affects geodynamic processes in the Earth's interior because it controls the physical and chemical properties of mineral aggregates including creep deformation, diffusive element transportation, seismic attenuation, and chemical mixing. Knowledge about grain size in the Earth's interior is therefore vital to understand mantle dynamics. Because of the lack of natural samples, it is impossible to know the grain size distribution in the lower mantle directly. Instead, it can be inferred from the history of lower-mantle rocks. There are two processes that affect grain size in the lower mantle. 1) Grain size reduction to nearly zero by phase transition across the phase boundaries, *i.e.*, dissociation of ringwoodite to bridgmanite + ferropericlase at the 660-km seismic discontinuity driven by the downward flow. 2) Grain growth over the geological time after the solidification or phase transition. Therefore, if whole mantle convection occurs, the grain sizes of the downward flowing material in the lower mantle can be estimated by the grain growth kinetics with an initial grain size of zero due to the phase transition at 660-km depth. Investigation of grain growth kinetics is thus important for understanding the properties and dynamics of the lower mantle.

In this study, we investigated the grain growth kinetics of bridgmanite that coexists with ferropericlase at 27 GPa, in the temperature interval 1400-2400 K, corresponding to the uppermost lower mantle conditions. Bridgmanite + ferropericlase aggregates with a grain size of less than 0.1 μm were pre-synthesized from natural olivine powder at 27 GPa and 1700 K for 5 min by means of multianvil experiments. The recovered aggregates were then embedded in CsCl powder within Pt capsules in multianvil cell assemblies and compressed to 27 GPa, followed by annealing at 1400-2400 K with durations ranging from 1.5 to 1000 min. The grain sizes of the bridgmanite in the run products were obtained from backscattered electron images (Fig. 3.4-8). As expected, the grain size in the run products systematically increases with increasing temperature and annealing duration (Fig. 3.4-8, Fig. 3.4-9).

The grain sizes obtained are fitted to the power-law relationship as follows:

$$d^n - {d_0}^n = kt \qquad (1)$$

where d_0 and d are the initial grain size of bridgmanite in the pre-synthesized sample and in the samples after annealing, respectively, k is the grain growth rate constant, t is the annealing duration, and n is the grain size exponent (coarsening exponent). The least-squares fitting suggests $n = 5.2 \pm 0.3$, whereas the k follows the Arrhenius relation with an activation enthalpy of 260 ± 20 kJ/mol.

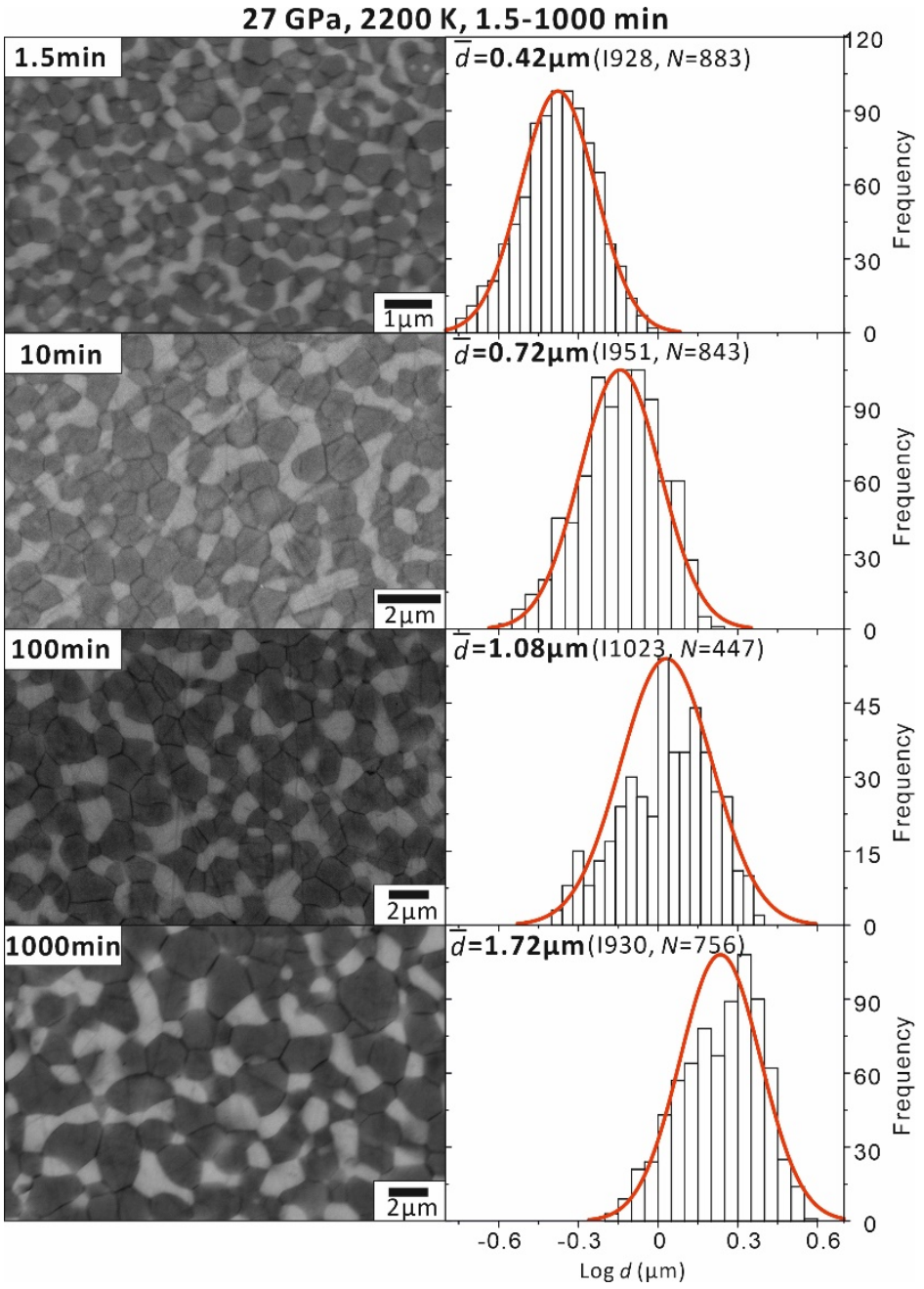

Fig. 3.4-8: Backscattered electron images (left) and grain size distributions (right) of the samples annealed at the same pressure and temperature conditions (27 GPa and 2200 K), but different run durations (1.5 to 1000 min). The grain size of bridgmanite (dark grains) show relatively narrow and symmetric Gaussian distributions. The average grain size increases systematically with increasing annealing duration.

Because of the phase transformation across the 660-km discontinuity in subducted slabs, the grain size of bridgmanite in the topmost lower mantle can be estimated based on the grain growth rate determined in this study and initial grain size of zero due to the phase transformation. By assuming a slab geotherm of 1600 K at 700 km depth, *i.e.*, 400 K lower than the mantle geotherm, over a geological time of 1-10 Myr (corresponding to tens to hundreds kilometre subduction depth), the grain size of bridgmanite will be ~ 30 to 45 μm. The grain size in the ambient mantle will follow the growth rate with an initial grain size determined by the origin and history of the rocks. If we assume the minimum case, *i.e.*, the initial grain size of zero, over a geological time of 100 Myr – 1 Gyr at the topmost lower mantle temperature (~ 2000 K), the grain size will be 150-230 μm. This is larger than the bridgmanite grain size in the subducted slabs by a factor of ~ 3 to 10 and the differences may cause a significant weakening of the slab relative to the ambient mantle if both deform by diffusion creep.

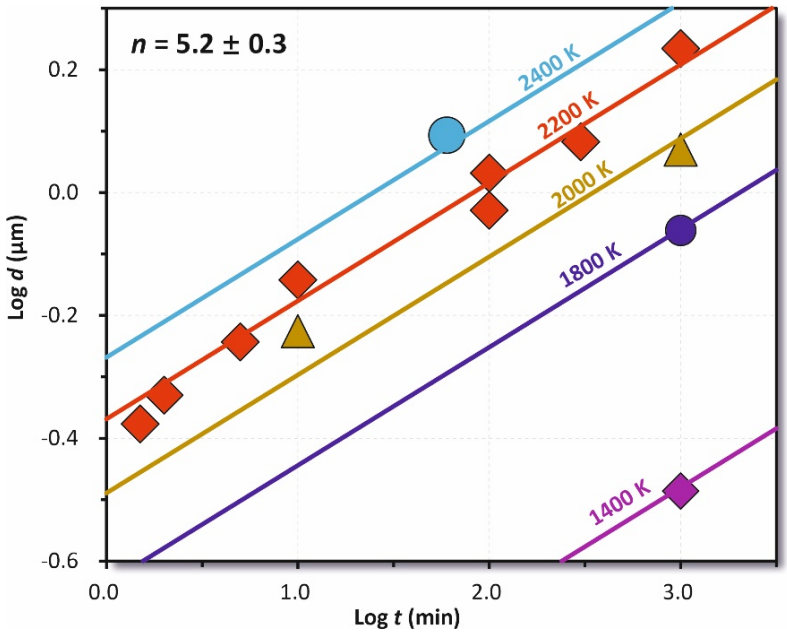

Fig. 3.4-9: Bridgmanite grain size evolution with time at 27 GPa, 1400-2400 K. The slope of the fitting lines represents 1/*n* in Eq. (1).

3.5 Fluids, melts and their interaction with minerals

The presence of small fractions of silicate melt in the mantle may have a strong effect on mantle convection and on the style on global tectonics on Earth. Many geodynamic models suggest that in order to stabilize plate tectonics, a channel of low viscosity is required below the plates and partial melting could be an efficient mechanism for generating such a channel. Moreover, partial melting could also explain the abrupt drop in seismic wave velocities at the lithosphere-asthenosphere boundary. However, partial melts can only be stabilized by the presence of volatiles, such as water, which are required to reduce solidus temperatures to ambient mantle conditions. Unfortunately, the effect of trace amounts of water on mantle melting is poorly understood, because it is difficult to precisely control such low water fugacities in experiments and detecting small fractions of melt is also a major challenge. The first contribution in this section of the annual report solves this problem by a new approach. Melting in the "haplobasaltic" anorthite-diopside system was studied at precisely controlled water fugacities in an internally-heated gas pressure vessel. This is a eutectic system, where large amounts of melt immediately form at the solidus, such that solidus temperatures can be accurately determined. The data clearly show that the effect of water on reducing the melting temperature of basalts is much stronger than previously thought. These results therefore make it quite plausible that there is indeed some partial melt present in the seismic low-velocity zone, which helps to "lubricate" the movement of tectonic plates.

Partial melts in the mantle may not only be present at the lithosphere-asthenosphere boundary, *i.e.*, at a depth of about 80-120 km, but also immediately above the 660 km discontinuity, which marks the top of the lower mantle. Here, an important question is whether melts may be gravitationally stable at this depth. The next contribution in this chapter investigates this problem by determining the precise composition and water content of such melts. These data are then used for calculating the expected melt densities. The melts are slightly less dense than the surrounding mantle, implying that they should ascend rather than accumulating at the 660 km discontinuity. However, the density difference is small, such that under some dynamic conditions, the formation of a melt layer may still be possible.

Aqueous fluids percolate through the mantle above subduction zones and in the crust, and the movement of such fluids is involved in many processes, such as the formation of hydrothermal ore deposits. How fluids move through the rock depends in a complex way on the wetting properties of the surfaces, the recrystallization of the matrix, and the formation of an interconnected fluid network. Three contributions look at these processes. In one study, dihedral angles of aqueous fluids were measured in olivine-fluid-systems at upper mantle pressures. The experiments show that under some conditions, the dihedral angle is larger for facetted crystal surfaces than for non-facetted ones. Moreover, the data raise the possibility that lattice preferred orientation of crystals, as it results from mantle flow, may also lead to permeability anisotropy. In another contribution, the movement of water through an olivine

matrix was directly measured in multianvil experiments. As one would expect, the mobility of water depends on the grain size of the sample. However, the grain size dependence inverts with increasing run duration, probably due to formation of an interconnected network of water saturated grain boundaries. Such network structures were also studied by X-ray tomography of synthetic fluid-bearing quartzite samples in another project.

The solubility of water in the minerals of the mantle controls the distribution of water in various mantle reservoirs and influences the stability of hydrous silicate melts. Therefore, this topic has been studied at BGI since decades; nevertheless, there are still many details, in particular on the temperature and compositional dependence of water solubility that require further study, as shown in four different contributions. Water solubilities in both Fe-bearing wadsleyite and in majorite coexisting with hydrous silicate melts were found to decrease with temperature, while the water solubility in Al-free stishovite appears much lower than suggested in some recent studies. Moreover, single-crystal neutron diffraction data of hydrous olivine suggest the presence of some vacancies on the Si site, possibly related to the incorporation of protons. Water contents in minerals and in silicate glasses are often measured by infrared spectroscopy. Due to the recent BGI development of a rapid-quench device for the multianvil apparatus, it was for the first time possible to prepare hydrous peridotite glasses and to calibrate the infrared extinction coefficients of hydrous species in these samples. The data nicely follow the trends defined by other compositions. This also implies that previous suggestions that these bands represent only a subset of OH species in the glass are in error.

The viscosity of a magma largely controls the style of volcanic activity, but the viscosities of relevant magma compositions are sometimes difficult to measure. Two contributions therefore show unconventional ways to estimate viscosities from spectroscopic or calorimetric data. The final contribution in this section of the annual report investigates the structure and properties of liquids in the Fe-Ni-C system relevant to Earth's outer core. These first-principles molecular dynamics simulations show that Ni actually behaves quite differently than Fe and therefore, including this element is essential for any realistic prediction of outer core properties.

a. *Upper mantle melting at low water fugacity (M. Putak Juriček and H. Keppler)*

Already trace amounts of water may strongly depress the melting point of peridotite. This effect could perhaps induce melting at the oceanic lithosphere-asthenosphere boundary, but significant melt fractions may be required to explain the observed shear-wave velocity reductions. Alternative mechanisms that do not involve melting have also been proposed to explain the geophysical observations. It remains therefore uncertain whether the shear-wave velocity reductions at the lithosphere-asthenosphere boundary may be related to partial melting and what kind of volatile concentrations are required to stabilize melt.

Due to water adsorption on powdered starting materials, the effect of ppm-level water contents on solidus temperatures cannot be investigated directly. Instead, low water fugacities can be very precisely controlled in melting experiments under H_2O-saturated conditions at low pressures. The effect of trace amounts of water on incipient melting may then be indirectly estimated from the experimentally established dry and H_2O-saturated solidi, water contents in near-solidus melts, and mineral/melt water partition coefficients. Experiments in the peridotite-H_2O system are further complicated by difficulties in recovering pristine silicate glasses from high pressures. Low viscosity hydrous basalts, formed by partial melting of peridotite, tend to precipitate crystalline products upon quenching. Discrimination of quench precipitates from subsolidus phases is subjective, and low-degree partial melts are difficult to identify in the run products. Most studies in the peridotite-H_2O system likely overestimated melting temperatures, as only high-degree partial melts are readily recognizable in quenched samples. We therefore suggest that current models underestimate the melting point depression due to these experimental challenges, and that water has a more prominent role in stabilizing low-degree partial melts in the mantle.

We designed a study to precisely measure the relationship between the melting point depression (ΔT) and the water content in near-solidus basaltic melts ($c_{H2O,melt}$). Experiments were performed using an internally-heated gas pressure vessel in the anorthite-diopside-H_2O system to determine the H_2O-saturated solidus temperatures – and therefore ΔT – as a function of pressure at 0.02-0.2 GPa. In this eutectic system, a high melt fraction is immediately produced at the solidus. Unlike in the peridotite-H_2O system, we could therefore easily determine the initial melting temperatures. The $c_{H2O,melt}$ was limited to realistic values by maintaining low confining pressures. Moreover, two separate series of experiments were performed to measure water solubility in haplobasaltic melts of the anorthite diopside system as a function of pressure and temperature. Extrapolating the water solubility in the melt to near-solidus conditions yields melt water contents that correspond to the experimentally observed ΔT. The results of this study are compared to previous models of the ΔT – $c_{H2O,melt}$ relationship, which were based entirely on melting experiments in the hydrous peridotite system (Fig. 3.5-1). As expected, the effect of water on the melting point depression is greater than previously thought. We observed the formation of basaltic melts with a total water content of 3 to 5 wt. % at approximately 50 °C lower temperatures, as compared to previous estimates from studies of hydrous peridotites (Fig. 3.5-1). Notably, while the scatter in the hydrous peridotite dataset is considerable, some data points do agree with our observation.

Preliminary calculations reveal that the presence of water alone may be able to induce melting along the oceanic lithosphere-asthenosphere boundary. Using different model parameters (plate cooling models, dry peridotite solidi, mineral/melt partition coefficients) from various literature sources, we estimate incipient melting to occur at 160 to 220 ppm of water. These values overlap considerably with the estimates of typical upper mantle water contents (100 to 200 ppm). Melting is predicted in a similar depth range to the observed oceanic lithosphere-

asthenosphere boundary. Along continental geotherms, a little more than 200 ppm of water may be enough to induce melting in active margins, but the effect of water alone on solidus temperatures is not sufficient to stabilize melt in most cratonic settings, at least not in equilibrium with any plausible bulk water content.

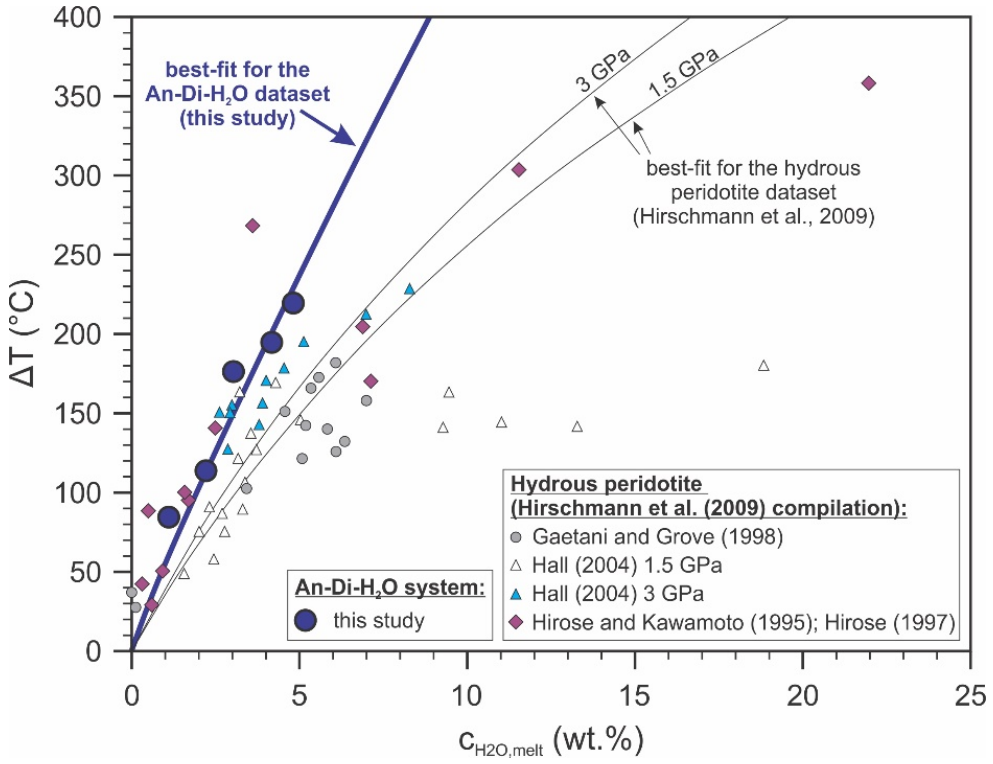

Fig. 3.5-1: The relationship between the solidus depression (ΔT) and water content in near-solidus basaltic melt ($c_{H2O,melt}$). The results from this study are compared to the previous estimates of the $\Delta T - c_{H2O,melt}$ relationship, which were based entirely on the data from hydrous peridotite studies. The cryoscopic approach for description of the melting point depression in silicate-H_2O systems is calibrated by the experimental data, and the curves in the image are the best-fit result of the calibrations. We used a 1-oxygen silicate molar unit (35 g/mol) and considered that water speciation (H_2O and OH^-) in silicate melts may be characterised by a temperature-dependent equilibrium constant. Data points from previous studies are from Hirschmann *et al.* (2009, PEPI 176:54) and references therein.

In the discussion above, we considered the isolated effect of water on the melting point depression of peridotite. However, the depleted mantle source likely contains trace amounts of CO_2 as well. A substantially greater depression of the melting point should be expected, as a result of the combined effect of water and CO_2. Accordingly, the extent of partial melting predicted from our melting model is likely only a minimum estimate. Partial melting may therefore be a plausible explanation for the seismic low-velocity zone in the upper mantle, even in cratonic regions.

b. *The water content in hydrous silicate melt at uppermost lower mantle conditions (H. Fei)*

The mantle transition zone is considered to be a major water reservoir because its dominant minerals, wadsleyite and ringwoodite, may contain up to ~ 1.0 wt. % of water. This is supported by several lines of evidence, including electrical conductivity, mineral viscosity, and a water-rich ringwoodite inclusion in a natural diamond. In contrast, the lower mantle should be relatively dry, because bridgmanite and ferropericlase may dissolve less than 0.1 wt. % water in their crystal structures. Dehydration melting should therefore occur during mantle convection as a result of the phase transformation of hydrous ringwoodite to bridgmanite and ferropericlase at the 660-km boundary. The question therefore arises whether a hydrous silicate melt is gravitationally stable at 660 km depth. This should be determined by the density contrast between the ambient transition zone, the lower mantle, and the hydrous silicate melt. Since the density of melt decreases with increasing water content, the water content of hydrous melt under 660-km depth conditions is critical for evaluating melt stability.

Because hydrous silicate melt is unquenchable at 660-km depth conditions, its water content cannot be measured directly. The water content was therefore estimated by mass balance calculation from multianvil experiments at 1600-2300 K and 23-23.5 GPa. Oxide mixtures with bulk compositions of $(Mg,Fe)_2SiO_4$ and $(Mg,Fe)SiO_3$ plus 5-22 wt. % H_2O were prepared from MgO, SiO_2, FeO, and $Mg(OH)_2$. The mixtures were loaded into Pt-Rh capsules and compressed to 23-23.5 GPa by multianvil experiments, followed by heating at 1600-2300 K with a duration of 5-1800 min. The run products contained quenched crystallized silicate melts and solid phases (mainly ringwoodite and/or bridgmanite). The compositions of the melts were analysed by electron microprobe. The melt fractions in the capsules were estimated from backscattered electron images. The water contents in the melts were calculated from mass balance by assuming that no water loss occurred at high temperatures, which was confirmed by time series experiments.

The experimental results show that the water content in melt systematically decreases from about 50 wt. % at 1600 K to 10 wt. % at 2300 K, and is relatively insensitive to the melt composition (Fig. 3.5-2). Increasing water content in the starting material increases the melt fraction, but does not affect the water content in the melt. At 1600-2000 K and 23.5 GPa, corresponding to the pressure and temperature conditions of slabs and surrounding mantle near 660 km depth, the density of dry silicate melts is 4.0-4.3 g/cm^3, whereas the partial molar volume of H_2O is 6.2-6.4 cm^3/mol. With the water content of 20-50 wt. % at 1600-2000 K as obtained in this study, the density of hydrous silicate melt near 660 km depth is estimated to be < 3.9 g/cm^3, which is lower than the density of the ambient transition zone (~ 4.0 g/cm^3). The hydrous melt at the topmost lower mantle is therefore gravitationally unstable. However, it may be retained at the depth of the 660 km discontinuity if downward flow of the mantle compensates for buoyant ascent of the melt.

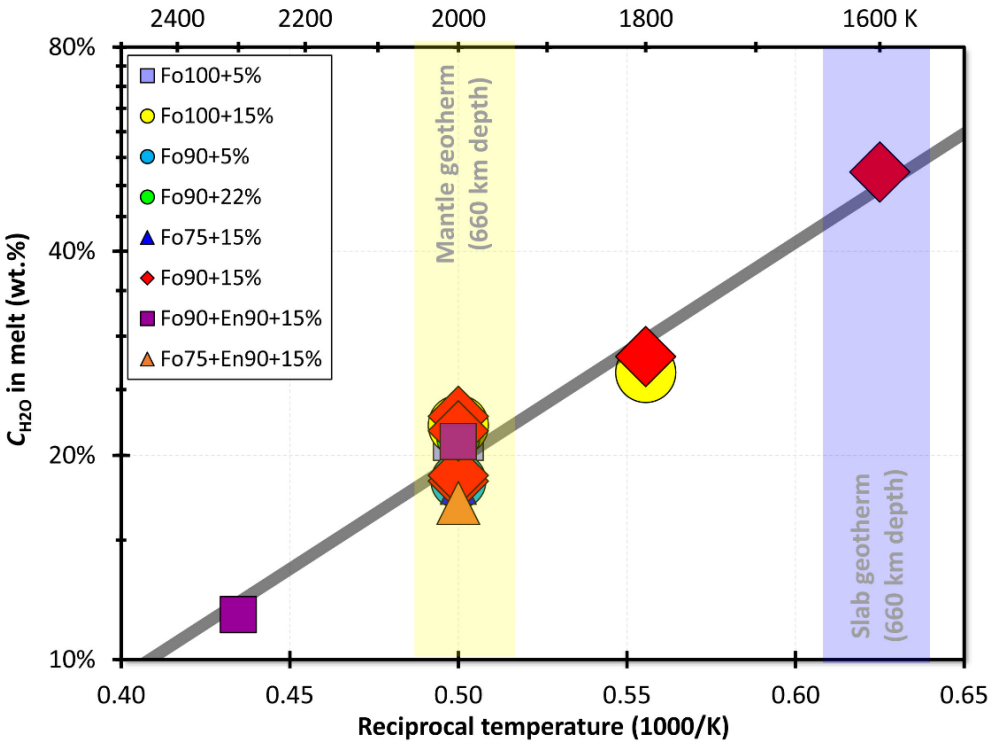

Fig. 3.5-2: The water content in hydrous silicate melt as a function of temperature at the pressure conditions of 23-23.5 GPa. Different symbols represent results from different starting materials with different Fe content, (Mg+Fe)/Si ratio, and bulk water content in the starting materials.

c. *The effect of faceting on olivine wetting properties (Y. Huang, T. Nakatani, S. Sawa and M. Nakamura/Sendai; C.A. McCammon)*

Pore geometry controls the fluid distribution in the mantle wedge and therefore affects element cycling and geophysical properties in subduction zones. The dihedral angle (θ) in the olivine-fluid system is a key parameter determining the fluid geometry in the mantle wedge. Both curved and faceted olivine-fluid interfaces occur in the system, but the effect of faceted planes on θ is poorly constrained and not well understood. We therefore measured the facet-bearing dihedral angles in the olivine-fluid system at various pressures (1-3 GPa), temperatures (800-1100 °C), and fluid compositions (pure H_2O, H_2O-NaCl, and H_2O-CO_2 systems). The experiments were conducted in an end-loaded piston-cylinder apparatus. The micro-texture of run products was studied with a field-emission type scanning electron microscope (SEM).

The results show that 1/3 of olivine-fluid dihedral angles involve faceted planes irrespective of the *P-T* conditions and fluid compositions. As shown in Figure 3.5-3, the θ values defined by the faceted-faceted (FF), faceted-curved (FC), and curved-curved (CC) interfaces are comparable in the pure H_2O systems at relatively low P–T conditions and in the H_2O–CO_2 system, where olivine solubility in the fluid is low (I group of experiments). On the other hand,

in the pure H_2O systems at high *P-T* conditions and in the H_2O–NaCl systems where the olivine solubility is high, the angles become larger in the following order: $\theta_{CC} < \theta_{FC} < \theta_{FF}$ (D group of experiments). These results contradict previous theoretical predictions that faceted planes with lower interfacial energy should result in low θ. To reveal the crystallographic orientation of

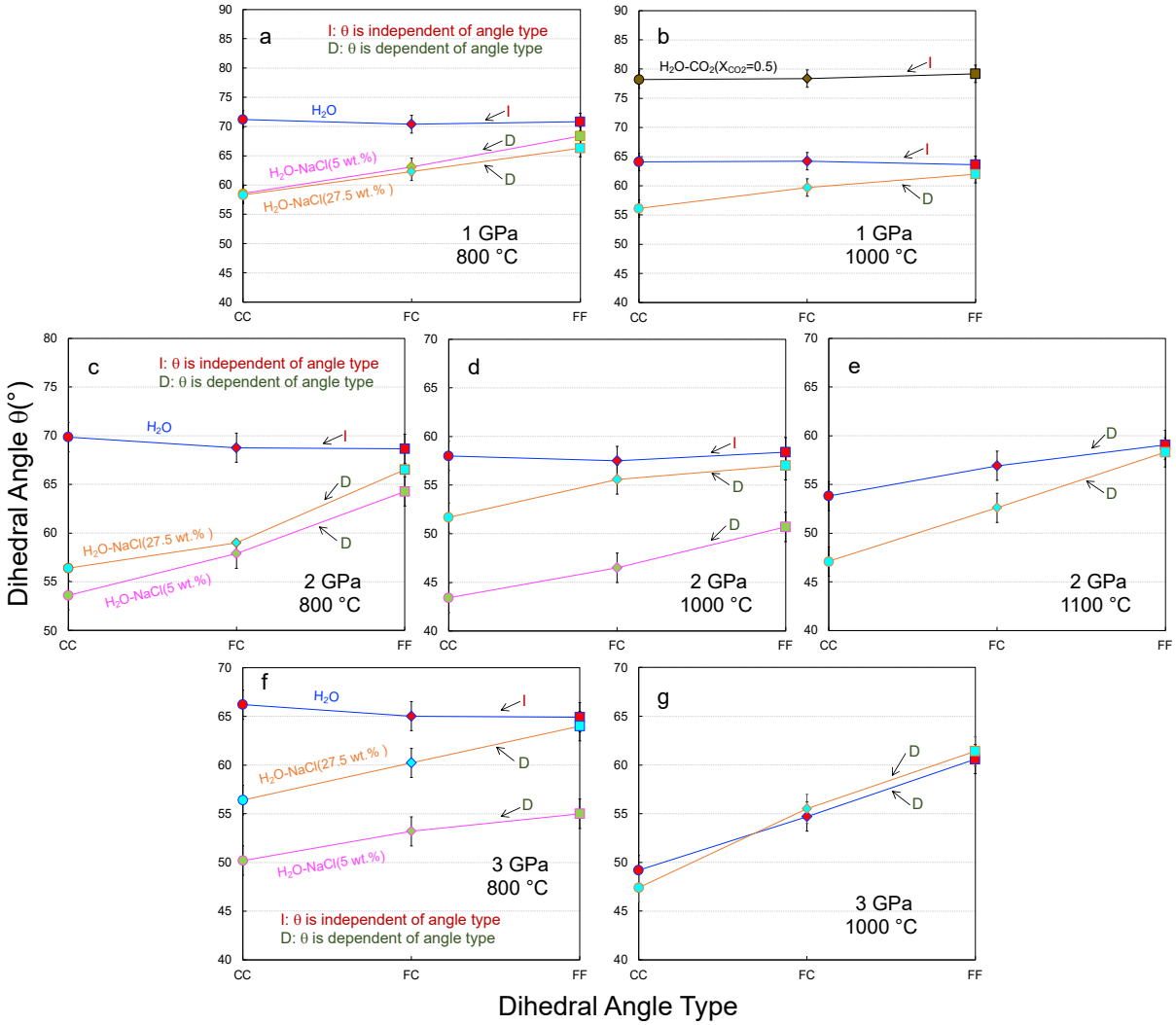

Fig. 3.5-3: Dependence of the median dihedral angles (θ) in the olivine-fluid system on the development of crystal facets at 1-3 GPa and 800-1100 °C. The fluid compositions are denoted by different colors in each panel. The error bar of ± 1.5° is shown in the panels. Abbreviations: ol = olivine; CC= curved-curved angle; FC = faceted-curved angle; FF = faceted-faceted angle; I, I group; D, D group of experiments.

olivine grain boundaries at triple junctions, which may affect the grain boundary energy, samples were investigated by electron back-scattered diffraction (EBSD). The results show that the run products do not have intense crystallographic preferred orientation (CPO), corresponding to the static compression conditions. Strikingly, the grain boundary plane distribution (GBPD) revealed that grain boundary planes of faceted and curved interfaces at the

triple junction were described by low Miller indices (such as (010), (001), (100)) for the I group experiments and by high Miller Indices (such as (015), (151), (152), (203)) for D group experiments (Fig. 3.5-4). This indicates that the grain boundary energies for FF, FC, and CC triple junctions are different, and facet-containing angles involve a lower grain boundary energy than CC angles. The grain boundary energy is mainly controlled by the crystallographic orientation, and interfacial energy is primarily controlled by both crystallographic orientation and solid solubility. The reduction of both grain boundary and interfacial energies results in the θ variation in the system. Surface energy minimization, including interfacial energy and grain-boundary energy, may be important for understanding the emergence of faceted planes in the system, and the physical properties of the texturally equilibrated fluid- or melt-bearing rocks.

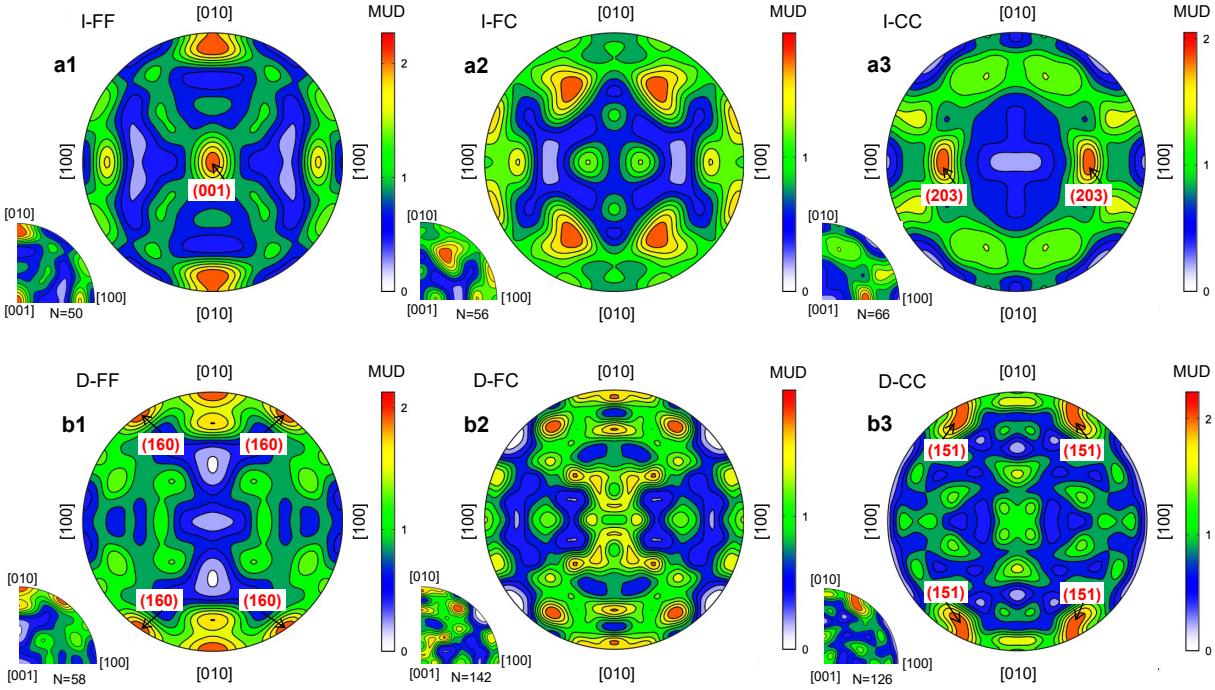

Fig. 3.5-4: Pole figures of grain boundary plane distributions. **a1-a3**, Grain boundary plane distribution in the I group experiments (where θ is independent of the angle type). **b1-b3,** Grain boundary plane distribution in the D group experiments (where the faceting increases θ). The equivalent olivine orientations obtained in the analysis were rearranged to fall into the first quadrant. Subsequently, by assuming that the grain boundary planes were equally distributed in each quadrant, the orientations in the first quadrant were copied in the other quadrants to obtain the pole figure. The analysed number (N) in the first quadrant is shown at the lower left in each pole figure. MUD is the multiples of uniform density, which shows the intensities in the color bar. Abbreviations: I, I group; D, D group; FF, faceted-faceted angle; FC, faceted-curved angle; CC, curved-curved angle.

In a mantle rock containing a saline fluid, the presence of faceting increases θ and critical fluid fraction, thus decreasing permeability. Therefore, the heterogeneity and tortuosity of fluid

distribution could be elevated by faceting in the mantle wedge, requiring a relatively high fluid fraction for establishing interconnected networks that generate high electrical conductivity anomalies. Moreover, our results suggest that permeability anisotropy may result from the anisotropy of the wetting properties of crystal faces under the extensive CPO generated by mantle flow.

d. *Mobility of water within an olivine matrix (A. Néri, L. Eberhard and D.J. Frost)*

Water is mobilized within the Earth's mantle through the destabilization of hydrous minerals that accompanies the subduction of the hydrated oceanic lithosphere. As water migrates through the mantle, it may transfer trace and major elements in the fluid phase. Water may also induce partial melting, and its solubility in nominally anhydrous minerals may influence their rheology and other transport properties. It is therefore essential to determine how water travels through rocks in the mantle.

The focus of this study is to examine the diffusivity of water through an initially dry mantle. Within a dense silicate matrix, water is generally considered to migrate through two different mechanisms: (1) diffusion along grain boundaries, and (2) free water percolation between grains. Both mechanisms are affected by the matrix grain size, but in the opposite direction. Indeed, the efficiency of diffusion along grain boundaries is proportional to the inverse of grain size, while percolation velocities are controlled by the matrix permeability that increases with the square of the grain size. Here, we are attempting to determine which mechanism controls water mobility within an olivine matrix using different matrix grain sizes.

To this aim, we have developed a new experimental setup. A sintered olivine core is sandwiched between a water source ($Al(OH)_3$) and a water sink (MgO), see Figure 3.5-5A. At high pressure and temperature (≈ 2.5 GPa and 500 °C), the water source dehydrates and releases water that is forced through the sintered olivine core due to the overpressure caused by the dehydration reaction. Water eventually reaches the water sink reservoir, progressively turning it into its hydrated form, namely brucite ($Mg(OH)_2$), see Figure 3.5-5B and the recovered sample in subfigure C. Time-series experiments were conducted with different olivine grain sizes, and the efficiency of water mobility was assessed from the thickness of the brucite layer and by recalculating a diffusion coefficient.

Results (Fig. 3.5-5D) show that for short times (18 h), small grain sizes allow a greater water flux than larger ones, with brucite layer thicknesses of ≈ 200 and ≈ 100 µm, respectively. However, for longer times (36 h), large grain sizes were able to increase the brucite layer thickness to ≈400 µm, while it barely increased for small grain sizes, *i.e.*, only up to ≈250 µm. Hence it appears that there is a switch in the mechanism of water transport through the olivine matrix. One explanation is that water is mobile through diffusion along grain boundaries until an interconnected network of water-saturated grain boundaries is formed between the water

source and sink reservoirs. The mechanism then switches to percolation, which is much more efficient for larger grain sizes than for smaller ones. A systematic increase of the mean grain size is also observed (Fig. 3.5-5E), highlighting an efficient dissolution process. Dissolution is similar to grain boundary diffusion in that it is also more efficient for small grain sizes and may control the early stages of water mobility.

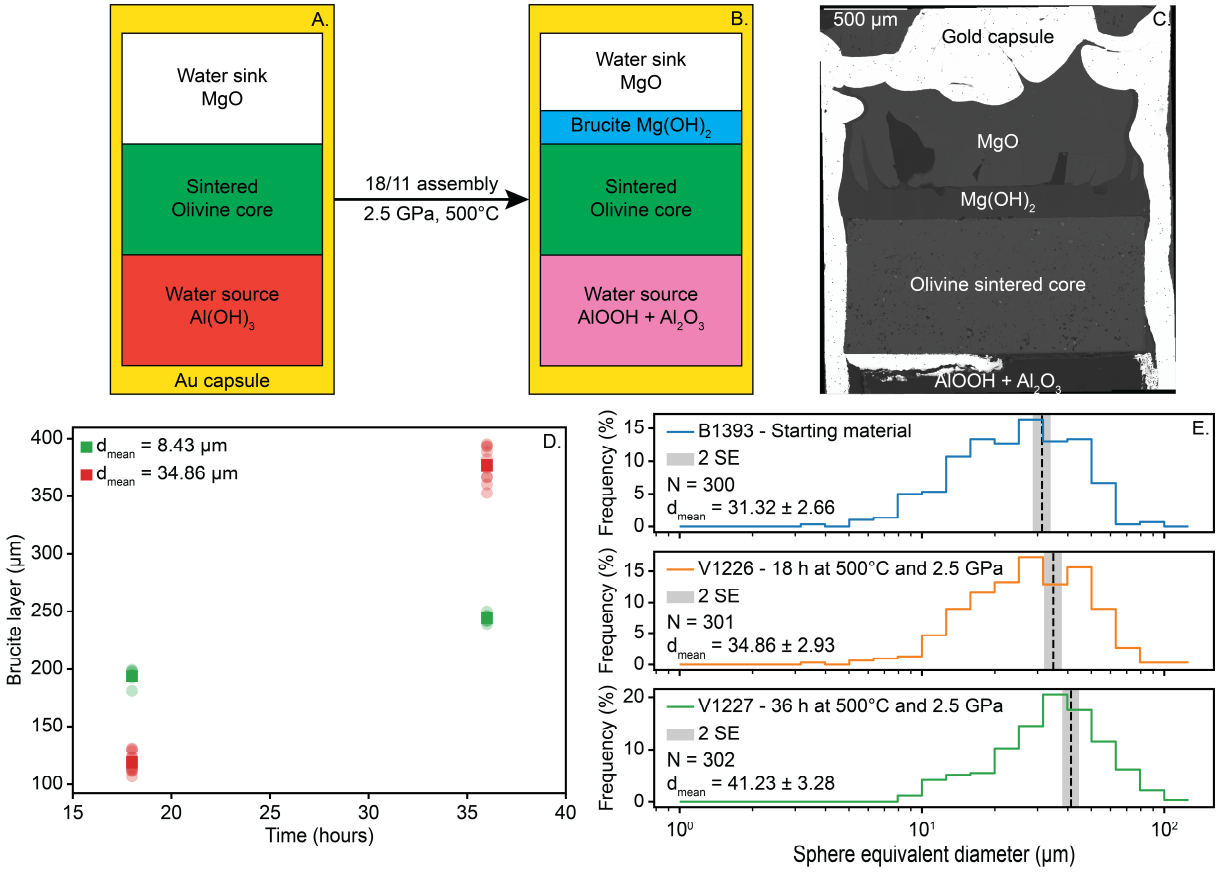

Fig. 3.5-5: Experiments on water mobility in an olivine matrix. (A) A schematic representation of the experimental setup at the beginning of the experiment. (B) At elevated pressure and temperature, the water reservoir is destabilized, and the released water travels through the olivine sintered core and partially hydrates the water sink reservoir. (C) SEM image of a recovered sample after 18 h at 2.5 GPa and 500 °C, using an olivine sintered core with a relatively small mean grain size. (D) Evolution of the brucite layer thickness as a function of time and for different grain sizes. (E) Evolution of the grain size in recovered samples as a function of the duration of the experiment.

e. *Grain growth-induced fluid segregation in deep-seated rocks (W. Fujita and M. Nakamura/Sendai, G.J. Golabek, P. Eichheimer and M. Thielmann; K. Uesugi/Hyogo)*

The segregation of geological fluids is an essential process controlling chemical differentiation and the physical properties of rocks in the Earth's interior. To understand the dependence of the efficiency of fluid segregation on microstructural development in polycrystalline aggregates,

we synthesised CHO fluid-bearing quartz aggregates with nominal fluid fractions between 1.9 and 18.0 % using the piston-cylinder apparatus at 900 °C and 1 GPa. The three-dimensional (3D) pore structure was successfully quantified by applying the pore network model (PNM) to X-ray microtomographic images, which showed distinctive differences in the 3D pore structure between CO_2-free and CO_2-bearing samples. The computed permeabilities suggest that permeability was controlled by interconnected porosity rather than by total porosity. The flow rates of each cross-sectional channel were also examined, which showed that permeability was largely controlled by the effective pathway (Fig. 3.5-6). The combined pore geometry observations and fluid flow simulation indicate that permeability is controlled by both fluid-solid wettability and grain-scale fluid distribution.

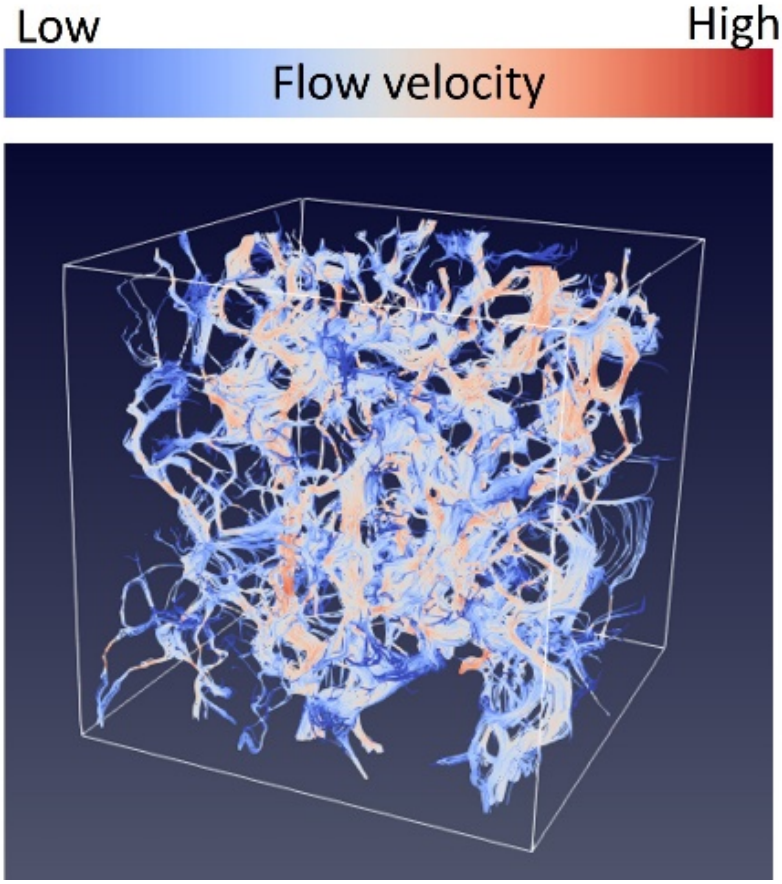

Fig. 3.5-6: Computed streamlines for fluid flow in a synthesised quartzite

f. *Water solubility in Fe-bearing wadsleyite at mantle transition zone temperatures (H. Fei and T. Katsura)*

Wadsleyite, with a chemical formula of $(Mg,Fe)_2SiO_4$, is the dominant mineral in the upper part of the mantle transition zone from 410 to 520 km depth. Because wadsleyite can contain up to ~ 3.0 wt. % H_2O as hydroxyl groups in its crystal structure, the transition zone is considered to be a major water reservoir in the Earth's interior. However, water solubility in

wadsleyite remains poorly constrained. Previous studies focused primarily on the Fe-free Mg_2SiO_4 endmember, which is not representative for Earth's interior, since wadsleyite in the mantle transition zone is Fe-bearing, and Fe may affect water solubility. Although a few studies investigated the water solubility in Fe-bearing wadsleyite, they covered only a limited temperature range.

We systematically investigated water solubility in Fe-bearing wadsleyite at 17.5 and 21 GPa as a function of temperature from 1500 to 2100 K, which covers the entire temperature range for wadsleyite stability in the Earth's interior from cold slabs to hot spots. The water solubility in Fe-free wadsleyite was also investigated for comparison. Wadsleyite single crystals were synthesised in multianvil experiments from mixtures of MgO, SiO_2, FeO, and $Mg(OH)_2$ with bulk compositions of Mg_2SiO_4 and $(Mg,Fe)_2SiO_4$ + 5 or 15 wt. % H_2O at 17.5-21 GPa, and 1500-2100 K. The wadsleyite crystals coexisted with hydrous silicate melt and high-pressure enstatite. The water contents (C_{H2O}) in the wadsleyite crystals were analysed by infrared spectroscopy.

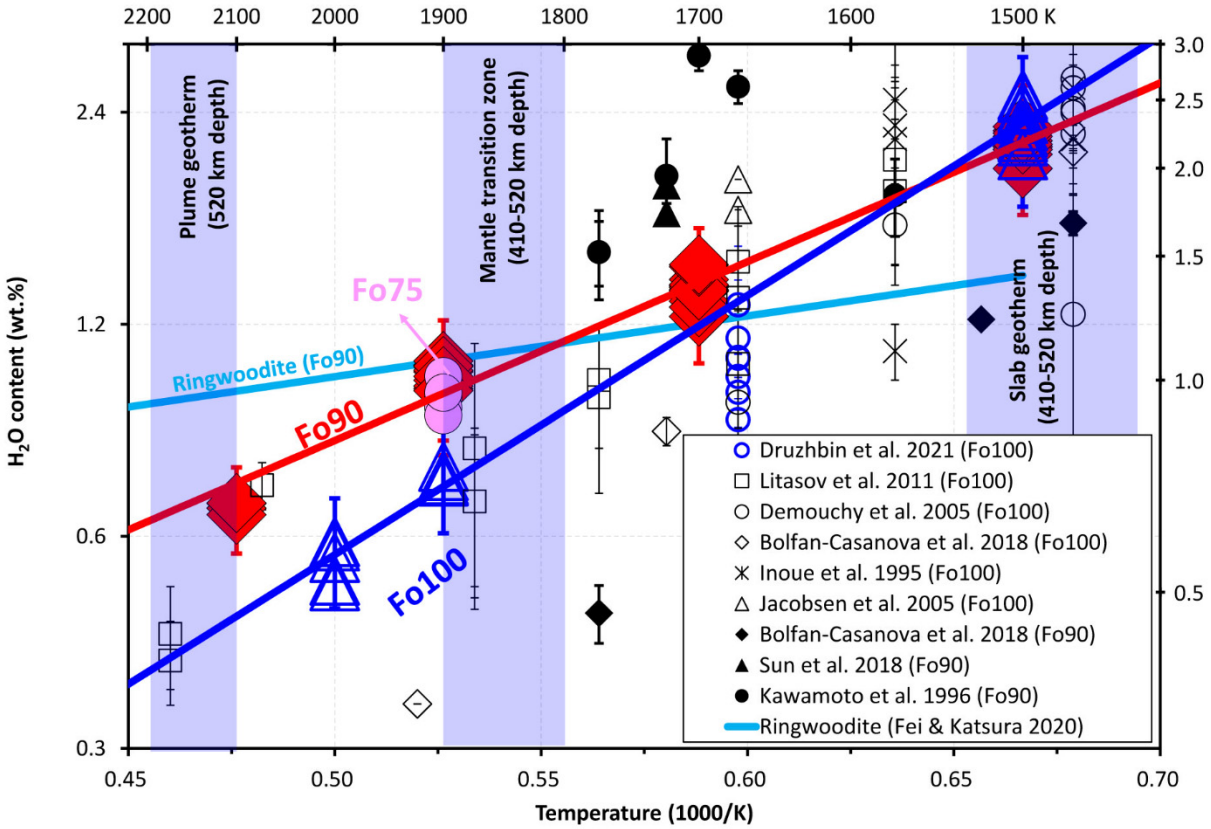

Fig. 3.5-7: Water content in Fe-free and Fe-bearing wadsleyite synthesised at 1500-2100 K. Fo90: Wadsleyite synthesised from $(Mg_{0.9}Fe_{0.1})_2SiO_4$ + H_2O. Fo75: Wadsleyite synthesised from $(Mg_{0.75}Fe_{0.25})_2SiO_4$ + H_2O. Fo100: The Mg_2SiO_4 endmember.

Water content in the Fe-free wadsleyite shows a clear temperature dependence (Fig. 3.5-7), decreasing from 2.4 wt. % at 1500 K to 0.6 wt. % at 2000 K. Similar to the Fe-free system, the

C_{H2O} in Fe-bearing wadsleyite also shows a negative temperature dependence, decreasing systematically from 2.2 wt. % at 1500 K to 0.65 wt. % at 2100 K, but the temperature dependence is smaller than for Fe-free wadsleyite. At 1500 K, the C_{H2O} values in Fe-free and Fe-bearing wadsleyite are essentially the same. But at 1900-2100 K, the Fe-bearing wadsleyite clearly contains more water than the Fe-free samples.

Although the H_2O solubility in wadsleyite decreases with increasing temperature, Fe-bearing wadsleyite may still contain approximately 1.0 wt. % H_2O in its crystal structure in the upper part of the mantle transition zone corresponding to 410-520 km depth for a geotherm of 1800-1900 K (Fig. 3.5-7). This value is essentially the same as that for ringwoodite at 520-660 km depth in the lower part of the mantle transition zone, assuming a geotherm of 1900-2000 K. Our data imply that the entire mantle transition could be H_2O-rich.

g. *Water solubility in majorite (D. Liu, N. Purevjav, H. Fei, A.C. Withers and T. Katsura)*

Water solubility in majorite, the second most abundant mineral in the mantle transition zone, is poorly constrained. Since the temperature has a large effect on the water solubility in nominally anhydrous minerals such as wadsleyite and ringwoodite, it is important to determine water solubility in majorite as a function of temperature to constrain the water storage capacity of the transition zone.

In this study, we synthesised majorite with compositions close to that expected for pyrolite at temperatures from 1670 to 2270 K at a pressure of 20 GPa using a multianvil press. All run products contained majorite coexisting with hydrous melt. The H_2O contents were measured by unpolarised Fourier-transform infrared spectrometry (FTIR). All examined majorite grains showed similar FTIR spectra despite variable compositions.

The water content in majorite decreases from 0.73 to 0.13 wt. % with increasing temperature from 1670 to 2270 K (Fig. 3.5-8). The water content in nominally anhydrous minerals is positively correlated with water activity in the system. With increasing temperature, melt fraction increases, and therefore the water content in melt decreases. As a result, the water activity in the system decreases, which causes the decrease of water content in the coexisting solid phases. The temperature dependence of water solubility in majorite is similar to that of wadsleyite, but distinctively higher than for ringwoodite (Fig. 3.5-8b). Water solubility is independent of the Al content in majorite. These results indicate that majorite contributes significantly to water storage in the transition zone. Majorite may be the main water reservoir at the top of the lower mantle.

When a slab crosses the 660-km discontinuity, hydrous ringwoodite should transform into bridgmanite, ferropericlase, and hydrous melt. Accompanying majorite coexisting with the hydrous melt could contain about 0.9 wt. % H_2O below the discontinuity if the temperature is

around 1600 K. A subsequent water release from majorite after the ringwoodite breakdown could form a melt-bearing layer at depths of 660 to 800 km. These melts could lower the viscosity in this region under subduction zones.

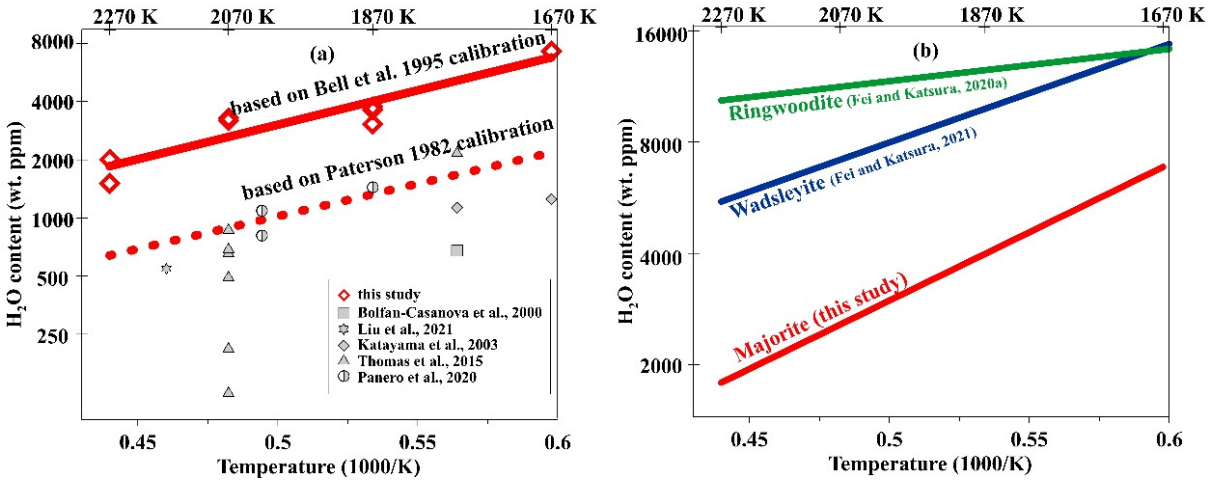

Fig. 3.5-8: Experimentally determined water solubilities in majoritic garnets as a function of temperature. The data shown by grey symbols are from previous studies.

h. *Water solubility in Al-free stishovite (N. Purevjav, H. Fei and T. Katsura)*

The water content in the lower mantle is thought to be much lower than in the overlying mantle transition zone and upper mantle, owing to the low water solubilities in the major lower mantle phases, bridgmanite, ferropericlase, and davemaoite ($CaSiO_3$). Nevertheless, stishovite, which is the high-pressure form of SiO_2 and one of the main phases in the subducting oceanic crust, could be a potential host of water in the lower mantle. A recent laser-heated diamond anvil cell study reported up to 10 wt. % H_2O in Al-free stishovite at pressures of 27-54 GPa and temperatures of 1300-2100 K, corresponding to the upper part of the lower mantle. However, in that study, water contents were simply estimated by comparing the unit-cell volumes of the hydrous samples with those of anhydrous samples, which may induce large uncertainties. Hence, the water content in Al-free stishovite needs to be quantitatively re-determined by more accurate experiments.

We synthesised large single crystals of stishovite at 22 GPa and 1573-2173 K under water-saturated conditions in multianvil experiments. The single crystals were polished on both sides and studied by unpolarised Fourier transform infrared spectroscopy (FTIR). Two or three crystals from each run were analysed, whereas five infrared spectra were taken from each crystal using a Bruker IFS 120 high-resolution FTIR spectrometer coupled with a Bruker IR microscope. After baseline subtraction and thickness normalization to 1 cm, the water contents in stishovite were calculated by integrating the OH bands between 2600 and 3400 cm^{-1} in each spectrum (Fig. 3.5-9), using the Paterson (1982) calibration.

Our results suggest that water solubility in Al-free stishovite under run conditions is 300-500 wt. ppm. These values are much smaller than those reported previously. The overestimation of water solubility in stishovite in previous studies is probably caused by the large uncertainties in the relationship between water content and unit-cell volume.

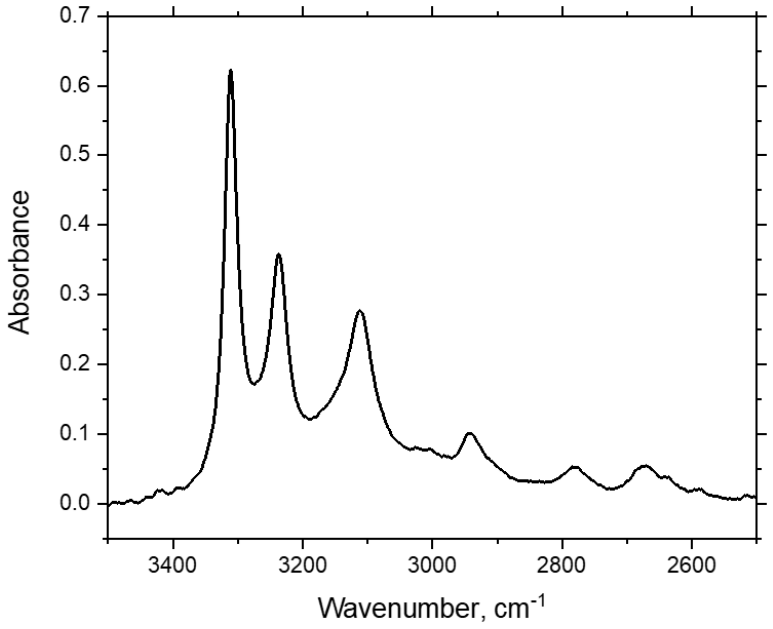

Fig. 3.5-9: A typical infrared spectrum of Al-free hydrous stishovite synthesised at 22 GPa and 1973 K. Sample thickness is 111 μm.

i. *Hydrogen incorporation mechanism in olivine (N. Purevjav, T. Boffa Ballaran, H. Fei, A.C. Withers and T. Katsura, in collaboration with C. Hoffmann/Oak Ridge)*

Olivine is the most abundant mineral in Earth's upper mantle. Thus, it may control the chemical and physical properties of this part of the Earth. Olivine may dissolve several hundred to several thousand wt. ppm H_2O in its structure, where the hydrogen can primarily substitute either for Mg or Si cations. These incorporation mechanisms significantly alter the defect chemistry of olivine and therefore affect elemental diffusivity, electrical conductivity, and rheological properties. However, the exact mechanisms of hydrogen incorporation in olivine are still debated.

The present study aims to understand the hydrogen incorporation mechanisms in hydrous olivine crystals at various pressures and SiO_2 activity conditions in Fe-bearing and Fe-free systems. We performed multianvil experiments in the MgO-SiO_2-$Mg(OH)_2$ and MgO-SiO_2-$Mg(OH)_2$-FeO systems at 10-12 GPa and 1523 K for heating durations of 48-96 h to produce chemically homogenous large single crystals of olivine. We used a combination of polarised infrared spectroscopy and single-crystal neutron diffraction for elucidating hydrogen positions and incorporation mechanisms in olivine at the atomic scale.

Chemically homogenous hydrous olivine crystals free of inclusions, cracks and twinning were measured at the TOPAZ single-crystal neutron diffractometer at Oak Ridge National Laboratory at 100-295 K. Our preliminary data suggest a substantial fraction of vacancies at the silicon site (Table 3.5-1). Two hydrogen-site anomalies around the tetrahedra suggest that hydrogen ions may primarily substitute for Si in the Fe-bearing olivine structure.

Table 3.5-1. Preliminary single-crystal neutron structure refinement data on hydrous olivine measured at 295 K.

Atoms	Coordinates			Occupancies	Displacement parameters					
	x	*y*	*z*		U_{11}x100	U_{22}x100	U_{33}x100	U_{12}x100	U_{13}x100	U_{23}x100
Mg1 Fe1	0	0	0	0.877(8) 0.123(8)	0.272(16)	0.479(34)	0.248(16)	0.019(16)	0	0
Mg2 Fe2	0.9905(1)	0.27742(8)	0.25	0.901(8) 0.099(8)	0.377(17)	0.271(36)	0.357(17)	0.020(16)	0	0
Si	0.4269(1)	0.0942(1)	0.25	0.976(7)	0.016(20)	0.118(46)	0.135(22)	0	0	0
O1	0.76604(9)	0.09171(8)	0.25	1.000	0.112(14)	0.419(34)	0.342(13)	0.023(14)	0	0
O2	0.2205(1)	0.44738(8)	0.25	1.000	0.332(14)	0.125(32)	0.375(14)	0	0	0
O3	0.27836(7)	0.16330(6)	0.03340(5)	1.000	0.311(10)	0.377(25)	0.310(11)	0.046(12)	0	0.155(10)

j. *Molar absorptivities of near-infrared OH^- and H_2O bands in peridotitic glasses (D. Bondar, A.C. Withers, D. Di Genova, H. Fei, H. Bureau/Paris; M. Wiedenbeck and F. Couffignal/ Potsdam; T. Katsura)*

Due to its availability, high sensitivity, non-destructive nature and the possibility to analyse small samples using a microscope attachment, infrared spectroscopy became a popular analytical tool to determine H_2O contents in materials science and geoscience in the past decades. In geoscience, it is used to quantify H_2O in both natural samples and experimental run products. Moreover, this technique not only allows to determine the total H_2O content, but also to estimate the abundances of different hydrous species, notably hydroxyl groups and water molecules.

One of the main challenges when quantifying H_2O contents by infrared spectroscopy is a choice of the appropriate molar absorption coefficient. In the case of silicate glass, the technique was calibrated previously for relatively silica-rich glasses of rhyolitic to basaltic compositions with non-bridging oxygen to tetrahedrally coordinated cation (NBO/T, a measure of degree of depolymerization) ratios from 0 to 0.8 and MgO contents from 0 to 10 wt. %. In this study, we expanded the compositional range to extremely depolymerized peridotitic glasses (NBO/T ≈ 2.5) with MgO content up to 43.5 wt. % and obtained molar absorption coefficients for the combination bands at 4500 cm^{-1} and 5200 cm^{-1}, which correspond to hydroxyl groups and water molecules, respectively. For this purpose, a one-of-a-kind set of peridotite glasses with H_2O contents from 0.2 to 4.5 wt. % was used. Total water contents of peridotitic glasses were determined by elastic recoil detection analysis in combination with secondary-ion mass spectrometry.

The integrated molar absorption coefficients of the combination bands at 4500 cm^{-1} and 5200 cm^{-1} were determined as $\varepsilon^*_{OH} = 134 \pm 20$ and $\varepsilon^*_{H2O} = 111 \pm 20$ liter $mol^{-1}cm^{-1}$, respectively. The latter was refined using the constant ratio of $\varepsilon_{H2O} / \varepsilon_{OH} = 0.83$ observed in the previous studies. These values follow the previously observed trend in more silica-rich glasses (Fig. 3.5-10), involving a linear decrease in molar absorption coefficient with decreasing silica content from rhyolitic over dacitic and andesitic to basaltic glasses. This finding has two important implications. Firstly, it refutes the hypothesis that the combination band at 4500 cm^{-1} only accounts for OH groups associated with network formers (Si, Al)-OH, and is not applicable to estimate OH^- species in highly depolymerized melts. We argue that it also accounts for OH^- groups associated with non-network cations (Mg, Ca)-OH and, therefore, it can be used to quantify water in depolymerized melts. Secondly, it means that using the obtained integrated molar absorption coefficients and their compositional dependencies, it is now possible to precisely quantify H_2O by infrared spectroscopy in a whole range of ultramafic glasses.

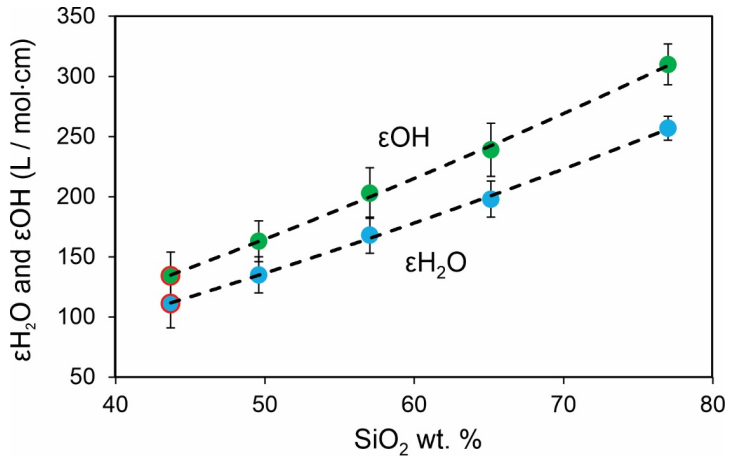

Fig. 3.5-10: Compositional dependence of integrated molar absorption coefficients for molecular H_2O and hydroxyl OH^- groups. From the highest to the lowest SiO_2 content, each pair of molar absorption coefficients corresponds to rhyolitic, dacitic, andesitic, basaltic and peridotitic glasses. The latter are outlined in red.

k. *Estimating the viscosity of volcanic melts from Brillouin data of their parental glasses (D. Di Genova, T. Boffa Ballaran and A. Kurnosov)*

Volcanic activity encompasses the slow extrusions of lava domes, relatively calm effusion of lava flows, as well as the extremely fast and dramatic injection of volcanic ash and gas into the atmosphere, and the deposition of fast-moving density currents on the Earth's surface. The study of the mechanisms that determine the timescale and style of eruptions is central to the assessment of natural hazards and risk mitigation.

Volcanoes erupt a multiphase high-temperature suspension (melt + crystals + gas bubbles) that is known as magma. Both the timescale and style of volcanic eruptions largely depend on a complex interplay between the physicochemical properties of magmas and processes that occur

during their ascent to the surface. Macroscopically, the flow of volcanic melts and their viscoelastic response to deformation are dominantly controlled by the shear viscosity η_s. The shear viscosity also affects microscale processes such as the kinetics of nucleation and growth of crystals and gas phases as well as their separation from the carrying liquid phase. The interaction and timescale of these processes ultimately impact the magma ascent pathway, thus concurring to determine the dynamics, fate and style of volcanic eruptions. Consequently, accurate knowledge of η_s is pivotal to simulate the expected eruptive scenarios of a given volcano and assess the associated risks.

The determination of the shear viscosity of volcanic melts is intrinsically based on viscosity data measured as a function of the liquid temperature T and chemical composition χ. High-quality viscosity data are essential to accurately parameterize $\eta_s(T, \chi)$ because small changes in χ in specific chemical domains can affect η_s by several orders of magnitude. However, experimental observations have recently reported that micro- and nano-scale modifications (*i.e.*, crystallization and/or phase separation) can occur within minutes when glasses are heated above the glass transition temperature (T_g, $\log_{10}\eta_s(T_g) = 12$) in the supercooled liquid region, or even within seconds at shallow undercooling when melts are subjected to fast cooling rates. These modifications dominantly result in the formation of iron-bearing nanocrystals that increase the shear viscosity through complex chemical and physical mechanisms, such as the chemical modification of the melt, formation of high-viscosity shells around crystals, and possible formation of aggregates that effectively increase the solid volume fraction in the melt.

Of particular interest here is an alternative experimental approach to estimate the viscosity of anhydrous and hydrous melts that is based on Brillouin light scattering and differential scanning calorimetry (DSC) measurements of volcanic glasses. This approach effectively minimizes or even avoids the impact of melt heat treatment and requires small (~ 10 mg) quantities of material. We explore a chemical space of dry and hydrous glasses that virtually encompass the full range of magmatism on Earth.

We used the Mauro-Yue-Ellison-Gupta-Allan (MYEGA) formulation that describes melt viscosity from the knowledge of three key parameters: melt fragility, $m(\chi)$; glass transition temperature, $T_g(\chi)$, and viscosity at infinite temperature, $\eta_\infty(\chi)$. The temperature dependence of the shear viscosity η_s is described according to:

$$\log_{10}\eta_s(T) = \log_{10}\eta_\infty + (12 - \log_{10}\eta_\infty)\frac{T_g}{T}\exp\left[\left(\frac{m}{12-\log_{10}\eta_\infty} - 1\right)\left(\frac{T_g}{T} - 1\right)\right]$$

where m is the melt fragility:

$$m = \left.\frac{\partial \log_{10}\eta_s}{\partial T_g/T}\right|_{T=T_g}$$

The melt fragility m describes how fast the melt viscosity increases when T_g is approached upon cooling. The glass transition T_g is, by definition, the temperature at which the melt viscosity is 10^{12} Pa s. The viscosity at infinite temperature, η_∞ can be considered constant (10^{-}

[2.9] Pa s) and independent on chemical composition. Therefore, one needs to know T_g and m to derive the viscosity of any volcanic melt as a function of T.

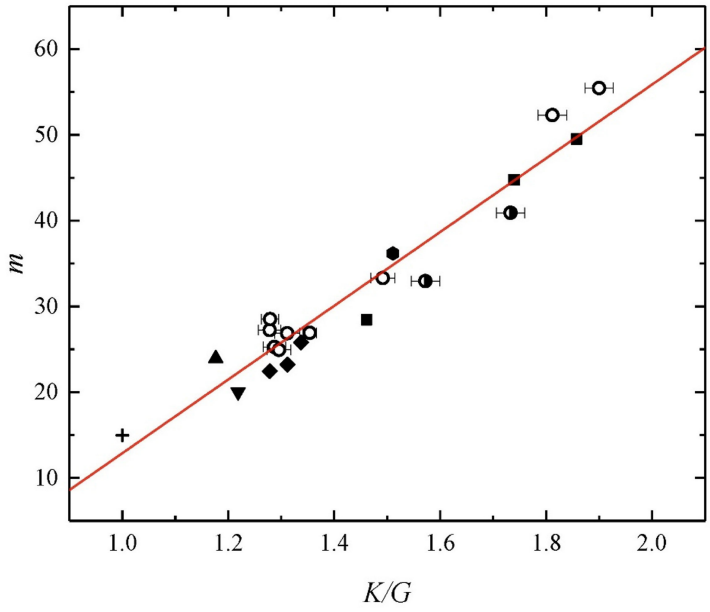

Fig. 3.5-11: Melt fragility as a function of spectroscopic parameters of glass. Relationship between the melt fragility m and the ratio of the bulk and shear moduli K/G of anhydrous samples.

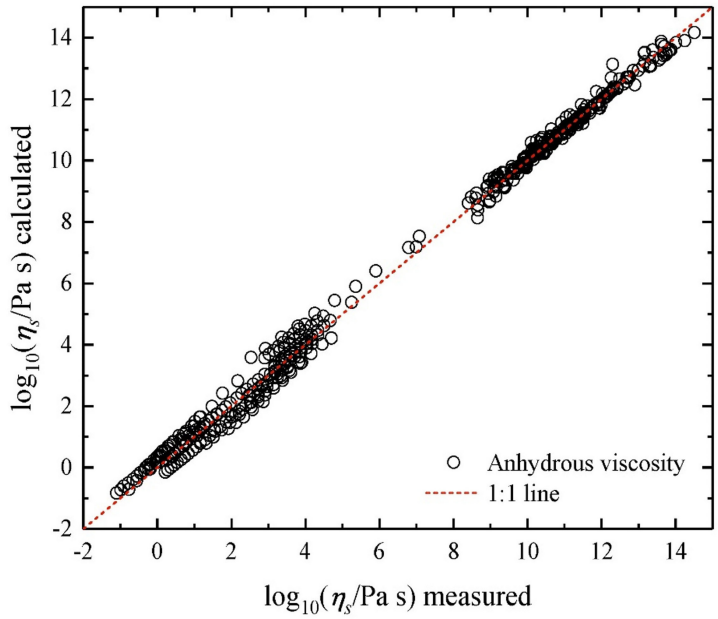

Fig. 3.5-12: Predictions of anhydrous viscosity used for model calibration. Comparison between anhydrous viscosity data (N_{dry} = 441) from the literature and MYEGA predictions using the melt fragility m derived by BLS data.

Here we show (Fig. 3.5-11) a correlation between the instantaneous bulk (K_∞) and shear (G_∞) elastic moduli of our volcanic glasses with m. Specifically, the elastic moduli were obtained from the longitudinal (v_p) and shear (v_s) sound velocities measured by Brillouin light scattering (BLS) and the results showed a linear correlation between K_∞/G_∞ and m. DSC data from the literature were used to derive the glass transition temperature T_g. We show (Fig. 3.5-12) that the combination of BLS and DSC allows the parameterization of melt viscosity at any temperature without the need to measure the viscosity.

Our study demonstrates that the viscosity of volcanic melts at eruptive temperatures can be accurately predicted from the spectroscopic analysis of the parental glass. We introduce a novel approach to derive the viscosity of volcanic melts covering over ~ 14 orders of magnitudes. The model was trained and validated at volcanologically relevant conditions using two large and non-overlapping anhydrous and hydrous datasets, encompassing virtually the entire range of magmatism on Earth. Our work opens a new scenario for modelling the chemical contribution to the viscosity of glass-forming melts on a physically substantiated basis using their parental glasses. This can be critical for volcanic liquids that tend to undergo modifications during viscosity measurements. Indeed, the possibility of deriving the viscosity of homogenous and nanocrystal-free volcanic melts enables the accurate quantification of the effect of nanocrystal formation on magma viscosity and therefore the eruptive dynamics of volcanoes.

I. *Modelling silicate melt viscosity using differential scanning calorimetry (D. Langhammer, D. Di Genova and G. Steinle-Neumann)*

The eruption dynamics of volcanoes is governed by the three *V*s of volcanology: viscosity, volatiles and volume. In this context, the presence of volatiles, water in particular, causes bubble formation by degassing, which releases a large amount of energy and increases the potential for an explosive eruption. Moreover, H_2O also exerts a strong influence of the shear viscosity η of the melt that constitutes the magma. Models to describe the dependence of η on temperature (T) and H_2O content are trained using experimentally derived η and are therefore sensitive to the quality of data. Viscometric measurements can be performed in two η ranges, both of which are subject to limitations: Around the glass transition temperature (T_g), with $\eta = 10^{12}$ Pas, melts measured in viscometry have been shown to develop (nano)crystals which influence η, while higher-T measurements are free from this problem. However, the high-T regime becomes experimentally difficult to access for water-bearing melt. Therefore, a method to reliably determine η of anhydrous and hydrous melts is of great importance for physical volcanology.

To enhance the quality of η data we use measurements from differential scanning calorimetry (DSC) to derive viscosities. DSC works on shorter timescales, is less arduous in sample preparation compared to traditional viscometric techniques, and minimizes (nano)crystallization. Viscosities are derived using an empirical linear dependence between the heating/cooling rate during a DSC measurement, η and characteristic DSC temperatures, via the shift factor K. Characteristic DSC temperatures are distributed around T_g only, making the high-T regime, where magmas are erupted, not directly accessible. Here, we use the assumption of a constant viscosity at infinite T ($\log \eta_\infty = -2.9$), with the value derived from fitting a large set of technical melts by the MYEGA model (see the previous chapter), to constrain the high-T behaviour of volcanic melts.

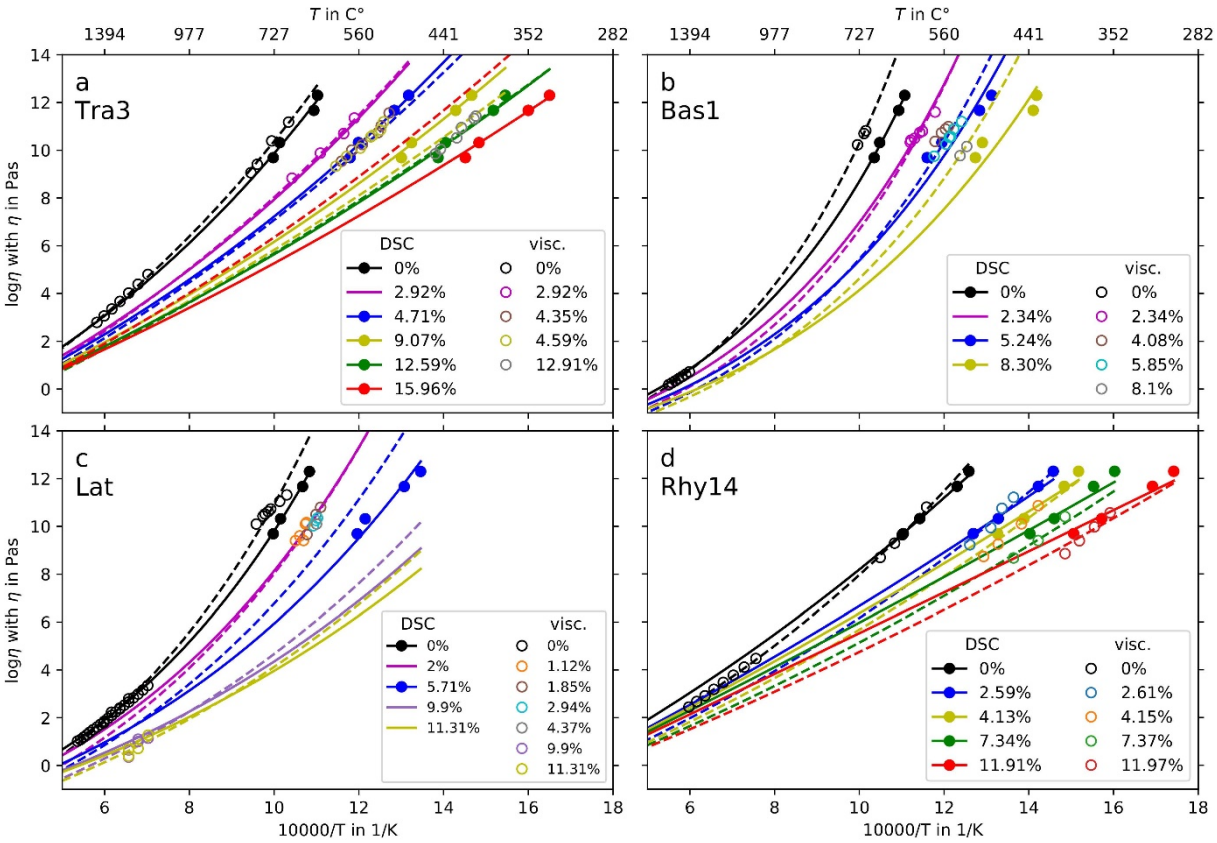

Fig. 3.5-13: Comparison of viscosity data for a trachyte (Tra3, a), a basalt (Bas1, b), a latite (Lat, c) and a rhyolite (Rhy14, d). DSC-derived viscosities (filled circles) are based on Di Genova *et al.* (Geochim. Cosmochim. Acta, *142*, 314, 2014) using appropriate shift factors *K*. Viscometry measurements (open circles) for Tra3 are from Romano *et al.* (Chem. Geol., *202*, 23, 2003), for Bas1 from Giordano and Dingwell (Bull. Volcanology, *65*, 82003), for Lat from Misiti *et al.* (Chem. Geol., *290*, 50, 2011), and for Rhy14 from Di Genova *et al.* (J. Volcanology and Geothermal Research, *249*, 201, 2013). Our fits to the DSC data (solid lines) use $\log \eta_\infty = -2.9$ as a constraint. For comparison, our fits to viscometric data from the same compositions are included (dashed lines). H_2O contents indicated in the legends by solid lines only (DSC column) show curves for which the DSC model is evaluated without DSC-derived η data available. Water content is given in mol. %.

We illustrate this approach by fitting anhydrous DSC-derived η data for four different samples (Fig. 3.5-13) with the MYEGA model, which we extend to describe H_2O dependence, using $\log \eta_\infty = -2.9$. Comparing these to viscometric η data shows some deviation in the vicinity of T_g as can be expected for melts with and without nanocrystal formation. At higher T, the model predictions based on the DSC data, derived around T_g only, are in very good agreement with viscometric measurements. These are assumed to be more reliable due to a much lower tendency of crystallization at high T. As introducing water into the melt results in the high-T regime becoming difficult to access for viscometry measurements, reliable predictive models are all the more important.

m. *Effects of composition in the liquid Fe–Ni–C system (E. Posner and G. Steinle-Neumann)*

The material properties of Fe–Ni–light element (LE) alloys at high pressure and temperature are required for understanding the origin and evolution of planetary cores. However, most previous experimental and theoretical studies in mineral physics have used pure liquid Fe or binary metals as core material analogues, which may oversimplify compositional effects. In particular, nickel is often assumed to be iron's "geochemical twin" owing largely to their similar atomic mass and radius, and has therefore been frequently excluded from the associated literature. However, the appropriateness of this simplifying assumption has recently come under debate. In this study, we performed first-principles molecular dynamics simulations to systematically investigate the Fe–Ni–C system, including (1) pure Fe and Ni, (2) binary Fe–Ni, Fe–C, and Ni–C, and (3) ternary Fe–Ni–C liquid compositions, at 3000 K and three simulation volumes corresponding to pressures (P) up to 83 GPa.

Liquid structural properties and coordination numbers analysed using partial radial distribution functions show that the average interatomic distance between two Fe atoms ($r_{\mathrm{Fe\text{-}Fe}}$) is sensitive to Ni ($X_{\mathrm{Ni}}$) and C ($X_{\mathrm{C}}$) concentration (Fig. 3.5-14). One might intuitively expect that higher concentrations of slightly larger Ni atoms would gently expand the Fe framework, *i.e.*, increase $r_{\mathrm{Fe\text{-}Fe}}$, while the smaller carbon atom should have the opposite effect. However, this is not observed: $r_{\mathrm{Fe\text{-}Fe}}$ decreases with increasing X_{Ni}, while it increases with X_{C}. Average $r_{\mathrm{Fe\text{-}C}}$ and $r_{\mathrm{Ni\text{-}C}}$ values also decrease with increasing X_{Ni} and generally remain constant between the two lowest P points, corresponding to a coordination change of carbon from ~ 6 to ~ 8, and then decrease with additional P once the coordination change is complete. Carbon clustering occurs in both binary (especially Ni–C) and ternary compositions with short-range $r_{\mathrm{C\text{-}C'}}$ values ranging from ~ 1.29 to ~ 1.57 Å, which overlaps with $r_{\mathrm{C\text{-}C}}$ in diamond and graphite. Most compositions show that $r_{\mathrm{C\text{-}C}}$ increases with P, which also reflects the carbon coordination change and increasing occupancy in larger quasi-interstitial voids.

Fe and Ni are commonly assumed to be essentially equivalent species (*i.e.*, "geochemical twins") in iron-rich liquid alloys. If true, the proportional contribution of Fe and Ni to a given total coordination number should be equal to their atomic fraction. We tested this hypothesis and found that this assumption generally does not hold in liquid Fe–Ni and Fe–Ni–C, especially for compositions with $X_{\mathrm{Ni}} > 0.25$, as demonstrated by deviations from zero shown in Figure 3.5-15. The results indicate that Fe and Ni show preferential packing behaviours: they each prefer to pack around themselves over each other, and Fe more strongly coordinates around C than Ni. This reflects the presence of Ni-C and – to a lesser extent – Fe-Ni repulsive forces and Fe-Fe and Ni-Ni attractive forces, which negates the assumption that Fe and Ni are "geochemical twins"; their equilibrium positions clearly distinguish between species.

The results presented here systematically show the effects of Ni and C on the structural properties of iron alloy liquids, which may affect the metal-silicate partitioning behaviour of elements (*e.g.*, sulphur) during planetary core formation. These findings thus highlight the need for renewed study of more realistic, multi-component, and particularly Fe–Ni–light element core analogue compositions to obtain accurate core model parameters.

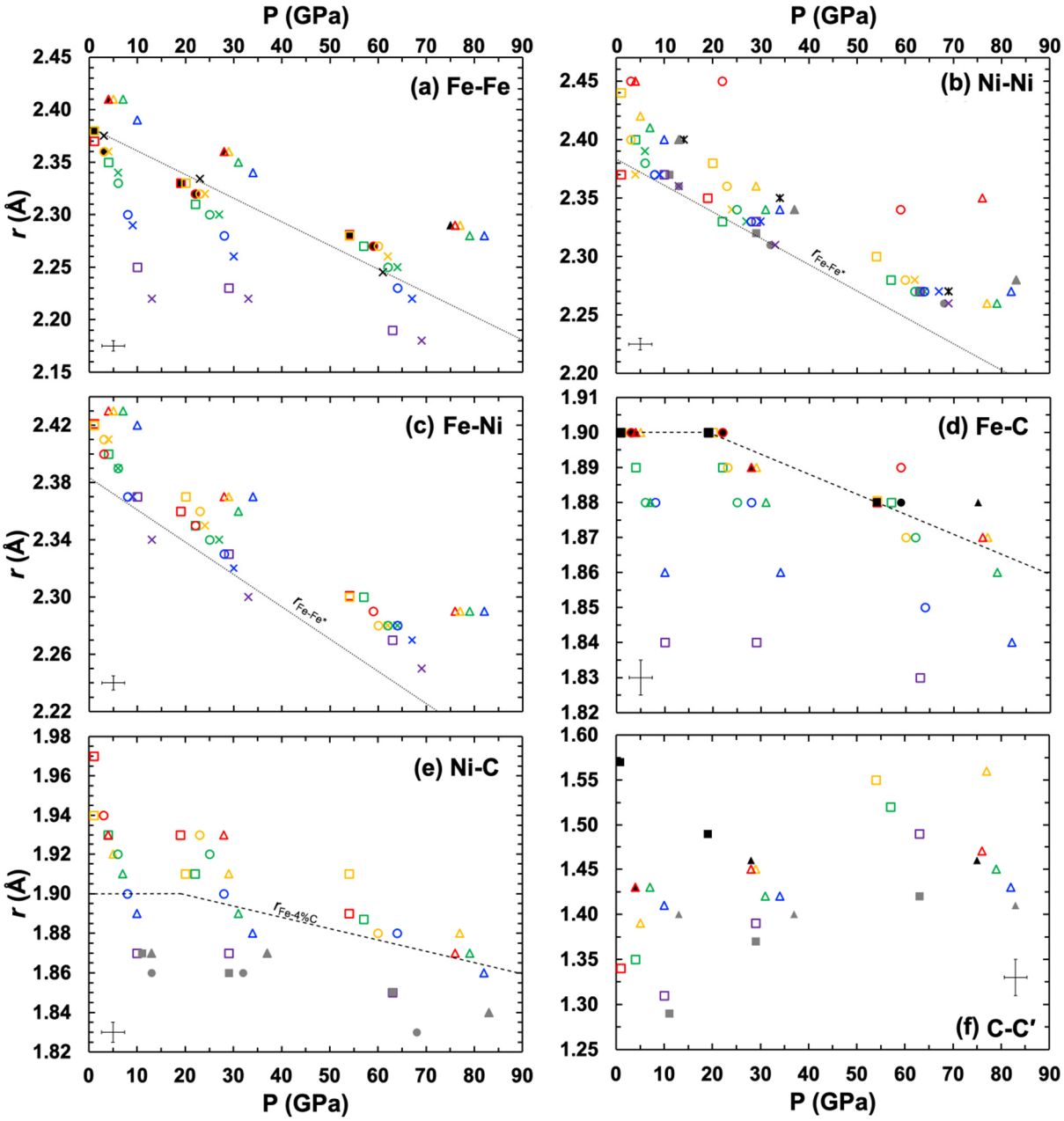

Fig. 3.5-14: Average radial positions r (*i.e.*, interatomic distances) of the first partial radial distribution peaks for all investigated compositions as a function of P. The dotted trend lines in (a–c) show a linear fit to $r_{\text{Fe-Fe}}$ in pure Fe, and the dashed trend lines in (d) and (e) show the step-wise fit to $r_{\text{Fe-C}}$ in Fe–4%C. The average distances between all atomic pairs except for C-C′ (*i.e.*, short-range C-C clustering peak) generally decrease with X_{Ni}, particularly for $r_{\text{Fe-Fe}}$, $r_{\text{Fe-C}}$, and $r_{\text{Ni-C}}$. The $r_{\text{Fe-Fe}}$ and $r_{\text{Fe-Ni}}$ values also increase with X_{C}. Some Ni-poor compositions show no Ni-Ni peak or only very large-r peaks (~ 6.2 Å) and are therefore not shown. The compositions are represented as follows: pure Fe (black crosses); pure Ni (black asterisks); Fe–Ni (colored crosses); Fe–C (black filled symbols); Ni–C (grey filled symbols); and Fe–Ni–C (unfilled colored symbols). Red, yellow, green, blue, and purple symbols represent 1–2, 5–7, 25, 50, and 90 at. % Ni, respectively. Circles, squares, and triangles represent 1, 4, and 20 at. % carbon, respectively.

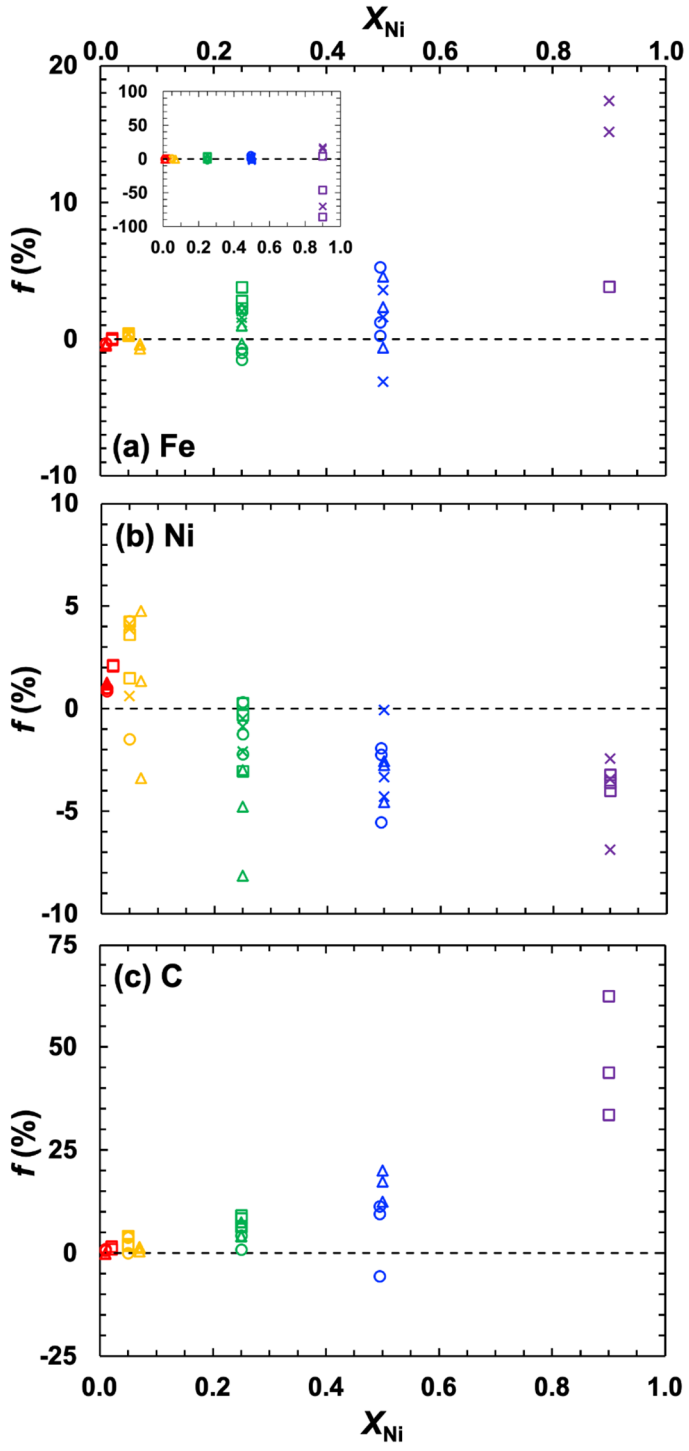

Fig. 3.5-15: Percent deviation f of the proportion of Fe atoms contributing to the total number of framework atoms (Fe + Ni) comprising the average coordination number of (a) Fe, (b) Ni, and (c) C, according to $f = (A - C)/C \times 100$, where $A = N_{a-\mathrm{Fe}}/(N_{a-\mathrm{Fe}} + N_{a-\mathrm{Ni}})$, $N_{a\text{-}b}$ represents the average number of nearest neighbors of species b surrounding an atom of species a, and $C = X_{\mathrm{Fe}}/(X_{\mathrm{Fe}} + X_{\mathrm{Ni}})$. The contributions of carbon to the total coordination number ($N_{a\text{-C}}$) are excluded because carbon is not a framework species. Dashed vertical lines indicate zero deviation, for which Fe and Ni are considered essentially identical substitutional species (*i.e.*, "geochemical twins"). The symbols are the same as those presented in the caption of Figure 3.5-14.

3.6 Rheology and Metamorphism

Rheology describes how materials deform in response to an applied external stress. For the Earth and other terrestrial planets, rheology is of fundamental importance for a range of dynamical processes such as faulting, earthquakes and the plastic solid-state flow of rocks. The rheology of the mantle is of particular importance for the Earth because it determines rates of large-scale solid-state convection, which is critical for understanding a broad range of dynamical evolutionary processes such as the Earth's thermal evolution, plate tectonics, the mixing of chemical heterogeneities, and the fate of subducted slabs. In order to understand such processes, experimental and theoretical studies of the rheology of rocks have been pursued for many years.

Experimental studies are performed by measuring the strain rate of a sample that is subjected to an applied stress. One difficulty is that the time scales of laboratory experiments are necessarily many orders of magnitude shorter than time scales of deformation in the Earth. This means that experimental stresses and deformation rates both need to be much higher than in nature. In order to apply experimental results to the Earth's interior, large extrapolations are required – which may not be valid because deformation mechanisms at the atomic level may differ in experiments and the Earth because of greatly-different stress levels. Additional problems arise because rheology is dependent on a large number of factors, including stress and strain rate, temperature, pressure, grain size, the density and nature of crystal defects, mineralogy, and the presence or absence of fluids.

Understanding the rheology of bridgmanite (silicate perovskite), the most abundant mineral in Earth's lower mantle, is essential for modelling the large-scale process of mantle convection. Studying bridgmanite rheology using conventional deformation experiments is extremely difficult because, in addition to the factors listed above, samples are extremely small, pressures need to be in excess of 25 GPa and measuring the applied stress is problematic. An alternative approach is to study the diffusion rates of the atomic species that are expected to control ductile flow. This is the approach adopted in the first contribution below, which describes a study of Si-Al interdiffusion in bridgmanite at 24 GPa and 2023-2300 K. Preliminary results suggest that the rate of Si-Al interdiffusion is 2 to 3 orders of magnitude slower than previously reported rates of silicon self-diffusion.

Rates of ductile deformation are generally enhanced by an increase in temperature, which increases rates of diffusion, and a reduction of grain size, which reduces distances across which diffusion needs to occur. The effects of these two parameters on subducting slabs are the subject of the second contribution. This is a numerical study of how grain size reduction combined with shear heating can cause the deep part of a subducting slab to sink and break away from the shallow part because of the negative buoyancy of the former. The results show that break-away depths depend strongly on the subduction velocity. The predictions of the model are consistent with observed depths of intermediate-depth earthquakes.

Deep focus earthquakes occur in the depth range 440-660 km. Their cause is enigmatic and has been the subject of debate for many years. Because of very high confining pressures in this depth range, the process of brittle fracture can be excluded. One possibility is that a combination of grain size reduction and shear heating leads to faulting by a runaway process. Alternatively, the transformation of metastable olivine to its high-pressure polymorphs, wadsleyite and ringwoodite, may result in "transformational faulting". This is considered to occur when the products of the transformation have a very small grain size which would allow high strain rates to occur in localized fault zones due to major rheological weakening. The third contribution below presents preliminary results of deformation experiments on Mg_2GeO_4 olivine, which transforms to spinel at much lower pressures than silicate olivine. The aim of this study is to evaluate the effect of the olivine grain size on transformational faulting.

High-pressure metamorphism of basaltic oceanic crust to form eclogite, consisting mainly of omphacitic pyroxene and garnet, is the topic of the final contribution in this section. Very fine-scale oscillatory zoning in the margins of an omphacite grain close to its contact with garnet is observed in an eclogite sample. Diffusion modelling indicates that the lack of homogenization of this zoning means that periods when fluids were present in the rock were extremely short, on the order of 50-5000 years.

a. *Al-Si interdiffusion in aluminous $MgSiO_3$ - bridgmanite evaluated by analytical scanning transmission electron microscopy (L. Czekay, N. Miyajima, C.A. McCammon and D.J. Frost)*

$MgSiO_3$-bridgmanite (Brg) is considered to be the dominant mineral in Earth's lower mantle. It occurs with an orthorhombic $GdFeO_3$-type perovskite structure with two cation positions: Si in octahedral coordination (B site substitution) and Mg occupying a larger pseudo-dodecahedral site (A site substitution). Aluminium (Al) is the most abundant trivalent cation substituting into bridgmanite. It can be incorporated either by substituting for Si, with charge balance provided through the formation of oxygen vacancies (OV), or by the charge-coupled substitution of Mg and Si by 2 Al. Diffusion studies in minerals are a fundamental tool for understanding the rheological properties of the mantle. Previous theoretical studies on deformational strain rates show that the key mechanism for deformation in bridgmanite is diffusion-controlled creep controlled by the slowest diffusing element, silicon. It is well accepted that the mantle must flow by solid-state creep. Consequently, its viscosity must depend on temperature (described by the activation energy) and pressure (described by the activation volume). Understanding Al-Si interdiffusion in bridgmanite is thus essential for understanding the rheology that controls mantle dynamics.

The aim of this study is to investigate Al-Si interdiffusion in Brg experimentally. Brg samples for the interdiffusion experiments were synthesised from pre-synthesised 0-5 mol. % Al_2O_3-bearing $MgSiO_3$ enstatite at 24 GPa and 2023 to 2300 K using high-pressure multianvil apparatus. In the next step, synthesised samples were placed together to form diffusion couples,

which were then annealed in subsequent experiments at the synthesis *P-T* conditions for 3, 6 and 21 hours. The resulting aluminium diffusion profiles were analysed across the diffusion interface in the recovered samples by scanning transmission electron microscopy (STEM) equipped with an energy-dispersive X-ray spectrometer (EDXS) (Fig. 3.6-1). In STEM-EDXS, compositions at the nanometre scale are evaluated and then used to infer Al substitution mechanisms in Al-bearing crystalline bridgmanite diffusion couples. The measured diffusion coefficient for interdiffusion (volume diffusion) is two to three orders of magnitude slower than the previously reported Si self-diffusion coefficient $D_{Si} = 1(1)\times10^{-18}$ m^2/s at 25 GPa and 2073 K.

We plan to perform diffusion experiments on bridgmanite at different temperatures and with different oxygen-vacancy concentrations to understand their influences on the diffusion-controlled creep rate. The resulting data will be used to place limits on deformational strain rates of bridgmanite in the lower mantle. Based on 2-dimensional element distributions in EDS chemical maps, diffusion experiments with a total volume of 1 mm^3 can be reliably conducted in a conventional multianvil press with careful sample preparation and chemical analysis of the recovered samples.

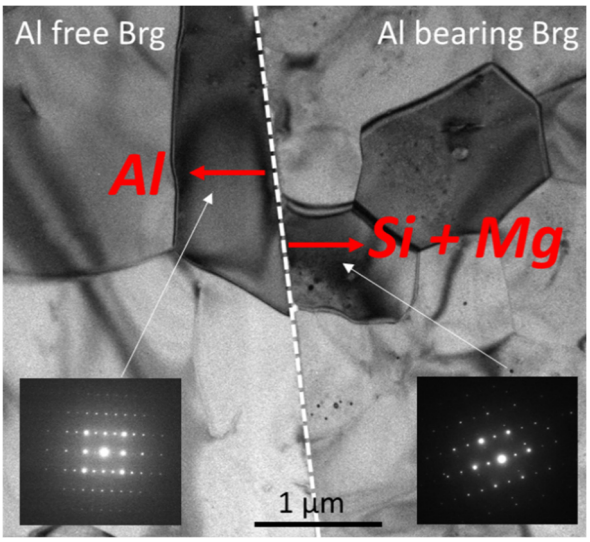

Fig. 3.6-1: A bright-field TEM image of a bridgmanite diffusion couple after an experiment at 24 GPa and 2023 K, indicating lattice diffusion of aluminium (Al), magnesium (Mg) and silicon (Si) in the charge-coupled substitution mechanism (indicated in red). Inserts: selected area electron diffraction patterns of oriented crystals. The white dashed line shows the location of the diffusion interface.

b. *Ductile weakening controls on the depth of slab break-off (M. Thielmann and S. Schmalholz/Lausanne)*

The process of slab break-off, where a subducting plate detaches from its shallower part due to its negative buoyancy, has been frequently invoked to explain a variety of different phenomena such as the occurrence of syn- and post-collisional magmatism, rapid surface uplift and subsidence as well as the spatial distribution of intermediate-depth earthquakes. However, there is also significant debate about whether the concept of slab break-off has been overused in the past. One reason for this ongoing debate lies within the still incompletely understood physical

processes that govern slab break-off. Recent studies have shown that ductile weakening processes have a major impact on this process and the timing of slab break-off.

In this study, we investigate the impact of two ductile weakening mechanisms - grain size reduction and shear heating - on the depth of slab break-off for a slab with a given subduction velocity. Based on previous studies, we employ a mathematical model of three coupled nonlinear ordinary differential equations that take into account these two weakening mechanisms and extend it to take into account a given subduction velocity. As the relative importance of grain size reduction or shear heating is currently unknown due to poor constraints of the respective material parameters, we first determine governing nondimensional parameter combinations using dimensional analysis. Having determined these parameters, we then employ our mathematical model to determine their control on slab break-off depth. The subduction velocity has a first-order impact on the depth of slab detachment, as can be seen in the example shown in Figure 3.6-2. For this specific example, slab detachment depths range from 0 km at very low subduction speeds to values of about 300-400 km at subduction speeds of 10 cm/yr. This is in broad agreement with observations of intermediate-depth seismicity in regions of ongoing slab detachment.

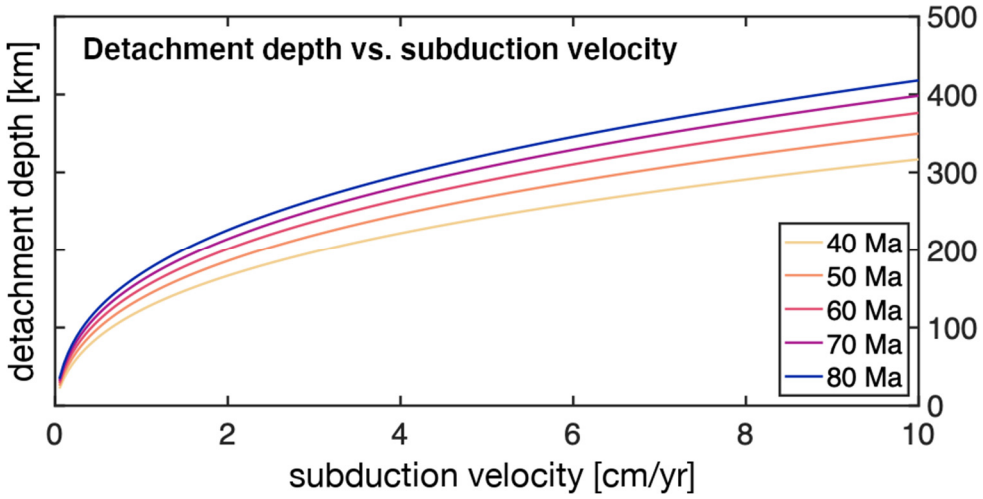

Fig. 3.6-2: Detachment depth vs. subduction velocity for oceanic slabs with different ages for typical Earth-like parameters. Results are re-dimensionalized to allow for a better comparison to observed data.

c. *Grain size dependency of the olivine-spinel phase transformational faulting mechanism for deep-focus earthquakes (S. Sawa, J. Muto and H. Nagahama/Sendai; N. Miyajima)*

Deep-focus earthquakes occur at depths that range from 440 km to 660 km in subducting slabs. Geophysical observations and deformation experiments show that the olivine-spinel phase transformational faulting mechanism may be the precursor of deep-focus earthquakes. This mechanism involves metastable olivine undergoing a phase transformation to fine-grained spinel with a shear instability developing as a consequence of the fine-grain size of the spinel.

Although the initial grain size of olivine is important for the kinetics of the transformation, and may determine whether transformational faulting occurs, previous studies have not investigated the initial grain size dependency of metastable olivine on the faulting mechanism. Therefore, we conducted deformation experiments on germanate olivine with grain sizes ranging from a few microns to hundreds microns.

Germanate olivine is an analog material of silicate olivine and undergoes a phase transformation to spinel at much lower pressures than silicate olivine. We prepared three sets of germanate olivine aggregates with different grain sizes: sample A: < 10 μm, B: < 100 μm, and C: > 100 μm. We conducted deformation experiments on samples A, B, and C with a Griggs-type solid-confining medium deformation apparatus. Confining pressure, temperature, and strain rate were 1.2 GPa, 900 °C, and 2.0×10^{-4} s^{-1}, respectively. The recovered samples were examined with a scanning electron microscopy (SEM), micro-Raman spectroscopy, and scanning transmission electron microscopy (STEM).

Based on stress-strain curves, stable slips occurred in all samples. Optical microscopy and Raman spectroscopy showed that olivine grains near the Pt capsule walls underwent a transformation to spinel in all samples. Possible faults which displace the Pt capsule were observed only in sample A (Fig. 3.6-3). SEM observations did not indicate the presence of spinel grains near the faults. Many shear bands composed of spinel grains were observed in samples B and C. Furthermore, in sample B we observed a few 'anti-cracks' which were elongated perpendicular to the maximum compression direction and are composed of fine-grained spinel. The faults in sample A, anti-cracks in sample B, and nano-shear bands were studied using TEM. With TEM, we observed nanocrystalline spinel along the fault in sample A (Fig. 3.6-4). In addition, spinel grains are present along the olivine grain boundaries. In sample B, The elongation direction of anti-cracks is normal to the maximum compression direction on the surface, but bands composed of fine-grained spinel developed oblique to the compression direction inside an olivine grain. Stacking faults were observed near the fine-grained spinel. According to the selected-area electron-diffraction image, (111) plane of spinel is oriented topotaxially along the (100) plane of olivine. However, the orientation of spinel bands was subparallel to that of the stacking faults. In sample C, nano shear bands composed of fine-grained spinel reported by previous experimental studies were observed along the (010) plane of olivine.

In the fine-grained olivine sample, the nucleation and growth of spinel grains occurred along grain boundaries and a fault. In the coarse-grained olivine, on the other hand, the nucleation and growth of spinel grains occurred inside the olivine grains without any observed faulting. Considering that the faulting occurred in olivine grains with a grain size of about 30 μm in previous experiments, this indicates that only the presence of fine-grained olivine results in deep-focus earthquakes, and coarse-grained olivine does not invoke them or promotes the shear instability. The temperature in the metastable olivine wedge is very low (*e.g.*, 600 °C in the Tonga slab). Therefore, fine-grained olivine in preexisting faults (*e.g.*, outer-rise faults and shear zones) can be subducted while maintaining a small grain size with the potential to produce deep-focus earthquakes.

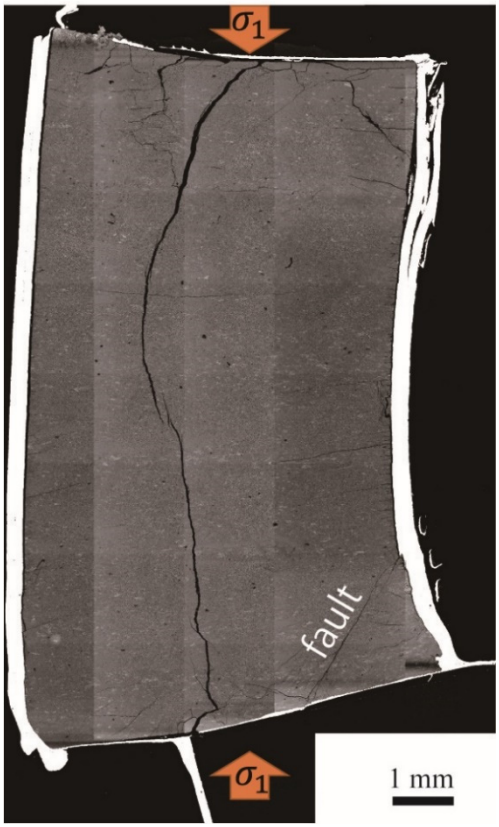

Fig. 3.6-3: Backscattered electron image of Sample A (grain size: < 10 µm). The vertical direction corresponds to the maximum compression direction (σ_1). A fault cuts the lower right part of the sample.

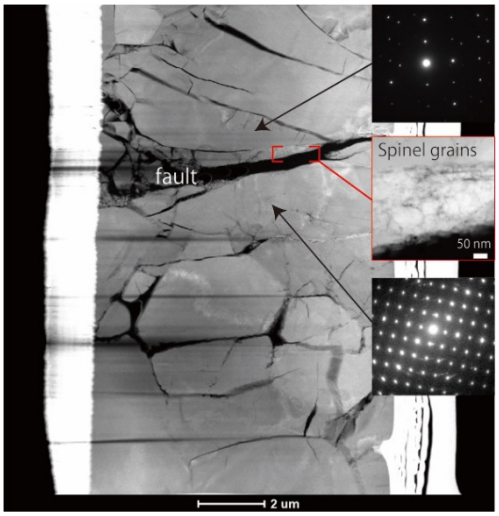

Fig. 3.6-4: STEM image of a fault and associated spinel in sample A (grain size: < 10 µm). The insets are selected area electron diffraction patterns of olivine across a fault and show that the crystal orientations of two olivine grains (upper and lower insets) across the fault are different. Spinel grains nucleated along the fault and olivine grain boundaries.

d. *Nanoscale cation-diffusion modeling in garnet-hosted omphacite: A preliminary result (R. Fukushima and T. Tsujimori/Sendai; N. Miyajima)*

Garnet and omphacite are the most common minerals in eclogites of high-pressure/ultrahigh-pressure (H*P*/UH*P*) metamorphic complexes. In typical low- to medium-temperature (*T*) eclogite, garnet occurs commonly as mm- to cm-sized porphyroblasts, whereas omphacites form the matrix and are often enclosed in the garnets. Owing to its high resistance to plastic deformation, such porphyroblastic garnet acts as a 'time capsule' to preserve various mineral

and fluid inclusions that coexisted during the garnet growth. Thus, sophisticated analyses of these enclosed materials can provide valuable information on the growth of host minerals, and thus unravel the tectonic histories of eclogite-bearing complexes.

Among eclogites in various geological settings, low-*T* eclogite, which is formed by the prograde subduction metamorphism of oceanic crust at depths > ~ 60 km, is particularly intriguing. Since the eclogite-forming metamorphic reactions involve intensive dehydration, petrological/mineralogical analyses of high-*P*/low-*T* rocks that underwent low-*T* eclogitization has the potential to clarify the behaviour and characteristics of fluids in subduction zones. For example, oscillatory zonings in minor- or trace-element concentrations are frequently observed in the rim regions of garnet porphyroblasts, and suggest that their formation is related to episodic fluid infiltrations during eclogitization of the subducting slab. Although recent studies have suggested such fluid pulses can occur within a period of less than a few million years (Myr), the lack of temporal resolution in geochronological approaches precludes further conclusions about this enigmatic phenomenon.

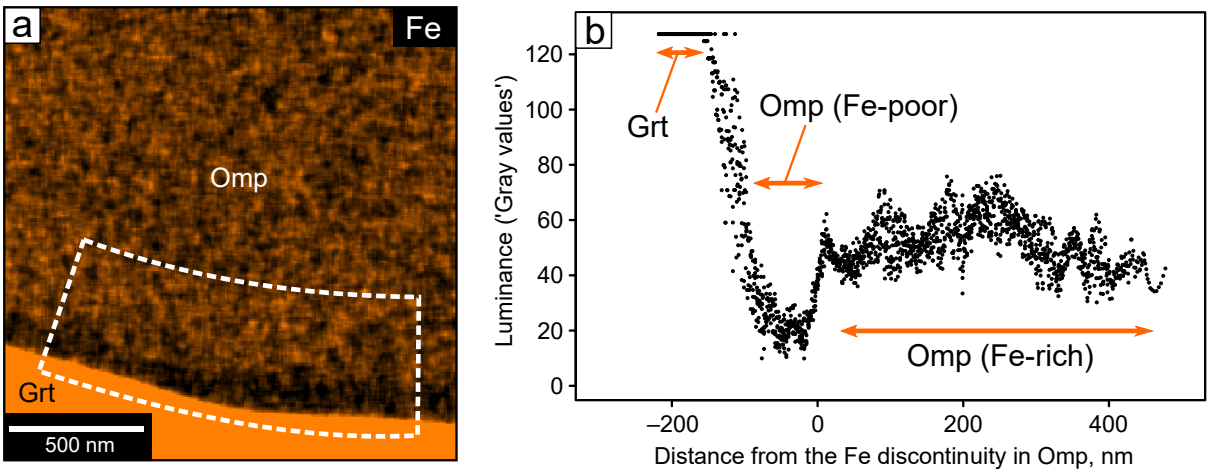

Fig. 3.6-5: Fe concentration profile in a garnet-hosted omphacite in the Syros low-*T* eclogite: (a) X-ray map (Fe Kα) of the investigated omphacite. Along the garnet-omphacite boundary, a syngenetic omphacite rim with distinctly lower Fe content is observed. (b) Representative Fe concentration profile of the area enclosed by the white dashed rectangle shown in (a). Omp = omphacite, Grt = garnet.

To overcome this limitation, we performed simple, nano-scale diffusion modeling based on a previously observed, syngenetic omphacite inclusion in garnet of the Syros eclogite. Focusing on Fe compositional heterogeneity in the garnet-hosted omphacite revealed by a Scanning TEM X-ray map (Fig. 3.6-5a), we conclude that the peak-*T* residence time of the eclogite was too short to erase the compositional profile by Fe^{2+}–Mg interdiffusion. We obtained the averaged concentration profile of Fe with the image processing program ImageJ (Fig. 3.6-5b). By fitting the profile with the calculation software PACE and tentatively fixing a value of the diffusion coefficient, we constrained the maximum annealing time to be no more than 50-5,000 years.

This suggests that the oscillatory-zoned garnet rim (~ 300 μm in width), which is a thin portion just outside the omphacite inclusion, grew rapidly at a rate of > 6-600 $cm^3 \cdot Myr^{-1}$. This nominal value is consistent with previously reported episodic garnet-growth rates. Although the uncertainty in the diffusion coefficient requires further careful consideration, our preliminary estimate might provide a critical constraint on fluid-enhanced garnet-growth kinetics during the low-*T* eclogitization. Specifically, this preliminary result demonstrates the potential of nano-scale geochemical analyses for discussing the short span (< ~ 10^6 years) of geological events enhanced by the presence of fluids, which have never been considered previously.

3.7 Material Science

At the Bayerisches Geoinstitut, unique *in situ* high-pressure equipment, expertise and sample characterization are available, which permit sophisticated and challenging research into the physics and chemistry of materials. Rather than a focus based on methodological advances – especially single-crystal X-ray diffraction – like in the past two years, many contributions to the material research section of this annual report highlight unexpected changes in chemistry of materials that are synthesized at extreme conditions in the diamond anvil cell.

This is exemplified by two contributions for very different material classes. Nitrogen dimers in alkali- and alkaline earth-nitrogen solids synthesized at high pressure deviate from the conventional understanding that anionic N_2 dimers only occur with integer formal charges. Instead, they display fractional values due to valence charge transfer from the metal cations. NaCl is typically considered to be an extremely inert and stable compound, but high-pressure experiments show that when loaded with metallic yttrium, an intriguing solid with Y_2ClC stoichiometry forms after heating; its structure can be viewed as a cubic close-packed network consisting of Cl and C, and the Y atoms occupying the octahedral voids. As NaCl is often loaded as an inert material in diamond anvil cell experiments, the reactivity illustrated here warrants careful examination of run products in terms of Cl and Na content.

As highly refractory materials, carbides are found in meteorites as presolar grains and are often used as abrasive materials, as an alternative to diamond due to generally larger temperature stability. One contribution to the current section explores the stability and equation of state of one polymorph of silicon carbide, 6H α-SiC, with the conclusion that this form may be stable relative to coexisting diamond and Si. Very different carbides on the basis of dysprosium are synthesized in the diamond anvil cell at high pressure and temperature, Dy_4C_3 and Dy_2C_3, with the latter not being observed previously. Borides are similarly refractive, and the synthesis of two new Rhenium borides, ReB_3 and ReB_4, is presented here.

Two high-pressure studies on manganese-based oxides continue the long-standing interest in transition metal oxides at Bayerisches Geoinstitut. Similar to Fe, the variable valence state of Mn cations makes this a rich system, and new structures for both Mn_2O_3 (ilmenite-type) and Mn_3O_4 (marokite-type) have been synthesized in the multianvil press. The relatively large crystals obtained have been characterized not only in terms of structure, but also electronic and magnetic properties.

With the discovery of high-temperature superconductivity at high pressure in metal hydrides, this class of materials has gathered significant attention in the physics community. Yttrium hydrides with unusual stoichiometry play an important role in the exploration of this phenomenon, and experiments presented here show the formation of a new type of yttrium hydride, with an inferred variable hydrogen content as a function of pressure. What makes this

phase particularly interesting is the fact that – contrary to the previously reported phase – it is not based on close-packed layers of yttrium atoms. The underlying hexagonal Y phase was subsequently stabilized for Y metal at 20 GPa, and competes with the previously established phases of yttrium.

The final contribution addresses the question of what defines a simple molecular solid and how it behaves at high pressure. Typically considered systems like H_2, N_2 or O_2 are complex due to many-body interactions governing their behaviour; by contrast, carbon tetrahalides (CX_4) show relatively simple bonding, and CF_4 – investigated here – may be considered a prototype. Its compression behaviour shows a transition from structures based on the arrangement of the molecules to close-packing of the halogen atoms.

a. *High-pressure $Na_3(N_2)_4$, $Ca_3(N_2)_4$, $Sr_3(N_2)_4$, and $Ba(N_2)_3$ featuring nitrogen dimers with non-integer charges and anion-driven metallicity (D. Laniel/Bayreuth, B. Winkler/Frankfurt/M., T. Fedotenko/Bayreuth, A. Aslandukova, A. Aslandukov/Bayreuth, S. Vogel/Munich, T. Meier, M. Bykov/Washington D.C., S. Chariton/Chicago, K. Glazyrin/Hamburg, V. Milman/Cambridge, V.B. Prakapenka/Chicago, W. Schnick/Munich, L.S. Dubrovinsky and N.A. Dubrovinskaia/ Bayreuth)*

In the last decade, the high-pressure (*P*) approach has established itself as the *de facto* method to explore nitrogen's chemistry. Among the discovered homoatomic polynitrogen species, anionic nitrogen dimers $[N_2]^{x-}$ were found to be ubiquitous and featured in more than twenty binary alkali-, alkaline earth- and transition metal-nitrogen solids. A defining characteristic of all these compounds is the integer formal charge of the $[N_2]^{x-}$ anions (with x = 1, 2, 3 or 4), with additional electrons populating the π^* antibonding states of the nitrogen dimers.

In the current research, high-*P* single-crystal X-ray diffraction experiments in laser-heated diamond anvil cells on binary alkali- and alkaline earth-nitrogen systems were performed. Marking a drastic rupture with the established paradigm, the synthesized $Na_3(N_2)_4$, $Ca_3(N_2)_4$, $Sr_3(N_2)_4$, and $Ba(N_2)_3$ compounds feature $[N_2]^{x-}$ with non-integer formal charge values (x = 0.67, 0.75 or 1.5). From the analysis of the length of the $[N_2]^{x-}$ units (Fig. 3.7-1) and the physical properties of the compounds bearing them, the charged nitrogen dimers are concluded to behave according to their non-integer charges. Employing *ab initio* calculations, we found that the essentially complete valence electron transfer from the metal cations to the $[N_2]^{x-}$ species gives rise to an anion-driven metallicity, with electrons being essentially solely delocalized on the antibonding π^* orbitals of nitrogen dimers. The electrons' delocalization is therefore key to enable the non-integer electron count of the dinitrogen species.

The flexibility of the $[N_2]^{x-}$ species as electron acceptors, combined with the sensitivity of their properties to their charge value, opens the way to electron-tunable technological materials.

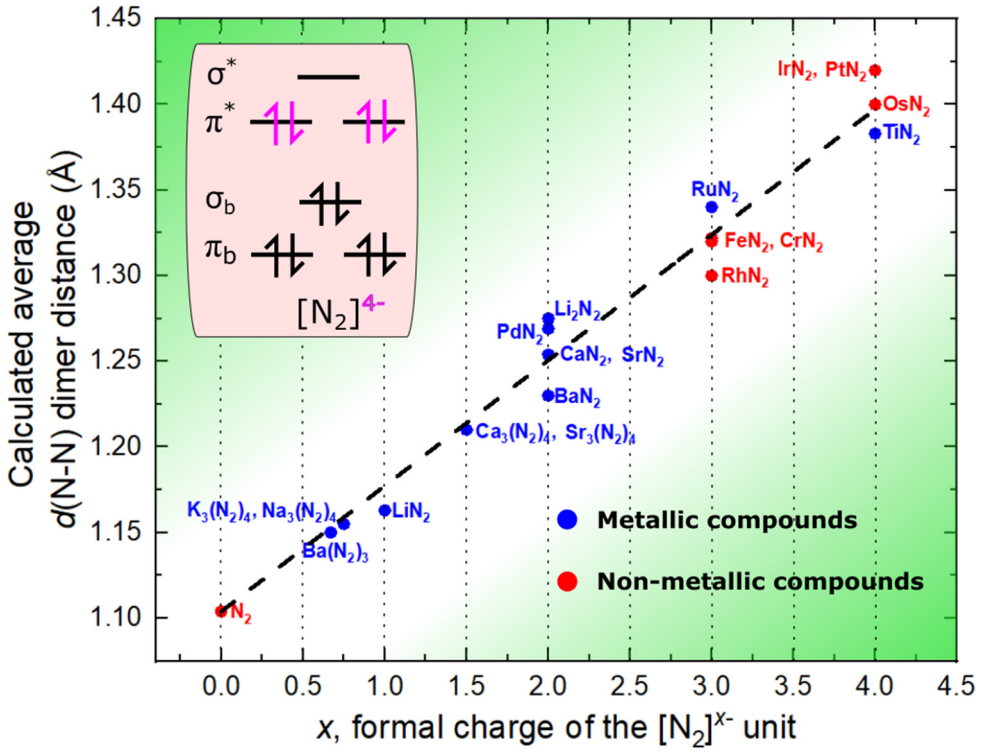

Fig. 3.7-1: Calculated (average) *d*(N-N) distances with respect to the formal charge x- of nitrogen dimers $[N_2]^{x-}$, for nineteen experimentally observed binary compounds containing $[N_2]^{x-}$ species produced under P. All distances were computed at 1 bar. Inset: Molecular orbital diagram of the pernitride $[N_2]^{4-}$.

b. *Chemical reactions between sodium chloride and yttrium under high pressure (Y. Yin, D. Laniel and A. Aslandukov/Bayreuth, A. Aslandukova, L.S. Dubrovinsky, N.A. Dubrovinskaia/ Bayreuth and M. Hanfland/Grenoble)*

High pressure (*P*) is known to significantly affect chemistry and reactivity of materials, and the synthesis of compounds with unusual stoichiometry at high *P* attracts attention because such compounds often demonstrate novel types of chemical bonding and may have interesting properties. Many novel high-*P* compounds cannot be predicted based on chemical rules valid at ambient conditions, and the recent discovery of numerous unconventional sodium and potassium halides (like Na_3Cl, $NaCl_3$, and KCl_3) at *P* of 20 to 70 GPa demonstrates this principle. NaCl halite, considered extremely stable, may become reactive at high *P* which may result in the synthesis of novel compounds with potentially unusual electronic, optical, and mechanical properties.

In order to further explore this hypothesis, we loaded the rare earth metal yttrium and dried NaCl powder into a diamond anvil cell (DAC) with a *P* chamber of 120 µm in diameter made in a rhenium gasket pre-indented to the thickness of 30 µm, and compressed the cell to 41 GPa. After double-side laser heating of the sample to ~ 2000 K with a YAG laser, samples were

characterized using Raman spectroscopy and synchrotron single-crystal X-ray diffraction (SCXRD) measurements at the European Synchrotron Radiation Facility. Among other run products, the SCXRD data allowed us to identify a new rhombohedral phase (Fig. 3.7-2) with chemical composition Y_2CCl. Density functional theory-based calculations perfectly reproduce the details of the Y_2CCl structure at 40 GPa and demonstrate that the phase is dynamically stable at the synthesis *P*.

In the novel carbidochloride, yttrium atoms form a distorted cubic close packing (*ccp*) (Fig. 3.7-2). If one considers Cl and C to be equally sized, alternating close-packed layers of C and Cl also form a distorted *ccp*. Thus, the structure can be described as a distorted NaCl (B1) type with carbon and chlorine atoms in the *ccp* arrangement and octahedral voids occupied by Y atoms. The Y-C distances (~ 2.30 Å) are significantly shorter than Y-Cl (~ 2.59 Å). One of the Y-Y contacts is relatively short (~ 3.14 Å), close to the Y-Y distances in yttrium metal, indicating a possible metallic character of the material.

The synthesis of Y_2CCl by a direct reaction of Y and NaCl in a laser-heated DAC suggests that sodium chloride is indeed not chemically inert at high *P* and temperature (*T*). This observation puts limits on the use of alkali halides as thermal insulation and a *P*-transmitting medium in DAC experiments at high *T*, but opens up great perspectives for the synthesis of novel materials with unusual chemistry.

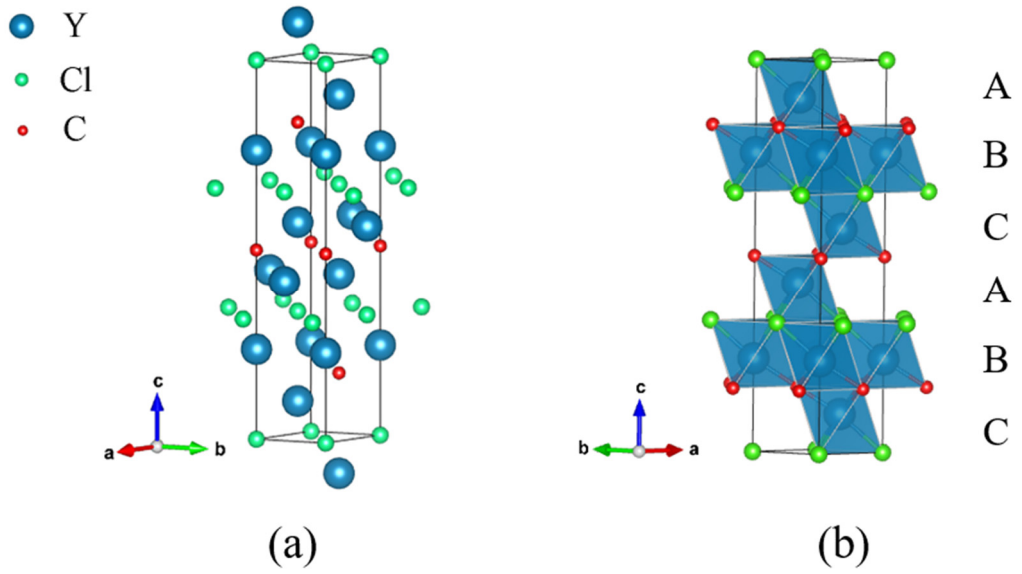

Fig. 3.7-2: Crystal structure of Y_2ClC at 41 GPa in the hexagonal setting (space group #166, $R\bar{3}m$, a = 3.364(2) Å, c = 17.72(7) Å; rhombohedral cell parameters are $a = b = c$ = 6.21 Å, $\alpha = \beta = \gamma = 31.46°$, and the structure is refined with R1 = 7.5 %). (a) Ball model with Y, Cl, and C atoms shown in blue, green, and red, respectively; (b) polyhedral model built of YC_3Cl_3 octahedra; A, B, C highlight the *ccp* formed by Y atoms themselves; the structure can be understood as *ccp* formed by C and Cl atoms together with the Y atoms occupying all of the octahedral voids.

c. *Equations of state of α-SiC (6H) from single-crystal X-ray diffraction data (I. Koemets, T. Ishii/Beijing, L.S. Dubrovinsky and M. Hanfland/Grenoble)*

Silicon carbide (SiC) is a natural material that has attracted great industrial interest due to its hardness, refractory, and semi-conductor properties. SiC is commonly found in the Solar System in the form of stardust and in chondrite meteorites, and has been proposed to potentially constitute a significant volume of planetary interiors in carbon-rich star systems. Here we report the first compressibility study on α-SiC (6H) using single-crystal X-ray diffraction (XRD) in a diamond anvil cell (DAC) up to a pressure of $P \sim 60$ GPa.

The structure of the α-SiC sample is characterized by six tetrahedral layers in the space group *P63mc* (186), with lattice parameters $a = 3.0814(8)$ Å and $c = 15.121(2)$ Å, ($V = 124.34(2)$ Å^3), indicative of the 6H polytype. Figure 3.7-3 shows the unit cell volume (V) as a function of P at ambient temperature. No phase transitions were observed during compression to 60 GPa. Reciprocal-space analysis of the SiC crystal at the highest obtained P (Fig. 3.7-3) did not reveal any extra reflections or splittings, which confirms that our results are in accordance with the literature data. Fitting the P-V data with a second-order Birch-Murnaghan equation of state yields $K_0 = 226.0(4)$ GPa and $V_0 = 124.34(2)$ Å^3, the latter fixed from the experimental data at ambient conditions.

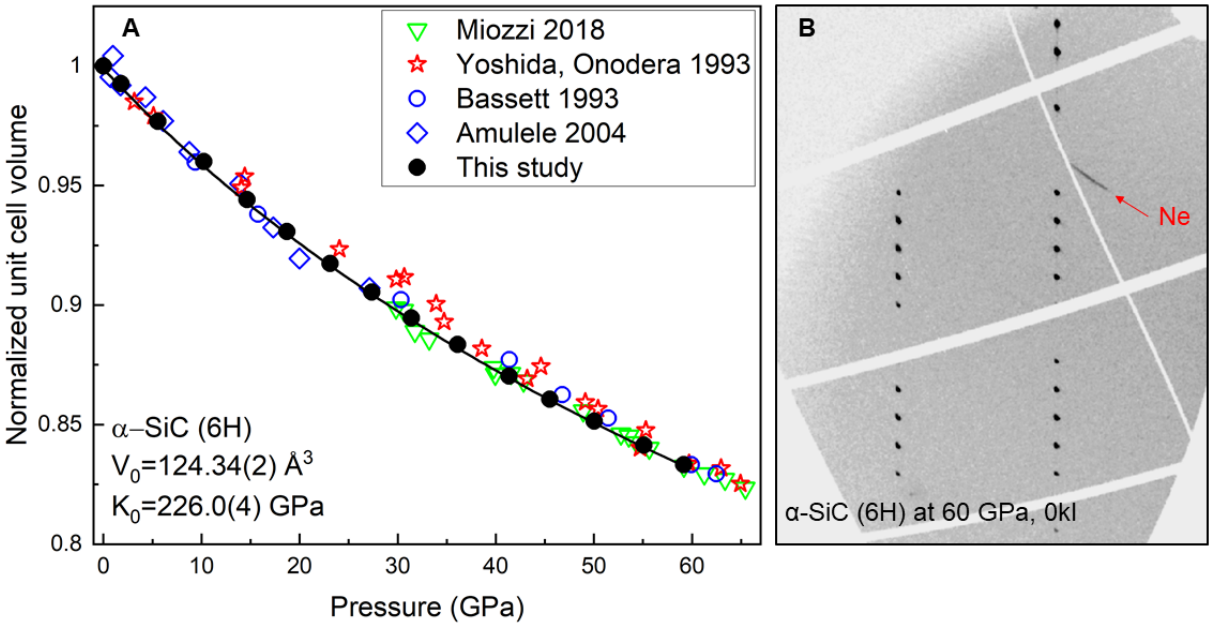

Fig. 3.7-3: A. An equation of state of α-SiC (6H). The black solid curve shows the fit of the experimental data (black circles) with a second-order Birch-Murnaghan equation of state with $V_0 = 124.34(2)$ Å^3 and $K_0 = 226.0(4)$ GPa. V_0 was fixed based on the data at ambient conditions. For comparison, we also show some experimental data for different SiC polytypes. B. Reflections of hexagonal *P63mc* α-SiC (6H) in the 0*kl* plane of a precession-like image in reciprocal space reconstructed using the UNWARP procedure within CrysAlis^{Pro} software. The diffraction image collected at ~ 60 GPa shows no sign of a phase transformation.

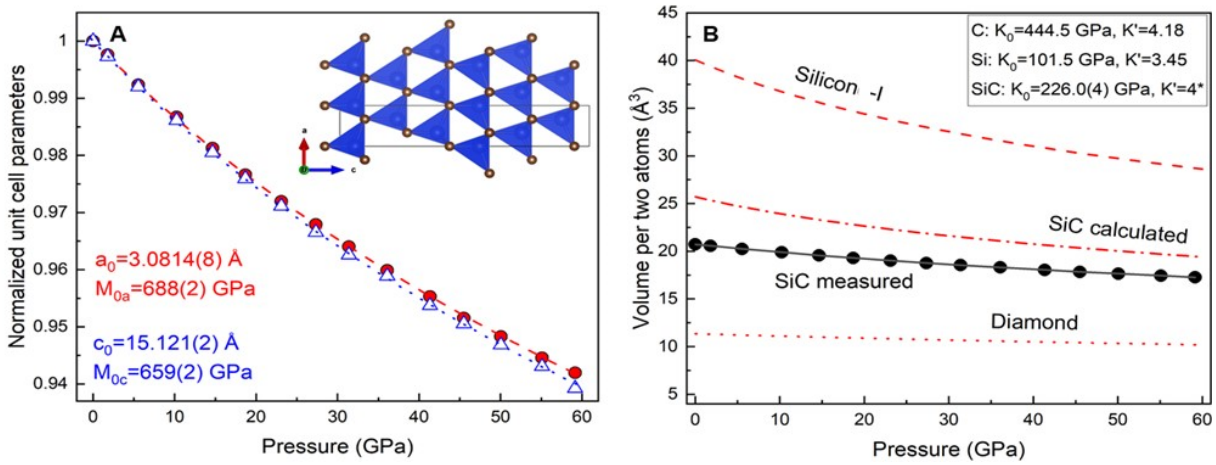

Fig. 3.7-4: A. Normalized unit cell parameters of α-SiC (6H) fitted with a second-order Birch-Murnaghan equation of state as a function of *P*. The compressibility is similar along the *a*- and *c*-axes with M_{0a} = 688(2) GPa and M_{0c} = 659(2) GPa. B. Volume of α-SiC (6H) during compression (black circles, black solid curve). The equations of state for diamond (red dotted curve after Dewaele *et al.*, Phys. Rev. B, 77, 094106, 2008) and Si-I with the diamond structure (red dashed curve after Anzellini *et al.*, Scientific Reports, 9, 15537, 2019) are shown for comparison. The red dash-dot curve represents the SiC volume calculated from Si-I and diamond volumes at given *P*. Note that Si-I is stable only up to ~ 13 GPa.

The *c*-axis is found to be slightly more compressible (M_{0c} = 659(2) GPa) than the *a*-axis (M_{0a} = 688(2) GPa) (Fig. 3.7-4). The tetrahedron volume decreased during compression from ~ 3.5 Å^3 at ambient conditions to ~ 3.0 Å^3 at 50 GPa. The bulk modulus obtained by fitting the SiC_4 tetrahedron volume with a second-order Birch-Murnaghan equation of state yields K_0 = 225.7(4) GPa, which is indistinguishable from that of the unit cell within the experimental uncertainty. The compressibility of bulk 6H-SiC is therefore governed by the compressibility of the Si-C bonds. A comparison of the compressibility in diamond and Si-I with the diamond structure shows that SiC has a smaller volume than the calculated average Si and C volumes per atom in the unit cells of diamond and Si-I (Fig. 3.7-4). This may indicate that SiC is thermodynamically favorable with respect to a mixture of Si and C over a wide *P* range.

d. *Synthesis of dysprosium carbides at high pressure in laser-heated DACs (F.Ia. Akbar and A. Aslandukov/Bayreuth, A. Aslandukova, N.A. Dubrovinskaia/Bayreuth, L.S. Dubrovinsky, S. Khandarkhaeva and T. Fedotenko/Hamburg)*

Carbides form an important family of compounds in research and industry due to interesting chemical, mechanical, electrical, magnetic and optical properties. The structure, bonding, and phase transitions of lanthanide carbides are of great interest due to their known and potential applications. High-pressure (*P*) effects on chemistry, phase relations, and bonding may significantly enhance the number of lanthanide carbides and lead to the formation of materials with fascinating crystal chemistry and unusual properties.

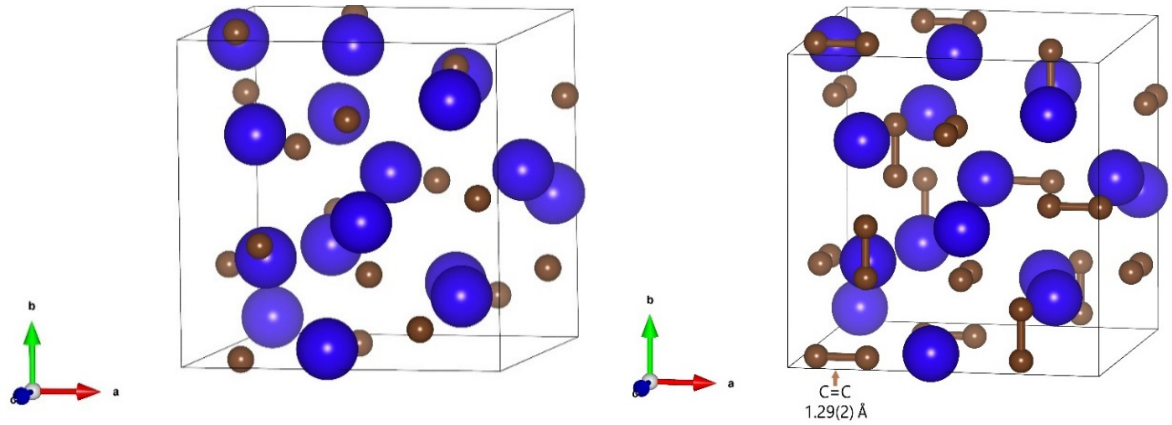

Fig. 3.7-6: Structures of dysprosium carbides, novel Dy_4C_3 (left) and Dy_2C_3 (right), synthesized at 19 GPa in a laser-heated diamond anvil cell. The blue and brown spheres represent dysprosium and carbon, respectively.

In this work, cubic dysprosium carbides Dy_4C_3 and Dy_2C_3 were synthesized by laser heating of Dy in a diamond anvil cell (DAC). We employed the BX90 type equipped with Boehler-Almax-type anvils (80° opening, culets of 250 μm in diameter). A rhenium gasket was indented to about 30 μm thickness, and a hole with a diameter of about 100 μm was laser-drilled in the center of the indentation forming a *P* chamber. Flakes of pure Dy were loaded into the *P* chamber together with dried NaCl (used as an insulator). After compression of the sample to ~ 19 GPa, dysprosium flakes were heated by a double-sided laser setup (NIR laser, 1070 nm wavelength) to a temperature of 2200 K. The DAC with the sample was transferred to the Extreme Conditions Beamline (PETRA III) for *in situ* X-ray diffraction of reaction products. Single-crystal diffraction data revealed the formation of two cubic dysprosium carbides, Dy_2C_3 and Dy_4C_3, from the reaction of Dy with the diamonds. Dysprosium sesqui-carbide, Dy_2C_3 crystallizes in space group *I-43d* (*Z* = *8*; *a* = 7.9224(5) Å at 19 GPa) (Fig. 3.7-6), a phase known at ambient conditions, with the significantly (~ 3.5 %) larger lattice parameter (*a* = 8.198(2) Å). The compound is an ethylide and contains C=C groups (Fig. 3.7-6), which are very incompressible to 19 GPa, with interatomic distances changing from 1.31 to 1.29 Å (~ 1.5 %). Dysprosium carbide Dy_4C_3 also crystallizes in space group *I-43* (*Z* = *4*, *a* = 7.4776(8) Å at 19 GPa) (Fig. 3.7-6). Such a compound has not been characterized previously, and its anti-Th_3P_4 structural type has not been described in the ISCD database for lanthanides carbides.

e. *Novel class of rhenium borides based on hexagonal boron networks interconnected by short B_2 dumbbells (E. Bykova, H. Fei, S.V. Ovsyannikov, A. Aslandukova, T. Katsura, N.A. Dubrovinskaia/Bayreuth and L.S. Dubrovinsky; E. Johansson, B. Alling and I.A. Abrikosov/ Linköping; M. Bykov/Köln; S. Chariton and V.B. Prakapenka/Chicago; S. Gabel, H. Holz and B. Merle/Nürnberg; A.F. Goncharov/Washington D.C.)*

Transition metal borides are attractive due to their mechanical, electronic and refractive properties. By synchrotron single-crystal X-ray diffraction experiments in laser heated diamond

anvil cells between 26 and 75 GPa, we identified a new class of rhenium borides that were recovered to ambient conditions. Rhenium triboride (ReB_3) and rhenium tetraboride (ReB_4) consist of close-packed single layers of rhenium atoms alternating with boron networks built from puckered hexagonal layers and short (~ 1.7 Å) B-B bonds (Fig. 3.7-7). The short and incompressible Re-B and B-B bonds oriented along the hexagonal *c*-axis contribute to low axial compressibility comparable with that of diamond. For material characterization, sub-millimeter samples of ReB_3 and ReB_4 were synthesized in a large-volume press at 33 GPa. Both compounds are metallic and hard.

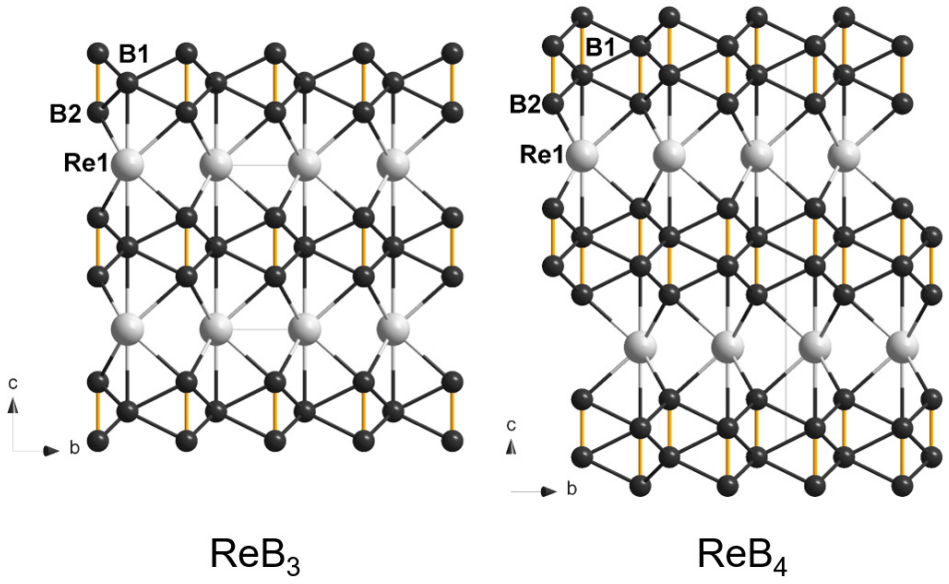

Fig. 3.7-7: Crystal structures of ReB_3 and ReB_4. The shortest B-B bonds are highlighted with orange color.

Geometrical, crystal-chemical, and theoretical analysis suggest that potential ReB_x compounds with $x > 4$ are based on the same principle of structural organization as in ReB_3 and ReB_4 and possess similar mechanical and electronic properties.

f. *Synthesis of ilmenite-type ε-Mn_2O_3 and its properties (S.V. Ovsyannikov, A.A. Tsirlin/ Augsburg, I.V. Korobeynikov/Yekaterinburg, N.V. Morozova/Yekaterinburg, A. Aslandukova, G. Steinle-Neumann, S. Chariton/Chicago, S. Khandarkhaeva, K. Glazyrin/Hamburg, F. Wilhelm/Grenoble, A. Rogalev/Grenoble and L.S. Dubrovinsky)*

In this work, we synthesized single crystals of Mn_2O_3 at pressures (*P*) of ~ 16-17 GPa and temperatures of 1500 K or above, with single-crystal X-ray diffraction revealing that ε-Mn_2O_3 crystallizes in an ilmenite-type structure with the rhombohedral $R\bar{3}$ symmetry (Fig. 3.7-8). This structure contains Mn ions in two different oxidation states, +2 and +4. To date, ilmenite-type

structures were not observed in any simple binary oxides, but are known for multi-cation oxides, in which disproportional charge distribution is common. The unit-cell parameters of this structure at normal conditions are a = 5.0148(8) Å and c = 14.1141(28) Å (V = 307.39(11) Å^3, with Z = 6). The calculated density of ε-Mn_2O_3 is 5.114 g/cm^3, ~ 2 % higher than the density of the conventional cubic-bixbyite phase α-Mn_2O_3.

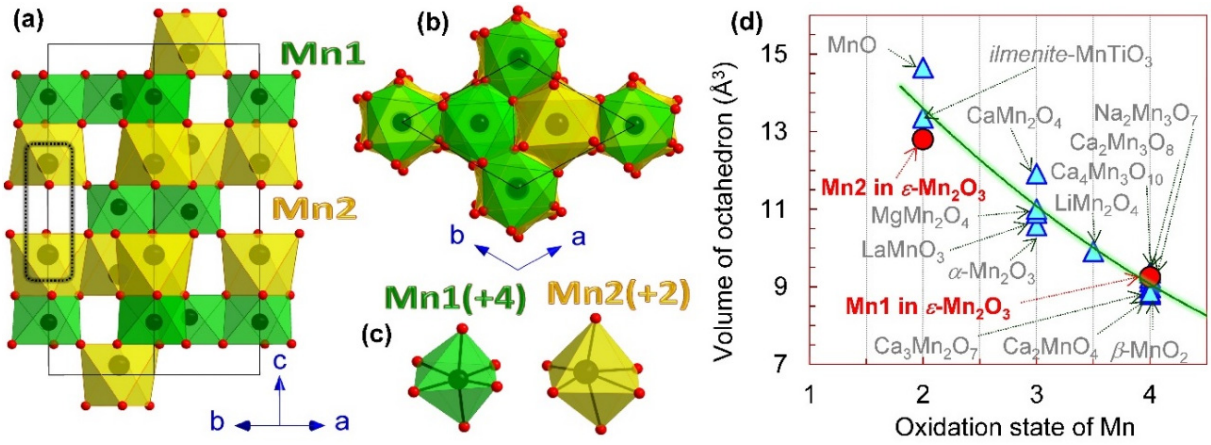

Fig. 3.7-8: (*a, b*) The crystal structure of ilmenite-type ε-Mn_2O_3 at ambient conditions in two different projections. (*c*) Oxygen octahedra of Mn1 and Mn2 atoms. (*d*) The volume of coordination octahedra as a function of oxidation state for Mn ions at ambient conditions, determined for manganese oxides with well-known oxidation states of cations, *e.g.*, for oxides containing Na^+, Li^+, Ca^{2+}, Mg^{2+}, La^{3+}, and Ti^{4+} cations. We considered high-quality data from the FIZ Karlsruhe database. Our data for the Mn1 and Mn2 octahedra in the structure of ilmenite-type ε-Mn_2O_3 are shown by red symbols. The solid line serves as a guide to the eye.

It appears that under moderate applied P, Mn_2O_3 tends to transform to a corundum-like structure, which is common for oxides of rather light transition-metals like Fe, V, Cr, and Ti, but simultaneously, the Mn^{3+} ions are subject to charge disproportionation and ordering. These two counteracting factors are likely responsible for the formation of the ilmenite-type structure. Using the bond valence sums method, we determined the average oxidation states for the cations occupying Mn1 and Mn2 sites as +4.05 and +1.95, respectively (Fig. 3.7-8). A significant difference in the volumes also corroborates the charge disproportionation between Mn1 and Mn2: Octahedral volumes of Mn1 and Mn2 atoms in the structure of ε-Mn_2O_3 are 9.25 Å^3 and 12.80 Å^3, respectively (Fig. 3.7-8). To provide better context, we analyzed an "octahedron volume – oxidation state" relationship for a dozen binary and ternary manganese oxides at ambient conditions in which the oxidation states of octahedral Mn cations are well known and vary between +2 and +4 (Fig. 3.7-8). In particular, we found that the ilmenite-type ε-Mn_2O_3 is structurally similar to ilmenite-type $Mn^{2+}Ti^{4+}O_3$. As seen in Figure 3.7-8, the divalent Mn2 cations are strongly displaced from the center of their coordination octahedra. However, these displacements compensate each other in pairs (one pair is highlighted in Figure

3.7-8), and hence, no spontaneous electrical polarization should appear in undoped stoichiometric ε-Mn_2O_3.

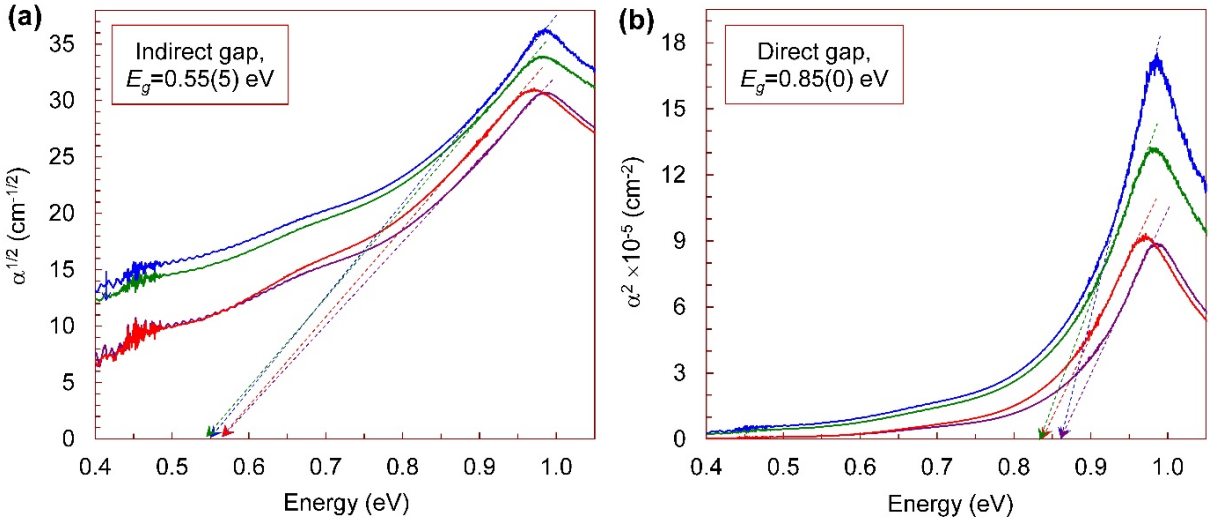

Fig. 3.7-9: Near-infrared absorption spectra (absorption coefficient α) of ilmenite-type ε-Mn_2O_3 acquired at ambient conditions on four different crystals (shown by different colors). The spectra are shown in two representations, as $\alpha^{1/2}$ *vs* energy (*a*) and as α^2 *vs* energy (*b*) to determine indirect and direct band gaps, respectively.

ε-Mn_2O_3 samples show an antiferromagnetic ordering transition around T_N = 210 K. Above this transition, we found an effective magnetic moment of about 6.0 μ_B/Mn. Thus, ε-Mn_2O_3 is characterized by predominantly antiferromagnetic interactions similar to other Mn_2O_3 polymorphs. We examined the electronic properties of ε-Mn_2O_3 by several techniques, including X-ray absorption, near-infrared absorption spectroscopy, electrical resistivity, and thermoelectric power measurements. At normal conditions, ilmenite-type ε-Mn_2O_3 showed a high electrical resistance, suggesting its semiconducting nature. To determine a band gap, we measured the absorption spectra of four selected single-crystalline double-polished samples. In the near-IR region, we observed a rather abrupt increase in the absorption coefficient with energy, suggesting the existence of a distinct band gap (Fig. 3.7-9), and we established that the ilmenite-type ε-Mn_2O_3 is an indirect-band-gap semi-conductor with a fundamental gap of E_g = 0.55(5) eV. A minimal direct band gap in this phase was found to be E_g = 0.85 eV. Note that perovskite-type ζ-Mn_2O_3, another previously studied high-*P* polymorph, has a similar band gap of E_g = 0.45 eV.

To probe a high-*P* response, we measured the electrical resistance as a function of applied *P* up to 10 GPa on one of the crystals and observed that the semiconducting properties of ε-Mn_2O_3 are preserved in this *P* range. Measuring the Seebeck coefficient (thermoelectric power) we found that our samples of ε-Mn_2O_3 are intrinsic semi-conductors with *n*-type electrical conductivity dominant. In contrast, the perovskite-type ζ-Mn_2O_3 has the dominant *p*-type conductivity at ambient *P*.

g. *Structural stability of marokite-type γ-Mn_3O_4 under high pressure (S.V. Ovsyannikov, A. Aslandukova, A. Aslandukov/Bayreuth, S. Chariton/Chicago, A.A. Tsirlin/Augsburg, I.V. Korobeynikov/Yekaterinburg, N.V. Morozova/Yekaterinburg, T. Fedotenko, S. Khandarkhaeva and L.S. Dubrovinsky)*

Synthetic manganese oxides and manganese-oxide minerals play an important role in different technological processes and applications. In this work, we investigated the formation of manganese oxide phases in samples with different nominal starting stoichiometries at high-pressure (P) – high-temperature (T) conditions in the P range of 10-24 GPa. We found that orthorhombic *Pbcm* marokite-type γ-Mn_3O_4 (Fig. 3.7-10) is the most stable mixed-valence phase that can be easily synthesized and quenched to ambient P. Magnetic, optical, and electronic properties of γ-Mn_3O_4 were also investigated at ambient P.

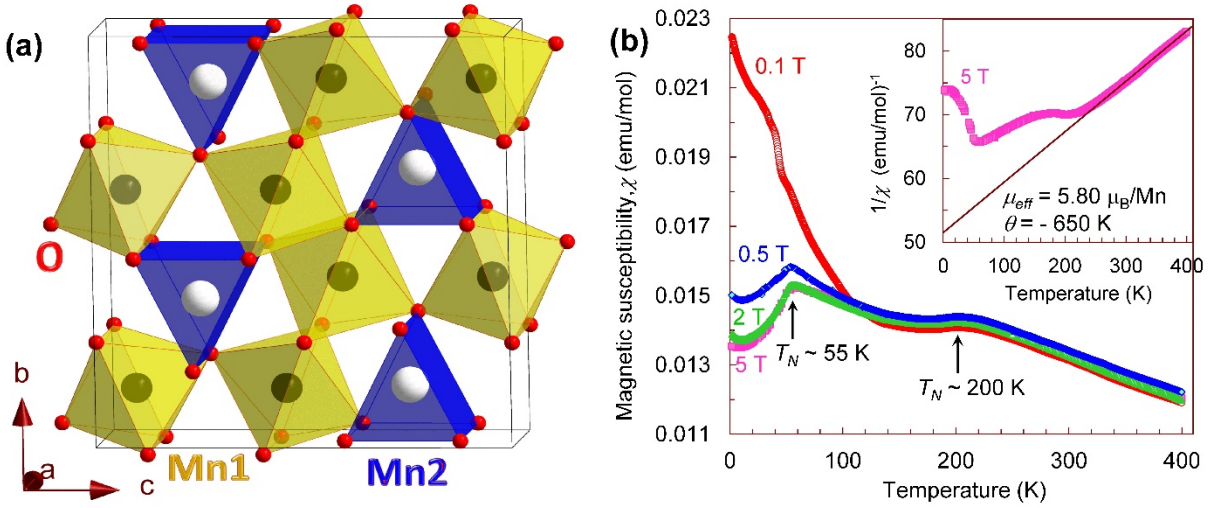

Fig. 3.7-10: (*a*) A unit cell of the marokite-type *Pbcm* crystal structure of γ-Mn_3O_4 at ambient conditions. The labels Mn1 and Mn2 indicate two different crystallographic positions for the Mn ions. (*b*) Temperature dependence of magnetic susceptibility (χ) in different magnetic fields. Arrows indicate two antiferromagnetic transitions at $T_N \sim 55$ K and ~ 200 K. The inset depicts the T dependence of the inverse magnetic susceptibility ($1/\chi$) in the magnetic field of 5 Tesla. Parameters of the Curie-Weiss fit are also given.

We synthesized single-crystal samples of the marokite-type γ-Mn_3O_4 phase from different nominal starting compositions at $P > 10$ GPa. We solved the crystal structure of the marokite-type Mn_3O_4 using single-crystal X-ray diffraction, and found a phase in the orthorhombic *Pbcm* space group (#57) and unit cell parameters $a = 3.0276(1)$ Å, $b = 9.8176(3)$ Å, and $c = 9.5799(3)$ Å ($V = 284.751(16)$ Å^3, with $Z = 4$). The Mn ions in this structure occupy two different crystallographic sites, oxygen octhedra and trigonal prisms (Fig. 3.7-10). As found from the bond valence sums analysis, the octahedra are filled by trivalent Mn, the trigonal prisms by divalent Mn. Generally, this crystal structure resembles the high-P polymorph of Fe_3O_4. Since the octahedral chains comprise only Mn^{3+} cations, this polymorph is a poor electrical conductor, as confirmed experimentally.

The magnetic susceptibility of the marokite-type γ-Mn_3O_4 revealed a broad bend around 200 K followed by a peak at 55 K (Fig. 3.7-10). Similar features were observed in magnetic fields ranging from 0.5 T to 5 T, whereas in low fields, an upturn is seen below 120 K, and the 55 K transition manifests itself by a step. Above 300 K, inverse susceptibility follows the Curie-Weiss behaviour with the effective paramagnetic moment of 5.80 μ_B/Mn and an antiferromagnetic Curie-Weiss T of -650 K (inset of Fig. 3.7-10). This effective moment is compatible with the scenario of Mn^{2+}/Mn^{3+} charge order inferred from the structural data. Indeed, a combination of spin-5/2 Mn^{2+} and spin-2 Mn^{3+} should lead to the spin-only effective moment of 5.26 μ_B/Mn, and an additional contribution from the orbital moment can be expected on the Mn^{3+} sites.

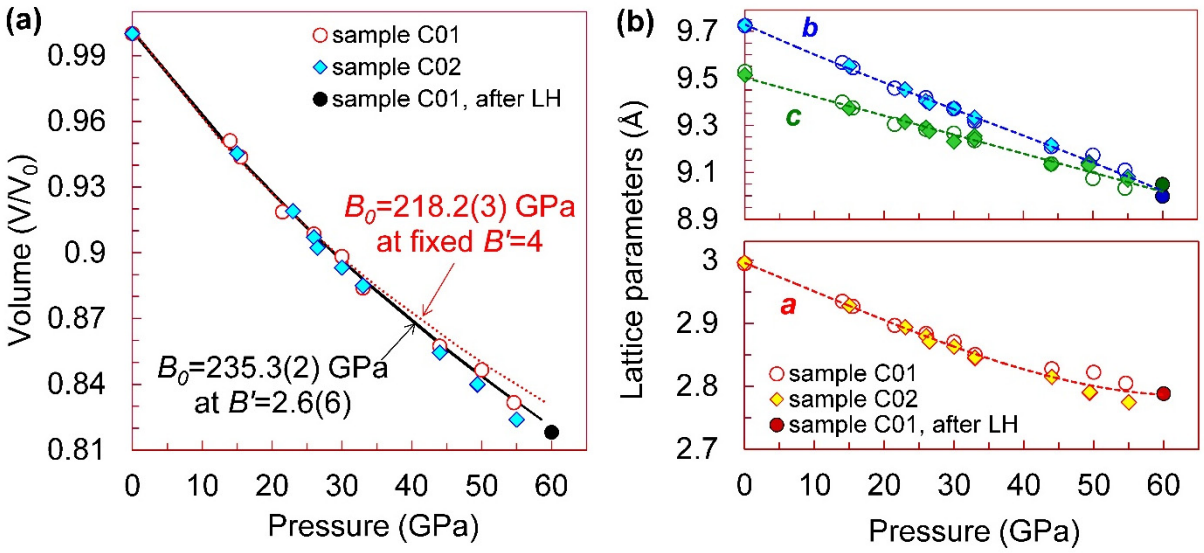

Fig. 3.7-11: Pressure dependence of the relative unit-cell volume (*a*) and lattice parameters (*b*) of single-crystal samples of the marokite-type γ-Mn_3O_4 at 293 K. The filled and open symbols correspond to two different samples. One point at 60.0 GPa was acquired after laser heating to more than 3500 K. Parameters of the equations of state are given in (*a*).

To examine the phase stability of marokite-type γ-Mn_3O_4 under high P, we selected two high-quality single crystals and carried out single-crystal X-ray diffraction experiments up to about 60 GPa at ID15 beamline of the European Synchrotron Radiation Facility using a wavelength of λ=0.29521 Å. For these studies, a diamond anvil cell (DAC) of a piston-cylinder-type (BX90) and a pre-indented Re gasket loaded with a Ne P-transmitting medium was utilized. We detected no phase transitions but found that compressibility of these crystals is strongly anisotropic, and the unit cell tends to deform toward a more symmetric tetragonal lattice (Fig. 3.7-11).

To estimate the bulk modulus, B_0 of this polymorph, we fit the third-order Birch-Murnaghan equation of state (EOS) to our data. We found B_0 = 235.3(2) GPa for a variable B'_0 = 2.6(6) (black solid curve in Fig. 3.7-11), and no satisfactory fit could be obtained with the fixed derivative, B'_0 = 4. If we restrict our consideration to the data below 30 GPa, we estimate B_0 = 218.2(3) GPa (red dashed curve in Figure 3.7-11) for fixed B'_0 = 4. Previous structural investigations of γ-Mn_3O_4 reported a significantly smaller bulk modulus, *e.g.*, B_0 = 166.6 GPa for powder, and B_0 = 176 GPa for nanorods (both for B'_0 = 4). The difference is probably related to the sample morphology (defects, vacancies, *etc.*) that can affect elastic properties.

The distortion of the γ-Mn_3O_4 unit cell toward a tetragonal-like lattice hints at potential stability of other phases in this *P* range. Structural phase transitions in oxides are often delayed due to high kinetic barriers, and in order to facilitate potential transformations, we heated up one sample inside the DAC at the maximal *P* above 3500 K using a high-power laser. After the sample was quenched to room *T*, the *P* inside the cell had increased to 60 GPa. The following X-ray diffraction examinations have shown that the sample preserved its single-crystallinity well and still adopted the pristine marokite-type structure. Thus, we can conclude that γ-Mn_3O_4 is the most stable phase of manganese oxides in this *P* region.

h. *Novel yttrium phase and its hydrides up to 51 GPa (A. Aslandukova, A. Aslandukov/Bayreuth, S.V. Ovsyannikov, T. Fedotenko, S. Khandarkhaeva, D. Laniel/ Bayreuth, L.S. Dubrovinsky, N.A. Dubrovinskaia/Bayreuth, K. Glazyrin/Hamburg and M. Hanfland/Grenoble)*

With the prediction of a series of high-T_C superconducting yttrium hydrides at pressures (*P*) beyond 100 GPa and the successful synthesis of superconducting YH_6, YH_7, YH_9, a systematic understanding of phase relations in the Y-H system has become of great importance in high-*P* physics. The structure of metal hydrides is typically based on the crystallography of the metal itself, a relation that we explore here in laser-heated (~ 2500 K) diamond anvil cell (DAC) experiments up to *P* ~ 50 GPa.

Yttrium adopts the hexagonal close-packed structure (*hcp*, space group $P6_3/mmc$, *hP*2 in the Pearson notation) at ambient conditions, and up to 100 GPa undergoes a series of phase transitions typical for rare-earth metals, in which structures differ only in the stacking arrangement of their close-packed atomic layers: *hcp* ($P6_3/mmc$, *hP*2) → *α-Sm type* (*R*-3*m*, *hR*9) → *dhcp* ($P6_3/mmc$, *hP*4) → *fcc* (*Fm*-3*m*, *cF*4) → *distorted-cF4* (*R*-3*m*, *hR*24). In our DAC experiments, yttrium metal was embedded in hydrogen-rich precursors (NH_3BH_3 or paraffin oil), and we synthesized a novel YH_x phase (space group *P6/mmm*, *Z* = 3, *a* = 5.299(1) Å, c = 3.145(7) Å, *V* = 76.51(17) $Å^3$ at 51 GPa). The atomic positions of yttrium are well-determined from synchrotron single-crystal diffraction data, but the location of the light hydrogen atoms cannot be constrained by X-rays, and therefore the H content was only estimated based on the difference in volume per yttrium atom between the synthesized YH_x phase and Y metal at the

same conditions, yielding a value of $x \approx 2$. Studies of the material upon decompression (Fig. 3.7-12) suggest that the hydrogen content in the YH_x phase successively decreases under decompression, and at ambient conditions, its atomic volume in the hexagonal *P6/mmm* structure (with $a = 5.781(1)$Å, $c = 3.344(1)$ Å, $V = 96.79(4)$ Å^3) coincides with that of Y metal.

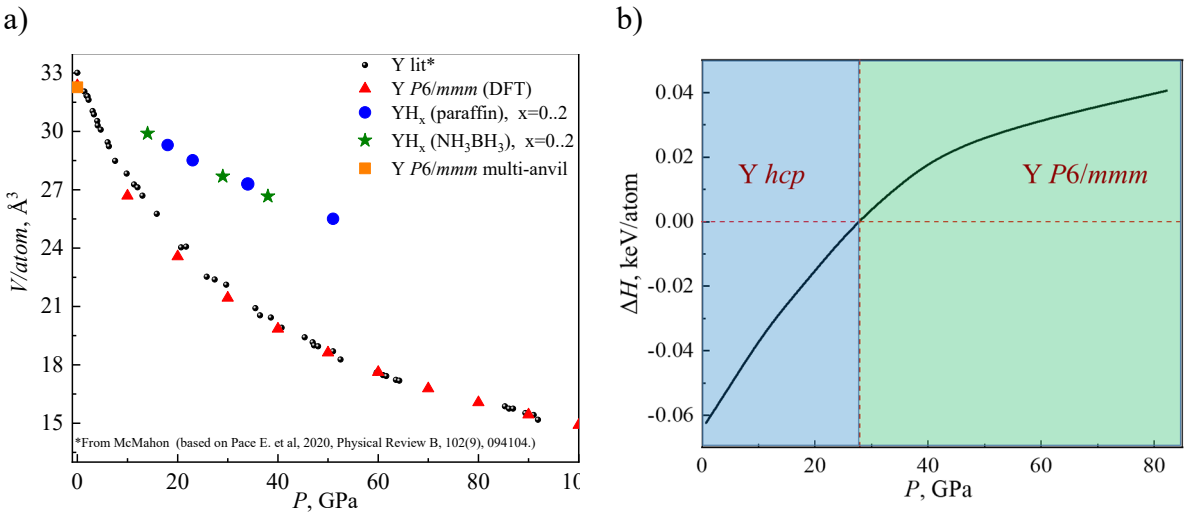

Fig. 3.7-12: a) Experimentally determined pressure dependence of the volume per yttrium atom for known Y phases (literature data in black), for YH_x from laser-heated DAC experiments with NH_3BH_3 and paraffin as hydrogen reservoirs (green stars and blue circles, respectively), for the *P6/mmm* Y phase from multianvil press (orange square), and the DFT-calculated pressure dependence of volume per yttrium atom for the *P6/mmm* Y phase (red triangles). b) Calculated enthalpy difference between the *hcp* and *P6/mmm* yttrium phases.

The observation of a novel yttrium phase with non-close-packed structure is very unexpected, and such a result requires confirmation from alternative high-*P* experiments. Yttrium metal was therefore compressed to 20 GPa and heated to 1900 K for 20 hours in the multianvil press without a hydrogen source. The single-crystal X-ray diffraction data from the recovered sample confirms the formation of the hexagonal *P6/mmm* yttrium phase. Density functional theory-based calculations of the equation of state (EOS) of the *P6/mmm* yttrium phase yields results that are comparable to EOS of the known close-packed yttrium phases. Enthalpy calculations further suggest that the *P6/mmm* yttrium phase is thermodynamically favorable over *hcp* (Fig. 3.7-12).

Thus, high *P* and high temperature allow us to synthesize an yttrium phase with a new structure type, and the experiments demonstrate that this modification of the metal can be stabilized to ambient conditions. This *P6/mmm* phase readily forms hydrides with variable composition under *P* that may play an important role in the synthesis of high-T_C superconducting yttrium hydrides at higher *P*.

i. *A reentrant phase transition and a novel polymorph revealed in high-pressure investigations of CF_4 up to 46.5 GPa (D. Laniel and T. Fedotenko/Bayreuth, B. Winkler/Frankfurt/M., A. Aslandukova, A. Aslandukov/Bayreuth, G. Aprilis/Grenoble, S. Chariton/Chicago, V. Milman/Cambridge, V.B. Prakapenka/Chiago, L.S. Dubrovinsky and N.A. Dubrovinskaia/ Bayreuth)*

The behaviour of simple molecular systems at extreme pressure (P) conditions is of great interest from a fundamental chemicophysical point of view, for planetary sciences and to provide a benchmark for theoretical calculations. While solids of H_2, O_2, CO and N_2 dimers are often hailed as ideal simple systems, they are in fact deeply complex on account of quantum effects, paramagnetic moment, electric dipole-dipole or electric quadrupole-quadrupole moments. Truly simple molecular systems lack these intermolecular interactions and are the closest approximations to noble gases; Carbon tetrahalide (CX_4) compounds are among the few that can legitimately be considered as simple since they have as their strongest intermolecular interaction van der Waals interactions and a weak electric octupole moment. As it stands, their high-P behaviour is largely unknown.

In this study, carbon tetrafluoride (CF_4) was investigated by Raman spectroscopy and synchrotron single-crystal X-ray diffraction (SCXRD) in a diamond anvil cell up to 46.5 GPa—the highest pressure thus far reported on any CX_4 solid. Based on these measurements, CF_4 is determined to undergo a series of phase transitions at room temperature, phase II $\xrightarrow{2.8\ \text{GPa}}$ phase III $\xrightarrow{\sim 20\ \text{GPa}}$ phase II^R. Phase II^R is isostructural to phase II; displaying a remarkable reentrant phase transition. Moreover, laser-heating phase II^R of CF_4 above 2000 K at 46.5 GPa led to the formation of a new polymorph of CF_4, phase IV. The structures of phase II^R, III, and IV were solved and their atomic coordinates refined on the basis of SCXRD. The comparison of the crystal structure of phase II^R, III and IV sheds light on the P-induced reorganization of the CF_4 units, unveiling a structural rearrangement from close packing of the tetrahedral molecules to close packing of the halogen atoms (Fig. 3.7-13).

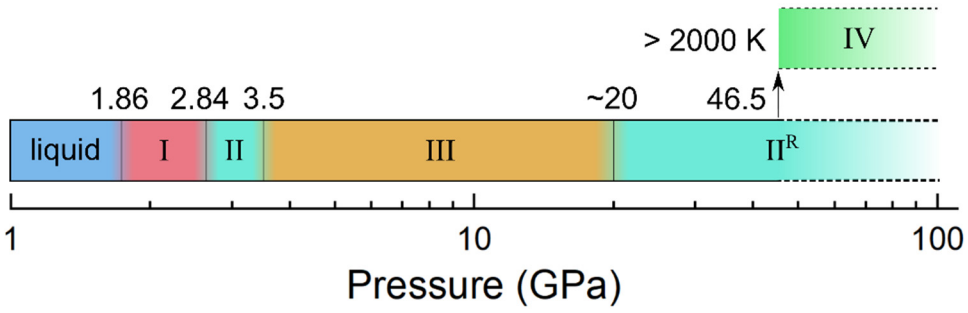

Fig. 3.7-13: A schematic representation of the stability domains of phase I (unidentified space group), phase II ($C2/c$), phase III ($P2_1/c$), phase II^R ($C2/c$) and phase IV ($Pa\bar{3}$) of CF_4. The regions with the dotted outlines highlight that above 46.5 GPa no experimental measurements have been reported. Theoretical calculations predicted the stability of phase II^R up to 108 GPa. The structural information on CF_4 below 8.7 GPa was obtained from the literature. The boundary between phase III and phase II^R is provisional, requiring further X-ray diffraction studies to determine the exact value.

Based on this investigation, the compression of any CX_4 compound is expected to increasingly lead to structures with a dense-packed arrangement of the halogen atoms, up to *P* where the electron density favors drastic chemical changes and electron delocalization resulting in polymerization, metallization, ionization or dissociation.

3.8 Methodological Developments

Since its inception, the Bayerisches Geoinstitut has been at the forefront of methodological developments in high-pressure research. Continued development of new and improved experimental, analytical, and modeling methods is required to remain at the cutting-edge of research on the structure, dynamics, and evolution of the Earth and planetary interiors.

This chapter presents six examples of developments for high-pressure experiments and two examples of software development conducted in 2021. In the first example, a method is developed for trapping high-pressure, high-temperature fluids using a single crystal diamond. Existing techniques for trapping high-pressure and high-temperature fluids using pores in diamond powders have suffered from inconsistent results. In contrast, the newly developed method provides more internally consistent results. The second contribution reports the development of a boron-doped diamond (BDD) furnace to generate ultrahigh temperature in multianvil experiments. A new, machinable BDD material was created by sintering BDD powder with a pitch binder to solve the problems of excessive hardness and brittleness in previous BDD furnace designs. Using this new material, temperatures up to 3300 K were stably generated. The third study uses piezoelectric crystals in deformation experiments to measure uniaxial stresses in samples at high pressures and temperatures. Since high temperatures induce signal leakage from the piezoelectric crystal, a unique furnace setup was designed to suppress leakage. Piezoelectric strain measurement will open up the possibility of *in situ* stress measurement, allowing us to perform deformation studies at BGI that have been previously possible only at synchrotron facilities. The fourth contribution presents measurements of temperature distributions in piston-cylinder samples heated by stepped furnaces. Developing new, low-temperature-gradient assemblies for the piston-cylinder will expand the range of studies that can be performed at the Bayerisches Geoinstitut. The fifth study reports the development of multianvil techniques that are optimized for cryogenic experiments in the neutron facility, FRM-II. This development paves the way for studying the mantles of icy solar system bodies. In contrast to these five reports on developments in large-volume press technology, the final two studies report the development of software packages. The sixth reports the development of new software for analyzing X-ray diffraction data from multi-grain samples in the DAC. The software offers a solution to the problem of processing large amounts of data generated in modern, high-energy X-ray diffraction experiments. The seventh contribution introduces a new software package for importing and visualizing geoscientific data in 3D. The software is used to create datasets that can be used as input for numerical models.

a. *The single-crystal diamond trap (SCDT): A new method to determine the composition of high-P-T fluid (S. Abeykoon and A. Audétat)*

The composition of aqueous fluids at high *P* and high *T* has been studied using various experimental techniques. One of the most widely used methods is the diamond trap method (DT). This method involves a layer of fine diamond powder in the sample capsule, such that fluid that is present during the high *P-T* run can infiltrate into the pore spaces of the diamond

layer and precipitate its solute content during quenching. However, recent studies revealed some problems with this approach, such as inconsistencies in measured mineral solubilities, and fractionation effects during the LA-ICP-MS analysis. In our newly developed single-crystal diamond trap (SCDT) method, the high *P-T* fluids are trapped in laser-drilled holes within a single-crystal diamond plate and subsequently analyzed by LA-ICP-MS using the same laser beam size as the one that was used to drill the holes. This technique allows more rigorous testing of the data reproducibility than in the case of the classical diamond trap, where the fluid resides within a large open network.

The SCDT is prepared by placing two polished, synthetic diamond plates of ~ 2.5 mm side length on top of each other, with one of the diamonds containing 9-12 laser-drilled holes ~ 80 µm diameter and ~ 50 µm depth (Fig. 3.8-1a). The two diamond plates are sealed into a platinum tube and then pressurized hydrostatically to several hundred bars. Afterwards, one side of the Pt capsule is cut open to allow fluid to access the trap at high *P, T* (Fig. 3.8-1b). This small diamond-containing Pt capsule is then loaded together with H_2O and crushed minerals (63-160 µm grain size) into a larger Pt capsule with 5.0 mm outer diameter, 4.6 mm inner diameter, and 10 mm length that is sealed by arc welding (Fig. 3.8-1c).

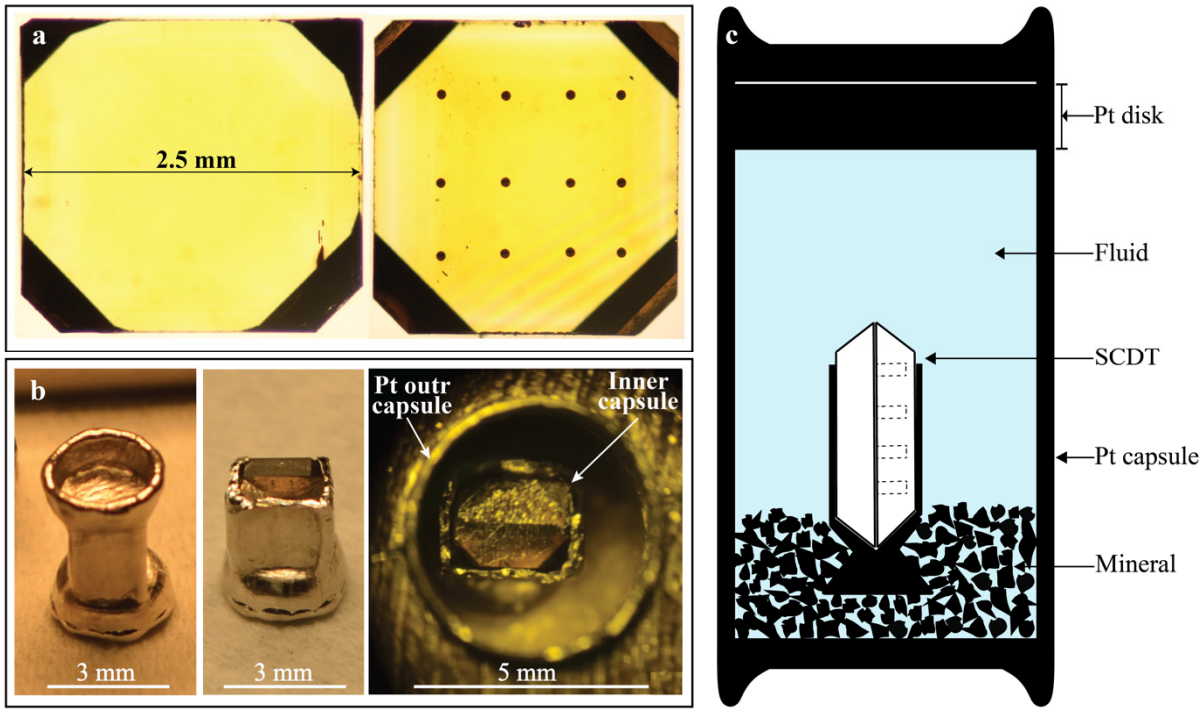

Fig. 3.8-1: (a) Photomicrographs of an undrilled (left) and a drilled (right) diamond plate. The holes measure ~ 80 µm in diameter and are ~ 50 µm deep; (b) A sealed and shrunk inner capsule (left); a one-side cut-open inner capsule (middle); and an inner capsule sitting inside a platinum outer capsule before filling with fluid; (c) a schematic drawing of the capsule setup, showing the cut-open inner capsule sitting on a bead of crushed minerals. The Pt disk was used to seal the fully fluid-filled Pt capsule of 5.0 mm diameter and 10 mm height.

The new SCDT method was tested for accuracy and reproducibility using low *P-T* tests and high *P-T* piston-cylinder experiments. The low *P-T* tests were performed by filling the holes with epoxy resins doped with known amounts of chemicals ($BaCO_3$, Al_2O_3, TiO_2 and CaF_2), or with known amounts of minerals (epidote, garnet and tourmaline) that were subsequently melted with MnO-doped $Li_2B_4O_7$. In addition, several classical DT experiments were performed for comparison. The high *P-T* tests were performed by measuring mineral solubilities at 1.0 GPa and 700-900 °C in the quartz–H_2O and olivine–enstatite–H_2O systems, for which reliable reference data exist. Recovered high *P-T* experimental charges were cut open, and the inner SCDT was opened quickly. Excess solution on the diamond with the holes was cleaned away using a razor blade. The solution was allowed to evaporate, and the precipitates in holes were then melted at 1000 °C with small amounts of MnO-doped $Li_2B_4O_7$ added, which reduces the spikiness of the LA-ICP-MS signals and minimizes element fractionation. Because this approach may result in partial loss of internal standard elements that are usually used for quantifying the LA-ICP-MS signals, we developed a new quantification procedure that works without any internal standard in the fluid but instead uses the carbon signal produced by ablated epoxy (3.8-2a) that was filled into the holes after melting the precipitates.

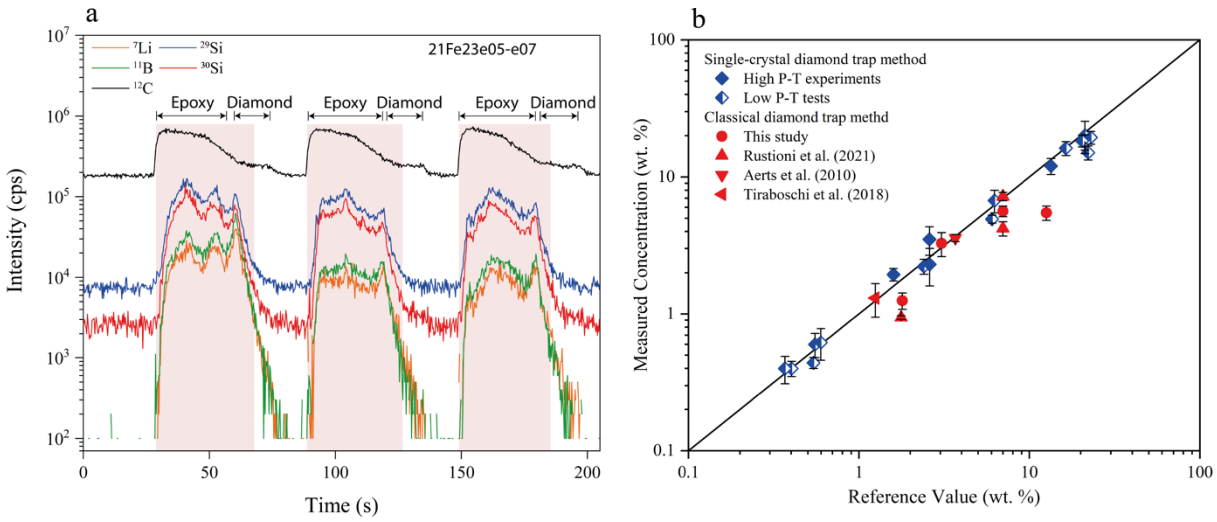

Fig. 3.8-2: (a) LA-ICP-MS signals of three holes of a SCDT experiment conducted in the quartz + water system at 1.0 GPa, 900 °C, resulting in 12.0±1.6 wt. % SiO_2 dissolved in the fluid. The shaded areas show the signal integration intervals of each hole. (b) Comparison between measured weight percentages and reference values for tests and experiments conducted with the SCDT method (blue diamonds) versus experiments conducted with silicate materials using the classical DT method (red circles and triangles). The black line represents the 1:1 line, *i.e.*, a perfect agreement between measured and reference values.

In all 15 tests and experiments conducted with the SCDT method, the measured concentrations agree with the reference values within 1-21 % (avg. 13 %). In contrast, four mineral solubility

experiments performed at identical conditions to the classical diamond-trap-method experiments returned concentrations deviating by 7-56 % (avg. 28 %) from the reference value (Fig. 3.8-2b). Furthermore, the strong fractionation effect that has been observed during the ablation of albite + H_2O in a classical diamond trap is efficiently prevented in the SCDT approach. The SCDT method thus represents a viable alternative to the classical diamond trap method.

b. *Machinable boron-doped diamond as a practical heating element in multianvil apparatuses (L. Xie)*

Expanding the achievable *P-T* range of multianvil experiments is required for cutting-edge studies beyond the limits of routinely achievable pressures and temperatures. X-ray transparency of the cell assemblies is also desired for *in situ* X-ray observation. Being both refractory and X-ray transparent, boron-doped diamond (BDD) has a great potential for resistance heating to expand the temperature range and X-ray transparency in the multianvil apparatus simultaneously. Much work has been done to optimize BDD material as a heater in multianvil apparatuses. To avoid manufacturing diamond directly, researchers used a graphite-boron composite (GBC) as a precursor of BDD in pioneer works. However, a significant pressure drop and unstable heating may occur due to the graphite–diamond conversion. In addition, anomalous melting may occur due to the formation of B_2O_3, which is formed through the oxidation of boron and acts as a fatal melting flux. To achieve excellent heating performance, researchers turned to high-pressure (HP) pre-synthesized BDD. This material shows an overwhelming advantage over GBC in heating performance, enabling stable generation of temperatures as high as ~ 4000 K. Unfortunately, however, the HP-BDD heater was hindered from widespread application owing to its high cost, and the tremendous effort and skill required for high-pressure synthesis and preparation of a tube shape. In order to lower the cost and effort, commercial BDD synthesized via chemical vapor deposition (CVD-BDD) was then tested as a heating element. The results were limited by the thickness of the available CVD-BDD block and the difficulty in manufacturing long tubes by laser, which, in turn, limits the application of CVD-BDD heater to larger cells. To overcome the limitation of the size of CVD-BDD heaters, a box-shaped heater, composed of four strips of thin CVD-BDD films, was proposed as a solution. However, the temperature gradient of the box-shaped heater is larger than that of a tubular heater, and the cell assembly becomes exceedingly complex.

In this study, a machinable BDD (MBDD) was created by sintering a mixture of BDD powder and a "binder pitch" consisting of long-chain alkanes (C_nH_{2n+2}), and annealing in Ar at 1273 K for 5 hours. The BDD powder was bound by a small amount of graphite (< 10 wt. %) during the sintering process. Tubes of the required dimensions (such as 1.2/0.7/4.0 mm in outer/inner diameter/length) can be manufactured from the MBDD block using a lathe or a computer numerical control machine (Fig. 3.8-3a-c). Owing to the low graphite content of MBDD, the graphite-diamond conversion has a negligible effect on heating performance. The MBDD

heater shows a comparable performance in the ultrahigh-temperature generation to high-pressure synthesized BDD heaters, generating temperatures higher than 3300 K and exceeding the melting point of Al_2O_3 at a pressure of 15 GPa (Fig. 3.8-3d). With good heating performance and excellent machinability, MBDD is a practical heating element for multianvil apparatuses. The achievement of stable temperature generation over 3300 K by MBDD heater enables many new applications, including various measurements on the physicochemical properties of melts under the Earth's mantle conditions.

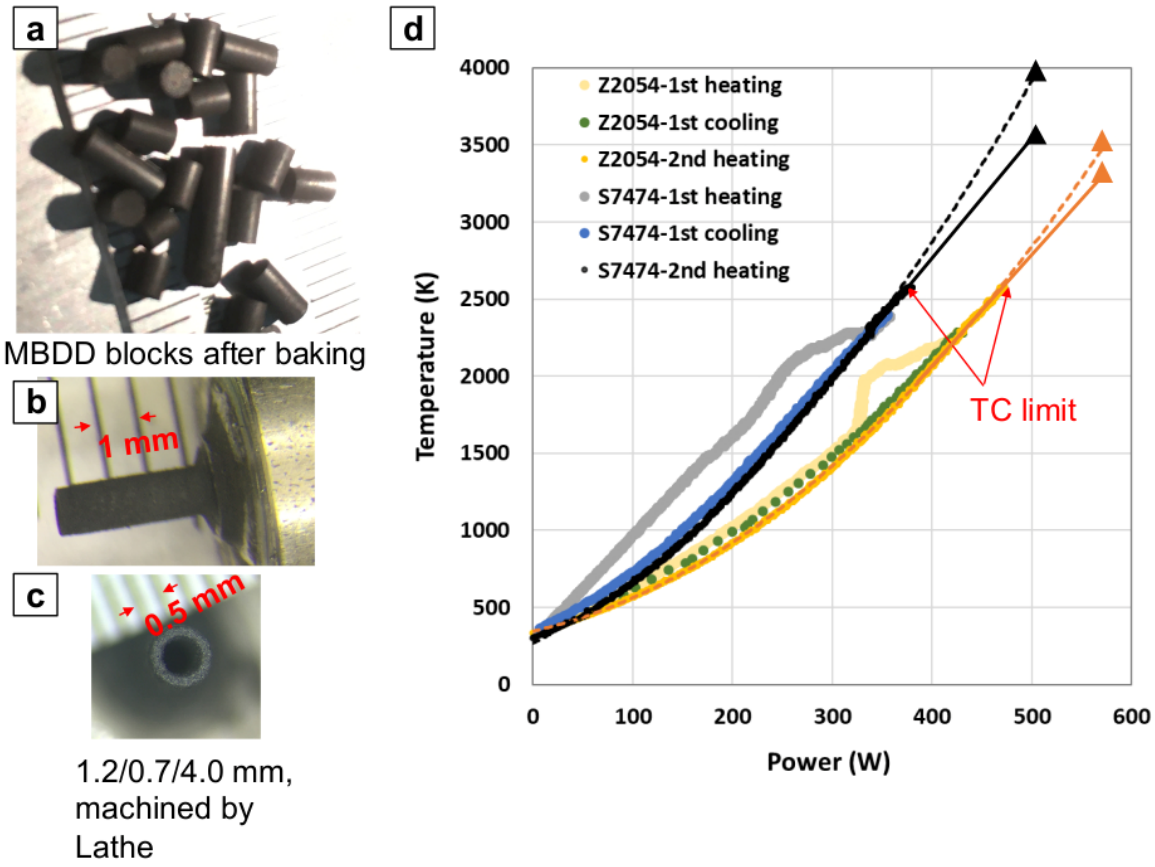

Fig. 3.8-3: A photo of sintered MBDD blocks (a), photos of a machined MBDD tube (b,c), and power–temperature diagrams for MBDD heaters (d). (d): The dashed lines are fitting lines using quadratic curves. The solid lines are linear fitting lines using data of temperature > 2000 K. The squares mark the highest power reached in corresponding experiments. TC: thermocouple.

c. *Towards the design of a high-pressure and -temperature assembly where deviatoric stresses can be determined* in situ *through the direct piezoelectric effect within the 6-axis large volume press (J.D. Dolinschi and D.J. Frost)*

The 6-axis large-volume cubic press allows the independent advancement of its 6 anvils. This provides the capability to perform deformation experiments on a cubic assembly at high-pressure and -temperature. Strain during deformation can be measured with displacement

sensors that track the advancement of each anvil. *Ex situ* measurements of deviatoric stresses can be performed through dislocation density determinations of calibrated silicate minerals, but these record only the final or integrated stress state and not the continuous or intermediate stresses during the deformation processes. Currently, *in situ* deviatoric stresses can be measured at high pressures and temperatures only by utilizing X-ray diffraction (XRD) methods at a synchrotron facility, which strongly limits the number of deformation experiments that can be accomplished.

This project aims to bring the capability for *in situ* stress measurement to any large-volume high-pressure deformation device without the need for synchrotron radiation. Piezoelectric crystals accumulate electric charge across their crystal faces in response to applied stress, owing to their non-centrosymmetric crystal symmetries. By placing a thin, round piezoelectric crystal disk in the deformation column and measuring the electric potential across the faces, *i.e.*, the voltage, it is possible to measure the deviatoric stress on a high-pressure sample. This measurement is continuous, *in situ,* and real-time. This opens up, for the first time, the capability to directly measure the deviatoric stress that a sample experiences during deformation at every point in the deformation process in real-time. Combining this with strain measurement using the displacement sensors on the anvils, allows in principle stress-strain curves, strain hardening, viscosity and stress relaxation times to be determined and potentially many other applications in any lab with a high-pressure deformation device without the need for synchrotron access.

Current efforts for the project have utilized single-crystal X-cut quartz as the piezoelectric crystal. Due to the phase transition from α-quartz to the non-piezoelectric β-quartz at 573 K at 1 bar, and to the increasing charge leakage through the piezoelectric crystal with increasing temperature, efforts have been made to create a large temperature gradient between the sample undergoing heating and the piezoelectric crystal, the goal of which is to keep the temperature at the piezoelectric crystal position as low as possible. To achieve this, the assembly geometry uses a graphite furnace in the bottom half of the cube around the sample and no furnace at the top of the cube where the piezoelectric crystal is placed (Fig. 3.8-4a). By utilizing this technique, the piezoelectric crystal is kept at approximately 450 °C cooler than the sample at 1000 °C (Fig. 3.8-4b). In this way, the quartz α- β transition is avoided, and charge leakage through the crystal is minimized.

Despite these efforts, the charge leakage at sample temperatures above 400 °C (180 °C on the piezoelectric crystal, see Fig. 3.8-4b) is large enough to affect the data (Fig. 3.8-5b), owing to the exponential inverse dependence of electrical resistivity on the temperature of quartz. The charge leakage causes constant voltage drift, which introduces large errors, as is clear in Figure 3.8-5c. In this experiment at 800 °C sample temperature (350 °C at the piezoelectric crystal, see Fig. 3.8-4b), the charge leakage was serious enough to introduce errors in the calculated deviatoric stress that were unreasonably high for the total strain. At these temperatures, the electrical resistance in the surrounding MgO drops to a level where MgO also acts as a charge leak pathway. Further refinement of the design will be necessary to decrease the charge leakage and minimize the voltage drift in the piezoelectric signal. This will include heating the graphite furnace using electrodes inserted through the side of the cube to avoid proximity to the crystal,

selecting a material with higher resistance to place around the quartz crystal to minimize charge leakage through the pathway around the crystal, and examining other piezoelectric crystals besides quartz with higher electrical resistance. Currently, using a piezoelectric crystal disk with a larger thickness is being investigated as a way of increasing the electrical resistance. Efforts are also ongoing to acquire deformation stress measurements based on other properties of piezoelectric crystals. Literature has shown a relationship between deformation stress, or deviatoric force on the crystal, and the capacitance of the crystal, the RC time constant of the charge on the crystal, and the shift in the resonant frequency of the piezoelectric crystal. These techniques will confirm the results from voltage measurements across the crystal faces.

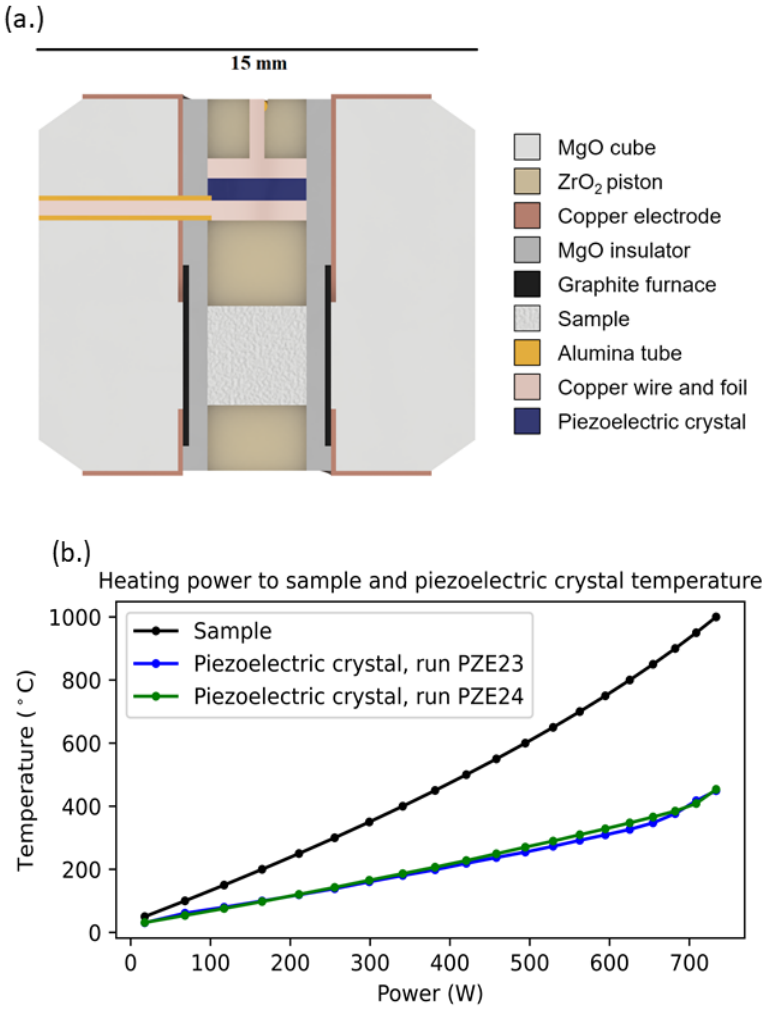

Fig. 3.8-4: (a) A cross-section view of the cubic assembly used in this project. The cube is a TEL 15/10 design. The central cylinder is 6 mm in diameter, allowing for 4 mm diameter, 4 mm tall samples. The piezoelectric crystal is kept out of and above the furnace to limit the heating of the crystal during experiments. The principal deformation stress σ_1 is oriented vertically in this cross-section. (b). A plot of temperature *vs*. heating power. The temperature within the sample area of the assembly is shown by the black line, and the temperature at the piezoelectric crystal by the green and blue lines. The green and blue lines are from different experimental runs. Both are measured at a pressure of 1 GPa.

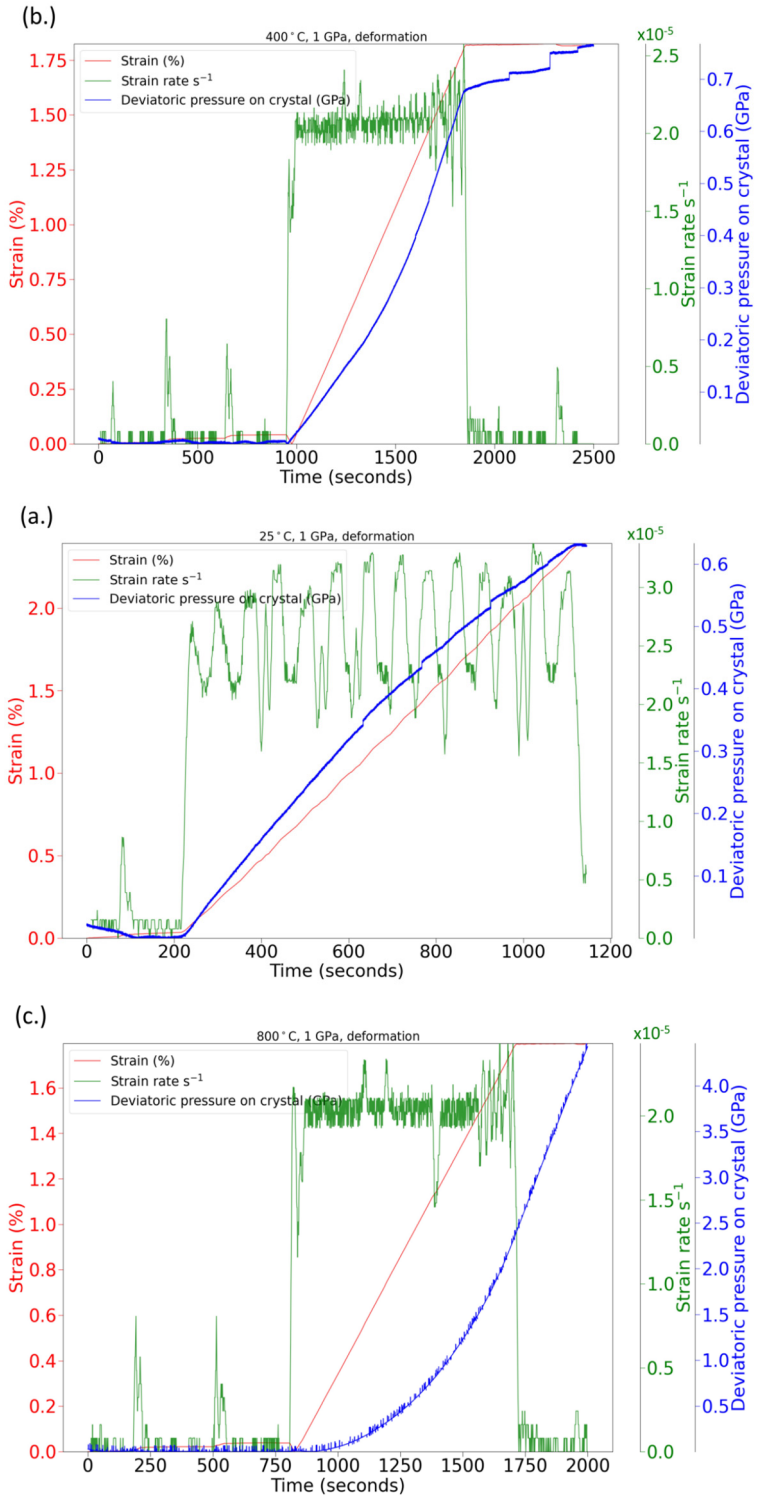

Fig. 3.8-5: (a.) A deformation experiment at 1 GPa pressure and no heating. The deformation was 18 minutes in length. (b.) A deformation experiment at 1 GPa pressure and heating of the sample to 400 °C. The deformation was 15 minutes in length. (c.) A deformation experiment at 1 GPa pressure and heating of the sample to 800 °C. The deformation was 15 minutes in length. For all three plots, the red line is total strain as a percentage, the green line is strain rate as measured by the press displacement sensors, and the blue line is the stress measured by the piezoelectric crystal. The jumps and irregularity in the green lines are due to the stepped movement of the press anvils. All were deformed at a strain rate of 2.3×10^{-5} s^{-1}. Currently, large errors arise in the 800 °C measurements due to charge leakage, which makes the stress determinations inaccurate and appear erroneously large.

d. *Exploring temperature gradients in piston cylinder assembly configurations (E.-M. Rogmann and C.A. McCammon)*

The piston cylinder apparatus plays a key role in studies of Earth processes that take place at depths down to 150 km. Accurate knowledge of experimental conditions (pressure,

temperature, oxygen fugacity) and their gradients are important for constructing realistic models to describe natural systems. As part of an ongoing review of laboratory practice, we have been exploring alternatives to the standard BGI assembly with a tapered graphite heater. The tapered design was originally developed to minimise temperature gradients across the sample, but experience has also revealed a number of drawbacks such as uneven deformation of the graphite heater during compression. We have therefore been testing a new design incorporating the same materials of the ½" standard assembly (talc, Pyrex and crushable alumina) but with a stepped graphite heater. We have also been exploring the possibility of a single-experiment determination of pressure based on Fe-Mg partitioning between iron-rich olivine and melt. Preliminary experiments using the diamond trap method showed large heterogeneities in run products, however.

We conducted piston cylinder experiments at 2 GPa and 1250 °C for 20 hours on a titanite-albite glass mixture and determined temperature based on the partitioning of Ca between partial melt and solid residue (see BGI Annual Report 2020). Ca compositions were determined using the electron microprobe and converted to temperatures based on the previously determined relation. We observed a hot spot at one end of the sample run with a tapered heater that deviated approximately 100 °C from the rest of the sample (Fig. 3.8-6a), which is consistent with previous observations of large temperature gradients due to non-reproducible behaviour of the tapered graphite heater. In contrast, the temperature gradient across the stepped heater sample was less than half as large (Fig. 3.8-6b).

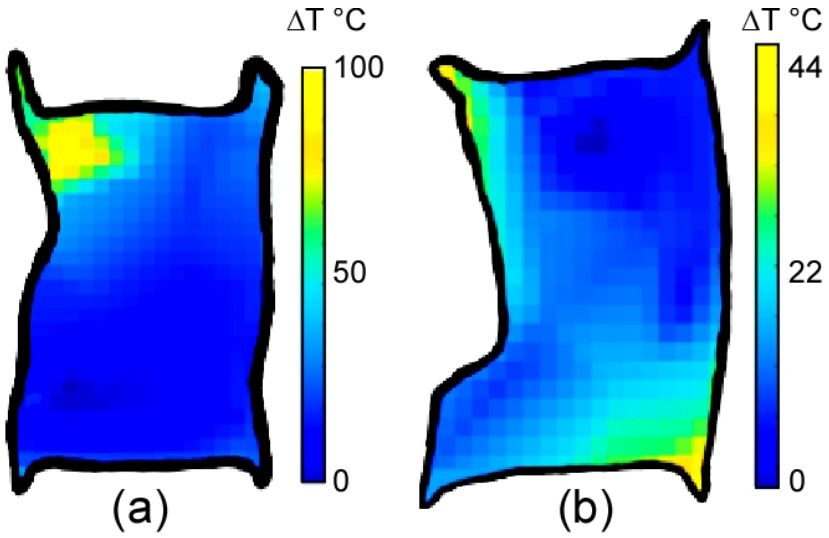

Fig. 3.8-6: Temperature distribution maps of piston cylinder run products. Experiments were carried out on a mixture of titanite and albite glass at 2 GPa and 1250 °C for 20 h using: (a) tapered graphite heater; (b) stepped graphite heater. Temperatures are based on Ca melt composition and each sample is roughly 4 mm in diameter (horizontal dimension). The temperature scales indicate the deviation from the minimum temperature measured for each run product. Blue is colder and yellow is warmer.

We also investigated Fe-Mg partitioning between olivine and melt using a diamond trap sample configuration with a stepped heater assembly. Preliminary experiments showed a large variation in iron composition of melt trapped in the diamond as well as a difference in oxygen fugacity between melt and residue according to Fe^{3+} measured using Mössbauer spectroscopy. These heterogeneities can be better understood from the results of a diamond trap experiment using titanite-albite glass starting material at the same conditions as above. Here we observed a substantial difference in Ca content of silicate melt between the region of the diamond trap compared to the region of solid residue (Fig. 3.8-7). One possibility is that melt entered the pore space of the diamond trap as soon as the glass melted and was not able to fully equilibrate with titanite outside the trap over the duration of the experiment. In this case the thermometer cannot be applied due to disequilibrium conditions. Disequilibrium can also explain heterogeneities observed in the olivine-melt experiments. Further experiments involving different diamond trap geometries and longer run times may help to resolve this issue.

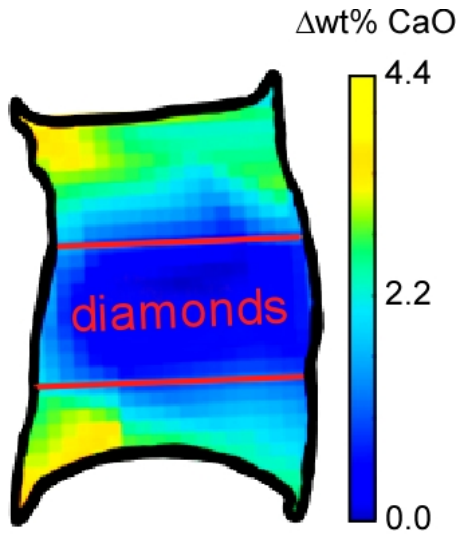

Fig. 3.8-7: Variation of Ca content in silicate melt following a piston cylinder experiment with a stepped heater and diamond trap sample configuration using the same starting material and run conditions as experiments shown in the previous figure. We interpret the large composition variation to be due to disequilibrium between different regions.

e. *Cryogenic recovery and deformation of high-pressure phases using the cooling system for the three-axis multianvil press SAPHiR at the FRM II (C. Howard and N. Walte/Garching)*

Multianvil presses are typically used to study the physical properties and phase equilibria of rocks and minerals under high-pressure and high-temperature conditions. SAPHiR is a multianvil press that will use neutrons to probe crystal structures and other properties of materials *in situ*. However, the data that can be collected using this instrument are limited by beam attenuation, parasitic scattering, and geometric restrictions from the high-pressure sample environment. In order to gain higher quality crystallographic and textural data that can complement future *in situ* measurements, it is desirable to be able to recover metastable high-pressure phases for *ex situ* analysis with other instruments, such as high-resolution neutron

diffraction and determination of crystallographic preferred orientations of deformed samples. Whilst such *ex situ* investigations of high-pressure and high-temperature phases have previously been routinely performed, low-temperature phases that are relevant for understanding frozen solar system objects, such as icy moons consisting of high-pressure ices and clathrates, could previously neither be investigated by, nor recovered from, multianvil presses.

To be able to investigate such materials and other materials of interest, such as high-entropy alloys and high-temperature superconductors, a cooling system was developed for SAPHiR that extends the temperature range to liquid nitrogen temperatures (see the previous year's annual report), enabling high-pressure phases to be cryogenically recovered. The use here of a multianvil press not only allows for static experiments, but also for controlled deformation to be performed with large sample volumes; there are few examples of other instruments that are capable of controlled deformation at low temperature, with these having limitations in either low maximum pressure or small sample volume.

In order to prepare upcoming neutron measurements on recovered samples of high-pressure urea phases and deformed high-pressure ice phases, we have tested and improved the sample environment and gasket geometry for allowing high-strain deformation and recovery of large volume samples under cryogenic conditions. Our experiments have shown that sample sizes up to ~ 130 mm^3 can be synthesised and cryogenically recovered to ambient pressure. Sample volumes can be further increased for high-resolution neutron studies by performing several identical high-pressure synthesis experiments, storing the recovered samples under liquid nitrogen, and combining them into one larger sample volume.

To assess the capability of deforming samples under cryogenic conditions, test experiments have been performed at temperatures ranging from < 100-135 K, pressures up to 2 GPa, and strain rates of 10^{-4} – 10^{-5} s^{-1} (Fig. 3.8-8). Since the danger of blowouts is generally increased under cryo-conditions, the gasket thickness had to be reduced for a given assembly size compared to high-temperature experiments, and unfired pyrophyllite gaskets had to be employed for deformation, in contrast to fired gaskets that will be used to reduce scattering for standard neutron experiments. Using these improvements, deformed samples can now reliably be recovered under cryogenic conditions, which will allow the determination of crystallographic preferred orientation of deformed high-pressure ices. To further reduce the blowout risk and to minimize scattering by the sample environment, the use of metallic gaskets and null-scattering alloys is also explored, which is possible due to the passive cooling that does not require the use of electrically insulating material. Once the FRM II reactor is restarted in early 2022, cryo-recovered samples from SAPHiR will be investigated with the FRM II instruments SPODI (a high-resolution powder diffraction instrument at the FRM II) and STRESSPEC (a powder diffractometer for crystallographic preferred orientation measurements).

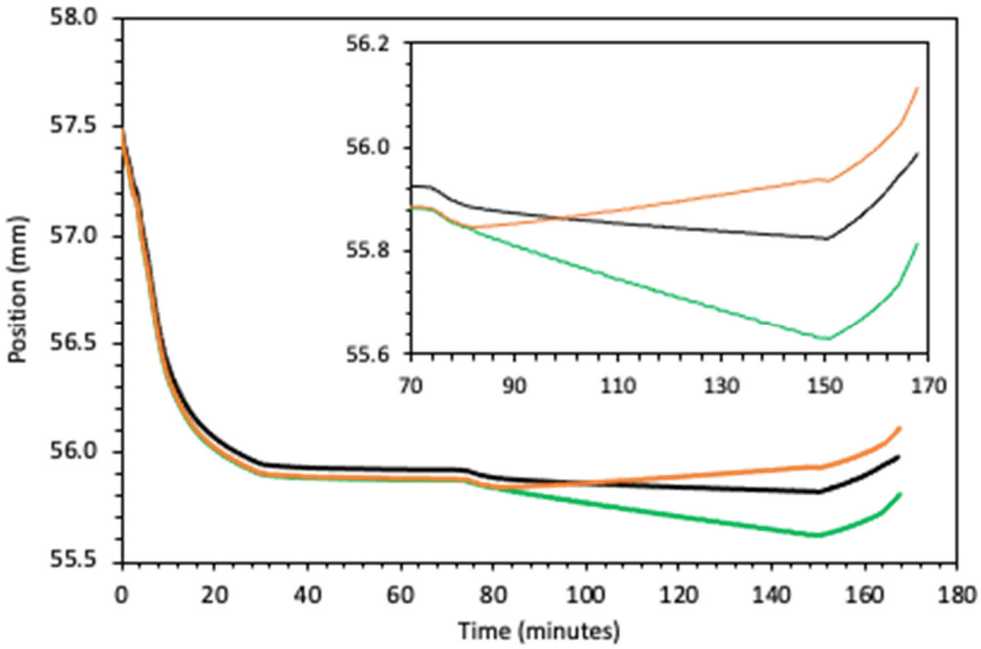

Fig. 3.8-8: (Experiment #SA208) Position of the secondary anvils during compression and deformation at ~ 100 K, and during cryogenic-recovery of the sample at *ca.* 80 K. (inset) position of the secondary anvils during deformation and cryo-recovery.

f. *Domain Auto Finder (DAFi) program: The analysis of X-ray diffraction data from multigrain samples (M. Aslandukov/Kharkiv, A. Aslandukov/Bayreuth, L.S. Dubrovinsky and N.A. Dubrovinskaia/Bayreuth)*

In the last decades, the development of 3rd and 4th generation synchrotrons, delivering monochromatic X-rays with a combination of very high brilliance and small beam size, has made it possible to apply single-crystal X-ray diffraction to polycrystalline samples. Using lab-based diffractometers, polycrystalline samples can be studied only by powder X-ray diffraction. In contrast, at the synchrotrons where the beam size becomes commensurate with the grain size (*e.g.,* beam size of 0.5 × 0.5 μm at the ESRF ID11 beamline), single-crystal diffraction from several crystallites of a polycrystalline sample caught under the beam can be observed. This approach is called multi-grain single-crystal X-ray diffraction and is becoming more and more popular. The power of multi-grain single-crystal X-ray diffraction has been demonstrated through the discovery of crystal structures of exotic compounds under high pressure in diamond anvil cells (DACs). Still, processing single-crystal X-ray diffraction data from multi-grain samples containing a lot of reflections is a complicated task, especially when we do not have any *a priori* information about the unit cell of the phases. In the case of studies under high pressures in the DAC apparatus, the search for the lattices of the individual grains (domains) becomes even more complicated due to the presence of parasitic reflections from the diamonds, the pressure-transmitting medium, the gasket, the seat material, *etc.* Therefore, software development for the automatic search of domains in the single-crystal X-ray diffraction data from multi-grain samples is an urgent task.

Here we report a program **DAFi** that takes coordinates of all reflections in reciprocal space and then finds all that are present in the XRD dataset of crystal lattices (Fig. 3.8-9). The algorithm does not need any *a priori* crystallographic knowledge. The algorithm is performed with C++ code, and the important advantage of the algorithm is the speed of data processing: the algorithm has $O(n^2 \cdot \log n)$ time complexity on single-core processor, where n is the number of reflections in the input XRD dataset, and the typical computational time is several minutes. Implementing multithreading capability allows this computational time to be decreased even further, reducing computational time in proportion to the number of cores. The further indexing of each of the found lattices can be easily done one by one in "one-click" with the standard indexing algorithms implemented in any available crystallographic program such as CrysAlis^{Pro}.

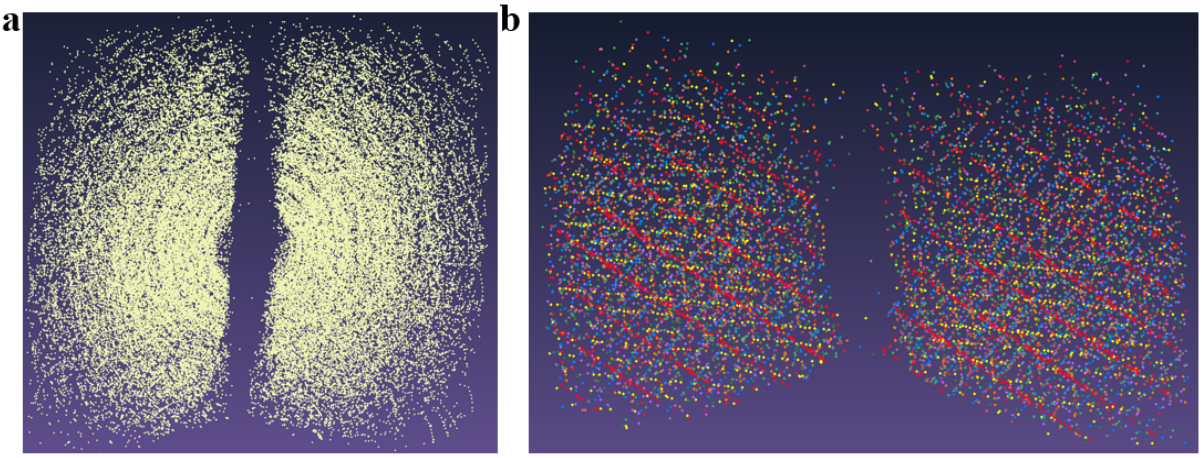

Fig. 3.8-9: Single-crystal X-ray diffraction of laser-heated Y embedded in molecular nitrogen in a DAC at 50 GPa (from P02.2 beamline of the PETRA III synchrotron) displayed in the reciprocal space: a) all 68846 reflections, b) the first 10 domains (marked with different colors) of reaction product Y_5N_{14} found by the DAFi program

g. *The Geophysical Model Generator: A set of tools to process geoscientific data (M. Thielmann, in collaboration with B. Kaus and A. Spang/Mainz)*

A common issue in geodynamic modelling lies within creating a model setup that is consistent with geophysical, geodetical and geological observables, such as seismic tomography, gravimetry, GPS measurements and surface topography. With the amount of data available from different data collections (*e.g.*, ETOPO1) or large-scale experiments (*e.g.*, USArray or AlpArray), the need for tools that allow for joint processing and analysis has grown significantly. In addition to this need, facilitating the creation of model setups for geodynamical models that honor the observations allows for effective interdisciplinary communication that will ultimately result in an increased understanding of the processes shaping our Earth.

To address this issue, we have developed a software package (GeophysicalModelGenerator.jl) that allows the user to import geoscientific data from various sources and in various formats. These datasets are then converted to a joint data format that allows to process them in a consistent manner. Moreover, our software package greatly facilitates the visualization of the different datasets in 3D (Fig. 3.8-10), thus allowing the determination of consistent features between them. Based on this joint interpretation, it is then possible to generate numerical model setups.

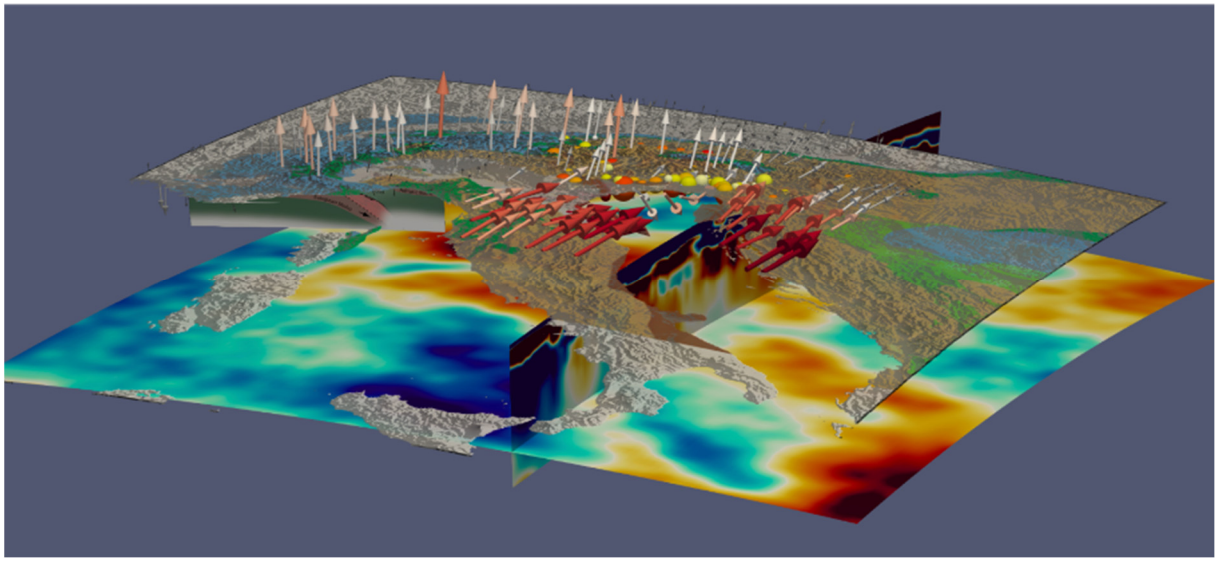

Fig. 3.8-10: Detachment depth vs. subduction velocity for oceanic slabs with different ages for typical Earth-like parameters. Results are re-dimensionalized to allow for a better comparison to observed data.

4. Publications, Conference Presentations, Seminars

4.1 Publications (published)

Supplement to **2020** (papers published at the end of 2020):

AUDÉTAT, A.; EDMONDS, M. (2020): Magmatic-hydrothermal fluids. – In: STEELE-MACINNIS, M.; MANNING, C.E. (Eds.): Hydrothermal fluids. Elements 16(6), 401-406, https://doi.org/10.2138/gselements.16.6.401

SCHRÖDER, C.; WAN, M.; BUTLER, I.B.; TAIT, A.; PEIFFER, S.; MCCAMMON, C.A. (2020): Identification of mackinawite and constraints on its electronic configuration using Mössbauer spectroscopy. Minerals 10(12), 1090, https://doi.org/10.3390/min10121090

TRYBEL, F.; COSACCHI, M.; MEIER, T.; AXT, V.M.; STEINLE-NEUMANN, G. (2020): Proton dynamics in high-pressure ice-VII from density functional theory. Phys. Rev. B 102, 184310, https://doi.org/10.1103/PhysRevB.102.184310

2021

a) Refereed international journals

ADAMS, D.J.; WANG, L.; STEINLE-NEUMANN, G.; PASSERONE, D.; CHURAKOV, S.V. (2021): Anharmonic effects on the dynamics of solid aluminium from ab-initio simulations. J. Phys.: Condens. Matter 33(17), 175501, https://doi.org/10.1088/1361-648X/abc972

ALBERS, E.; BACH, W.; PÉREZ-GUSSINYÉ, M.; MCCAMMON, C.; FREDERICHS, T. (2021): Serpentinization-driven H_2 production from continental break-up to mid-ocean ridge spreading: unexpected high rates at the West Iberia margin. Front. Earth Sci. 9, 673063, https://doi.org/10.3389/feart.2021.673063

ARATÓ, R.; AUDÉTAT, A. (2021): Titanomagnetite – silicate melt oxybarometry. – In: MORETTI, R.; NEUVILLE, D.R. (Eds.): Magma redox geochemistry. Geophysical Monograph Series 266, 369-380, https://doi.org/10.1002/9781119473206.ch18

ASLANDUKOV, A.; ASLANDUKOVA, A.; LANIEL, D.; KOEMETS, I.; FEDOTENKO, T.; YUAN, L.; STEINLE-NEUMANN, G.; GLAZYRIN, K.; HANFLAND, M.; DUBROVINSKY, L.; DUBROVINSKAIA, N. (2021): High-pressure yttrium nitride, Y_5N_{14}, featuring three distinct types of nitrogen dimers. J. Phys. Chem. C 125(32), 18077-18084, https://doi.org/10.1021/acs.jpcc.1c06210

ASLANDUKOVA, A.; ASLANDUKOV, A.; YUAN, L.; LANIEL, D.; KHANDARKHAEVA, S.; FEDOTENKO, T.; STEINLE-NEUMANN, G.; GLAZYRIN, K.; DUBROVINSKAIA, N.; DUBROVINSKY, L. (2021): Novel high-pressure yttrium carbide γ-Y_4C_5 containig [C_2] and nonlinear [C_3] units with unusually large formal charges. Phys. Rev. Lett. 127, 135501, https://doi.org/10.1103/PhysRevLett.127.135501

AUDÉTAT, A. (2021): Comment on ZHANG, et al.: "Ti-in-quartz thermobarometry and TiO_2 solubility in rhyolitic melts: New experiments and parametrization." Earth Planet. Sci. Lett. 561, 116847, https://doi.org/10.1016/j.epsl.2021.116847

AUDÉTAT, A.; MIYAJIMA, N.; WIESNER, D.; AUDINOT, J.-N. (2021): Confirmation of slow Ti diffusion in quartz by diffusion couple experiments and evidence from natural samples. Geology 49(8), 963-967, https://doi.org/10.1130/G48785.1

BARBER, N.D.; EDMONDS, M.; JENNER, F.; AUDÉTAT, A.; WILLIAMS, H. (2021): Amphibole control on copper systematics in arcs: Insights from the analysis of global datasets. Geochim. Cosmochim. Acta 307, 192-211, https://doi.org/10.1016/j.gca.2021.05.034

BEYER, C.; KURNOSOV, A.; BOFFA BALLARAN, T.; FROST, D.J. (2021): High-pressure and high-temperature single-crystal X-ray diffraction of complex garnet solid solutions up to 16 GPa and 823 K. Phys Chem Minerals 48, 17, https://doi.org/10.1007/s00269-021-01139-5

BEYER, C.; MYHILL, R.; MARQUARDT, K.; MCCAMMON, C. (2021): A reversed redox gradient in Earth's mantle transition zone. Earth Planet. Sci. Lett. 575, 117181, https://doi.org/10.1016/j.epsl.2021.117181

BINDI, L.; SINMYO, R.; BYKOVA, E.; OVSYANNIKOV, S.V.; MCCAMMON, C.; KUPENKO, I.; ISMAILOVA, L.; DUBROVINSKY, L.; XIE, X. (2021): Discovery of elgoresyite, $(Mg,Fe)_5Si_2O_9$: Implications for novel iron-magnesium silicates in rocky planetary interiors. ACS Earth Space Chem. 5(8), 2124-2130, https://doi.org/10.1021/acsearthspacechem.1c00157

BLANCHARD, I.; ABEYKOON, S.; RUBIE, D.C.; FROST, D.J. (2021): Sulfur content at sulfide saturation of peridotitic melt at upper mantle conditions. Am. Mineral. 106, 1835-1843, https://doi.org/10.2138/am-2021-7649

BONDAR, D.; FEI, H.; WITHERS, A.C.; ISHII, T.; CHANYSHEV, A.; KATSURA, T. (2021): A simplified rapid-quench multi-anvil technique. Rev. Sci. Instrum. 92, 113902, https://doi.org/10.1063/5.0062525

BORISOVA, A.Y.; ZAGRTDENOV, N.R.; TOPLIS, M.J.; BOHRSON, W.A.; NÉDÉLEC, A.; SAFONOV, O.G.; POKROVSKI, G.S.; CEULENEER, G.; BINDEMAN, I.N.; MELNIK, O.E.; JOCHUM, K.P.; STOLL, B.; WEIS, U.; BYCHKOV, A.Y.; GURENKO, A.A.; SHCHEKA, S.; A. TEREHIN, S., POLUKEEV, V.M.; VARLAMOV, D.A.; CHARITEIRO, K.; GOUY, S.; DE PARSEVAL, P. (2021): Hydrated peridotite – basaltic melt interaction part I: Planetary felsic crust formation at shallow depth. Front. Earth Sci. 9, 640464, https://doi.org/10.3389/feart.2021.640464

BUCHEN, J.; STURHAHN, W.; ISHII, T.; JACKSON, J. (2021): Vibrational anisotropy of δ-(Al,Fe)OOH single crystals as probed by nuclear resonant inelastic X-ray scattering. Eur. J. Mineral. 33(4), 485-502, https://doi.org/10.5194/ejm-33-485-2021

BYKOV, M.; FEDOTENKO, T.; CHARITON, S.; LANIEL, D.; GLAZYRIN, K.; HANFLAND, M.; SMITH, J.; PRAKAPENKA, V.; MAHMOOD, M.; GONCHAROV, A.; PONOMAREVA, A.; TASNÁDI, F.; ABRIKOSOV, A.; MASOOD, T.B.; HOTZ, I.; RUDENKO, A.; KATSNELSON, M.; DUBROVINSKAIA, N.; DUBROVINSKY, L.; ABRIKOSOV, I. (2021): High-pressure synthesis of dirac materials: Layered van der Waals bonded BeN4 polymorph. Phys. Rev. Lett. 126, 175501, https://doi.org/10.1103/PhysRevLett.126.175501

BYKOV, M.; BYKOVA, E.; PONOMAREVA, A.; ABRIKOSOV, I.; CHARITON, S.; PRAKAPENKA, V.; MAHMOOD, M.; DUBROVINSKY, L.; GONCHAROV, A. (2021): Stabilization of polynitrogen anions in tantalum–nitrogen compounds at high pressure. Angew. Chem. Int. Ed. 60(16), 9003-9008, https://doi.org/10.1002/anie.202100283

BYKOVA, E.; BYKOV, M.; CHARITON, S.; PRAKAPENKA, V.B.; GLAZYRIN, K.; ASLANDUKOV, A.; ASLANDUKOVA, A.; CRINITI, G.; KURNOSOV, A.; GONCHAROV, A.F. (2021): Structure and composition of CSH compounds up to 143 GPa. Phys. Rev. B 103, L140105, https://doi.org/10.1103/PhysRevB.103.L140105

CAMBIONI, S.; JACOBSON, S.; EMSENHUBER, A.; ASPHAUG, E.; RUBIE, D.C.; GABRIEL, T.; SCHWARTZ, S.; FURFARO, R. (2021): The effect of inefficient accretion on planetary differentiation. Planet. Sci. J. 2, 93, https://doi.org/10.3847/PSJ/abf0ad

CASSETTA, M.; DI GENOVA, D.; ZANATTA, M.; BOFFA BALLARAN, T.; KURNOSOV, A.; GIAROLA, M.; MARIOTTO, G. (2021): Estimating the viscosity of volcanic melts from the vibrational properties of their parental glasses. Sci Rep 11, 13072, https://doi.org/10.1038/s41598-021-92407-5

CHANG, J.; AUDÉTAT, A. (2021): LA-ICP-MS analysis of crystallized melt inclusions in olivine, plagioclase, apatite and pyroxene: quantification strategies and effects of post-entrapment modifications. Journal of Petrology 62(4), egaa085, https://doi.org/10.1093/petrology/egaa085

CHANG, J.; AUDÉTAT, A.; LI, J.-W. (2021): In-situ reaction-replacement origin of hornblendites in the Early Cretaceous Laiyuan complex, North China Craton, and implications for its tectono-magmatic evolution. Journal of Petrology 62(5), egab030, https://doi.org/10.1093/petrology/egab030

CHANG, J.; AUDÉTAT, A.; LI, J.-W. (2021): Tectono-magmatic controls on decratonic gold deposits. Contrib Mineral Petrol 176, 69, https://doi.org/10.1007/s00410-021-01824-2

CHANYSHEV, A.; BONDAR, D.; FEI, H.; PUREVJAV, N.; ISHII, T.; NISHIDA, K.; BHAT, S.; FARLA, R.; KATSURA, T. (2021): Determination of phase relations of the olivine–ahrensite transition in the Mg_2SiO_4–Fe_2SiO_4 system at 1740 K using modern multi-anvil techniques. Contrib Mineral Petrol 176, 77, https://doi.org/10.1007/s00410-021-01829-x

CRINITI, G.; KURNOSOV, A.; BOFFA BALLARAN, T.; FROST, D.J. (2021): Single-crystal elasticity of $MgSiO_3$ bridgmanite to mid-lower mantle pressure. JGR Solid Earth 126(5), e2020JB020967, https://doi.org/10.1029/2020JB020967

COMODI, P.; FASTELLI, M.; CRINITI, G.; GLAZYRIN, K.; ZUCCHINI, A. (2021): High pressure behavior of mascagnite from single crystal synchrotron X-ray diffraction data. Crystals 11(8), 976, https://doi.org/10.3390/cryst11080976

CRINITI, G.; KURNOSOV, A.; BOFFA BALLARAN, T.; FROST, D.J. (2021): Single-crystal elasticity of $MgSiO_3$ bridgmanite to mid-lower mantle pressure. JGR Solid Earth 126(5), e2020JB020967, https://doi.org/10.1029/2020JB020967

DRUZHBIN, D.; FEI, H.; KATSURA, T. (2021): Independent hydrogen incorporation in wadsleyite from oxygen fugacity and non-dissociation of H_2O in the reducing mantle transition zone. Earth Planet. Sci. Lett. 557, 116755, https://doi.org/10.1016/j.epsl.2021.116755

FEDOTENKO, T.; SOUZA, D.S.; KHANDARKHAEVA, S.; DUBROVINSKY, L.; DUBROVINSKAIA, N. (2021): Isothermal equation of state of crystalline and glassy materials from optical measurements in diamond anvil cells. Rev. Sci. Instrum. 92, 063907, https://doi.org/10.1063/5.0050190

FEDOTENKO, T.; KHANDARKHAEVA, S.; DUBROVINSKY, L.; GLAZYRIN, K.; SEDMAK, P.; DUBROVINSKAIA, N. (2021): Synthesis and compressibility of novel nickel carbide at pressures of Earth's Outer Core. Minerals 11(5), 516, https://doi.org/10.3390/min11050516

FEI, H.; KATSURA, T. (2021): Water solubility in Fe-bearing wadsleyite at mantle transition zone temperatures. Geophys. Res. Lett. 48(9), e2021GL092836, https://doi.org/10.1029/2021GL092836

FEI, H.; FAUL, U.; KATSURA, T. (2021): The grain growth kinetics of bridgmanite at the topmost lower mantle. Earth Planet. Sci. Lett. 561, 116820, https://doi.org/10.1016/j.epsl.2021.116820

FEI, H. (2021): Water content of the dehydration melting layer in the topmost lower mantle. Geophys. Res. Lett. 48(1), e2020GL090973, https://doi.org/10.1029/2020GL090973

FROSSARD, P.; GUO, Z.; SPENCER, M.; BOYET, M.; BOUVIER. A. (2021): Evidence from achondrites for a temporal change in Nd nucleosynthetic anomalies within the first 1.5 million years of the inner solar system formation. Earth Planet. Sci. Lett. 566, 116968, https://doi.org/10.1016/j.epsl.2021.116968

FUKUSHIMA, R.; TSUJIMORI, T.; MIYAJIMA, N. (2021): Various antiphase domains in garnet-hosted omphacite in low temperature eclogite: A FIB–TEM study on heterogeneous ordering processes. Am. Mineral. 106(10), 1596-1605, https://doi.org/10.2138/am-2021-7784

GATTACCECA, J.; MCCUBBIN, F.; BOUVIER, A.; GROSSMAN, J.; BULLOCK, E.; CHENNAOUI AOUDJEHANE, H.; DEBAILLE, V.; D'ORAZIO, M.; KOMATSU, M.; MIAO, B.; SCHRADER, D. (2021): The Meteoritical Bulletin, No. 109. Meteorit Planet Sci 56(8), 1626-1630, https://doi.org/10.1111/maps.13714

GHOSH, S.; TIWARI, K.; MIYAHARA, M.; ROHRBACH, A.; VOLLMER, C.; STAGNO, V.; OHTANI, E.; RAY, D. (2021): Natural Fe-bearing aluminous bridgmanite in the Katol L6 chondrite. PNAS 118(40), e2108736118, https://doi.org/10.1073/pnas.2108736118

GOLABEK, G.J.; JUTZI, M. (2021): Modification of icy planetesimals by early thermal evolution and collisions: Constraints for formation time and initial size of comets and small KBOs. Icarus 363, 114437, https://doi.org/10.1016/j.icarus.2021.114437

GORELOVA, L.; PAKHOMOVA, A.; KRZHIZHANOVSKAYA, M.; PANKIN, D.; KRIVOVICHEV, S.; DUBROVINSKY, L.; KASATKIN, A. (2021): Crystal structure evolution of slawsonite $SrAl_2Si_2O_8$ and paracelsian $BaAl_2Si_2O_8$ upon compression and decompression. J. Phys. Chem. C 125(23), 13014-13023, https://doi.org/10.1021/acs.jpcc.1c02949

HAMADA, M.; KAMADA, S.; OHTANI, E.; SAKAMAKI, T.; MITSUI, T.; MASUDA, R.; HIRAO, N.; OHISHI, Y.; AKASAKA, M. (2021): Synchrotron Mössbauer spectroscopic and X-ray diffraction study of ferropericlase in the high-pressure range of the lower mantle region. Phys. Rev. B 103, 174108, https://doi.org/10.1103/PhysRevB.103.174108

HUANG, R.; BOFFA BALLARAN, T.; MCCAMMON, C.; MIYAJIMA, N.; FROST, D.J. (2021): The effect of Fe-Al substitution on the crystal structure of $MgSiO_3$ bridgmanite. JGR Solid Earth, 126, e2021JB021936, https://doi.org/10.1029/2021JB021936

HUANG, R.; BOFFA BALLARAN, T.; MCCAMMON, C.; MIYAJIMA, N.; DOLEJS, D.; FROST, D.J. (2021): The composition and redox state of bridgmanite in the lower mantle as a function of oxygen fugacity. Geochim. Cosmochim. Acta 303, 110-136, https://doi.org/10.1016/j.gca.2021.02.036

HUANG, Y.; GUO, H.; NAKATANI, T.; UESUGI, K.; NAKAMURA, M.; KEPPLER, H. (2021): Electrical conductivity in texturally equilibrated fluid-bearing forsterite aggregates at 800 °C and 1 GPa: Implications for the high electrical conductivity anomalies in mantle wedges. JGR Solid Earth 126(9), e2020JB021343, https://doi.org/10.1029/2020JB021343

IKUTA, D.; OHTANI, E.; HIRAO, N. (2021): Two-phase mixture of iron-nickel-silicon alloys in the Earth's inner core. Commun Earth Environ 2, 225, https://doi.org/10.1038/s43247-021-00298-1

ISHII, T.; OHTANI, E. (2021): Dry metastable olivine and slab deformation in a wet subducting slab. Nat. Geosci. 14, 526-530, https://doi.org/10.1038/s41561-021-00756-7

ISHII, T.; CRINITI, G.; BYKOVA, E.; DUBROVINSKY, L.; KATSURA, T.; ARII, H.; KOJITANI, H.; AKAOGI, M. (2021): High-pressure syntheses and crystal structure analyses of a new low-density $CaFe_2O_4$- related and $CaTi_2O_4$-type $MgAl_2O_4$ phases. Am. Mineral. 106(7), 1105-1112, https://doi.org/10.2138/am-2021-7619

JENNINGS, E.S., JACOBSON, S.A., RUBIE, D.C., NAKAJIMA, Y.; VOGEL, A.K.; ROSE-WESTON, L.A.; FROST, D.J. (2021): Metal-silicate partitioning of W and Mo and the role of carbon in controlling their abundances in the bulk silicate earth. Geochim. Cosmochim. Acta 293, 40-69, doi.org/10.1016/j.gca.2020.09.035

KATSURA, T.; FEI, H. (2021): Asthenosphere dynamics based on the H_2O dependence of element diffusivity in olivine. National Science Review 8(4), nwaa278, https://doi.org/10.1093/nsr/nwaa278

KHANDARKHAEVA, S.; FEDOTENKO, T.; CHARITON, S.; BYKOVA, E.; OVSYANNIKOV, S.; GLAZYRIN, K.; LIERMANN, H.-P.; PRAKAPENKA, V.; DUBROVINSKAIA, N.; DUBROVINSKY, L. (2021): Structural diversity of magnetite and products of its decomposition at extreme conditions. Inorg. Chem. 61(2), 1091-1101, https://doi.org/10.1021/acs.inorgchem.1c03258

KOEMETS, E.; BYKOV, M.; BYKOVA, E.; CHARITON, S.; APRILIS, G.; FEDOTENKO, T.; CLÉMENT, S.; ROUQUETTE, J.; HAINES, J.; CERANTOLA, V.; GLAZYRIN, K.; ABAKUMOV, A.; ISMAILOVA, L.; MCCAMMON, C.; PRAKAPENKA, V.B.; HANFLAND, M.; LIERMANN, H.-P.; SVITLYK, V.; ROSA, A.; IRIFUNE, T.; LEONOV, I.; PONOMAREVA, A.V.; ABRIKOSOV, I.A.; DUBROVINSKAIA, N.; DUBROVINSKY, L. (2021): Revealing the complex nature of structure and bonding of binary high-pressure compound FeO_2. Phys. Rev. Lett. 126, 106001, https://doi.org/10.1103/PhysRevLett.126.106001

KOEMETS, E.; FEDOTENKO, T.; KHANDARKHAEVA, S.; BYKOV, M.; BYKOVA, E.; THIELMANN, M.; CHARITON, S.; APRILIS, G.; KOEMETS, I.; LIERMANN, H.-P.; HANFLAND, M.; OHTANI, E.; DUBROVINSKAIA, N.; MCCAMMON, C.; DUBROVINSKY, L. (2021): Chemical stability of FeOOH at high pressure and temperature, and oxygen recycling in early Earth history. European Journal of Inorg. Chem. 2021(30), 3048-3053, https://doi.org/10.1002/ejic.202100274

LANGHAMMER, D.; DI GENOVA, D.; STEINLE-NEUMANN, G. (2021): Modelling the viscosity of anhydrous and hydrous volcanic melt. Geochemistry, Geophysics, Geosystems 22, e2021GC009918, https://doi.org/10.1029/2021GC009918

LANIEL, D.; ASLANDUKOVA, A.; ASLANDUKOV, A.; FEDOTENKO, T.; CHARITON, S.; GLAZYRIN, K.; PRAKAPENKA, V.; DUBROVINSKY, L.; DUBROVINSKAIA, N. (2021): High-Pressure synthesis of the β-Zn_3N_2 nitride and the α-ZnN_4 and β-ZnN_4 polynitrogen compounds. Inorg. Chem. 60(19), 14594-14601, https://doi.org/10.1021/acs.inorgchem.1c01532

LANIEL, D.; WINKLER, B.; KOEMETS, E.; FEDOTENKO, T.; CHARITON, S.; MILMAN, V.; GLAZYRIN, K.; PRAKAPENKA, V.; DUBROVINSKY, L.; DUBROVINSKAIA N. (2021): Nitrosonium nitrate (NO^+ NO^{3-}) structure solution using in situ single-crystal X-ray diffraction in a diamond anvil cell. IUCrJ 8(2), 208-214, https://doi.org/10.1107/S2052252521000075

LANIEL, D.; BINCK, J.; WINKLER, B.; VOGEL, S.; FEDOTENKO, T.; CHARITON, S.; PRAKAPENKA, V.; MILMAN, V.; SCHNICK, W.; DUBROVINSKY, L.; DUBROVINSKAIA, N. (2021): Synthesis, crystal structure and structure–property relations of strontium orthocarbonate, Sr_2CO_4. Acta Cryst. B77, 131-137, https://doi.org/10.1107/S2052520620016650

LA SPINA, G.; ARZILLI, F.; LLEWELLIN, E.W.; BURTON, M.R.; CLARKE, A.B.; DE' MICHIELI VITTURI, M.; POLACCI, M.; HARTLEY, M.E.; DI GENOVA, D.; MADER, H.M. (2021): Explosivity of basaltic lava fountains is controlled by magma rheology, ascent rate and outgassing. Earth Planet. Sci. Lett. 553, 116658, https://doi.org/10.1016/j.epsl.2020.116658

LE GALL, N.; ARZILLI, F.; LA SPINA, G.; POLACCI, M.; CAI, B.; HARTLEY, M.E.; ATWOOD, R.C.; DI GENOVA, D.; NONNI, S.; LLEWELLIN, E.W.; BURTON, M.R.; LEE, P.D. (2021): *In situ* quantification of crystallisation kinetics of plagioclase and clinopyroxene in basaltic magma: implications for lava flow. Earth Planet. Sci. Lett. 568, 117016, https://doi.org/10.1016/j.epsl.2021.117016

LI, Y.; AUDÉTAT, A.; LIU, Z.; WANG, F. (2021): Chalcophile element partitioning between Cu-rich sulfide phases and silicate melt and implications for the formation of Earth's continental crust. Geochim. Cosmochim. Acta 302, 61-82, https://doi.org/10.1016/j.gca.2021.03.020

LICHTENBERG, T.; DRĄŻKOWSKA, J.; SCHÖNBÄCHLER, M.; GOLABEK, G.J.; HANDS, T. (2021): Bifurcation of planetary building blocks during Solar System formation. Science 371, 365-370, https://doi.org/10.1126/science.abb3091

LIU, Z.; FEI, H.; CHEN, L.; MCCAMMON, C.; WANG, L.; LIU, R.; WANG, F.; LIU, B.; KATSURA, T. (2021): Bridgmanite is nearly dry at the top of the lower mantle. Earth Planet. Sci. Lett. 570, 117088, https://doi.org/10.1016/j.epsl.2021.117088

LIU, Z.; LIU, R.; SHANG, Y.; SHEN, F.; CHEN, L.; HOU, X.; YAO, M.; CUI, T.; LIU, B.; KATSURA, T. (2021): Aluminum solubility in bridgmanite up to 3000 K at the top lower mantle. Geosci. Front. 12(2), 929-935, https://doi.org/10.1016/j.gsf.2020.04.009

MANTHILAKE, G.; MOOKHERJEE, M.; MIYAJIMA, N. (2021): Insights on the deep carbon cycle from the electrical conductivity of carbon-bearing aqueous fluids. Sci Rep 11, 3745, https://doi.org/10.1038/s41598-021-82174-8

MATSUOKA, M.; NAKAMURA, T.; MIYAJIMA, N.; HIROI, T.; IMAE, N.; YAMAGUCHI, A. (2022): Spectral and mineralogical alteration process of naturally-heated CM and CY chondrites. Geochim. Cosmochim. Acta 316, 150-167, https://doi.org/10.1016/j.gca.2021.08.042

MCCAMMON, C. (2021): Mössbauer spectroscopy with high spatial resolution: Spotlight on geoscience. – In: YOSHIDA, Y.; LANGOUCHE, G. (Eds.): Modern Mössbauer Spectroscopy: New Challenges Based on Cutting-Edge Techniques, Springer, pp. 221-266, https://doi.org/10.1007/978-981-15-9422-9_5

MCGUIRE, C.; KOMABAYASHI, T.; THOMPSON, S.; BROMILEY, G.; ISHII, T.; GREENBERG, E.; PRAKAPENKA, V.B. (2021): P-V-T measurements of Fe_3C to 117 GPa and 2100 K: implications for stability of Fe_3C phase at core conditions. Am. Mineral. 106(8), 1349-1359, https://doi.org/10.2138/am-2021-7581

MÉNDEZ, A.S.J.; TRYBEL, F.; HUSBAND, R.; STEINLE-NEUMANN, G.; LIERMANN, H.-P.; MARQUARDT, H. (2021): Bulk modulus of H_2O across the ice VII – ice X transition measured by time-resolved X-ray diffraction in dynamic Diamond Anvil Cell experiments. Phys. Rev. B 103, 064104, https://doi.org/10.1103/PhysRevB.103.064104

MEIER, T.; ASLANDUKOVA, A.; TRYBEL, F.; LANIEL, D.; ISHII, T.; KHANDARKHAEVA, S.; DUBROVINSKAIA, N.; DUBROVINSKY, L. (2021): In situ high-pressure nuclear magnetic resonance crystallography in one and two dimensions. Matter and Radiation at Extremes 6, 068402, https://doi.org/10.1063/5.0065879

MÉNDEZ, A.S.J.; TRYBEL, F.; HUSBAND, R.; LIERMANN, H.-P.; MARQUARDT, H.; STEINLE-NEUMANN, G. (2021): Bulk modulus of H2O across the ice VII–ice X transition measured by time-resolved x-ray diffraction in dynamic diamond anvil cell experiments. Phys. Rev. B 103, 064104, https://doi.org/10.1103/PhysRevB.103.064104

MIYAHARA, M.; YAMAGUCHI, A.; OHTANI, E.; TOMIOKA, N.; KODAMA, Y. (2021): Complicated pressure–temperature path recorded in the eucrite Padvarninkai. Meteorit Planet Sci 56(8), 1443-1458, https://doi.org/10.1111/maps.13724

MOROZOVA, N.V.; KOROBEYNIKOV, I.V.; OVSYANNIKOV, S.V. (2021): Colossal enhancement of the thermoelectric power factor in stress-released orthorhombic phase of SnTe. Appl. Phys. Lett. 118, 103903, https://doi.org/10.1063/5.0043954

MOROZOVA, N.V.; KOROBEYNIKOV, I.V.; SHKVARINA, E.G.; TITOV, A.A.; TITOV, A.N.; OVSYANNIKOV, S.V. (2021): Stress-controlled *n-p* conductivity switch based on intercalated $ZrTe_2$. Appl. Phys. Lett. 119, 053103, https://doi.org/10.1063/5.0050611

NAKAJIMA, M.; GOLABEK, G.J.; WÜNNEMANN, K.; RUBIE, D.C.; BURGER, C.; MANSKE, L.; MELOSH, H.J.; JACOBSON, S.A.; HULL, S.D. (2021): Scaling laws for the geometry of an impact-induced magma ocean. Earth Planet. Sci. Lett. 568, 116983, https://doi.org/10.1016/j.epsl.2021.116983

OHIRA, I.; JACKSON, J.M.; STURHAHN, W.; FINKELSTEIN, G.J.; KAWAZOE, T.; TOELLNER, T.S.; SUZUKI, A.; OHTANI, E. (2021): The influence of δ-(Al,Fe)OOH on seismic heterogeneities in Earth's lower mantle. Sci Rep 11, 12036, https://doi.org/10.1038/s41598-021-91180-9

OHTANI, E. (2021): Hydration and dehydration in Earth's interior. Annual Review of Earth and Planetary Sciences 49, 253-278, https://doi.org/10.1146/annurev-earth-080320-062509

OKUCHI, T.; SETO, Y.; TOMIOKA, N.; MATSUOKA, T.; ALBERTAZZI, B.; HARTLEY, N.J.; INUBUSHI, Y.; KATAGIRI, K.; KODAMA, R.; PIKUZ, T.A.; PUREVJAV, N.; MIYANISHI, K.; SATO, T.; SEKINE, T.; SUEDA, K.; TANAKA, K.A.; TANGE, Y.; TOGASHI, T.; UMEDA, Y.; YABUUCHI, T.; YABASHI, M.; OZAKI, N. (2021): Ultrafast olivine-ringwoodite transformation during shock compression. Nat Commun 12, 4305, https://doi.org/10.1038/s41467-021-24633-4

OVSYANNIKOV, S.V.; ASLANDUKOVA, A.A.; ASLANDUKOV, A.; CHARITON, S.; TSIRLIN, A.A.; KOROBEYNIKOV, I.V.; MOROZOVA, N.V.; FEDOTENKO, T.; KHANDARKHAEVA, S.; DUBROVINSKY, L. (2021): Structural stability and properties of marokite-type γ-Mn_3O_4. Inorg. Chem. 60, 13440-13452, https://doi.org/10.1021/acs.inorgchem.1c01782

OVSYANNIKOV, S.V.; TSIRLIN, A.A.; KOROBEYNIKOV, I.V.; MOROZOVA, N.V.; ASLANDUKOVA, A.A.; STEINLE-NEUMANN, G.; CHARITON, S.; KHANDARKHAEVA, S.; GLAZYRIN, K.; WILHELM, F.; ROGALEV, A.; DUBROVINSKY, L. (2021): Synthesis of ilmenite-type ε-Mn_2O_3 and its properties. Inorg. Chem. 60, 13348-13358, https://doi.org/10.1021/acs.inorgchem.1c01666

PAKHOMOVA, A.; FUCHS, B.; DUBROVINSKY, L.; DUBROVINSKAIA, N.; HUPPERTZ, H. (2021): Polymorphs of the gadolinite-type borates ZrB_2O_5 and HfB_2O_5 under extreme pressure. Chem. Eur. J. 27(19), 6007-6014, https://doi.org/10.1002/chem.202005244

PEIFFER, S.; KAPPLER, A.; HADERLEIN, S.; SCHMIDT, C.; BYRNE, J.; KLEINDIENST, S.; VOGT, C.; RICHNOW, H.; OBST, M.; ANGENENT, L.; BRYCE, C.; MCCAMMON, C.; PLANER-FRIEDRICH, B. (2021): A biogeochemical–hydrological framework for the role of redox-active compounds in aquatic systems. Nat. Geosci. 14, 264-272, https://doi.org/10.1038/s41561-021-00742-z

REBAZA, A.M.; POSNER, E.S.; THIELMANN, M.; RUBIE, D.C.; STEINLE-NEUMANN, G. (2021): Experimental determination of carbon diffusion in liquid iron at high pressure. Am. Mineral. 106(12), 1950-1956, https://doi.org/10.2138/am-2021-7644

ROBINSON, P.; MCENROE, S.A.; HARRISON, R.J.; FABIAN, K.; HEIDELBACH, F.; JACKSON, M. (2021): Lamellar magnetism and exchange bias in billion-year-old metamorphic titanohematite with nanoscale ilmenite exsolution lamellae – III. Atomic-magnetic basis for experimental results. Geophysical Journal International 226(2), 1348-1367, https://doi.org/10.1093/gji/ggab176

RUSTIONI, G.; AUDÉTAT, A.; KEPPLER; H. (2021): A systematic assessment of the diamond trap method for measuring fluid compositions in high-pressure experiments. Am. Mineral. 106, 28-37, https://doi.org/10.2138/am-2020-7453

RUSTIONI, G.; AUDÉTAT, A.; KEPPLER; H. (2021): The composition of subduction zone fluids and the origin of the trace element enrichment in arc magmas. Contrib Mineral Petrol 176, 51, https://doi.org/10.1007/s00410-021-01810-8

SATTA, N.; CRINITI, G.; KURNOSOV, A.; BOFFA BALLARAN, T.; ISHII, T.; MARQUARDT, H. (2021): High-pressure elasticity of δ-(Al, Fe) OOH single crystals and seismic detectability of hydrous MORB in the shallow lower mantle. Geophys. Res. Lett. 28(23), e2021GL094185, https://doi.org/10.1029/2021GL094185

SAWA, S.; MUTO, J.; MIYAJIMA, N.; SHIRAISHI, R.; KIDO, M.; NAGAHAMA, H. (2021): Strain localization bands in fine-grained aggregates of germanate olivine and pyroxene deformed by a Griggs type apparatus. Int. J. Rock Mech. Min. Sci. 144, 104812, https://doi.org/10.1016/j.ijrmms.2021.104812

SAWA, S.; MIYAJIMA, N.; MUTO, J.; NAGAHAMA, H. (2021): Strain-induced partial serpentinization of germanate olivine with a small amount of water. Am. Mineral. 106, 1789-1796, https://doi.org/10.2138/am-2021-7735

SERGHIOU, G.; ODLING, N.; REICHMANN, H.-J.; JI, G.; KOCH-MUELLER, M.; FROST, D.J.; WRIGHT, J.P.: BOEHLER, R.; MORGENROTH, W (2021): Hexagonal Si-Ge class of semiconducting alloys prepared by using pressure and temperature. Chem. Eur. J. 27(57), 14217-14224, https://doi.org/10.1002/chem.202102595

SIERSCH, N.C.; KURNOSOV, A.; CRINITI, G.; ISHII, T.; BOFFA BALLARAN, T.; FROST, D.J. (2021): The elastic properties and anisotropic behavior of $MgSiO_3$ akimotoite at transition zone pressures. Phys. Earth Planet. Inter. 320, 106786, https://doi.org/10.1016/j.pepi.2021.106786

STABILE, P.; SICOLA, S.; GIULI, G.; PARIS, E.; CARROLL, M.R.; DEUBENER, J.; DI GENOVA, D. (2021): The effect of iron and alkali on the nanocrystal-free viscosity of volcanic melts: A combined Raman spectroscopy and DSC study. Chem. Geol. 559, 119991, https://doi.org/10.1016/j.chemgeo.2020.119991

SU, X.; ZHAO, C.; XU, L.; LV, C.; SONG, X.; ISHII, T.; XIAO, Y.; CHO, P.; SUN, Q.; LIU, J. (2021): Spectroscopic evidence for the Fe^{3+} spin transition in iron bearing δ-AlOOH at high pressure. Am. Mineral., 106(11), 1709-1716, https://doi.org/10.2138/am-2021-7541

TANG, H.; YUAN, X.; CHENG, Y.; FEI, H.; LIU, F.; LIANG, T.; ZENG, Z.; ISHII, T.; WANG, M.; KATSURA, T.; SHENG, H.; GOU, H. (2021): Synthesis of paracrystalline diamond. Nature 599, 605-610, https://doi.org/10.1038/s41586-021-04122-w

TASNÁDI, F.; BOCK, F.; PONOMAREVA, A.; BYKOV, M.; KHANDARKHAEVA, S.; DUBROVINSKY, L.; ABRIKOSOV, I. (2021): Thermodynamic and electronic properties of ReN2 polymorphs at high pressure. Phys. Rev. B 104, 184103, https://doi.org/10.1103/PhysRevB.104.184103

TOMIOKA, N.; BINDI, L.; OKUCHI, T.; MIYAHARA, M.; IITAKA, T.; LI, Z.; KAWATSU, T.; XIE, X.; PUREVJAV, N.; TANI, R.; KODAMA, Y. (2021): Poirierite, a dense metastable polymorph of magnesium iron silicate in shocked meteorites. Commun Earth Environ 2, 16, https://doi.org/10.1038/s43247-020-00090-7

TRYBEL, F.; MEIER, T.; WANG; B.; STEINLE-NEUMANN, G. (2021): Absence of proton tunneling during the hydrogen-bond symmetrization in δ-AlOOH. Phys. Rev. B 104, 104311, https://doi.org/10.1103/PhysRevB.104.104311

WEIß, S.; RADHA, A.V.; ERTL, M.; MCCAMMON, C.; BREU, J. (2021): Sustainable oxygen evolution catalysis – Electrochemical generation of Mössbauerite via corrosion engineering of steel. Mater. Adv. 2, 5650-5656, https://doi.org/10.1039/D1MA00381J

WERE, P.; KEPPLER, H. (2021): Trace element fractionation between biotite, allanite, and granitic melt. Contrib Mineral Petrol 176, 74, https://doi.org/10.1007/s00410-021-01831-3

XIE, L.; CHANYSHEV, A.; ISHII, T.; BONDAR, D.; NISHIDA, K.; CHEN, Z.; BHAT, S.; FARLA, R.; HIGO, Y.; TANGE, Y.; SU, X.; YAN, B.; MA, S.; KATSURA, T. (2021): Simultaneous generation of ultrahigh pressure and temperature to 50 GPa and 3300 K in multi-anvil apparatus. Rev. Sci. Instrum. 92(10), 103902, https://doi.org/10.1063/5.0059279

XIE, L.; YONEDA, A.; KATSURA, T.; ANDRAULT, D.; TANGE, Y.; HIGO, Y. (2021): Direct viscosity measurement of peridotite melt to lower-mantle conditions: a further support for a fractional magma-ocean solidification at the top of the lower mantle. Geophys. Res. Lett. 48(19), e2021GL094507, https://doi.org/10.1029/2021GL094507

XIE, L. (2021): Machinable boron-doped diamond as a practical heating element in multi-anvil apparatuses. Rev. Sci. Instrum. 92, 023901, https://doi.org/10.1063/5.0036771

XU, F.; MORARD, G.; GUIGNOT, N.; RIVOLDINI, A.; MANTHILAKE, G.; CHANTEL, J.; XIE, L.; YONEDA, A.; KING, A.; BOULARD, E.; PANDOLFI, S.; RYERSON, F.J.; ANTONANGELI, D. (2021): Thermal expansion of liquid Fe-S alloy at high pressure. Earth Planet. Sci. Lett. 563, 116884, https://doi.org/10.1016/j.epsl.2021.116884

YAO, J.; FROST, D.J.; STEINLE-NEUMANN, G. (2021): Lower mantle melting: Experiments and thermodynamic modelling in the system MgO-SiO_2. JGR Solid Earth 126(12), e2021JB022568, https://doi.org/10.1029/2021JB022568

YOSHIDA, M.; MIYAHARA, M.; SUGA, H.; YAMAGUCHI, A.; TOMIOKA, N.; SAKAI, T.; OHFUJI, H.; MAEDA, F.; OHIRA, I.; OHTANI, E.; KAMADA, S.; OHIGASHI, T.; INAGAKI, Y.; KODAMA, Y.; HIRAO. N. (2021): Elucidation of impact event recorded in the lherzolitic shergottite NWA 7397. Meteorit Planet Sci 56(9), 1729-1743, https://doi.org/10.1111/maps.13735

YUAN, L.; STEINLE-NEUMANN, G. (2021): The helium elemental and isotopic compositions of the Earth's core based on ab initio simulations. JGR Solid Earth 126(10), e2021JB023106, https://doi.org/10.1029/2021JB023106

ZHANG, B.; LIN, Y.; MOSER, D.E.; HAO, J.; LIU, Y.; ZHANG, J.; BARKER, I.R.; LI, Q.; SHIEH, S.R.; BOUVIER, A. (2021): Radiogenic Pb mobilization induced by shock metamorphism of zircons in the Apollo 72255 Civet Cat norite clast. Geochim. Cosmochim. Acta 302, 175-192, https://doi.org/10.1016/j.gca.2021.03.012

ZHANG, B.; LIN, Y.; MOSER, D.E.; HAO, J.; LIU, Y.; ZHANG, J.; BARKER, I.R.; LI, Q.; SHIEH, S.R.; BOUVIER, A. (2021): Timing of the lunar Mg-suite magmatism constrained by SIMS U-Pb Dating of Apollo Norite 78238. Earth Planet. Sci. Lett. 569, 117046, https://doi.org/10.1016/j.epsl.2021.117046

ZHU, M.-H.; MORBIDELLI, A.; NEUMANN, W.; YIN, Q.-Z.; DAY, J.M.D.; RUBIE, D.C.; ARCHER, G.J.; ARTEMIEVA, N.; BECKER, H.; WÜNNEMANN K. (2021): Common feedstocks of late accretion for the terrestrial planets. Nat Astron 5, 1286-1296, https://doi.org/10.1038/s41550-021-01475-0

4.2 Publications (submitted, in press)

ABEYKOON, S.; AUDÉTAT, A.: The single-crystal diamond trap (SCDT): a new method to determine the composition of high-P-T fluids. Contrib. to Mineral. Petrol. (in press)

ARZILLI, F.; POLACCI, M.; LA SPINA, G.; LE GALL, N.; BURTON, M.R.; LLEWELLIN, E.W.; TORRES-OROZCO, R.; DI GENOVA, D.; HARTLEY, M.E.; BROOKER, R.A.; NEAVE, D.A.; MADER, H.M.; GIORDANO, D.; ATWOOD, R.; LEE, P.D.: Dendritic crystallization in hydrous basaltic magmas controls magma mobility within the Earth's crust. Nat Commun (submitted)

AUDÉTAT, A.: A plea for more skepticism towards fluid inclusions (II): homogenization via halite dissolution in brine inclusions from magmatic-hydrothermal systems is commonly the result of postentrapment modifications. Econ Geol (submitted)

BLANCHARD, I.; RUBIE, D.C.; JENNINGS, E.S.; FRANCHI, I.A.; ZHAO, X.; PETITGIRARD, S.; MIYAJIMA, N.; JACOBSON, S.A.; MORBIDELLI, A.: The metal–silicate partitioning of carbon during Earth's accretion and its distribution in the early solar system. Earth Planet. Sci. Lett. (in press), https://doi.org/10.1016/j.epsl.2022.117374

BLUNDY, J.; MELEKHOVA, E.; ZIBERNA, L.; HUMPHREYS, M.; CERANTOLA, V.; BROOKER, R.; MCCAMMON, C.; PICHAVANT, M.; ULMER, P.: Effect of redox on Fe-Mg-Mn exchange between olivine and melt and an oxybarometer for basalts. Contrib. to Mineral. Petrol. (submitted)

BONDAR, D.; ZANDONÀ, A.; WITHERS, A.C.; FEI, H.; DI GENOVA, D.; MIYAJIMA, N.; KATSURA, T.: Rapid-quenching of high-pressure depolymerized hydrous silicate (peridotitic) glasses. J Non Cryst Solids (accepted), https://doi.org/10.1016/j.jnoncrysol.2021.121347

BRITVIN, S.N.; VLASENKO, N.; ASLANDUKOV, A.; ASLANDUKOVA, A.; DUBROVINSKY, L.; GORELOVA, L.; KRZHIZHANOVSKAYA, M.; VERESHCHAGIN, O.; BOCHAROV, V.; SHELUKHINA, Y.; LOZHKIN, M.; ZAITSEV, A.; NESTOLA, F.: Natural cubic perovskite, Ca (Ti, Si, Cr) O3-δ, a versatile potential host for rock-forming and less-common elements up to Earth's mantle pressure. Am. Mineral. (in press)

CHANYSHEV, A.; ISHII, T.; BONDAR, D.; BHAT, S.; KIM, E.J.; FARLA, R.; NISHIDA, K.; LIU, Z.; WANG, L.; NAKAJIMA, A.; YAN, B.; TANG, H.; CHEN, Z.; HIGO, Y.; TANGE, Y.; KATSURA, T.: Depressed 660-km discontinuity caused by akimotoite-bridgmanite transition. Nature (in press)

CRINITI, G.; ISHII, T.; KURNOSOV, A.; GLAZYRIN, K.; BOFFA BALLARAN, T.: High-pressure phase transition and equation of state of hydrous Al-bearing silica. Geophys. Res. Lett. (submitted)

DOMINIJANNI, S.; MCCAMMON, C.A.; OHTANI, E.; IKUTA, D.; SAKAMAKI, T.; ISHII, T.; CRINITI, G.; DUBROVINSKY, L.; KHANDARKHAEVA, S.; FEDOTENKO, T.; GLAZYRIN, K.; UCHIYAMA, H.; FUKUI, H.; BARON, A.: Sound velocity measurements of B2-Fe-Ni-Si alloy under high pressure by inelastic X-ray scattering: Implications for the composition of Earth's core. Geophys. Res. Lett. (submitted)

EBERHARD, L.; THIELMANN, M.; EICHHEIMER, P.; SUZUKI, A.; FUJITA, W.; UESUGI, K.; NAKAMURA, M.; GOLABEK, G.J.; FROST, D.J.: A new method for determining fluid flux at high pressures applied to the dehydration of subduction zone serpentinites. Geochemistry, Geophysics, Geosystems (submitted)

FEI, H.; KATSURA, T.: The effect of oxygen fugacity on ionic conductivity in olivine. Geosci. Front. (in press), https://doi.org/10.1016/j.gsf.2021.101270

FEI, H.; LIU, Z.; HUANG, R.; KAMADA, S.; HIRAO, N.; KAWAGUCHI, S.; MCCAMMON, C.; KATSURA, T.: Pressure destabilizes oxygen vacancies in bridgmanite. JGR Solid Earth (accepted)

GÜLCHER, A.J.P.; GOLABEK, G.J.; THIELMANN, M.; BALLMER, M.D.; TACKLEY, P.J.: Narrow, fast, and "cold" mantle plumes caused by strain-weakening rheology in Earth's lower mantle. Geochemistry, Geophysics, Geosystems (submitted)

HUANG, D.; MURAKAMI, M.; BRODHOLT, J.; MCCAMMON, C.; PETITGIRARD, S.: Structural evolution in a pyrolitic magma ocean under mantle conditions. Earth Planet. Sci. Lett. (submitted)

IKUTA, D.; OHTANI, E.; FUKUI, H.; ISHIKAWA, D.; BARON, A.Q.R.: Sound velocity of hcp-iron to densities higher than the Earth's core. Phys. Rev. Lett. (submitted)

ISHII, T.; CRINITI, G.; OHTANI, E.; PUREVJAV, N.; FEI, H.; KATSURA, T.; MAO, H.K.: Superhydrous aluminous post-stishovite as a major lower-mantle H_2O carrier. Nat. Geosci. (submitted)

ISHII, T.; OHTANI, E.; SHATSKIY, A.: Aluminum and hydrogen partitioning between bridgmanite and high-pressure hydrous phases: Implications for water storage in the lower mantle. Earth Planet. Sci. Lett. (submitted)

ISHII, T.; MCCAMMON, C.; KATSURA, T.: Iron and aluminum substitution mechanism in bridgmanite in the system $MgSiO_3$-$FeAlO_3$-MgO. Contrib. to Mineral. Petrol. (submitted)

ISHII, T.; MIYAJIMA, N.; CRINITI, G.; HU, Q.; GLAZYRIN, K.; KATSURA, T.: High pressure-temperature phase relations of basaltic crust up to mid-mantle conditions. Earth Planet. Sci. Lett. (accepted)

KATSURA, T.: Adiabatic temperature profile in the mantle, revised. JGR Solid Earth (submitted)

KHANDARKHAEVA, S.; FEDOTENKO, T.; CHARITON, S.; BYKOVA, E.; OVSYANNIKOV, S.V.; GLAZYRIN, K.; LIERMANN, H.-P.; PRAKAPENKA, V.; DUBROVINSKAIA, N.; DUBROVINSKY, L.: Unordinary structural diversity of magnetite and products of its decomposition at extreme conditions. Inorg. Chem. (submitted)

KISEEVA, E.S.; KOROLEV, N.; KOEMETS, I.; ZEDGENIZOV, D.A.; UNITT, R.; MCCAMMON, C.; ASLANDUKOVA, A.; KHANDARKHAEVA, S.; FEDOTENKO, T.; GLAZYRIN, K.; BESSAS, D.; APRILIS, G.; CHUMAKOV, A.I.; KAGI, H.; DUBROVINSKY, L.: Subduction-related oxidation of the lower mantle: evidence from diamond inclusions. Nat Commun (submitted)

LIU, H.; ZHU, Q.; XU, X.; FEI, H.; YANG, X.: High electrical conductivity of olivine at oxidizing conditions of the shallow mantle and geophysical implications. JGR Solid Earth (accepted)

MAH, J.; BRASSER, R.; BOUVIER, A.; MOJZSIS, S.J.: Effects of pebble accretion on the growth of planetesimals in the inner Solar System. Monthly Notices of the Royal Astronomical Society (submitted)

MCGOWAN, N.; GRIFFIN, W.L.; PEARSON, N.J.; O'REILLY, S.Y.; CLARK, S.M.; ROQUE-ROSELL, J.; MARCUS, M.A.; MCCAMMON, C.A.: The oxidation state of Fe in chromite by μ-XRF and K-edge μ-XANES: Evidence for deep Earth processes? Chem. Geol. (submitted)

MORBIDELLI, A.; BAILLIÉ, K.; BATYGIN, K.; CHARNOZ, S.; GUILLOT, T.; RUBIE, D.C.; KLEINE, T.: Contemporary formation of early solar system planetesimals at two distinct radial locations. Nat. Astron. (in press)

MURAKAMI, M.; GONCHAROV, A.F.; MIYAJIMA, N.; YAMAZAKI, D.; HOLTGREWE, N. (2021): Radiative thermal conductivity of single-crystal bridgmanite at the core-mantle boundary with implications for thermal evolution of the Earth. Earth Planet. Sci. Lett. (accepted)

NATHAN, G.; RUBIE, D.C.; JACOBSON, S.A.: Constraining the origin of Mars with simulations of multi-stage core formation. Icarus (submitted)

OHTANI, E. (2021): The Earth's Interior: From the perspective of Mineral Science. Journal of Geography (Chigaku Zasshi) (in press), in Japanese

PATRICK, M.; INDARES, A.; MCCAMMON, C.: The influence of ferric iron on phase stability in midpressure anatectic aluminous gneisses. Can. Mineral. (submitted)

SATTA, N.; CRINITI, G.; KURNOSOV, A.; BOFFA BALLARAN, T.; ISHII, T.; MARQUARDT, H.: High-pressure elasticity of δ-(Al,Fe)OOH single crystals and seismic detectability of hydrous MORB in the shallow lower mantle. Geophys. Res. Lett. (in press)

SATTA, N.; MIYAHARA, M.; OZAWA, S.; MARQUARDT, H.; NISHIJIMA, M.; ARAI, T.; OHTANI, E.: Apollo 15 regolith breccia provides first natural evidence for olivine incongruent melting. Am. Mineral. (in press)

SCARANI, A.; VONA, A.; DI GENOVA, D.; AL-MUKADAM, R.; ROMANO, C.; DEUBENER, J.: Determination of cooling rates of glasses over four orders of magnitude. Contrib. to Mineral. Petrol. (submitted)

SIERSCH, N.C.; CRINITI, G.; KURNOSOV, A.; BOFFA BALLARAN, T.; LIU, Z.; ISHII, T.; FROST, D.J.; YU, T.; WANG, Y.: The influence of Al_2O_3 on the structural properties of $MgSiO_3$ akimotoite. Am. Mineral. (submitted)

SIERSCH, N.C.; KURNOSOV, A.; CRINITI, G.; ISHII, T.; BOFFA BALLARAN, T.; FROST, D.J.: The elastic properties and anisotropic behavior of $MgSiO_3$ akimotoite at transition zone pressures. Phys. Earth Planet. Inter. (in press)

STROHM, C.; APRILIS, G.; KUPENKO, I.; VASIUKOV, D.M.; CERANTOLA, V.; CHUMAKOV, A.; RÜFFER, R.; MCCAMMON, C.; DUBROVINSKY, L.: Fully time resolved synchrotron Mössbauer spectroscopy for pulsed laser heating experiments in diamond anvil cells. J. Synchrotron Radiat. (submitted)

VLASOV, K; KEPPLER, H.: Electrical conductivity of KCl-H_2O fluids in the crust and lithospheric mantle. JGR Solid Earth (submitted)

WANG, L.; CHANYSHEV, A.; MIYAJIMA, N.; KAWAZOE, T.; BLAHA, S.; CHANG, J.; KATSURA, T.: Small effect of water incorporation on dislocation mobility in olivine: Negligible creep enhancement and water-induced fabric transition in the asthenosphere. Earth Planet. Sci. Lett. (accepted)

WOODLAND, A.; UENVER-THIELE, L.; BOFFA BALLARAN, T.; MIYAJIMA, N.; ROSBACH, K.; ISHII, T.: Stability of Fe_5O_6 and its relation to other Fe-Mg-oxides at high pressures and temperatures. Am. Mineral. (accepted)

ZHANG, D.; AUDÉTAT, A.: A plea for more skepticism towards fluid inclusions (I): postentrapment changes in fluid density and fluid salinity are very common. Econ Geol (submitted)

4.3 Presentations at scientific institutions and at congresses

ABEYKOON, S.; HOWARD, C.M.; DOMINIJANNI, S.; EBERHARD, L.; FROST, D.J.; BOFFA BALLARAN, T.; KURNOSOV, A.; TERASAKI, H.; SAKAMAKI, T.; SUZUKI, A.; OHTANI, E.; SANO-FURUKAWA, A.; ABE, J.: 04.-09.07.2021, Goldschmidt Virtual 2021: "Deuterium content and site occupancy in iron sulphide at high pressure and high temperature: Implications for the oxidation of early Earth's mantle"

ALBERS, E.; BACH, W.; PÉREZ-GUSSINYÉ, M.; MCCAMMON, C.; FREDERICHS, T.: 19.-30.04.2021, EGU General Assembly 2021, online: "How much energy for life (H_2) is generated by serpentinization at passive continental margins?", EGU21-1469

ALBERS, E.; BACH, W.; PÉREZ-GUSSINYÉ, M.; MCCAMMON, C.; FREDERICHS, T.: 19.-24.09.2021, GeoKarlsruhe 2021, Karlsruhe, Germany: "Unexpected high amounts of H_2 produced during serpentinization at magma-poor rifted margins"

APRILIS, G.; PAKHOMOVA, A.; CHARITON, S.; KHANDARKHAEVA, S.; MELAI, C.; BYKOVA, E.; BYKOV, M.; FEDOTENKO, T.; KOEMETS, E.; MCCAMMON, C.; CHUMAKOV, A.I.; HANFLAND, M.; DUBROVINSKAIA, N.; DUBROVINSKY, L.: 01.-03.03.2021, EMPG-XVII, virtual meeting[*A]: "The effect of pulsed laser heating on the stability of ferropericlase at high pressures"

AUDÉTAT, A: 23.-26.11.2021, SPP 2238 – Dynamics of Ore Metals Enrichment – DOME, 2nd Young researcher networking event, Potsdam, Germany: "Synthetic fluid inclusions"

BLANCHARD, I.; JENNINGS, E.S.; FRANCHI, I.A.; ZHAO, X.; PETITGIRARD, S.; MIYAJIMA, N.; JACOBSON, S.A.; RUBIE, D.C.: 01.-03.03.2021, EMPG-XVII, virtual meeting[*A]: "Fate of carbon during the formation of Earth's core"

BOFFA BALLARAN, T.: 16.12.2021, Jilin University, State Key Laboratory of Superhard Materials, Changchun, P.R. China: "Single-crystals X-ray diffraction in Geoscience"

BOFFA BALLARAN, T.: 17.12.2021, Jilin University, State Key Laboratory of Superhard Materials, Changchun, P.R. China: "Mineral elasticity probed by means of Brillouin spectroscopy"

BONDAR, D.; FEI, H.; WITHERS, A.C.; KATSURA, T.: 01.-03.03.2021, EMPG-XVII, virtual meeting[*A]: "Rapid-quench multi-anvil technique"

BOUVIER, A.: 13.04.2021, Online Spring Seminar Series, Trinity College, Department of Geology, Dublin, Ireland: "Making Earth: a recipe from meteorites?"

BOUVIER, A.: 21.07.2021, GP-EES Online Seminar Series, Tohoku University, Sendai, Japan, "Planetary materials and the chronology of solar system formation"

BOUVIER, A.; MA, N.; NEUMANN, W.; NÉRI, A.; SCHWARZ, W.H.; LUDWIG, T.; TRIELOFF, M.; KLAHR, H.: 13.-24.09.2021, Europlanet Science Congress 2021, virtual meeting (*invited*): "Early and sequential accretion of planetesimals in an outer region of the protoplanetary disc", EPSC Abstracts Vol. 15, EPSC2021-846

BOUVIER, A.: 25.10.2021, Online Seminar Series, Salem State University, Department of Geological Sciences, Salem, USA: "What meteorites can tell us about Earth and Solar System formation"

BUCHEN, J.; STURHAHN, W.; ISHII, T.; JACKSON, J.M.: 01.-03.03.2021, EMPG-XVII, virtual meeting[*A]: "Vibrational anisotropy of δ-(Al,Fe)OOH: a nuclear resonant inelastic X-ray scattering study on single crystals"

CHANYSHEV, A.; BONDAR, D.; FEI, H.; PUREVJAV, N.; ISHII, T.; NISHIDA, K.; BHAT, S.; FARLA, R.; KATSURA, T.: 26.-30.07.2021, Conference on Science at Extreme Conditions (CSEC-2021), Edinburgh, U.K. (online): "Determination of the olivine-ahrensite binary loop in the $(Mg,Fe)_2SiO_4$ system at 1740 K using multi-anvil techniques"

CHANYSHEV, A.; BONDAR, D.; FEI, H.; PUREVJAV, N.; ISHII, T.; NISHIDA, K.; BHAT, S.; FARLA, R.; KATSURA, T.: 22.-24.09.2021, Multianvil Workshop – UltraLVP, Bayerisches Geoinstitut, Bayreuth, Germany (virtual): "Determination of the olivine-ahrensite phase relations in the $(Mg,Fe)_2SiO_4$ system at 1740 K using multi-anvil techniques"

CIALDELLA, L.; WIEDENBECK, M.; KEPPLER, H.: 01.-03.03.2021, EMPG-XVII, virtual meeting[*A]: "The solubility of N_2 in silicate melts"

CRINITI, G.; ISHII, T.; KURNOSOV, A.; GLAZYRIN, K.; BOFFA BALLARAN, T.: 04.-09.07.2021, Goldschmidt Virtual 2021: "High-pressure phase transition and equation of state of hydrous aluminous silica"

CRINITI, G.; KURNOSOV, A.; GLAZYRIN, K.; HUSBAND, R.J.; LIU, Z.; BOFFA BALLARAN, T.; FROST, D.J.: 13.-17.12.2021, AGU Fall Meeting 2021, New Orleans, USA (virtual): "Effect of $AlAlO_3$ and $MgAlO_{2.5}$ incorporation on the equation of state of $MgSiO_3$ bridgmanite"

CZEKAY, L.; MIYAJIMA, N.; MCCAMMON, C.; FROST, D.: 29.08.-02.09.2021, EMC2020, 3rd European Mineralogical Conference, Cracow, Poland (virtual): "Al, Si interdiffusion under lower mantle conditions: analytical TEM study of Al-bearing bridgmanite"

CZEKAY, L.; MIYAJIMA, N.; MCCAMMON, C.; FROST, D.: 22.-24.09.2021, Multianvil Workshop – UltraLVP, Bayerisches Geoinstitut, Bayreuth, Germany (virtual): "Aluminous bridgmanite for Al, Si interdiffusion experiments by using a multianvil press"

DI GENOVA, D.: 11.05.2021, University of Pavia, Italy (online): "From macro, to micro, to nano: Known-knowns and -unknowns in volcanology"

DI GENOVA, D.: 04.-09.07.2021, Goldschmidt Virtual 2021: "Research and funding opportunities in geochemistry in Germany"

DOLINSCHI, J.; FROST, D.J.: 19.-30.04.2021, EGU General Assembly 2021, online: "Development of in situ measurement of solid-state deformation in a large anvil press utilizing a piezoelectric crystal", EGU21-6928

DOMINIJANNI, S.; MCCAMMON, C.A.; OHTANI, E.; IKUTA, D.; SAKAMAKI, T.; ISHII, T.; CRINITI, G.; DUBROVINSKY, L.S.; KHANDARKHAEVA, S.; FEDOTENKO, T.; GLAZYRIN, K.; UCHIYAMA, H.; FUKUI, H.; BARON, A.Q.R.: 01.-03.03.2021, EMPG-XVII, virtual meeting[*A]: "Sound velocity measurements of B2-Fe-Ni-Si alloy under high pressure by inelastic X-ray scattering: Implications for the composition of Earth's core"

DOMINIJANNI, S.; MCCAMMON, C.A.; OHTANI, E.; IKUTA, D.; SAKAMAKI, T.; ISHII, T.; CRINITI, G.; DUBROVINSKY, L.S.; KHANDARKHAEVA, S.; FEDOTENKO, T.; GLAZYRIN, K.; UCHIYAMA, H.; FUKUI, H.; BARON, A.Q.R.: 07.-11.06.2021, Earth, Sea and Sky VI: International Joint Graduate Program Workshop in Earth and Environmental Sciences, Sendai, Japan: "Sound velocity measurements of B2-Fe-Ni-Si alloy under high pressure by inelastic X-ray scattering: Implications for the composition of Earth's core"

DOMINIJANNI, S.; STAGNO V.; MCCAMMON, C.; MIYAJIMA, N.; IRIFUNE, T.; FROST, D.: 29.08.-02.09.2021, EMC2020, 3rd European Mineralogical Conference, Cracow, Poland (virtual): "Iron oxidation state of ferropericlase coexisting with carbonate and diamond: Implications for the origin of superdeep diamonds"

DUBROVINSKY, L.S.: 29.03.2021, HPCAT-GSECARS seminars, APS, Lemont, USA (*invited*): "Role of high-pressure Fe-O-H chemistry in oxygen recycling in early Earth history"

DUBROVINSKY, L.S.: 14.-22.08.2021, 25th Congress of the International Union of Crystallography, Prague, Czech Republic (*plenary talk*): "High Pressure Crystallography Unlimited"

DUBROVINSKY, L.S.: 09.11.2021, State Key Laboratory of Crystal Materials, Jinan, P.R. China (*invited*): "Progress in structural studies at high pressures"

DUBROVINSKY, L.S.: 07.12.2021, KIT webinar on Advancing Frontiers of Geosciences, Germany (*invited*): "High-pressure Fe-O-H chemistry and Earth oxygen cycle"

FARLA, R.; MA, S.; CHANYSHEV, A.; SONNTAG, S.; ISHII, T.; KATSURA, T.: 01.-03.03.2021, EMPG-XVII, virtual meeting[*A]: "High-pressure geoscience research at the Large Volume Press beamline P61B, PETRA III"

FEI, H.; LIU, Z.; HUANG, R.; KAMADA, S.; HIRAO, N.; KAWAGUCHI, S.; MCCAMMON, C.; KATSURA, T.: 22.-24.09.2021, Multianvil Workshop – UltraLVP, Bayerisches Geoinstitut, Bayreuth, Germany (virtual): "Fe^{3+} substitution mechanism in bridgmanite"

FEI, H.: 22.-24.09.2021, Multianvil Workshop – UltraLVP, Bayerisches Geoinstitut, Bayreuth, Germany (virtual): "Water content in hydrous silicate melt at the topmost lower mantle conditions"

FEI, H.: 25.11.2021, Jilin University, State Key Laboratory of Superhard Materials, Changchun, P.R. China (online): "Water and electrical conductivity in the Earth's mantle"

FROSSARD, P.; SPENCER, M.; GUO, Z.; BOYET, M.; BOUVIER, A.: 04.-09.07.2021, Goldschmidt Virtual 2021: "Evidence from achondrites for a temporal change in Nd nucleosynthetic anomalies within the first 1.5 million years of the inner solar system formation", Abstract 6888

FROST, D.; CRINITI, G.; HUANG, R.; KURNOSOV, A.; BOFFA BALLARAN, T.; MCCAMMON, C.: 12.03.2021, University College London, Department of Earth Sciences, London, U.K. (virtual): "The composition of the Earth's lower mantle- the top part at least"

FROST, D.; HUANG, R.; MCCAMMON, C.; BOFFA BALLARAN, T.: 04.-09.07.2021, Goldschmidt Virtual 2021: "Diamond formation through mineral hydration at the base of the transition zone"

FUKUSHIMA, R.; TSUJIMORI, T.; MIYAJIMA, N.: 07.-11.06.2021, Earth, Sea and Sky VI: International Joint Graduate Program Workshop in Earth and Environmental Sciences, Sendai, Japan: "Various antiphase domains in garnet-hosted omphacite in low temperature eclogite: A FIB–TEM study on heterogeneous ordering processes"

GOLABEK, G.J.; JUTZI, M.: 30.08.2021, German-Swiss Geodynamics Workshop, Bad Belzig, Germany: "Modification of cometesimal interiors by early thermal evolution and collisions"

GREER, J.; ZHANG, B.; ISHEIM, D.; SEIDMAN, D.N.; BOUVIER, A.; HECK, P.R.: 15.-21.08.2021, 84th Annual Meeting of the Meteoritical Society, Chicago, USA: "Atom probe tomography of 4.45 Ga Lunar zircon from the Apollo 17 Civet Cat Norite Clast", Abstract 6134

HIN, R.C.: 25.11.2021, ETH Zürich, Institute for Geochemistry and Petrology, Zürich, Switzerland: "Does accretional vapour loss play a dominant role in shaping planetary compositions?"

IKUTA, D.; OHTANI, E.; FUKUI, H.; ISHIKAWA, D.; BARON, A.Q.R.: 30.05.-06.06.2021, Japan Geoscience Union Meeting 2021, online: "Sound velocity of hcp-iron at extreme pressure by inelastic x-ray scattering measurement"

IKUTA, D.; OHTANI, E.; FUKUI, H.; SAKAMAKI, T.; ISHIKAWA, D.; BARON, A.Q.R.: 06.-09.09.2021, Workshop on meV-Resolved Inelastic X-ray Scattering (online): "IXS measurements in extreme conditions: A multi-megabar primary pressure scale and the structure of the Earth's core"

IKUTA, D.; OHTANI, E.; FUKUI, H.; SAKAMAKI, T.; ISHIKAWA, D.; BARON, A.Q.R.: 18.-20.10.2021, The 62nd High Pressure Conference of Japan, Himeji, Japan: "Primary pressure scale of rhenium to multi-megabar pressures by inelastic x-ray scattering"

IKUTA, D.; OHTANI, E.; FUKUI, H.; ISHIKAWA, D.; BARON, A.Q.R.: 18.-20.10.2021, The 62nd High Pressure Conference of Japan, Himeji, Japan: "Determination for compressional wave velocity of hcp-iron to multi-megabar pressures by inelastic X-ray scattering"

ISHII, T.; OHTANI, E.: 30.05.-06.06.2021, Japan Geoscience Union Meeting 2021, online: "Water content in olivine and its polymorphs coexisting with hydrous phases under water undersaturated conditions", session number: S-IT20

ISKRINA, A.; BOBROV, A.; SPIVAK, A.; EREMIN, N.; MARCHENKO, E.; DUBROVINSKY, L.: 01.-03.03.2021, EMPG-XVII, virtual meeting*A: "Synthesis, structural features and isomorphism of oxide phases in the Ca-Al-O system at P-T parameters of the transition zone and lower mantle of the Earth"

KATSURA, T.: 19.01.-01.02.2021, Satellite Workshop: 'In situ high P studies using the Large Volume Press at P61B', European XFEL Users' Meeting 2021 – DESY Photon Science Users' Meeting 2021 (invited): "Recent results and future projects for high-pressure-temperature in situ X-ray diffraction experiments at beam line P61B"

KATSURA, T.: 16.-17.09.2021, ErUM-Pro Match-Making workshop (FLASH & PETRA III), virtual: "Further development of multianvil experiments in P61B, DESY"

KATSURA, T.; WANG, L.; CHANYSHEV, A.; BLAHA, S.; MIYAJIMA, N.; KAWAZOE, T.: 22.-24.09.2021, Multianvil Workshop – UltraLVP, Bayerisches Geoinstitut, Bayreuth, Germany (virtual): "Recent results and future projects for high-pressure-temperature in situ X-ray diffraction experiments at beam line P61B, Determination of the H_2O-content dependence on the dislocation mobility in olivine by means of the dislocation recovery technique"

KATSURA, T.; CHANYSHEV, A.; ISHII, T.; BONDAR, D.; BHAT, S.; KIM, E.J.; FARLA, R.; NISHIDA, K.; LIU, Z.; WANG, L.; HIGO, Y.; TANGE, Y.: 21.-25.11.2021, 10th Asian Conference on High Pressure Research (virtual), Korea (*invited*): "Accurate determination of the akimotoite-bridgmanite transition and dissociation of ringwoodite to bridgmanite plus periclase and a new interpretation for the depression of the 660-km discontinuity under cold subduction zones"

KATSURA, T.: 13.-17.12.2021, AGU Fall Meeting 2021, New Orleans, USA (virtual): "Adiabatic temperature profile in the mantle, revisited"

KEPPLER, H.: 22.-23.03.2021, Dynamics of Ore Metal Enrichment, SPP 2238 General Assembly (online): "Cassiterite solubility, tin partitioning, and the origin of porphyry tin deposits"

KIM, E.J.; FEI, H.; NISHIDA, K.; KATSURA, T.: 22.-24.09.2021, Multianvil Workshop – UltraLVP, Bayerisches Geoinstitut, Bayreuth, Germany (virtual): "Phase relation of bridgmanite, ferropericlase, and CF-phase $MgAl_2O_4$ upon compression up to 40 Gpa"

KUKIHARA, K.; MIYAHARA, M.; YAMAGUCHI, A.; TAKAHASI, Y.; TAKEICHI, Y.; TOMIOKA, N.; OHTANI, E.: 16.-18.09.2021, 2021 Annual meeting of Japan Association of Mineralogical Society (JAMS), Hiroshima University, Japan (online): "Multi-probe microscopy analysis of NWA 10153 and NWA 6148"

LA SPINA, G.; ARZILLI, F.; LLEWELLIN, E.W.; BURTON, M.; CLARKE, A.B.; DE' MICHIELI VITTURI, M.; POLACCI, M.; HARTLEY, M.; DI GENOVA, D.; MADER, H.M.: 19.-30.04.2021, EGU General Assembly 2021, online: "Role of rheology, ascent rate and outgassing on fragmentation: implications for basaltic lava fountains", EGU21-10661

LEDOUX, E.; CHANTEL, J.; HILAIRET, N.; SVITLYK, V.; BYKOV, M.; BYKOVA, E.; APRILIS, G.; FADEL, A.; MERKEL, S.: 01.-03.03.2021, EMPG-XVII, virtual meeting*A: "In-situ studies of olivine-wadsleyite transformation and related microstructures at 18-22 GPa and 1400-1700 K"

LIBON, L.; SPIEKERMANN, G.; SIEBER, M.J.; KAA, J.; DOMINIJANNI, S.; BIEDERMANN, N.; APPEL, K.; MORGENROTH, W.; ALBERS, C.; MCCAMMON, C.; RODDATIS, V.; HENNET, L.; WILKE, M.: 01.-03.03.2021, EMPG-XVII, virtual meeting[*A]: "Experimental investigation of the phase stability in the bridgmanite-magnesite system"

LIBON, L.; SPIEKERMANN, G.; SIEBER, M.J.; KAA, J.; DOMINIJANNI, S.; ALBERS, C.; MORGENROTH, W.; BIEDERMANN, N.; APPEL, K.; MCCAMMON, C.; RODDATIS, V.; HUSBAND, R.; GLAZYRIN, K.; HENNET, L.; WILKE, M.: 04.-09.07.2021, Goldschmidt Virtual 2021: "Carbon in the deep Earth: The fate of magnesite in the lower mantle"

LIBON, L.; SPIEKERMANN, G.; SIEBER, M.J.; KAA, J.; DOMINIJANNI, S.; ALBERS, C.; MORGENROTH, W.; BIEDERMANN, N.; APPEL, K.; MCCAMMON, C.; RODDATIS, V.; HUSBAND, R.; GLAZYRIN, K.; HENNET, L.; WILKE, M.: 26.-30.07.2021, Conference on Science at Extreme Conditions (CSEC-2021), Edinburgh, U.K. (online): "The fate of magnesite in the Earth's lower mantle"

LIU, Z.; CHEN, L.; FEI, H.; MCCAMMON, C.; WANG, L.; LIU, B.; KATSURA, T.: 22.-24.09.2021, Multianvil Workshop – UltraLVP, Bayerisches Geoinstitut, Bayreuth, Germany (virtual): "Water solubility in nominally anhydrous minerals at the top of the lower mantle"

MA, N.; NEUMANN, W.; NÉRI, A.; SCHWARZ, W.H.; LUDWIG, T.; TRIELOFF, M.; KLAHR, H.; BOUVIER, A.: 04.-09.07.2021, Goldschmidt Virtual 2021: "Rapid and repeated accretion of planetesimals in an outer region of the protoplanetary disc", Abstract 3852

MAN, L.; FROST, D.J.: 04.-09.07.2021, Goldschmidt Virtual 2021: "The incorporation of Mg into core-forming melts during the accretion of terrestrial planets”

MARQUARDT, H.; SAN JOSÉ MÉNDEZ, A.; HUSBAND, R.; LIERMANN, H.-P.: 01.-03.03.2021, EMPG-XVII, virtual meeting[*A]: "Elastic softening of $(Mg_{0.8}Fe_{0.2})O$ ferropericlase across the iron spin crossover measured by time-resolved x-ray diffraction in a dynamic diamond-anvil cell"

MARZOTTO, E.; HSIEH, W.-P.; ISHII, T.; CHAO, K.-H.; GOLABEK, G.J.; THIELMANN, M.; TSAO, Y.-C.; LIN, J.-F.; OHTANI, E.: 30.05.-06.06.2021, Japan Geoscience Union Meeting 2021, online (*invited*): "Effect of water on lattice thermal conductivity of ringwoodite and its implications for the thermal evolution of descending slabs"

MCCAMMON, C.; WEI, Q.; GILDER, S.: 01.-03.03.2021, EMPG-XVII, virtual meeting[*A]: "Magnetic transitions in iron-nickel alloy at high pressure"

MCCAMMON, C.: 18.03.2021, Initiative for Science in Europe webinar, online: "Research grant evaluation"

MCCAMMON, C.; SZLACHTA, V.; BYRNE, J.M.: 07.-11.06.2021, Earth, Sea and Sky VI: International Joint Graduate Program Workshop in Earth and Environmental Sciences, Sendai, Japan: "Banded iron formations as a window to ancient oceans"

MCCAMMON, C.; HOCKMANN, K.; WEGNER, L.; PEIFFER, S.; PLANER-FRIEDRICH, B.; BURTON, E.: 13.-17.12.2021, AGU Fall Meeting 2021, New Orleans, USA (virtual): "Bringing bad things together with other things to make new forms that are safer for us and our world"

MELAI, C.; FROST, D.; BOFFA BALLARAN, T.; MCCAMMON, C.: 04.-09.07.2021, Goldschmidt Virtual 2021: "The oxygen fugacity of sublithospheric diamond formation and the conditions encountered during their ascent to the surface"

MERGNER, V.; KUPENKO, I.; SPIEKERMANN, G.; PETITGIRARD, S.; LIBON, L.; CHARITON, S.; SERGEEV, I.; STEINBRÜGGE, R.; KRUG, M.; SANCHEZ-VALLE, C.: 01.-03.03.2021, EMPG-XVII, virtual meeting[*A]: "Sound velocities of FeSi at high P-T conditions and implications for the structure of the core-mantle-boundary"

MIYAJIMA, N.: 01.-03.03.2021, EMPG-XVII, virtual meeting[*A]: "Al, Si interdiffusion in iron-free majoritic garnet: TEM of a polycrystalline diffusion couple"

NÉRI, A.; FROST, D.J.: 01.-03.03.2021, EMPG-XVII, virtual meeting[*A]: "Seismic signature of isolated iron-sulfur melt pockets: experimental acoustic wave velocity measurements"

NEUMANN, W.; MA, N.; NÉRI, A.; SCHWARZ, W.H.; LUDWIG, T.; TRIELOFF, M.; KLAHR, H.; BOUVIER, A.: 15.-21.08.2021, 84th Annual Meeting of the Meteoritical Society, Chicago, USA: "Thermal history and structure of the tafassite parent body", Abstract 6153

OHTANI, E.; IKUTA, D.; DOMINIJANNI, S.; MCCAMMON, C.; HIRAO, N.; FUKUI, H.; UCHIYAMA, H.; BARON, A.Q.: 30.05.-06.06.2021, Japan Geoscience Union Meeting 2021, online: "Existence of the two-phase mixture of HCP and B2 phases in the inner core"

OHTANI, E.; ISHII, T.: 30.05.-06.06.2021, Japan Geoscience Union Meeting 2021, online: "Role of water in subducting slabs: dry phase transformation kinetics in wet slabs"

OHTANI, E.: 29.08.-02.09.2021, EMC2020, 3rd European Mineralogical Conference, Cracow, Poland (virtual): Plenary Lecture: "High pressure mineral physics of the deep mantle and core" (Award lecture of 2019 IMA medal)

OHTANI, E.; IKUTA, D.; FUKUI, H.; SAKAMAKI, T.; ISHIKAWA, D.; BARON, A.Q.: 16.-18.09.2021, 2021 Annual meeting of Japan Association of Mineralogical Society (JAMS), Hiroshima University, Japan (online): "Density deficit of the Earth's inner core revealed by a multi-megabar rhenium pressure scale"

OHTANI, E.; ISHII, T.; SHATSKIY, A.; IKUTA, D.: 18.-20.10.2021, The 62nd High Pressure Conference of Japan, Himeji, Japan: "Partitioning of water between high pressure hydrous minerals and nominally anhydrous minerals and its roles in the Earth's interior"

OVSYANNIKOV, S.V.; BYKOV, M.; MEDVEDEV, S.A.; NAUMOV, P.G.; JESCHE, A.; TSIRLIN, A.A.; BYKOVA, E.; CHUVASHOVA, I.; KARKIN, A.E.; DYADKIN, V.; CHERNYSHOV, D.; DUBROVINSKY, L.S.: 21.-25.11.2021, 10th Asian Conference on High Pressure Research (virtual), Korea (*invited*): "Room-temperature Verwey-type transition in high-pressure iron oxide (Fe_5O_6)"

PAUSCH, T.; VAZHAKUTTIYAKAM, J.; WITHERS, A.C.; JOACHIM-MROSKO, B.; KONZETT, J.: 01.-03.03.2021, EMPG-XVII, virtual meeting[*A]: "Tuite, γ-$Ca_3(PO_4)_2$ in peridotitic bulk composition: Phase stability and volatile incorporation in the upper to lower mantle transition zone"

POHLNER, J.; EL KORH, A.; CHIARADIA, M.; MCCAMMON, C.; GROBÉTY, B.; KLEMD, R.: 29.08.-02.09.2021, EMC2020, 3rd European Mineralogical Conference, Cracow, Poland (virtual): "Inter-mineral Fe isotope fractionation in eclogites of the Münchberg massif (Germany) as a function of oxidation state"

POHLNER, J.E.; KORH, A.E.; CHIARADIA, M.; MCCAMMON, C.; RUBATTO, D.; KLEMD, R.; GROBÉTY, B.: 19.-20.11.2021, 19th Swiss Geoscience Meeting, Geneva, Switzerland: "Inter-mineral iron and oxygen isotope fractionation in eclogites of the Münchberg Massif (Germany)"

PUREVJAV, N.: 14.06.2021, Technische Universität München, Germany, online (*invited*): "Water incorporation mechanisms in the Earth's deep mantle minerals by neutron diffraction"

PUREVJAV, N.; BOFFA BALLARAN, T.; FEI, H.; WITHERS, A.C.; HOFFMANN, C.; KATSURA, T.: 22.-24.09.2021, Multianvil Workshop – UltraLVP, Bayerisches Geoinstitut, Bayreuth, Germany (virtual): "Hydrogen incorporation mechanism in olivine by time-of-flight single crystal neutron diffraction"

REGER, P.M.; ZHANG, B.; GANNOUN, A.M.; REGELOUS, M.; AGEE, C.B.; BOUVIER, A.: 15.-21.08.2021, 84th Annual Meeting of the Meteoritical Society, Chicago, USA: "Chronology of the Unique Angrite Northwest Africa 10463", Abstract 6235

REGER, P.M.; ZHANG, B.; GANNOUN, A.M.; REGELOUS, M.; AGEE, C.B.; BOUVIER, A.: 01.-05.11.2021, GAC-MAC London 2021 Joint Annual Meeting, London, Canada (online): "Chronology of the Unique Angrite Northwest Africa 10463", Abstract p. 265

RUSTIONI, G.; AUDÉTAT, A.; KEPPLER, H.: 01.-03.03.2021, EMPG-XVII, virtual meeting[*A]: "Assessment of the reliability of the diamond trap method to determine the composition of high-pressure aqueous fluids"

SAN JOSÉ MÉNDEZ, A.; TRYBEL, F.; HUSBAND, R.; STEINLE-NEUMANN, G.; LIERMANN, H.-P.; MARQUARDT, H.: 01.-03.03.2021, EMPG-XVII, virtual meeting[*A]: "Time-resolved X-ray diffraction measurements of the ice VII – ice X transition in a dynamic diamond-anvil cell"

SATTA, N.; CRINITI, G.; KURNOSOV, A.; BOFFA BALLARAN, T.; ISHII, T.; MARQUARDT, H.: 01.-03.03.2021, EMPG-XVII, virtual meeting[*A]: "High pressure single-crystal elasticity of δ-$(Al_{0.97}Fe_{0.03})OOH$"

SATTA, N.; MORALES, L.F.G.; CRINITI, G.; KURNOSOV, A.; BOFFA BALLARAN, T.; SPEZIALE, S.; MARQUARDT, H.: 13.-17.12.2021, AGU Fall Meeting 2021, New Orleans, USA (virtual): "Single-crystal elasticity of antigorite at high pressures and seismic signature of subducted antigorite-bearing rocks"

SAWA, S.; MIYAJIMA, N.; MUTO, J.; NAGAHAMA, H.: 07.-11.06.2021, Earth, Sea and Sky VI: International Joint Graduate Program Workshop in Earth and Environmental Sciences, Sendai, Japan: "Strain-induced partial serpentinization of germanate olivine with a small amount of water"

SCARANI, A.; VONA, A.; AL-MUKADAM, R.; DI GENOVA, D.; DEUBENER J.: 06.-09.04.2021, 4. Conferenza "A. Rittmann per Giovani" 2021 (online): "Estimating cooling rates recorded by glass-forming melts: a DSC calibration"

SCHWARZ, W.H.; HOPP, J.; LUDWIG, T.; BOUVIER, A.; TRIELOFF, M.; MA, N.; GAIL, H.-P.; NEUMANN, W.: 15.-19.03.2021, 52nd Lunar and Planetary Science Conference, virtual: "Pb-Pb ages of chondritic phosphates", Abstract 1981

STABILE, P.; SICOLA, S.; GIULI, G.; PARIS, E.; CARROLL, M.R.; DEUBENER, J.; DI GENOVA, D.: 01.-03.03.2021, EMPG-XVII, virtual meeting[*A]: "A combined Raman spectroscopy and DSC study on the nanocrystal-free viscosity of volcanic melts"

STAGNO, V.; BINDI, L.; BONECHI, B.; GREAUX, S.; IRIFUNE, T.; LUPI, S.; MARRAS, G.; MCCAMMON, C.A.; NAZZARI, M.; PICCIRILLI, F.; POE, B.T.; ROMANO, C.; SCARLATO, P.: 22.-24.09.2021, Multianvil Workshop – UltraLVP, Bayerisches Geoinstitut, Bayreuth, Germany (virtual): "Synthesis and characterization of Na-rich cubic majorite"

THIELMANN, M.; GOLABEK, G.; MARQUARDT, H.: 19.-30.04.2021, EGU General Assembly 2021, online: "The importance of phase morphology for rheology of ferropericlase-bridgmanite mixtures", EGU21-4384

THIELMANN, M.; SCHMALHOLZ, S.: 30.08.2021, German-Swiss Geodynamics Workshop, Bad Belzig, Germany: "Contributions of grain size reduction and shear heating to slab detachment"

VLASOV, K.; KEPPLER, H.: 01.-03.03.2021, EMPG-XVII, virtual meeting[*A]: "Electrical conductivity of H_2O-KCl fluids up to 4 GPa and 900 °C"

WEGNER, L.; BURTON, E.; MCCAMMON, C.; PEIFFER, S.; PLANER-FRIEDRICH, B.; HOCKMANN, K.: 14.10.2021, 13th BayCEER Workshop, Bayreuth: "Mobility of toxic antimony during aeration of Fe(II)-rich waters"

YUAN, L.; STEINLE-NEUMANN, G.: 09.-10.09.2021, 9th Joint Workshop on High Pressure, Planetary and Plasma Physics (HP4), Münster (virtual): "Thermal conductivity of $CaSiO_3$ perovskite at high pressure and temperature determined by machine learning potentials"

[*A] **EMPG-XVII – 17th International Symposium on Experimental Mineralogy, Petrology and Geochemistry, Potsdam, Germany (virtual meeting), 01.-03.03.2021**

4.4 Lectures and seminars at Bayerisches Geoinstitut

ABEYKOON, Sumith, Bayerisches Geoinstitut, Bayreuth, Germany (online): "Deuterium content and site occupancy in iron sulphide at high pressure and high temperature: Implications for the oxidation of early Earth's mantle", 28.10.2021

ALVARO, Matteo, Università degli Studi di Pavia, Experimental Mineralogy Lab, Department of Earth and Environmental Science, Pavia, Italy (online): "Mineral inclusions trapped in mineral hosts: A natural 'high pressure' experiment", 15.04.2021

BANERJEE, Anupam, Indian Institute of Science, Center for Earth Sciences, Bangalore, India (online): "Calcium isotopic compositions of carbonatites and implications for crustal recycling through time", 06.10.2021

CALOGERO, Meredith, University of Michigan, Earth and Environmental Sciences, Ann Arbor, USA (online): "High-resolution numerical thermal modeling of the mechanisms and timescales of mixed rhyolite genesis and transport as a consequence of basalt influx: applications to the long valley volcanic field, CA", 13.09.2021

CAMPOMENOSI, Nicola, Universität Hamburg, Mineralogisch-Petrographisches Institut, Hamburg, Germany (online): "Raman spectroscopy on mineral inclusions: defining P and T of metamorphic processes", 11.11.2021

CARTIER, Camille, Université de Lorraine, France (online): "A large proto-Mercury as the aubrite parent body", 02.12.2021

CERANTOLA, Valerio, European XFEL, Hamburg, Germany (online): "New frontiers in extreme conditions science at the European Free Electron Laser", 18.11.2021

COMBONI, Davide, ESRF Grenoble, France (online): "High-pressure behaviours and phase transitions in borates", 28.01.2021

CRINITI, Giacomo, Bayerisches Geoinstitut, Bayreuth, Germany (online): "Single-crystal elasticity of $MgSiO_3$ bridgmanite to mid-lower mantle pressure", *Academy Commission Business Meeting*, 07.05.2021

DEBRET, Baptiste, Institut de Physique du Globe de Paris, France (online): "Redox record of the serpentinized forearc mantle wedge", 17.05.2021

FUCHS, Lukas, Goethe-Universität Frankfurt, Geodynamics, Frankfurt/M., Germany (online): "Deformation and rheological memory in plate-like mantle convection", 10.06.2021

FURI, Evelyn, CRPG Nancy, France (online): "Origin and evolution of nitrogen on planetary bodies in the inner solar system", 21.10.2021

GIORDANO, Guido, Universitá Roma Tre, Dipartimento di Science, Roma, Italy (online): "Temperatures of pyroclastic density currents and the case of a preserved vitrified brain tissue at Herculaneum (Vesuvius 79 AD eruption)", 27.05.2021

HU, Justin, University of Chicago, Department of Geopyhsical Sciences, Chicago, USA (online): "Heating events in the nascent Solar System recorded by rare earth element isotopic fractionation in refractory inclusions", 21.01.2021

KRUPP, Alena, Bayerisches Geoinstitut, Bayreuth, Germany (online): "27Al-NMR of aluminium-bearing bridgmanite", 23.09.2021

KUMARI, Seema, Indian Institute of Technology, Department of Earth Sciences, Kanpur, India (online): "Open system evolution of long-lived and short-lived isotope systems in Earth's reservoirs: Implications for core formation, late accretion, and crust-mantle differentiation", 15.09.2021

KURNOSOV, Alexander, Bayerisches Geoinstitut, Bayreuth, Germany (online): "Flexible CO_2 laser heating system coupled with Brillouin spectroscopy", 25.11.2021

KUWAYAMA, Yasuhiro, Universität Tokyo, Department of Earth and Planetary Science, Tokyo, Japan (online): "Density and sound velocity of liquid Fe at high pressure: Implications for the composition of the Earth's core", 10.05.2021

MORBIDELLI, Alessandro, Observatoire de la Cote d'Azur, Nice, France (online): "Contemporary formation of early Solar System planetesimals at two distinct radial locations. Implications on Earth's origin", 09.12.2021

MUNDL-PETERMEIER, Andrea, Universität Wien, Department für Lithosphärenforschung, Wien, Austria (online): "Tungsten isotopes and their implications for the evolution of Earth's mantle", 17.06.2021

ORTENZI, Gianluigi, Deutsches Zentrum für Luft- und Raumfahrt, Berlin, Germany (online): "Interior-surface-atmosphere interactions: simulation of rocky planets outgassing and volatile chemical speciation for the C-O-H system", 17.09.2021

PAHLEVAN, Kaveh, SETI Institute, Mountain View, USA (online): "Magma ocean outgassing on Earth and Mars recorded in D/H", 25.01.2021

PAUL, Jyotirmoy, Indian Institute of Science, Bangalore, India (online): "On survival and destruction of cratons", 01.07.2021

PUSOK, Adina, Universität Oxford, Department of Earth Sciences, Oxford, U.K. (online): "Building models of mid-ocean ridges: application of buoyancy-driven flow due to chemical heterogeneities", 20.05.2021

QUANZ, Sascha, ETH Zurich, Institute for Particle Physics and Astrophysics, Zurich, Switzerland (online): "Towards the direct detection of terrestrial exoplanets"

RÜPKE, Lars, GEOMAR Kiel, Germany (online): "Oceanic Transform Faults revisited – are they extensional at depth?", 24.06.2021

SANO-FURUKAWA, Asami, J-PARC, Japan (online): "Studies on planetary material at PLANET: high pressure neutron diffractometer at J-PARC", 31.05.2021

SCHÖNBÄCHLER, Maria, ETH Zurich, Institute of Geochemistry and Petrology, Zurich, Switzerland (online): "Building planets: Lessons from meteorites", 11.02.2021

SIKDAR, Jinia, University of Wollongong, Australia (online): "Insights into Earth's early accretion history from Si, Mg, and Fe isotope composition of enstatite chondrites", 04.10.2021

STAGNO, Vincenzo, Sapienza University Rome, Dipartimento di Scienze della Terra, Rome, Italy (online): "Viscosity and molecular structure of CO_2-bearing melts in the interior of Earth", 12.07.2021

THIEMENS, Maxwell, Vrije Universiteit Brussel, Chemistry Department, Brussels, Belgium (online): "Isotopic perspectives on lunar formation and evolution", 05.10.2021

WICHT, Johannes, Max Planck Institut für Sonnensystemforschung, Göttingen, Germany (online): "Simulating the Geodynamo: From fast waves to slow changes of reversal rates", 04.02.2021

4.5 Conference organization

01.-03.03.2021, 17th International Symposium on Experimental Mineralogy, Petrology and Geochemistry, online, Scientific Committee (D. DOLEJŠ, F. HOLTZ, S. JAHN, S. KLEMME, F. LANGENHORST, M. KOCH-MÜLLER, C. MCCAMMON, C. SANCHEZ-VALLE, M. WILKE)

19.-30.04.2021, EGU General Assembly 2021: 'Solving geoscience problems using mineralogy' (J. INGRIN, C. MCCAMMON, J. MAJZLAN, E. ZHITOVA)

19.-30.04.2021, EGU General Assembly 2021, Session PS1.1 'Rocky planets around the Sun and other stars – bulk, interiors, atmospheres, and their interdependent evolution', online (H. WANG, G. GOLABEK, C. DORN, C. GILLMANN, D.J. BOWER, A. HUNT)

04.-09.07.2021, Goldschmidt Virtual 2021, Chair of the Science and Organising Committees (D.J. FROST, M. BOYET)

29.08.-01.09.2021, Deutsch-Schweizerischer Geodynamik Workshop, Bad Belzig, Germany (G. GOLABEK)

29.08.-03.09.2021, EMC2020, 3rd European Mineralogical Conference, Cracow, Poland (virtual): 'Spotlight on oxidation state and other redox proxies from Earth's surface to core' (F. GAILLARD, C. MCCAMMON, V. STAGNO)

22.-24.09.2021, International Workshop on 'Development of multianvil technology and its applications to Earth and material sciences' virtual by Zoom (T. KATSURA)

5. Visiting Scientists

5.1 Visiting scientists funded by the Bayerisches Geoinstitut

KIESSL, Nico, Staatliche Fachoberschule Traunstein, Germany: 06.-09.09.2021

MASOTTA, Matteo, Università di Pisa, Dipartimento di Scienze della Terra, Pisa, Italy: 26.-30.09.2021

5.2 Visiting scientists supported by other externally funded BGI projects

ASLANDUKOV, Matvii, Kharkiv National University of Radio Electronics, Ukraine: 20.10.-30.12.2021 (DFG[*B])

WALTE, Nico, TU München, Forschungs-Neutronenquelle Heinz Maier-Leibnitz (FRM II), Garching, Germany: 19.-23.07.2021, 27.09.-01.10.2021 (BMBF[*A])

[*A] BMBF: Bundesministerium für Bildung und Forschung

[*B] DFG: Deutsche Forschungsgemeinschaft

5.3 Visitors (externally funded)

DWIVEDI, Anand Prashant, European X-ray Free Electron Laser GmbH, Schenefeld, Germany: 04.-08.10.2021

FACCINCANI, Luca, Università degli Studi di Ferrara, Dipartimento di Fisica e Scienze della Terra, Ferrara, Italy: 22.09.-21.12.2021

FUCHS, Lukas, Goethe-Universität Frankfurt/M., Geodynamics Research Group, Frankfurt/M., Germany: 05.-07.10.2021

GÜLCHER, Anna, ETH Zurich, Institute of Geophysics, Zurich, Switzerland: 05.-07.10.2021

HECKEL, Catharina, Goethe-Universität Frankfurt/M., Institut für Geowissenschaften, Frankfurt/M, Germany: 11.-15.10.2021

KULKA, Britany, University of Oxford, Department of Earth Sciences, Oxford, U.K.: 13.-31.12.2021

LEINENWEBER, Kurt, Arizona State University, Eyring Materials Center, Tempe, USA: 13.-17.11.2021

NAVROTSKY, Alexandra, Arizona State University, School of Molecular Sciences, Tempe, USA: 15.-17.11.2021

PAUSCH, Tristan, Universität Innsbruck, Institut für Mineralogie und Petrographie, Austria: 13.-23.09.2021, 19.-26.11.2021

RASHCHENKO, Sergey, Novosibirsk State University, Sobolev Institute of Geology and Mineralogy, Novosibirsk, Russia: 29.11.-04.12.2021

RÖSCHE, Constanze, Universität Hamburg, Mineralogisch-Petrographisches Institut, Hamburg, Germany: 06.-10.12.2021

SAWA, Sando, Tohoku University, Department of Earth Science, Sendai, Japan: 03.-26.10.2021, 26.11.-10.12.2021

SCHELHORN, Andreas, Universität Ulm, Institut für Organische Chemie III, Ulm, Germany: 10.-12.11.2021, 16.-19.11.2021

SHARP, Thomas, Arizona State University, School of Earth and Space Exploration, Tempe, USA: 13.-17.11.2021

SIERSCH, Nicki, Sorbonne Université, IMPMC, Paris, France: 08.-16.06.2021, 28.06.-02.07.2021, 23.08.-03.09.2021

TAKAHASHI, Naoko, Tohoku University, Department of Earth Science, Sendai, Japan: 06.-24.12.2021

VAZHAKUTTIYAKAM, Jaseem, Universität Innsbruck, Institut für Mineralogie und Petrographie, Austria: 13.-22.09.2021

6. Additional scientific activities

6.1 Habilitation/Theses

Habilitation

MEIER, Thomas: Superconductivity: Principles, applications and the quest for room temperature.

Ph.D. theses

FERREIRA, Filippe: The role of grain boundaries for the deformation and grain growth of olivine at upper mantle conditions.
KOEMETS, Egor: The crystal chemistry of iron oxides and oxyhydroxides at extreme conditions: implications for the deep Earth's oxygen cycle.
MARZOTTO, Enrico: A combined study on Earth's deep water cycle using numerical modelling and laboratory experiments.
MÉNDEZ, Alba S.J.: Planetary materials studied by time-resolved X-ray diffraction under compression in dynamic diamond anvil cells.
YAO, Jie: Constraints on magma ocean crystallization in the early Earth: Experiments, thermodynamics and ab initio simulations.

M.Sc. theses

KRUPP, Alena: ^{27}Al-NMR of aluminium-bearing bridgmanite.
PUTRA, Rizaldi: Melt chemistry control on crystal and bubble formation in basalts.

6.2 Honours and awards

BYKOVA, Elena	Wallenberg Academy Fellow 2021 of the Knut and Alice Wallenberg Foundation, Sweden
ISHII, Takayuki	Early Career Award 2021 of the Mineral and Rock Physics Sektion of the American Geophysical Union

6.3 Editorship of scientific journals

AUDÉTAT, Andreas	Associate Editor "Journal of Petrology" Associate Editor "Economic Geology

BOUVIER, Audrey	Associate Editor "Geochimica et Cosmochimica Acta" Guest Editor "Progress in Earth and Planetary Sciences", Special Issue "Thermal, dynamical, and chemical processes in our early Solar System"
DI GENOVA, Danilo	Editorial Board Member "Journal of Volcanology and Geothermal Research"
DUBROVINSKY, Leonid	Member, Editorial Board of the Journal of "High Pressure Research" Member, Advisory Board, Minerals
KEPPLER, Hans	Editorial Board "Contributions to Mineralogy and Petrology" Editorial Board "ACS Earth and Space Chemistry"
MCCAMMON, Catherine	Chief Editor and Managing Editor "Physics and Chemistry of Minerals"
MIYAJIMA, Nobuyoshi	Associate Editor "European Journal of Mineralogy"

6.4 Membership of scientific advisory bodies

BOFFA BALLARAN, Tiziana	"EMU Research Excellence Medal" Medallist Committee member Member of the proposal review panel "Hard condensed matter – structures" at Elettra synchrotrone, Trieste, Italy
BOUVIER, Audrey	Chair, Nomenclature Committee of the Meteoritical Society Chair, Evaluation panel CE49, Agence Nationale de la Recherche Member, V. M. Goldschmidt Award Committee, Geochemical Society Member, Hayabusa2 initial sample analysis chemistry team, Japan Aerospace Exploration Agency Member, Mars Sample Return Caching Strategy Steering Committee, NASA and ESA Member, International Lunar Research Team, ESA Member, Scientific committee, ATTARIK Foundation

DUBROVINSKY, Leonid	Member, Review Panel of Canadian Light Source Chair Subcomission on Spectroscopy, Diffraction, and new Instrumentations in Mineral Physics of the International Mineralogical Association Member Review Panel of PETRA III Member Review Panel of Research Council of Lithuania
FROST, Dan	Member, Bavarian Academy of Sciences Member, German National Academy of Sciences (Leopoldina) Member of the Selection committee for Alexander von Humboldt Professorships Member, Royal Society Scientific Advisory Committee of the GeoForschungsZentrum Potsdam Member, Starting Grant Rewiew Panel P10, European Research Council
KEPPLER, Hans	Member, German National Academy of Sciences (Leopoldina) Member, Bavarian Academy of Sciences Member, Advisory Board, Dachverband Geowissenschaften
MCCAMMON, Catherine	Chair, Starting Grant Panel PE10, European Research Council Chair, Governance Review Task Force, American Geophysical Union Member, Project Review Panel P01, PETRA III Member, Beamline Review Panel ID18, ESRF Member, Council, International Mineralogical Association Member, Fellows Committee, VGP section, American Geophysical Union Member, Award Committee of the International Board on the Applications of Mössbauer Spectroscopy Chair, Sub-committee "Earth's Deep Interior" of the Commission of the Physics of Minerals, International Mineralogical Association Member, International Scientific Committee, 23rd General Meeting of the International Mineralogical Association, 2022

7. Scientific and Technical Personnel

Name		Position	Duration in 2021	Funding source
ABEYKOON, Sumith	M.Sc.	Wiss. Mitarbeiter	to 31.07 from 01.08.	IRTG Leibniz
ASLANDUKOV, Andrii	M.Sc.	Wiss. Mitarbeiter	from 17.12.	DFG
ASLANDUKOVA, Alena	M.Sc.	Wiss. Mitarbeiterin		DFG
AUDÉTAT, Andreas	Dr.	Akad. Oberrat		BGI
BAUER, Gerald	Dipl.-Ing. (FH)	Techn. Angestellter		BGI
BOFFA BALLARAN, Tiziana	Dr.	Akad. Oberrätin		BGI
BONDAR, Dmitry	M.Sc.	Wiss. Mitarbeiter		DFG
BOUVIER, Audrey	Prof. Dr.	Professorin		BGI
BUCHERT, Petra		Fremdsprachen-Sekretärin		BGI
BYKOVA, Elena	Dr.	Wiss. Mitarbeiterin	from 01.10.	DFG
CALVO, Lucas		Student. Hilfskraft	to 30.06. 01.07.-30.11. from 01.12.	DFG UBT DFG
CHAKRABORTI, Amrita	Dr.	Wiss. Mitarbeiterin	from 01.09.	DFG
CHANG, Jia	Dr.	Wiss. Mitarbeiter	from 15.01.	DFG
CHANYSHEV, Artem	Dr.	Wiss. Mitarbeiter	to 30.06. from 01.07.	BMBF EU
CIALDELLA, Laura	M.Sc.	Wiss. Mitarbeiterin	to 14.10.	IRTG
CRINITI, Giacomo	M.Sc.	Wiss. Mitarbeiter		Leibniz
CZEKAY, Laura	M.Sc.	Wiss. Mitarbeiterin		DFG
DINIUS, Anna		Verwaltungsangestellte		BGI
DI GENOVA, Danilo	Dr.	Akad. Rat a.Z.	to 15.12.	BGI
DOLINSCHI, Jonathan	M.Sc.	Wiss. Mitarbeiter	to 30.11. from 01.12.	DFG Leibniz
DOMINIJANNI, Serena	M.Sc.	Wiss. Mitarbeiter	to 31.07. 01.08.-30.10.	IRTG Leibniz
DUBROVINSKY, Leonid	Apl. Prof. Dr.	Akad. Direktor		BGI
EBERHARD, Lisa	M.Sc.	Wiss. Mitarbeiterin	to 31.08.	Leibniz
FEDOTENKO, Timofey	Dr.	Wiss. Mitarbeiter	01.07.-30.09.	DFG
FANG, Jing	Dr.	Stipendiat	to 30.04.	DAAD
FEI, Hongzhan	Dr.	Wiss. Mitarbeiter		BGI
FISCHER, Heinz		Mechaniker		BGI
FLANIGAN, Michaela	M.Sc.	Wiss. Mitarbeiterin	to 08.09.	Leibniz
FROST, Daniel	Prof. Dr.	Stellvertr. Leiter		BGI

GOLABEK, Gregor	Prof. Dr.	Professor		BGI
HEIDELBACH, Florian	Dr.	Wiss. Mitarbeiter		BGI
HIN, Remco	Dr.	Wiss. Mitarbeiter		EU
HOWARD, Christopher	Dr.	Wiss. Mitarbeiter		BMBF
HUANG, Rong	Dr.	Wiss. Mitarbeiterin	to 15.05.	Leibniz
KATSURA, Tomoo	Prof. Dr.	Professor		BGI
KEPPLER, Hans	Prof. Dr.	Leiter		BGI
KIM, Eun Jeong	Dr.	Wiss. Mitarbeiterin	to 28.02.	EU
		Stipendiatin	from 01.03.	AvH
KOEMETS, Iuliia	M.Sc.	Wiss. Mitarbeiterin	to 31.05.	DFG
KRAUßE, Detlef	Dipl.-Inform. (FH)	Techn. Angestellter		BGI
KRIEGL, Holger		Haustechniker		BGI
KRUPP, Alena	B.Sc.	Student. Hilfskraft	to 31.03.	BGI
KUBIK, Edith	Dr.	Wiss. Mitarbeiterin	from 01.08.	BGI/VP
KURNOSOV, Alexander	Dr.	Wiss. Mitarbeiter		DFG
LANGHAMMER, Dominic	M.Sc.	Wiss. Mitarbeiter		DFG
LINHARDT, Sven		Elektrotechniker		BGI
LIU, Dan		Stipendiatin	to 19.12.	CSC
LIU, Siqi		Stipendiat		CSC
MAN, Lianjie	M.Sc.	Wiss. Mitarbeiter		Leibniz
MARZOTTO, Enrico	M.Sc.	Wiss. Mitarbeiter	to 14.02.	IRTG
MATTHÄUS, Rebecka		Chem.-Techn. Assistentin		BGI
MCCAMMON, Catherine	Privatdozentin Dr.	Akad. Direktorin		BGI
MEIER, Thomas	Dr.	Wiss. Mitarbeiter	to 30.06.	DFG
MELAI, Caterina	M.Sc.	Wiss. Mitarbeiterin		Leibniz
MIYAJIMA, Nobuyoshi	Dr.	Akad. Oberrat		BGI
NÉRI, Adrien	Dr.	Wiss. Mitarbeiter		Leibniz
NJUL, Raphael		Präparator		BGI
OVSYANNIKOV, Sergey	Dr.	Wiss. Mitarbeiter		DFG
PAUL, Jyotirmoy	Dr.	Wiss. Mitarbeiter	from 02.11.	EU
PICCOLO, Andrea	Dr.	Wiss. Mitarbeiter	from 01.11.	DFG
PÖPPELBAUM, Melanie	B.Sc.	Student. Hilfskraft	to 31.03.	DFG
			01.04.-30.09.	UBT
			from 01.10.	DFG
POSNER, Esther	Dr.	Wiss. Mitarbeiterin		DFG
POTZEL, Anke		Chem.-Techn. Assistentin		BGI
POTZEL, Janina		Sekretärin		BGI

PUREVJAV, Narangoo	Dr.	Wiss. Mitarbeiterin		BGI/VP
PUTAK JURIČEK, Marija	M.Sc.	Wiss. Mitarbeiterin	to 15.01.	EU
			16.01.-31.05.	DFG
PUTRA, Rizaldi	B.Sc.	Student. Hilfskraft	to 30.09.	BGI
RAMMING, Gerd		Elektroniker		BGI
RAUSCH, Oliver		Mechaniker		BGI
ROGMANN, Elena	B.Sc.	Student. Hilfskraft	to 31.03.	DFG
			01.04.-30.11.	BGI
			from 01.12.	DFG
ROTHER, David Alexander		Präparator		BGI
RUBIE, David C.	Prof. Dr.	Professor	to 30.04.	EU
			from 01.05.	DFG
RUSTIONI, Greta	Dr.	Wiss. Mitarbeiterin		DFG
SCHULZE, Hubert		Präparator		EU
SCHULZE, Kirsten	Dr.	Wiss. Mitarbeiterin	01.06.-31.08.	DFG
STEINLE-NEUMANN, Gerd	Privatdozent Dr.	Akad. Oberrat		BGI
TANG, Hu	Dr.	Stipendiat	from 01.08.	AvH
THIELMANN, Marcel	Dr.	Wiss. Mitarbeiter	to 31.05.	BGI/VP
			from 01.06.	DFG
TRENZ, Ulrike		Biol.-Techn. Assistentin		BGI
ÜBELHACK, Stefan		Mechaniker		BGI
VALDIVIA MUNOZ, Pedro Antonio	M.Sc.	Wiss. Mitarbeiter	from 01.10.	DFG
VLASOV, Kirill	M.Sc.	Wiss. Mitarbeiter	to 28.02.	BMBF
			from 01.03.	DFG
WANG, Fei	Dr.	Wiss. Mitarbeiter	from 01.07.	EU
WANG, Lin	Dr.	Wiss. Mitarbeiter		EU
WANG, Xiaoyu	B.Sc.	Student. Hilfskraft	to 30.06.	DFG
			from 01.07.	BGI
WIESNER, Dorothea		Techn. Assistentin		BGI
WITHERS, Antony	Dr.	Wiss. Mitarbeiter		BGI
XIE, Longjian	Dr.	Wiss. Mitarbeiter	to 14.11.	Carnegie
YUAN, Liang	Dr.	Wiss. Mitarbeiter	to 17.01.	DFG
			18.01.-30.04.	BGI/VP
		Stipendiat	from 01.05.	AvH
ZHANG, Jingbo	M.Sc.	Stipendiat	from 15.01.	CSC
ZHAO, Ran	B.Sc.	Student. Hilfskraft	to 31.03.	DFG
			01.04.-30.09.	BGI
			from 01.10.	DFG

Abbreviations/explanations:

AvH	Alexander von Humboldt Foundation
BGI	Staff Position of Bayerisches Geoinstitut
BGI/VP	Visiting Scientists' Program of Bayerisches Geoinstitut
BMBF	Federal Ministry of Education and Research
Carnegie	Carnegie Institution of Washington
DAAD	German Academic Exchange Service
CSC	China Scholarship Council
DFG	German Science Foundation
EU	European Union
IRTG	International Research Training Group "Deep Earth Volatile Cycles"
Leibniz	Leibniz-Preis der Deutschen Forschungsgemeinschaft Prof. Frost
UBT	Universität Bayreuth

Index